Novel applications of Maxwell's equations to quantum and thermal phenomena

ARCHIVES

by

Alexander P. McCauley

B.S., California Institute of Technology (2006)

Submitted to the Department of Physics
in partial fulfillment of the requirements for the degree of

Doctor of Philosophy

at the

MASSACHUSETTS INSTITUTE OF TECHNOLOGY

August 2011

© Massachusetts Institute of Technology 2011. All rights reserved.

Author .....
Department of Physics
August 26th, 2011

Certified by .....
Steven G. Johnson
Associate Professor of Applied Mathematics
Thesis Supervisor

Certified by .....
John D. Joannopoulos
Francis Wright Davis Professor of Physics
Thesis Supervisor

Accepted by .....
Krishna Rajagopal
Associate Department Head for Education

Novel applications of Maxwell's equations to quantum and thermal phenomena

by

Alexander P. McCauley

Submitted to the Department of Physics
on August 26th, 2011, in partial fulfillment of the
requirements for the degree of
Doctor of Philosophy

Abstract

This thesis is concerned with the extension of Maxwell's equations to situations far removed from standard electromagnetism, in order to discover novel phenomena. We discuss our contributions to the efforts to describe quantum fluctuations, known as Casimir forces, in terms of classical electromagnetism. We prove that chirality in metamaterials can have no appreciable effect on the Casimir force, and design an alternative metamaterial in which the structure can have a strong effect on the Casimir force. We present a geometry that exhibits a repulsive Casimir force between metallic objects in vacuum, and describe our efforts to enhance this repulsive force using the numerical techniques that we and others developed. We then show how our techniques can be extended to study the physics of near-field radiative heat transfer, computing for the first time the exact heat transfer and power flux profiles between a plate and non-spherical objects. We find in particular that the heat flux profile is non-monotonic in separation from the cone tip. Finally, we demonstrate how techniques to compute photonic bandstructures in periodic systems can be extended to certain types of *quasi*-periodic structures, termed photonic-quasicrystals (PQCs).

Thesis Supervisor: Steven G. Johnson
Title: Associate Professor of Applied Mathematics

Thesis Supervisor: John D. Joannopoulos
Title: Francis Wright Davis Professor of Physics

Acknowledgments

I can only begin by thanking my adviser Prof. Steven G. Johnson for all of his time an insight. Aside from many things too numerous to describe, I learned from him the real benefit of doing things the *right* way. Much new work in science follows from the seemingly effortless way in which previous knowledge and work can be extended into new directions, provided it is first understood in the most general context possible. Steven is a master of this process, and over the years I have learned by emulation how to go beyond my instinct for quick-and-dirty solutions.

I am grateful to my co-adviser Prof. John Joannopoulos for our discussions on the "big-picture" aspects of my research, as well as for all of his help on my post grad school career options.

It has been a great privilege to work with my friends and collaborators: Dr. Alejandro Rodriguez-Wong, Dr. Homer Reid as well as Dr. Matthias Krüger, and Dr. Michael Levin. I have had a great time with the other SGJ group members, in particular Dr. Hila Hashemi, Dr. Ardavan Oskooi, and Dr. Karen Lee, as well as Dr. Peter Bermel and Dr. Aristeidis Karalis as well as other CMT alumna, including Dr. Maissam Barkeshli, Dr. S. Jamal Rahi, and Dr. Nan Gu, and Prof. Ken Kamrin and Dr. Ramis Movassagh from the applied math department. I would also like to thank my friend Steve Voinea; additionally, I want to give an special thanks to my friend Dr. Kasia Gora.

Lastly, I would like to thank my parents, my grandmother, Alison and Toby, Steven and Irwin for being such wonderful family.

This thesis is dedicated to my wonderful wife Katherine.

Contents

1 Introduction **29**

1.1 A brief introduction to Casimir forces 29

1.2 Casimir Forces in the time domain 31

1.3 The quest for Casimir repulsion 32

1.3.1 A Casimir metamaterial that does not work 33

1.3.2 A Casimir metamaterial that *does* work 33

1.3.3 Genuinely repulsive Casimir forces in vacuum 35

1.4 From quantum fluctuations to thermal fluctuations 37

1.5 Applying periodic techniques to non-periodic structures 39

2 Computing Casimir forces in the time domain **41**

2.1 Introduction 41

2.2 Background 42

2.2.1 The Stress Tensor Formulation and the Conductivity Mapping 42

2.2.2 Complex frequency and Wick rotation 44

2.2.3 Conductivity Mapping in the frequency domain 45

2.3 Mapping to the time domain 48

2.4 Harmonic Expansion 52

2.4.1 Numerical Implementation 54

2.5 Applications 54

2.5.1 Two-dimensional systems 55

2.5.2 Dispersive Materials 58

2.5.3 Three dimensions with cylindrical symmetry 61

2.5.4 Periodic Boundary Conditions 63
2.5.5 Full 3d computations: stable confinement in 3d 64
2.6 Finite temperature with FDTD 67
2.7 An alternative material transformation 70
2.8 Concluding Remarks 71
Appendix 2A: Functional treatment of $g(t)$ 72
Appendix 2B: Harmonic expansion in cylindrical coordinates 76

3 Microstructure effects for Casimir forces in chiral metamaterials 79
3.1 Introduction 79
3.2 Background 80
3.2.1 Casimir forces and Metamaterials 80
3.2.2 Chiral Metamaterials 81
3.3 Definitions and Methodology 83
3.4 Bent-arm crosses 84
3.4.1 Computational Method 85
3.4.2 Results 86
3.5 Omega particles 88
3.5.1 Computational Method 89
3.5.2 Results 92
3.5.3 Validity of EMA and the dilute approximation 94
3.6 Conclusions 96
Appendix 3: Computing multipole moments in BEM 96

4 Structural anisotropy and orientation-induced Casimir repulsion in fluids 101
4.1 Introduction 101
4.2 Preliminary Discussion 102
4.3 Method 105
4.4 Results 107
4.4.1 Vacuum-separated slabs 107

4.4.2 Fluid-separated slabs and tunable repulsion 109
4.4.3 Comparison with EMA 113
4.4.4 Forces for other geometries 116
4.5 Conclusions 118
Appendix 4A: Details of Computational Methods 118
Appendix 4B: Suppression of non-specular scattering 126

5 Casimir repulsion between metallic objects in vacuum 129
5.1 Introduction 129
5.2 Repulsion in the dipole regime 131
5.2.1 Symmetry Argument 131
5.2.2 Non-ideal geometric effects 133
5.2.3 3d force predictions 138
5.2.4 Stability 140
5.3 Casimir-Polder forces 142
5.3.1 More Directions of Anisotropy 145
5.3.2 Off-axis displacement 148
5.4 Repulsion beyond the dipole regime 149
5.4.1 Enhancement of fringing fields 152
5.4.2 Multiple cylinders and uniaxial capsules 156
5.5 Conclusions 161

6 Modeling near-field radiative heat transfer from sharp objects using a general 3d numerical scattering technique 163
6.1 Introduction 164
6.2 Method 165
6.2.1 Fluctuational Electrodynamics 165
6.2.2 Computation 168
6.3 Results 175
6.3.1 Total Power Transfer 176
6.3.2 Spatially-resolved Poynting flux 180

6.4 Conclusions 183
Appendix 5: Derivation of the $\mathbb{O}$ Operators 184

7 Computation and visualization of photonic quasicrystal spectra via Bloch's theorem 191

7.1 Introduction and Background 192
7.1.1 Quasicrystals via cut-and-project 194
7.1.2 Supercell approach 197
7.2 Computations in Higher Dimensions 198
7.2.1 Bloch's theorem and numerics for quasicrystals 200
7.2.2 The spectrum of the quasicrystal 201
7.3 One-dimensional results 202
7.3.1 Fibonacci quasicrystal 202
7.3.2 Defect modes 210
7.3.3 Continuously varying the cut angle 213
7.3.4 Smooth superspace structures 216
7.3.5 Optimization of one-dimensional smoothed structures 217
7.4 Two-dimensional results 220
7.4.1 Octagonal Quasicrystals 220
7.5 Concluding Remarks 223
7.5.1 Minimum sufficient conditions for a slice to densely fill the superspace unit cell 224
7.5.2 Spectral Correspondence 225

8 Conclusions and Outlook 227

List of Figures

1-1 Illustration of the basic physics behind Casimir forces. Left: a fluctuating dipole gives rise to an electric field, which induces a dipole polarization on a nearby neutral atom. This in turn produces a dipole field that interacts with the first dipole, resulting in an interaction energy. Right: in general, the interacting materials are no longer neutral particles, but extended objects composed of many fluctuating dipoles. 30

1-2 Three-dimensional configuration showing stable levitation. At the equilibrium point, the force of gravity counters the Casimir force, while the Casimir force from the walls of the spherical indentation confine the sphere laterally 32

1-3 Unit cell of the isotropic chiral metamaterial examined in Chapter 3: perfectly conducting "omega" particles in vacuum. The shaded cube indicates the relative positions in the unit cell 34

1-4 Configuration examined in Chapter 4. Each slab consists of a single periodic array of cylindrical wires embedded in a semi-infinite substrate; the goal is to create for each slab an effective anisotropic medium. Of interest here is the change in the force from when the wires are aligned (Top) and when they are crossed (Bottom). When the medium between the plates is a properly chosen fluid, we show that the force switches sign as a function of orientation for certain separations. . . . 35

1-5 Configuration used in Chapter 5 to achieve a repulsive force between an elongated particle and a thin plate with a hole, illustrated in panel (a). The physical mechanism relies on a symmetry argument involving the coupling of the dipole field of the particle to the plate, illustrated in panel (b). 37

1-6 Total thermal transfer between a silica plate and doped silicon objects of various shapes. The plate is semi-infinite, and the objects all have height equal to $1\,\mu$m in the z-direction. The plate/environment temperature is $T_P = 300\,$K and the objects are at temperature $T_A = 600\,$K. Red dots denote results with the sphere scattering matrix determined analytically, the only case in which we have an analytic solution for the scattering matrix. 38

1-7 Unit cell of the Fibonacci "superspace" dielectric, which when sliced along the X direction (which makes an angle $\tan\phi = \frac{1+\sqrt{5}}{2}$ with the horizontal) will yield a one-dimensional quasicrystal. We will see that this one-dimensional structure inherits many of the properties of the two-dimensional superspace. 39

2-1 Partial force as defined in eq. (2.23) for one-dimensional parallel plates as a function of time t. (Inset): Relative error $\Delta(t)$ as a function of t on a semi log scale. 50

2-2 $|\Im g(t)|$ for various values of σ, illustrating the transition from t^{-1} to $t^{-1/2}$ power-law decay as σ increases. Because there are strong oscillations in $g(t)$ at the Nyquist frequency for intermediate σ, for clarity we plot the positive and negative terms in $g(t)$ as separate components. 51

2-3 Schematic showing the two-dimensional piston-like configuration of [156]: Two perfectly conducting circular cylinders of radius R, separated by a distance a, are sandwiched between two perfectly conducting plates (the materials are either perfect metallic or perfect magnetic conductors). The separation between the blocks and the cylinder surface is denoted as h. 52

2-4 Differing harmonic expansions of the source currents (red) on the surface S. The left part shows an expansion using point sources, where each dot represents a different simulation. The right part corresponds to using $f_n(\mathbf{x}) \sim \cos(x)$ for each side of S. Either basis forms a complete basis for all functions in S. 54

2-5 Force for the double cylinders of [156] as a function of sidewall separation h/a, normalized by the PFA force $F_{\mathrm{PFA}} = \hbar c\zeta(3)d/8\pi a^3$. Red/blue/black squares show the TE/TM/total force in the presence of metallic sidewalls, as computed by the FDTD method (squares). The solid lines indicate the results from the scattering calculations of [156], showing excellent agreement. Dashed lines indicate the same force components, but in the presence of perfect magnetic-conductor sidewalls (computed via FDTD). Note that the total force is non-monotonic for electric sidewalls and monotonic for magnetic sidewalls. 57

2-6 (Color Online) $\Gamma^E_{yy;n=2}(t,\mathbf{x})$ snapshots (blue/white/red = positive/zero/negative) for the $n = 2$ term in the harmonic cosine expansion on the leftmost face of S for the double blocks configuration of [166] at selected times (in units of a/c). 58

2-7 Relative contribution of harmonic moment n in the cosine basis to the total Casimir force for the double blocks configuration (shown in the inset) 59

2-8 Force per unit length between long silicon waveguides suspended in air [103], determined by the FDTD method (red triangles). Also shown is the analogous one-dimensional computation assuming silicon plates of finite thickness (blue dashes), and the result $F = \pi^2/240d^4A$ for perfect metals (assuming plate area A equal to the interaction area of the waveguides). 60

2-9 Force as a function of outer sidewall spacing h/a for the cylindrically-symmetric piston configuration shown in the figure. Both plates are perfect metals, and the forces for both perfect metallic and perfect magnetic conductor sidewalls are shown. Note that in contrast to Fig. 2-5, here the force is monotonic in h/a for the metallic case and non monotonic for the magnetic case. 62

2-10 The Casimir force between a periodic array of Silicon waveguides and a Silicon/Silica substrate, as the array/substrate separation is varied. The system is periodic in the x-direction and translation-invariant in the z-direction, so the computation involves a set of two-dimensional simulations. 63

2-11 Three-dimensional configuration showing stable levitation. At the equilibrium point, the force of gravity counters the Casimir force, while the Casimir force from the walls of the spherical indentation confine the sphere laterally 65

2-12 Total (Casimir + gravity) vertical (z) force on the silica sphere (depicted in the inset) as the height h of the sphere's surface above the indentation surface is varied. The point of vertical equilibrium occurs at $h \sim 450$ nm. 66

2-13 Casimir restoring force on the sphere as a function of lateral displacement dx, when the vertical position is fixed at $h = 450$ nm, the height at which gravity balances the Casimir force 67

2-14 Plot of the force error (force after a finite time integration vs. the force after a very long run time) for $g(t)$ determined from a numerical transform as in Ref. 172 and from the analytic transform of the high-frequency components. Inset: $\Im[g(-t)]$ obtained without a cut-off, in which the high-frequency divergence is integrated analytically. Compare with Fig. 1 of Ref. 172. 74

3-1 Interactions between two chiral metamaterials [213]. The shaded box indicates a unit cell; the structures are periodic in the transverse direction. Nearest neighbor bars on opposing structures are colored yellow. In the EMA, the forces should obey $F_{SC} < F_{OC}$. By contrast, in the pairwise-force approximation the force is determined by the number of overlapping nearest-neighbor bars, as indicated: $F_{OC} > F_{SC}$ when the centers are aligned (left column), but $F_{OC} < F_{SC}$ when they are displaced by $L/2$ (right column). 84

3-2 Relative force difference $(F_{OC} - F_{SC})/F_{OC}$ for the left (red) and right (blue) columns of Fig. 3-1 for PEC (solid) and dispersive gold for $a = 1\ \mu m$ (dashed). From Fig. 3-1, the sign difference is due to proximity effects. The inset shows a zoom of the large-z regime, along with the EMA prediction (black). 86

3-3 *Top:* Unit cell of isotropic chiral metamaterial: PEC "omega" particles in vacuum. Shaded cube indicates relative positions in unit cell. *Bottom:* Effective-medium parameters, as a function of imaginary frequency $\omega = i\xi$, deduced directly from imaginary-ω scattering data. $\mu(0) \neq 1$ because the particles are PEC. 88

3-4 Forces (in dilute approximation) between chiral media from Fig. 3-3, for the SC (blue) and OC (red) cases. The range of the force across all transverse (x) displacements is shaded, and normalized by the minimum of the force over all x. For $z \lesssim 3.1a$, chirality is not well-defined (curves overlap). Only when curves are distinct and x-independent can the systems be described as chiral metamaterials. *Inset:* Frequency integrand of the relative force difference at $z = 3.6a$. The smallness of the $\omega = 0$ term is an indicator that this difference is due to chirality and not anisotropy (see text). 93

4-1 Configuration examined in the text. Each slab consists of a single periodic array of cylindrical wires embedded in a semi-infinite substrate; the goal is to create for each slab an effective anisotropic medium. Of interest here is the change in the force from when the wires are aligned (Top) and when they are crossed (Bottom). When the medium between the plates is a properly chosen fluid, we show that the force switches sign as a function of orientation for certain separations. . . . 103

4-2 Ratio of the Casimir force between crossed wire arrays (F_{crossed}) over aligned wires ($F_{\text{aligned}}(y)$) between vacuum-separated nanowires of perfect metal, gold, and doped silicon (dopant density $10^{20}/\text{cm}^3$). $a \to \infty$ corresponds to using non-dispersive $\varepsilon(i\xi \to 0)$ for all materials (because ξ is in units of c/a). Shaded regions indicate the range of values that F_{aligned} takes over all relative lateral displacements y of the wire centers, with their higher (lower) boundary indicating the force for $y = 0$ ($y = a/2$). PFA predicts, via eq. (4.1), that the maximum of this ratio should exceed 1, which is only true for Si at $d/a \sim 0.6$, and for gold/perfect metal at lower separations. Inset: details of the configuration examined. 110

4-3 Casimir pressure for the same parameters as the inset to Fig. 4-2, with a silica substrate and ethanol between the two slabs. Positive values indicate an attractive force, negative values (shaded) repulsive. Both $a \to \infty$ and $a = 100\,\text{nm}$ are shown. As in Fig. 4-2, shaded regions denote the range of y-displacements. When the wires are aligned (blue), the force is always attractive, but when the wires are crossed (red), the force turns repulsive at a critical separation $d > d_c$, which depends on a. 112

4-4 Forces computed for the configuration of Fig. 4-3 using the Proximity Force Approximation (PFA), for $a = 100\,\text{nm}$. For convenience in applying the PFA, square wires of width r are used instead of circular wires (the exact results are not qualitatively changed). We see that the behavior of Fig. 4-3 is not qualitatively captured: the force is always attractive for crossed wires, and the bound eq. (4.1) is strictly satisfied. Similar results are obtained for $a \to \infty$. 113

4-5 Effective-medium parameters for the system of Fig. 4-3 derived from scattering data for a length scale $a = 100\,\text{nm}$. $\varepsilon_{\parallel}$ is the effective dielectric parallel to the wires (black), and $\varepsilon_{\perp}$ the effective dielectric perpendicular to the wires (blue). The dielectrics of the constituent materials gold, silica, and ethanol are shown for reference. These dispersions will be used to compute the Casimir force in the effective-medium approximation below. 114

4-6 Results for the force computed in the Effective-medium Approximation (EMA) using an effective homogeneous, anisotropic permittivity tensor $\overleftrightarrow{\varepsilon}$, via the method described in Appendix 4A. As in Fig. 4-3, results for both a infinite (i.e., non-dispersive materials) and $a = 100\,\text{nm}$ are shown, for both crossed and aligned configurations. Although quantitatively inaccurate over the range plotted, the EMA does qualitatively capture the behavior of the force a opposed to PFA. Also shown are d_c, the location of the attractive-repulsive transitions for the crossed wires ($d_c = 0.18a$ for $a \to \infty$ and is not shown). 115

4-7 Forces for sphere-plate (red) and cylinder-plate configurations, for $a = 100\,\text{nm}$. In both cases, the wire pattern of Fig. 4-1 is stamped onto the surface of both objects, which have radii of curvature $R = 200\,\mu\text{m}$. The cylinder length is chosen to be $L = 16\,\mu\text{m}$ so that the two force curves have comparable magnitude; however the cylinder-plate force is proportional to L and so will be much larger in magnitude for a more realistic $L \sim R$. 117

4-8 Feynman rules for the diagrammatic expansion of the Casimir energy, following Ref. 110. In our notation, planewave states are indexed by their reciprocal lattice vector $\mathbf{G}_\perp = (G_y, G_z)$; frequency, polarization, and the conserved reduced Bloch vector $\mathbf{k}_\perp$ are suppressed as our focus is on non-specular (i.e., $\mathbf{G}_\perp$ not conserved) reflections. Here $\mathbb{U}$ is the free-space translation matrix, and $\mathbb{R}_i$ the scattering matrix for object i (= 1, 2 for our case). Primes on the polarizations (e.g., y') denote distinct wavevectors. 126

4-9 Lowest-order diagrams representing the contribution of non-specular scattering events to the Casimir energy, constructed using the rules of Fig. 4-8. Because we are measuring the energy of interaction between two objects, successive interaction vertices must involve different objects. On the left, when both objects 1 and 2 are directed along the z-axis, a non-specular event can occur in a 2-vertex diagram. However, when the wires are crossed, the lowest-order allowed non-specular process involves a 4-vertex diagram. 127

5-1 (a): Schematic (not to scale) of the idealized plate-particle configuration. An elongated metallic particle is centered above a perfectly thin metallic plate with a hole of radius R and width $W = 2R$. The particle is constrained to only move along the z axis and cannot rotate. (b): The key to the symmetry argument is that at $z = 0$, the electric field $\mathbf{E}$ of a z-directed dipole cannot couple to the thin plate, as $\mathbf{E}(z = 0) \cdot \hat{\mathbf{z}} = 0$. 131

5-2 Schematic of the potential energy $U(z)$ relative to the energy at infinite separation $U(\infty)$ for the particle of Fig. 5-1. From Fig. 5-1(b), this quantity must be zero at $z = 0$. Furthermore, the force for $z \to \infty$ must be attractive, implying that $U(z \to \infty) - U(\infty) < 0$ with positive slope. The simplest behavior for such a function is shown here, implying a repulsive region around $z = 0$. 132

5-3 (a): Induced charges on a two-dimensional plate due to a permanent electric dipole (red) normal to the plate. Positive charges will cluster at the points closest to the dipole, attracted to the negative charge. This leaves a negative charge excess farther away from the center. (b): Induced charges when the dipole is parallel to the plate. Now the induced charges on the plate are antisymmetric, and it is clear that the energy of the dipole is lowest at $z = 0$, leading to an attractive force. 134

5-4 2d force between a thin PEC plate and a perfectly anisotropic particle (i.e., no transverse dimension), scaled by the particle height h, as a function of vertical displacement d for a range of h. The shaded region in the main panel denotes a repulsive force. The scale-invariance of the force curve holds for $h < 0.1W$, but deviations become significant for $h \sim 0.5W$. Inset: force frequency integrand for $h = 0.001W$ at a fixed $d = 0.2W$, demonstrating that the repulsive effect holds at all frequencies for an idealized geometry. 135

5-5 Dependence of the force on aspect ratio γ for a fixed particle height $h = 0.0025W$ and a perfectly thin plate $t = 0$. Decreasing γ always decreases the force. Inset: frequency integrand for three values of the force at a fixed $d = 0.2W$. 136

5-6 Combined thickness and aspect ratio effects on the repulsive force for fixed $h = 0.0025W$. Inset: frequency integrands for a perfectly thin $t = 0$ plate and a finite $t = 0.1W$ thickness plate, for fixed separation $d = 0.2W$ and aspect ratio $\gamma = 4$. 138

5-7 Repulsive forces in a three-dimensional geometry. The repulsive force holds for both $t = 0$ and $t = 20\,\text{nm}$ for both PEC and gold. The vertical dashed line at $d = 170\,\text{nm}$ indicates the location of a separating plane for all configurations. Interestingly, gold has a slightly stronger repulsive force, which is explained in the text. Shown for reference is the force for a 30 nm radius PEC sphere, which is always attractive. Inset: geometry used for the force computations. 139

5-8 Transverse force on a small cylinder as a function of the lateral displacement r. For $r \neq 0$ the force is always away from the $r = 0$ axis, indicating instability in the transverse direction. 141

5-9 Energy as a function of rotation angle θ of the cylinder; the energy is at a relative maximum for $\theta = 0$, indicating that there is also an instability in θ. The energy minimum occurs at $\theta = 90°$ for which the dipole is parallel to the plate. 142

5-10 Different components to the Casimir-Polder energy: Γ_{zz} and Γ_{rr} of the tensor defined in eq. (5.2) as a function of vertical displacement d for the zero-thickness plate-with-hole. The Casimir-Polder energy is proportional to a weighted trace of the Γ tensor. For comparison, Γ_{zz} is shown for a metallic plate without a hole (black dashed line). . . . 145

5-11 Casimir-Polder energy for an anisotropic atom: Γ_{zz} for different plate thickness t as a function of vertical displacement d. Finite thickness attenuates the non-monotonic effect on the Casimir-Polder energy. Shown for reference is the energy for a solid plate. 146

5-12 A more isotropic repulsive effect due to two cylinders: similar to Fig. 5-3, the induced charge density due to an electrostatic dipole polarized along the z-direction will yield a repulsive force for small z. In contrast to a plate-with-hole, one component (Γ_{xx} is zero, leading to a flattening of the total energy for a $(1, 1, 3)$ dipole. 147

5-13 Casimir-Polder energy for off-axis displacements. Left: $\Gamma_{zz}(r, z)$ as both z and r are varied, for a $t = 0$ plate. Right: $\Gamma_{rr}(r, z)$ for the same case. The striking feature is that Γ_{zz} is enhanced for off-axis displacements. This leads to an instability for an atom, but below we will see how this can lead to a genuine increase in the repulsive force. 148

5-14 Configurations used in Sec. 5.4. *Top*: Reference configuration for comparison. *Top Left*: Geometry illustrating the single plate-needle configuration. *Top Right*: Casimir force vs. vertical height z for the configuration in the top left panel. Positive forces denote repulsion. *Bottom*: The two generalizations considered here: *Bottom Left*: Replacing a single cylinder with a ring of N (in the figure, $N = 10$) cylinders, each of which is more closely spaced to the edge of the hole. *Bottom Right*: An idealized version of the cylinder ring configuration, consisting of a cylinder of uniaxial conductance in the vertical (z) direction. 150

5-15 The effect of fringing fields on F_z, the z-component of the Casimir force for a single metallic cylinder: for a fixed z, F_z is enhanced as r increases. Plotted above is F_z for several values of z/R, normalized by the maximum of the repulsive force ($0.0278\,\hbar c/R^2$) for $x = 0$. As $r \to R$, F_z undergoes a very strong enhancement, peaking at approximately 55 for $r \sim 0.8R$ and $z = 0.2R$. For every z, as x increases pairwise attractive forces take over and F_z switches sign (note that for $r \neq 0$ there is an attractive force F_x between the cylinder and the plate edge, so the total Casimir force is not strictly repulsive in this case). Shown for reference in the inset is F_z (in units of $\hbar c/R^2$) at $r = 0$. 153

5-16 The effect of plate thickness on the Casimir force on a single cylinder. For each panel, the plate thickness is fixed and the Casimir force (maximized over $z > 0$) on a single cylinder is plotted as a function of x. The force for different values of cylinder height h are shown (for each h, the aspect ratio of the cylinder is fixed). For small t (Top), decreasing the cylinder size can actually lead to an increased repulsion for $x \sim R$. Increasing t (Middle and Bottom) leads to a decreased repulsion for all cylinders at all x, but the effect is strongest for small h cylinders. . . 155

5-17 Enhancement of Casimir repulsion with a a realistic geometry (Fig. 5-14, Bottom Left): in place of a single cylinder, a ring of N cylinders is placed at radius r (shown for $N = 5$ in the inset). The cylinders have height $h/R = 0.64$, and for computational tractability the plate thickness t is zero. For small N the force increases linearly, with slope corresponding approximately to the magnitude of enhancement of Fig. 5-15. As N increases, the effect saturates. As in previous figures, the force is maximized over z. 157

5-18 Forces (maximized over z) for a thick cylindrical capsule composed of uniaxial conductor (Fig. 5-14, Bottom Right). In contrast to previous figures, here the plate thickness is fixed to $t = 20\,\mathrm{nm}$ and the hole radius R is varied to three different values. For each R, the force is computed, as a function of capsule radius r, for capsule heights $h = 0.5R$ (solid lines) and $h = 0.64R$ (dashed lines). *Inset*: z-force enhancement factors as a function for both values of h for $R = 2\,\mu\mathrm{m}$, which approximates a thin plate. The maximum force is approximately $10\,\mathrm{fN}$. 159

6-1 Total thermal transfer between a silica plate and doped silicon objects of various shapes. The plate is semi-infinite, and the objects all have height equal to $1\,\mu$m in the z-direction. The plate/environment temperature is $T_P = 300\,\mathrm{K}$ and the objects are at temperature $T_A = 600\,\mathrm{K}$. Red dots denote results with the sphere scattering matrix determined analytically, the only case in which we have an analytic solution for the scattering matrix. 166

6-2 Cone meshes used in the present section. The points at the tops of these objects are those nearest to the plate, and thus require the highest mesh density. 174

6-3 Heat transfer for the cone-plate systems from Fig. 6-1, plotted on a semilog scale to suggest that the total power transfer diverges logarithmically for small z. For clarity, data for $\theta = 90°$ is scaled by a factor of 2, and $\theta = 40°$ by a factor of 4. Dashed lines so a linear fit to the data for $20\,\mathrm{nm} \leq z \leq 200\,\mathrm{nm}$, shifted downwards for clarity. . . . 177

6-4 Schematic used to derive eq. (6.16). In the text, we consider fixing z and varying the cone height from h_1 to h_2; the heat transfer from the pink region in the right-hand cone varies as $\log(h_2/h_1)$. 178

6-5 Poynting flux at the origin for the geometries of Fig. 6-1 with plate/environment temperature $T_P = 300\,\mathrm{K}$ and object temperature $T_A = 600\,\mathrm{K}$, using the single-polarization approximation (SPA) for the sphere and cylinders. The magenta line denotes the sphere-plate without the SPA, and the horizontal dashed line denotes the threshold used for the crossectional flux profiles of Fig. 6-6. 179

6-6 Spatially-resolved heat flux profiles at the substrate surface. z is chosen to fix Poynting flux at $x = 0$ at $10^{-3}(2\pi)^2 hc/\mu\mathrm{m}^4$. For the sphere and cylinders we have used the SPA (see text). 181

6-7 Extra-fine mesh used to compute the spatially-resolved Poynting flux for a $\theta = 90°$ cone, in which the mesh is highly concentrated at the tip. In total, approximately 12,000 mesh elements are used. This mesh illustrates the advantage of using a cylindrical-wave basis: spherical waves would have requires a much more uniform meshing of the cone surface, whereas here we can concentrate our mesh points near the tip. 182

6-8 Spatially-resolved heat flux profiles (arbitrary units) at the substrate surface for three cones. The profiles are normalized so that their maximal value is equal to 1. For comparison, the profile for a cylinder of radius $d = 400\,\text{nm}$ (using the SPA) is shown as well. 183

6-9 Schematic showing the physical meaning behind the $\mathbb{O}$ matrices; the processes are discussed in more detail in the text. 189

7-1 Unit cell of the Fibonacci superspace dielectric. The physical dielectric is obtained by taking a slice at an angle $\tan\phi = \tau$. Black/white are the dielectric constants of the structure factor material and air, chosen to be $\varepsilon = 4.84$ and $\varepsilon = 2.56$, respectively. 195

7-2 Error in the lower band edge as a function of the supercell period, which is $\sqrt{p^2+q^2}$, where p/q is a rational approximate to $\tau = \frac{1+\sqrt{5}}{2}$. The dashed black line indicates quadratic convergence, consistent with the fact that $|p/q - \tau| \sim \frac{1}{p^2+q^2}$. Inset: bandstruture for the $p = 34$, $q = 21$ approximate. The $k_x = 0$ point of the red band indicates the frequency points used for the convergence. 197

7-3 *Left:* Frequency spectrum ω of the Fibonacci quasicrystal vs. "wave-vector" k_x. The blue lines indicate spurious states which arise due to finite resolution effects (see text). *Right:* Corresponding density of states $\rho(\omega)$ computed using a transfer-matrix technique with a supercell of 10^4 layers. 203

7-4 Enlarged view of the Fibonacci spectrum showing a gap with a spurious band crossing it. Insets show the magnetic field $|H_z|$ for the spurious band at various k_x—the localization of this mode around the X-parallel edges of the dielectric indicate that this is a discretization artifact. . . 204

7-5 Identification and removal of spurious modes in one dimension. Left: spectrum of the Fibonacci quasicrystal, as in Fig. 7-3. We have superposed a black dashed line to indicate that the spurious modes appear to largely follow a linear dispersion relation. Right: density-of-states computed by removing all modes that satisfy $\lambda(\mathbf{H}) \geq 0.9$, where λ is defined in eq. (7.4). All spurious modes in the large bandgaps have vanished. 206

7-6 Fourier-space spectrum $|\mathbf{H_G}|^2$ of a spurious mode, on a log scale: dashed white line denotes the "physical" X direction in which fluctuations carry an energy penalty, and the solid white line denotes the "un-physical" Y direction. Circle denotes the peak in the mode's Fourier-space support, which occurs at the boundary of the computational cell. 207

7-7 Fourier-space spectrum $|\mathbf{H_G}|^2$ of a physical mode, on a log scale. In contrast to Fig. 7-6, the primary support of this mode occurs in the center of the computational cell. 208

7-8 Plot of the magnetic field amplitude $|H_z|$ for a band-edge state taken along a slice of the two-dimensional superspace (in the ϕ direction). *Inset:* Two-dimensional superspace field profile (red/white/blue indicates positive/zero/negative amplitude). 209

7-9 Electric field energy distribution of the band edge states of gaps 1 and 2 in Fig. 7-3. Although they have a complex small-scale structure, the large-scale variation is easily understood in terms of the structure of the superspace. 210

7-10 Dielectric for the Fibonacci chain with $\varepsilon = 2.56$ (light blue), and a defect—an additional $\varepsilon_d = 8.0$ layer, shown in gray. 211

7-11 Varying the defect epsilon for resolutions 50 (blue) and 100 (red). The thickness of the defect is fixed to 0.02 lattice constants. The number of spurious modes increases with the resolution, the true defect state being the lowest of these modes. 212

7-12 Semi-log plots of the magnetic field magnitude H_z for the lowest (top) and highest (bottom) defect state for the configuration shown in Fig. 7-10. *Insets:* Two-dimensional superspace visualizations of the defect states. Note the additional node in the lower figure (corresponding to an unphysical oscillation). 214

7-13 Projected band structure vs. cut angle ϕ, showing different one-dimensional quasicrystal realizations. The vertical red line indicates the spectrum when the slope is the golden ratio τ (the spectra of ϕ and $\pi - \phi$ are equivalent) 215

7-14 Bandstructure for the smooth superspace structure $\varepsilon(x, y) = 1+4e^{-(\sin^2(x)+\sin^2(y))}$ at two resolutions: thick lines denote 6 pixels / a, and thin lines denote 32 pixels / a. We will demonstrate that the bandstructure for this dielectric converges *exponentially* in resolution by examining the frequency ω_{lower}, indicated on the figure, which is at a relative maximum of the lower band edge (colored red) at a fixed $k_0 \approx 0.75(2\pi/a)$. . . . 217

7-15 Demonstration of exponential convergence with resolution of a smooth superspace structure. A plot of the error in ω_{lower} from Fig. 7-14 (relative to resolution 32) shows exponential convergence. The superspace dielectric structure, given by eq. (7.5), is shown in the inset. 218

7-16 Optimization of the fractional bandgap for a 1d quasicrystal: starting with a smoothed version of the Fibonacci structure (top left), which has the indicated band structure, we allow every pixel to be a free parameter, ranging from $1 \leq \varepsilon \leq 10$. Even though the cut angle is $\tan\phi = \tau$, the three structures shown are actually *periodic*. After optimization, all structures exhibit an approximately 67% fractional bandgap, which is the same as an optimized 1d photonic crystal with the same smoothing parameters. 219

7-17 Bandstructure for a 3/2 supercell approximate to the octagonal PQC of high dielectric rods. The real-space structure is shown in the inset, with a unit cell marked by the dashed red box. 221

7-18 Mode density plot for the super*space* octagonal structure, with the same structural parameters as Fig. 7-17, for a resolution of 10 pixels per a. At this resolution, the bandgaps are not fully resolved to high accuracy. 222

7-19 Schematic showing the superspace slice X (left) and the projected slice modulo 1 into the unit cell $\bar{X}$ (right), along with the intersection $\bar{T}$ of $\bar{X}$ with the $s = 0$ hyperplane. 224

Chapter 1

Introduction

This thesis is concerned with the application of Maxwell's equations to novel situations. We will see how classical computational techniques developed over many decades may be applied to situations well outside of their original intended scope. Our main application will be to the field of Casimir forces, to which we apply these techniques to the search for novel physical effects. We will then find that the techniques and intuition developed for this task can readily be applied to the field of thermal transfer. Finally, we will examine photonic quasicrystals, and see how computational techniques designed to solved Maxwell's equations for periodic systems can be extended into higher dimensions to treat certain types of aperiodic structures.

1.1 A brief introduction to Casimir forces

You may have encountered Casimir forces before in the guise of van der Waals forces. As shown in Fig. 1-1(Left), quantum fluctuations in the electron orbitals of a neutral atom give rise to electric fields, which in turn polarize nearby neutral atoms; these polarization fields interact with the progenitor atom, giving rise to an interaction energy that depends on the relative separation of the two atoms. The Casimir force refers to the generalization of this effect to the situation, shown in Fig. 1-1(Right), in which extended, charge-neutral objects interact via their quantum fluctuations.

The idea of a fluctuation-induced force is not actually new and is certainly not

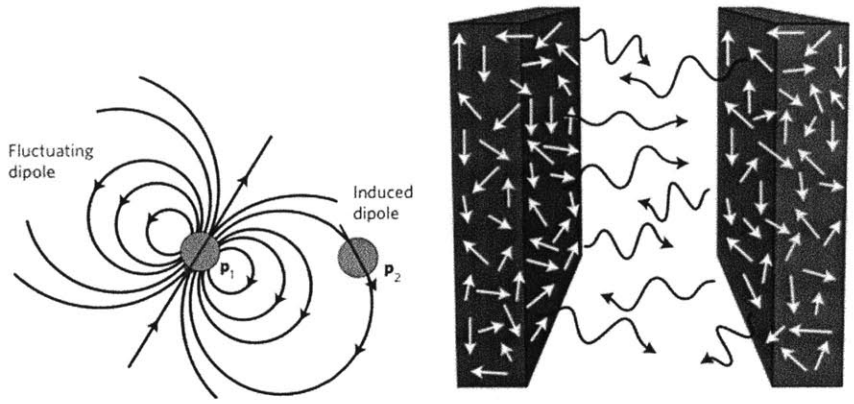

Figure 1-1: Illustration of the basic physics behind Casimir forces. Left: a fluctuating dipole gives rise to an electric field, which induces a dipole polarization on a nearby neutral atom. This in turn produces a dipole field that interacts with the first dipole, resulting in an interaction energy. Right: in general, the interacting materials are no longer neutral particles, but extended objects composed of many fluctuating dipoles.

confined to the realm of quantum mechanics. Fluctuation-induced forces appear as a consequence of the free-energy of a system: the dynamics is not determined solely by the "energy" (i.e., by the Hamiltonian) of the system, but by the combination of this energy and the entropic effects of thermal fluctuations [61]. The interesting difference between classical statistical dynamics and the Casimir effect is that this fluctuation-induced force occurs even at *zero* temperature. However, unlike normal quantum phenomena, which typically require the system to be in a delicate coherent superposition of quantum states, the Casimir effect results from a fully incoherent averaging of quantum processes. Therefore, it provides an unusually robust manifestation of quantum mechanics [1].

This quantum-mechanical origin of the Casimir effect gave it sustained theoretical interest from its discovery in the late 1940s through the end of the 20th century. However, the real paradigm shift for Casimir physics occurred in the late 1990s with two contemporaneous developments: first, Casimir forces were for the first time unambiguously measured in experiments involving simple (e.g., sphere-plate) geometries.

[1]Of course, the most robust manifestation is probably the Exclusion Principle, without which matter could not be stable. The Casimir effect is rather one of the more robust of the "obscure" quantum-mechanical effects.

Second, device fabrication reached the nanoscales over which Casimir forces become one of the dominant (usually detrimental) effects. The former development made the theoretical exploration of Casimir forces in novel geometries experimentally relevant, and the latter gave a clear goal for these efforts: controlling these nanoscale forces in microdevices. Much has been accomplished in the ensuing decade, and our knowledge of Casimir physics beyond the idealizations of the mid-20th century has been greatly advanced. In this thesis I will discuss my modest contribution to this effort.

1.2 Casimir Forces in the time domain

With the desire to understand Casimir forces in new and novel geometries came efforts to develop new and novel techniques for computing these forces - the computational idealizations of the pre-digital age were no longer sufficient. Several very successful techniques were developed towards this end; for the most part, the work in this thesis is concerned with applying these techniques to the search for novel Casimir effects. The techniques themselves will usually show up indirectly whenever we look "under the hood"; in-depth discussions can be found in other works, especially in the theses of my colleagues S. Jamal Rahi, Alejandro Rodriguez, and M. T. Homer Reid. The one exception will occur in the next chapter, in which I discuss in-depth a computational technique that I helped adapt to Casimir forces that makes use of the finite-difference time-domain (FDTD) (the workhorse of the computational electrodynamics industry) [119, 143, 172]. Alex and Steven had already been working on this, and my contribution involved analyzing some of the properties of the method, as well as implementing it in a fully three-dimensional setting and applying it to a variety of cases. The nice property of FDTD is that, while not as efficient as other methods (e.g., the boundary-element method), it is one of the most robust computational tools around - once you get it working, you can do any shape, any material, and any boundary condition. As an example, we present the first rigorous results showing three-dimensional stable confinement, illustrated in Fig. 1-2, due to the three-fold combination of geometry, material dispersion, and gravity.

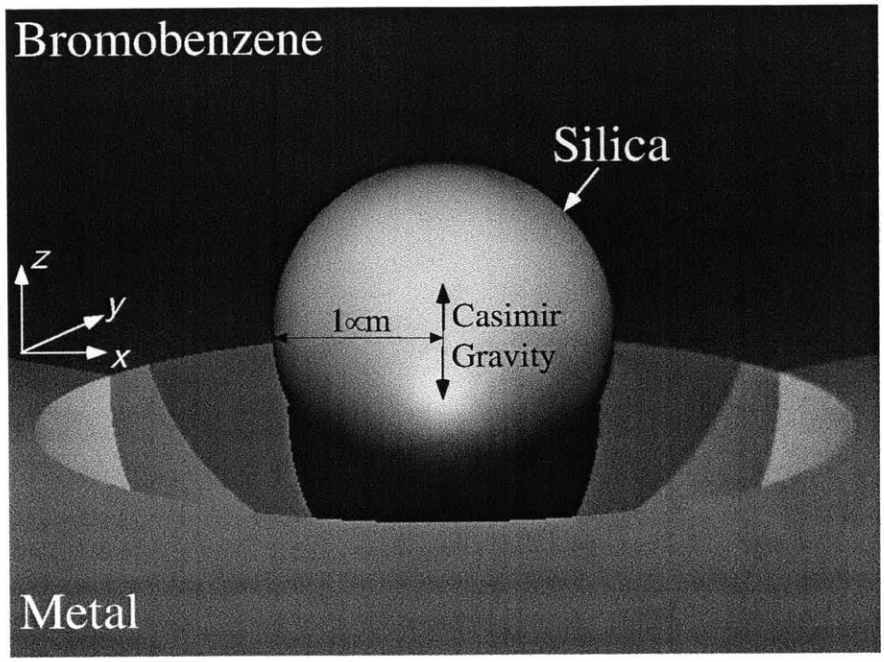

Figure 1-2: Three-dimensional configuration showing stable levitation. At the equilibrium point, the force of gravity counters the Casimir force, while the Casimir force from the walls of the spherical indentation confine the sphere laterally

1.3 The quest for Casimir repulsion

A large motivation for the study of Casimir forces arose from trying to solve the problem of "stiction" - Casimr forces cause the components of micro-devices to get stuck together when they get too close, causing device failure. An important question was whether or not it is possible to change the *sign* of the force by changing the *shape* of the objects. It is well-known that repulsive forces can be achieved with a properly-chosen intervening fluid [44]; this "repulsion" is basically the competition of two attractive Casimir forces, much as a boat floating on water follows purely from an attractive gravitational force (and the Exclusion Principle!). However, although we will make use of it at times, this effect is not directly relevant for device applications, which generally operate in air. The question then is whether *vacuum*-separated objects can experience repulsive forces.

1.3.1 A Casimir metamaterial that does not work

As described in more detail in Chapter 3, for a time it was thought that so-called "metamaterials" may be used to generate Casimir repulsion. Basically, it is known that for optical applications a periodic material with a complex microstructure may be used to mimic a homogeneous material of exotic optical properties. Such ideas have had some success in the field of electromagnetism. However, the application of the metamaterial concept to Casimir forces suffers from many problems, one of which was the lack of rigorous calculations. Instead, uncontrolled approximations were used in which the metamaterial nature of the material was assumed from the beginning, rather than being derived from *ab-initio* physics. In Chapter 3, we will apply the methods we and others developed for computing Casimir forces to rigorously examine the properties of a certain "chiral" metamaterial, using the exact geometry of the structure without an *a priori* metamaterial assumption [122]. In addition to employing the FDTD approach discussed in Chapter 2, we implemented another approach based on a synthesis of the analytic, scattering-theory formulation of Casimir forces and the fully numeric, boundary-element approach, combining the advantages of both techniques to analyze the complex geometry of Fig. 1-3 (which represents an idealization of a chiral metamaterial), a geometry which neither technique alone would have been able to handle.

We find that the hope-for exotic properties are overwhelmed by non-ideal and mundane effects; that is, the pairwise surface-surface attraction that so well-predicts the simplest Casimir geometries also governs at least the qualitative nature of geometries such as Fig. 1-3. We find that not even a force reduction can occur with these materials, making further research in their direction a fruitless endeavor.

1.3.2 A Casimir metamaterial that *does* work

After disproving the validity of the chiral metamaterial viewpoint, a natural question is to ask whether or not there are conditions under which such a viewpoint is in fact valid for Casimir forces. In Chapter 4 we find an instance in which this is true: for

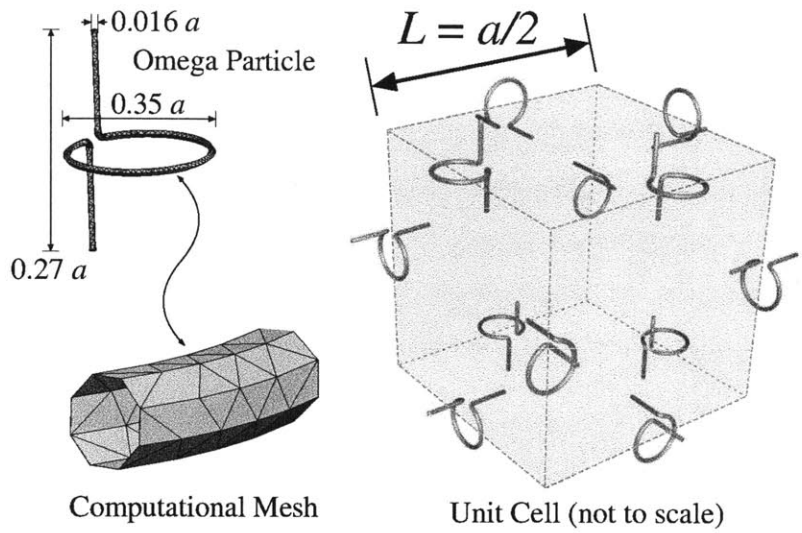

Figure 1-3: Unit cell of the isotropic chiral metamaterial examined in Chapter 3: perfectly conducting "omega" particles in vacuum. The shaded cube indicates the relative positions in the unit cell

the configuration of Fig. 1-4, we find that long conducting wires embedded on the surface of a dielectric plate can mimic the behavior of a homogeneous, anisotropic material in such a way as to greatly modify the Casimir force [121]. For example, we find that with a properly-chosen fluid in between the two plates, the Casimir force can be switched from attractive to repulsive by rotating one plate. We will rigorously show that this result cannot follow from a simple pairwise sum of plate-plate forces, but rather is a manifestation of the metamaterial effect, and that further this effect holds down to surprisingly small separations (on the order of half the lattice spacing a in Fig. 1-4).

While this system appears somewhat fanciful, it is not in fact too far away from current technology: arrays of wires embedded in plates have been made at very small length scales, and the Casimir forces arising in these geometries at these length scales are *almost* within detectable limits of present technology. Therefore, it may make an interesting experiment in the near future. However, although this demonstrates an interesting way to modulate the sign of the Casimir force with geometry, we are still forced to make use of an intervening fluid if we are to obtain a repulsive Casimir

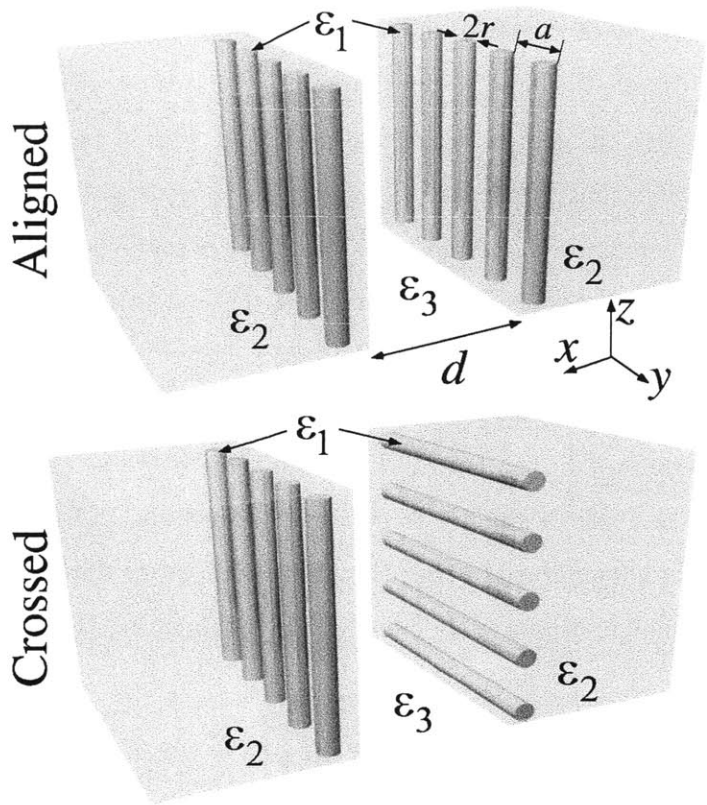

Figure 1-4: Configuration examined in Chapter 4. Each slab consists of a single periodic array of cylindrical wires embedded in a semi-infinite substrate; the goal is to create for each slab an effective anisotropic medium. Of interest here is the change in the force from when the wires are aligned (Top) and when they are crossed (Bottom). When the medium between the plates is a properly chosen fluid, we show that the force switches sign as a function of orientation for certain separations.

force.

1.3.3 Genuinely repulsive Casimir forces in vacuum

Slightly before our work on chiral metamaterials, it was shown [155] that Casimir repulsion is impossible in this regime. Therefore, any possible Casimir repulsion must occur in a system that radically departs from the metamaterial concept. In Chapter 5, we will show how, in collaboration with Michael Levin, we were able to finally devise a system for which geometry alone is responsible for a repulsive Casimir force [101, 120]. The system is shown in Fig. 1-5, and the repulsive force arises from

the geometric anisotropy of the small particle above a plate. The key physical insight that Michael had (which is detailed in Chapter 5) relies on a symmetry argument involving the electrostatic properties of a dipole field with a perfectly-conducting thin plate. We applied our numerical techniques to show that this repulsive effect still holds when both geometric and material idealities are removed: repulsive Casimir forces can exist between non-perfect conductors without infinitesimal dimensions in any direction. However, as we discuss in Chapter 5, although this force is repulsive it is not *stable*, and the dynamics will ultimately lead to attraction if the particle of Fig. 1-5 is not confined in the lateral direction. This is consistent with Ref. 155, which proved that any such repulsive force must be unstable. Therefore, these two results are nicely complementary in that they have completely determined the range of Casimir force behavior that can be achieved by engineering the geometry of the objects.

It turns out from the exact numerics that our repulsive force is very small - on the order of *atto*-Newtons for realistic dimensions. This is far too small to be detected in experiments. The later two sections of Chapter 5 will present my explorations into how to convert this into a detectable effect: first by examining (in collaboration with Simen Ellingsen) the Casimir-Polder force where the particle of Fig. 1-5 is replaced by a Rydberg atom, and then by examining more novel geometries in which the particle cannot be treated as a dipole: by replacing the particle with multiple cylinders arrayed across the hole, or by a large uniaxial capsule in which the conductivity is only perpendicular to the plate (the physical realization could be, e.g., a forest of vertically-grown carbon nanotubes). We find that the force can be enhanced a thousand-fold, however, the resulting force is still in the tens of femto-Newtons at best, and the fabrication challenges are formidable.

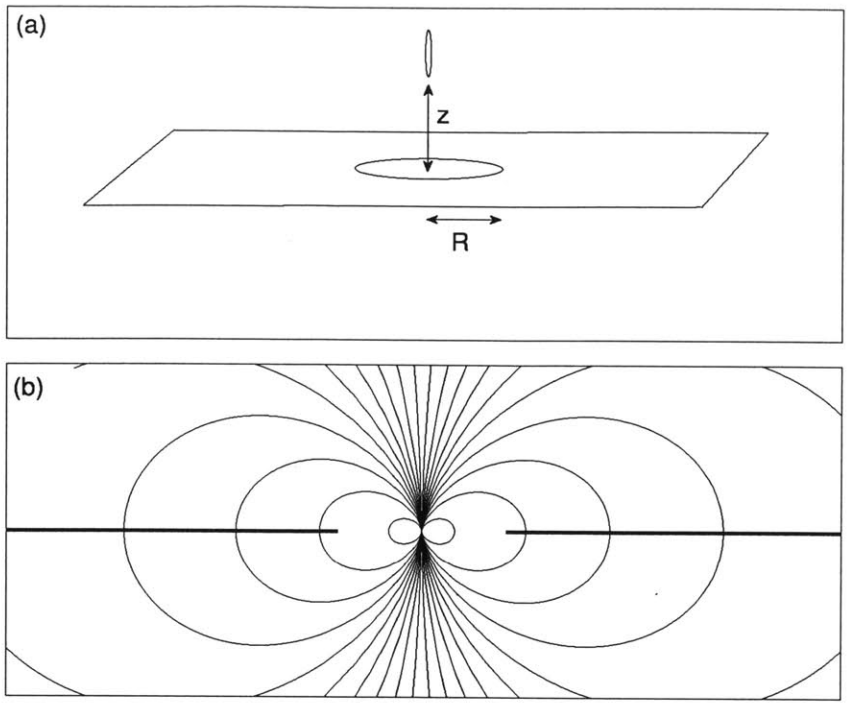

Figure 1-5: Configuration used in Chapter 5 to achieve a repulsive force between an elongated particle and a thin plate with a hole, illustrated in panel (a). The physical mechanism relies on a symmetry argument involving the coupling of the dipole field of the particle to the plate, illustrated in panel (b).

1.4 From quantum fluctuations to thermal fluctuations

The physics of Casimir interactions can be described by the coupling of fluctuating currents on one object to absorptive mechanisms of another. It turns out that the physics of radiative thermal transfer, in which the heat from one object is transferred to another, cooler object can be described by the same formalism. Furthermore, many of the computational techniques developed for Casimir forces can be readily applied to this process as well. This should not be too surprising as thermal transfer involves at the most basic level the same coupling of fluctuating current sources to absorptive processes on another object. The physics of non-contact heat transfer is interesting in that, similar to the Casimir force, the effect becomes greatly enhanced

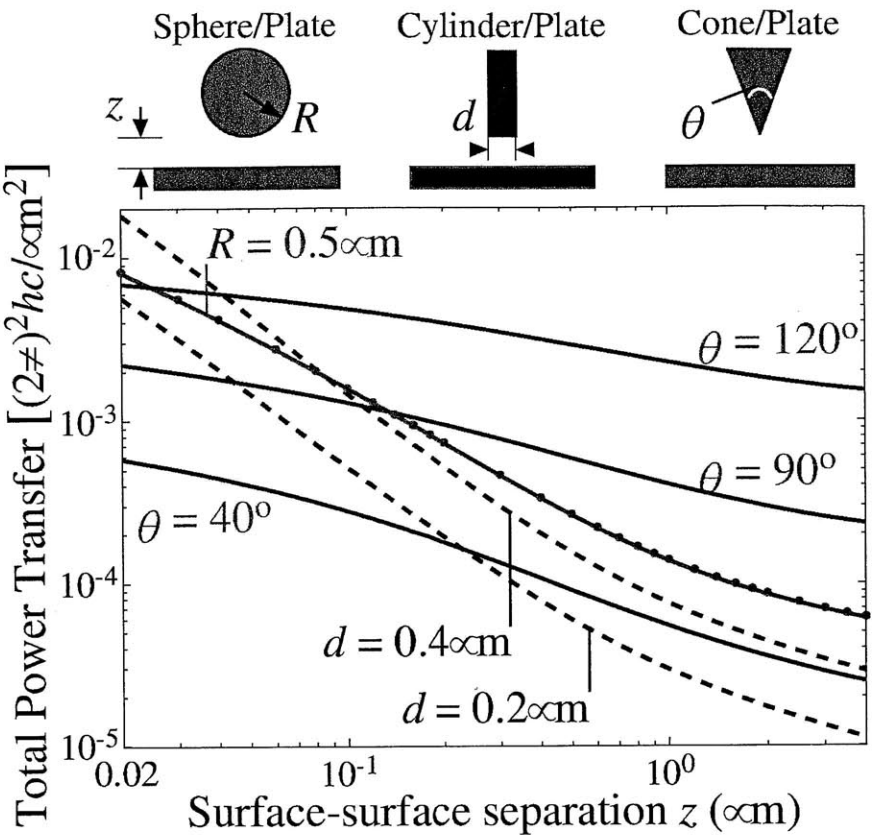

Figure 1-6: Total thermal transfer between a silica plate and doped silicon objects of various shapes. The plate is semi-infinite, and the objects all have height equal to $1\,\mu$m in the z-direction. The plate/environment temperature is $T_P = 300\,$K and the objects are at temperature $T_A = 600\,$K. Red dots denote results with the sphere scattering matrix determined analytically, the only case in which we have an analytic solution for the scattering matrix.

at low separations (although not as dramatically as the Casimir force).

In the past few years several experiments have confirmed this predicted enhancement for the sphere-plate configuration, setting the stage for a similar sequence of events as for Casimir forces ten years ago. However, with most of the infrastructure in place the theoretical advancement has occurred rather quickly. In Chapter 5 we will discuss our efforts [118], in collaboration with Matthias Krüger, to examine the effect of corners and sharp edges on the near-field thermal transfer. The technique builds on the hybrid method we implemented in Chapter 3, involving a combination of analytic and numerical techniques. In particular, we look at thermal transfer for

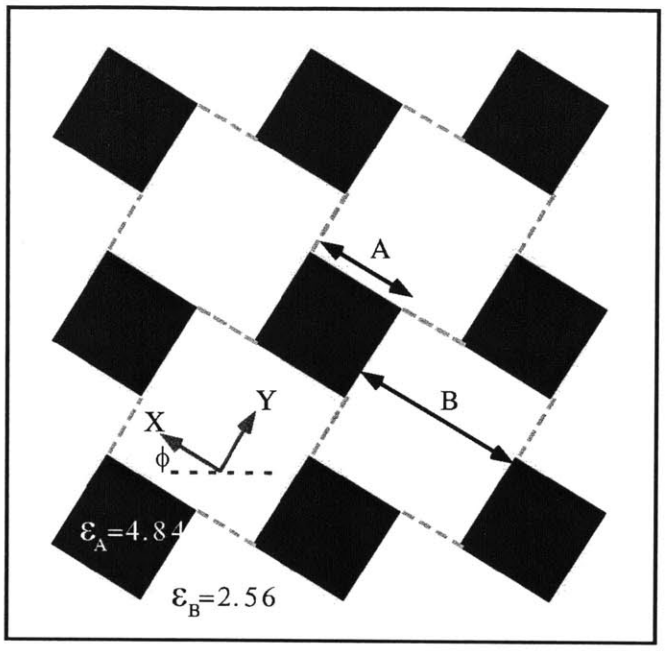

Figure 1-7: Unit cell of the Fibonacci "superspace" dielectric, which when sliced along the X direction (which makes an angle $\tan\phi = \frac{1+\sqrt{5}}{2}$ with the horizontal) will yield a one-dimensional quasicrystal. We will see that this one-dimensional structure inherits many of the properties of the two-dimensional superspace.

cylinder-plate and cone-plate configurations. While the physics of cylinder-plate heat transfer appears to follow an intuitive pairwise-additive law, we have found two interesting effects concerning the cone-plate configuration: the thermal transfer diverges *logarithmically* as the separation goes to zero, and the spatially-resolved heat *flux* profile exhibits a local *minimum* nearest the cone tip, a result that does not follow from pairwise interactions. Rather, we can explain this effect using our arguments about electrostatic dipoles from Chapter 5. These results hint at the potential for interesting near-field thermal transfer effects in the future.

1.5 Applying periodic techniques to non-periodic structures

Until the late 1980s, it was assumed that the only natural materials exhibiting long-range order would be periodic structures, and for thousands of years it has been

known that periodic structures admit only certain symmetry groups; for example, there can be no periodic structure in three dimensions exhibiting icosahedral symmetry. Therefore, it was assumed that ordered structures could only exhibit crystallographic symmetry. However, this changed in 1984 with the discovery of a three-dimensional substance with long-range order exhibiting icosahedral symmetry [186]. Subsequent investigation revealed that this substance was a three-dimensional *quasi*-crystal. These structures, while not being periodic, possess long-range order and have much higher symmetry than their periodic counterparts.

Drawing inspiration from these discoveries, researchers in optics realized that photonic structures, termed photonic quasicrystals (PQCs), can be fabricated mimicking this quasicrystalline structure[2]. The interesting feature of these structures is that, like their periodic cousins photonic crystals, PQCs support photonic bandgaps. The hope for PQCs is that their higher degree of symmetry can lead to a more symmetric bandstructure, perhaps allowing bandgaps to persist at lower index contrast than ordinary photonic crystals.

In Chapter 7, we will examine a technique by which photonic quasicrystals can be re-expressed as periodic structures in higher dimensions [77, 171]. In collaboration with Alejandro Rodriguez, we develop a method to solve a modified version of Maxwell's equations directly in the higher-dimensional space. Although this method is not very efficient (especially for higher-dimensional PQCs), examining the spectra of one-dimensional PQCs affords some physical insight into the behavior of their bandstructure, notably, that some of the periodic nature of the higher-dimensional space is inherited by the lower-dimensional PQC.

[2]Of course, here there is no question of existence - if the structures can be imagined, they can almost certainly be made. This is apparent in Islamic art, where quasicrystalline patterns have been used for centuries.

Chapter 2

Computing Casimir forces in the time domain

2.1 Introduction

In this chapter, we introduce a theoretical framework for computing Casimir forces via the standard finite-difference time-domain (FDTD) method of classical computational electromagnetism [194] (for which software is already widely available). The starting point is an idea that Steven and Alex worked on, reviewed in Sec. 2.2.3, that involves introducing an artificial conductivity into the problem; this procedure greatly improves the efficiency of the time-domain method. Following this, I give details of the mathematical formulation of the time-domain method in Sec. 2.3, including a numerical demonstration that the use of the conductivity contour of Sec. 2.2.3 gives exponential convergence of results with simulation runtime. We will also introduce a weight function $g(t)$ which will play an important role for finite-temperature effects. In Sec. 2.4 we introduce a harmonic expansion technique that we developed which further improves the efficiency of FDTD techniques. Then, in Sec. 2.5 we present a number of applications of this method to demonstrate Casimir force computations on various geometries. This specific method was developed as a modification of Steven's FDTD code MEEP. We validate our method by demonstrating agreement with known semi-analytic results for double pistons between parallel sidewalls

in Sec. 2.5.1. In Sec. 2.5.3 we present a double-piston scenario with cylindrical symmetry, in Sec. 2.5.4 we examine systems with periodic boundary conditions, and finally in Sec. 2.5.5 we present the first fully 3d force computations for dielectric objects, demonstrating how geometry, gravity, and material dispersion can be used to achieve stable confinement in three dimensions. In Sec. 2.6 we discuss work done with Kai Pan that demonstrates how to extend the FDTD formulation to finite temperature. The theoretical formulation involves a non-trivial subtlety dealing with the zero-frequency pole that we will discuss. Finally, in the Appendix we present details of the derivations of the harmonic expansion for cylindrical coordinates, and mathematical details of the computation of $g(t)$.

2.2 Background

This chapter serves as our jumping-off point into the theory of Casimir forces. The present formulation relies heavily on previously-established theory for Casimir forces, to which we give a brief introduction here. Further details can be found in Refs. [105, 112, 126, 127]. We also review the work that Alex and Steven did to formulate the problem in the time domain.

2.2.1 The Stress Tensor Formulation and the Conductivity Mapping

The Casimir force on a body can be expressed [105] as an integral over any closed surface S (enclosing the body) of the mean electromagnetic stress tensor $\langle T_{ij}(\mathbf{r},\omega)\rangle$. Here $\mathbf{r}$ denotes spatial position and ω the frequency. In particular, the force in the ith direction is given by:

$$F_i = \int_0^\infty d\omega \oiint_S \sum_j \langle T_{ij}(\mathbf{r},\omega)\rangle \, dS_j \,, \tag{2.1}$$

The stress tensor is expressed in terms of correlation functions of the the field

operators $\langle E_i(\mathbf{r},\omega)E_j(\mathbf{r}',\omega)\rangle$ and $\langle H_i(\mathbf{r},\omega)H_j(\mathbf{r}',\omega)\rangle$:

$$\langle T_{ij}(\mathbf{r},\omega)\rangle = \mu(\mathbf{r},\omega)\left[\langle H_i(\mathbf{r})\,H_j(\mathbf{r})\rangle_\omega - \frac{1}{2}\delta_{ij}\sum_k \langle H_k(\mathbf{r})\,H_k(\mathbf{r})\rangle_\omega\right] + \varepsilon(\mathbf{r},\omega)\left[\langle E_i(\mathbf{r})\,E_j(\mathbf{r})\rangle_\omega - \frac{1}{2}\delta_{ij}\sum_k \langle E_k(\mathbf{r})\,E_k(\mathbf{r})\rangle_\omega\right], \quad (2.2)$$

where both the electric and magnetic field correlation functions can be written as derivatives of a vector potential operator $\mathbf{A}^E(\mathbf{r},\omega)$:

$$E_i(\mathbf{r},\omega) = -i\omega A_i^E(\mathbf{r},\omega) \quad (2.3)$$

$$\mu H_i(\mathbf{r},\omega) = (\nabla\times)_{ij}A_j^E(\mathbf{r},\omega) \quad (2.4)$$

We explicitly place a superscript on the vector potential in order to refer to our choice of gauge [eqs. (2.3) and (2.4)], in which $\mathbf{E}$ is obtained as a time-derivative of $\mathbf{A}$. The fluctuation-dissipation theorem relates the correlation function of $\mathbf{A}^E$ to the photon Green's function $G_{ij}^E(\omega;\mathbf{r},\mathbf{r}')$:

$$\langle A_i^E(\mathbf{r},\omega)A_j^E(\mathbf{r}',\omega)\rangle = -\frac{\hbar}{\pi}\Im G_{ij}^E(\omega,\mathbf{r},\mathbf{r}'), \quad (2.5)$$

where G_{ij}^E is the vector potential A_i^E in response to an electric dipole current $\mathbf{J}$ along the $\hat{\mathbf{e}}_j$ direction:

$$\left[\nabla\times\frac{1}{\mu(\mathbf{r},\omega)}\nabla\times\ -\omega^2\varepsilon(\mathbf{r},\omega)\right]\mathbf{G}_j^E(\omega;\mathbf{r},\mathbf{r}') = \delta(\mathbf{r}-\mathbf{r}')\hat{\mathbf{e}}_j, \quad (2.6)$$

Here $\mathbf{G}_j^E$ is viewed as a vector $(G_{xj}^E, G_{yj}^E, G_{zj}^E)$ with the $\nabla\times$ operators acting on these vector indices. Given G_{ij}^E, one can use eqs. (2.3) and (2.4) in conjunction with eq. (2.5) to express the field correlation functions at points $\mathbf{r}$ and $\mathbf{r}'$ in terms of the photon

Green's function:

$$\langle E_i(\mathbf{r},\omega)E_j(\mathbf{r}',\omega)\rangle = \frac{\hbar}{\pi}\omega^2 \Im G^E_{ij}(\omega;\mathbf{r},\mathbf{r}') \tag{2.7}$$

$$\langle H_i(\mathbf{r},\omega)H_j(\mathbf{r}',\omega)\rangle = -\frac{\hbar}{\pi}(\nabla\times)_{il}(\nabla'\times)_{jm}\Im G^E_{lm}(\mathbf{r},\mathbf{r}',\omega), \tag{2.8}$$

In order to find the force via eq. (2.1), we must first compute $G^E_{ij}(\mathbf{r},\mathbf{r}'=\mathbf{r},\omega)$ at every $\mathbf{r}$ on the surface of integration S, and for every ω [105]. Equation (2.6) can be solved numerically in a number of ways, such as by a finite-difference discretization [167]: this involves discretizing space and solving the resulting matrix eigenvalue equation using standard numerical linear algebra techniques [9, 196]. We note that finite spatial discretization automatically regularizes the singularity in G^E_{ij} at $\mathbf{r}=\mathbf{r}'$, making G^E_{ij} finite everywhere [167].

2.2.2 Complex frequency and Wick rotation

The present form of eq. (2.6) is of limited computational utility because it gives rise to an oscillatory integrand with non-negligible contributions at all frequencies, making numerical integration difficult [167]. However, the integral over ω can be re-expressed as the imaginary part of a contour integral of an analytic function by commuting the ω integration with the $\Im$ operator in eqs. (2.7) and (2.8). Physical causality implies that there can be no poles in the integrand in the upper complex plane. The integral, considered as a complex contour integral, is then invariant if the contour of integration is deformed above the real frequency axis and into the first quadrant of the complex frequency plane, via some mapping $\omega \to \omega(\xi)$. This allows us to add a positive imaginary component to the frequency, which causes the force integrand to decay rapidly with increasing ξ [173]. In particular, upon deformation, eq. (2.6) is mapped to:

$$\left[\nabla\times\frac{1}{\mu(\mathbf{r},\omega)}\nabla\times - \omega^2(\xi)\varepsilon(\mathbf{r},\omega)\right]\mathbf{G}^E_j(\xi;\mathbf{r},\mathbf{r}') = \delta(\mathbf{r}-\mathbf{r}')\hat{\mathbf{e}}_j, \tag{2.9}$$

and eqs. (2.7) and (2.8) are mapped to:

$$\langle E_i(\mathbf{r},\omega)E_j(\mathbf{r}',\omega)\rangle = \frac{\hbar}{\pi}\omega^2 G^E_{ij}(\omega;\mathbf{r},\mathbf{r}') \tag{2.10}$$

$$\langle H_i(\mathbf{r},\omega)H_j(\mathbf{r}',\omega)\rangle = -\frac{\hbar}{\pi}(\nabla\times)_{il}(\nabla'\times)_{jm}G^E_{lm}(\mathbf{r},\mathbf{r}',\omega), \tag{2.11}$$

Equation (2.1) becomes:

$$F_i = \Im\int_0^\infty d\xi \frac{d\omega}{d\xi} \oiint_{\text{surface}} \sum_j \langle T_{ij}(\mathbf{r},\omega)\rangle\, dS_j\,, \tag{2.12}$$

[Note that a finite spatial grid (as used in the present approach) requires no further regularization of the integrand, and the finite value of all quantities means there is no difficulty in commuting the $\Im$ operator with the integration.]

2.2.3 Conductivity Mapping in the frequency domain

As discussed in the previous section, it is known that we can choose from a general class of frequency contours, provided that they satisfy $\omega(\xi = 0) = 0$ and remain above the real ξ axis. In practice, the only contour to have been used is the contour $\omega(\xi) = i\xi$, referred to as a Wick rotation, which is known to yield a force integrand that is smooth and exponentially decaying in ξ [105]. A Wick rotation guarantees a strictly positive-definite and real-symmetric Green's function, making eq. (2.6) solvable by the most efficient numerical techniques (e.g. the conjugate-gradient method) [196].

For the purpose of FDTD, the obvious approach would be to apply a Wick rotation to the equations of motion, solve these via FDTD, and then Fourier transform the results to obtain the complex-frequency Green's function. However, it turns out that a Wick rotation is unstable in the time domain because it implies the presence of gain [173]. On the other hand, not performing any contour deformation, although leading to stable equations of motion (these are just the usual FDTD equations), leads to very long simulation times because the fields decay only slowly, or for the case of, e.g., one-dimensional parallel plates, do not decay at all. We will prove in the Appendix that the force will still converge with simulation time t, but this

convergence will in general be $O(1/t)$, and in practice this gives runtimes far too long to be of practical use. The key idea that Steven and Alex had to solve this problem is that the frequency contour need not be limited to Wick rotations; as discussed above, any contour $\omega(\xi)$ in the first quadrant is suitable in the frequency domain. Steven and Alex had an idea for how to find a contour suitable for the time domain, and it relies on the observation that eq. (2.9) can be viewed as the Green's function at real "frequency" ξ and *complex dielectric*:

$$\varepsilon_c(\mathbf{r}, \xi) = \frac{\omega^2(\xi)}{\xi^2}\varepsilon(\mathbf{r}) \tag{2.13}$$

that is, the contour mapping can be seen as a mapping on the physical *material* rather than the frequency. Integrating along a frequency contour $\omega(\xi)$ is therefore equivalent to modifying the dispersion of the medium via eq. (2.13). Consequently, the time domain equations of motion under this mapping correspond to evolution of the fields in an effective dispersive medium given by $\varepsilon_c(\mathbf{r}, \xi)$. It is important to emphasize that the original physical system ε at a frequency ω is the one in which Casimir forces and fluctuations appear; the dissipative system ε_c at a frequency ξ is merely an artificial technique introduced to compute the Green's function.

The choice that Alex and Steven realized as ideal for FDTD is an $\varepsilon_c(\mathbf{r}, \xi)$ corresponding to a medium with frequency-independent conductivity σ (although it turns out that there is an even better choice that will be discussed below in Sec. 2.7):

$$\varepsilon_c(\mathbf{r}, \xi) = \varepsilon(\mathbf{r})\left(1 + \frac{i\sigma}{\xi}\right) \leftrightarrow \omega(\xi) = \xi\sqrt{1 + \frac{i\sigma}{\xi}} \tag{2.14}$$

This contour has four main advantages: first, the stability of the results is guaranteed by the physical nature of a conductivity σ; second, it is implemented in many FDTD solvers currently in use; third, it is numerically stable; and fourth, it can be efficiently implemented without an auxiliary differential equation [194]. In this case,

the equations of motion in the time domain are given by:

$$\frac{\partial \mu \mathbf{H}}{\partial t} = -\nabla \times \mathbf{E} \tag{2.15}$$

$$\frac{\partial \varepsilon \mathbf{E}}{\partial t} = \nabla \times \mathbf{H} - \sigma \varepsilon \mathbf{E} - \mathbf{J} \tag{2.16}$$

Note that, in the time domain, the frequency of the fields is ξ, and not ω, i.e. their time dependence is $e^{-i\xi t}$. The only role of the conductivity σ here is to introduce an imaginary component to the product $\varepsilon\omega^2$ in correspondence with a complex-frequency mapping. It also explicitly appears in the final expression for the force, eq. (2.12), as a multiplicative (Jacobian) factor. We expect in general that the addition of a non-zero σ will have the effect that the fields will decrease exponentially in simulation time t for sufficiently large t, a fact that we confirm by direct simulation below.

The full force integral is then expressed in the symmetric form:

$$F_i = \Im \frac{\hbar}{\pi} \int_{-\infty}^{\infty} d\xi \; g(\xi) \left(\Gamma_i^E(\xi) + \Gamma_i^H(\xi) \right), \tag{2.17}$$

where

$$\Gamma_i^E(\xi) \equiv \oiint_S \sum_j \varepsilon \left(G_{ij}^E(\mathbf{r}) - \frac{1}{2}\delta_{ij} \sum_k G_{kk}^E(\mathbf{r}) \right) dS_j \tag{2.18}$$

$$\Gamma_i^H(\xi) \equiv \oiint_S \sum_j \frac{1}{\mu} \left(G_{ij}^H(\mathbf{r}) - \frac{1}{2}\delta_{ij} \sum_k G_{kk}^H(\mathbf{r}) \right) dS_j \tag{2.19}$$

represent the surface-integrated field responses in the frequency domain, with $G_{ij}(\mathbf{r}) \equiv G_{ij}(\mathbf{r}, \mathbf{r}; \xi)$. For notational simplicity, we have defined the weight function:

$$g(\xi) \equiv \frac{\omega^2}{i\xi \mathcal{J}(\xi)} \frac{d\omega}{d\xi} \Theta(\xi) \tag{2.20}$$

Here, the path of integration has been extended to the entire real ξ-axis with the use of the unit-step function $\Theta(\xi)$ for later convenience.

The product of the fields with $g(\xi)$ naturally decomposes the problem into two parts: computation of the surface integral of the field correlations Γ, and of the

function $g(\xi)$. The Γ_i contain all the structural information, and are straightforward to compute as the output of any available FDTD solver with no modification to the code. This output is then combined with $g(\xi)$, which is easily computed analytically, and integrated in eq. (2.38) to obtain the Casimir force.

2.3 Mapping to the time domain

We now discuss how the force computation problem can be mapped entirely into the time domain, which will help considerably in understanding the dependence of the results on the simulation time. It is straightforward to evaluate eq. (2.38) in the frequency domain via a dipole current $\mathcal{J}(t) = \delta(t)$, which yields a constant-amplitude current $\mathcal{J}(\xi) = 1$. Using the conductivity contour eq. (2.14), corresponding to eqs. (2.15) and (2.16), we find the following explicit form for $g(\xi)$:

$$g(\xi) = -i\xi\left(1 + \frac{i\sigma}{\xi}\right)\frac{1 + i\sigma/2\xi}{\sqrt{1 + i\sigma/\xi}}\Theta(\xi) \tag{2.21}$$

One important feature of eq. (2.21) is that $g(\xi) \to \sqrt{i\sigma^3/\xi}$ becomes singular in the limit as $\xi \to 0$. Assuming that $\Gamma^E(\xi)$ and $\Gamma^H(\xi)$ are continuous at $\xi = 0$ (in general they will not be zero), this singularity is integrable. However, it is cumbersome to integrate in the frequency domain, as it requires careful consideration of the time window for calculation of the field Fourier transforms to ensure accurate integration over the singularity.

An elegant alternative, however, is to use the convolution theorem to re-express the frequency (ξ) integral of the product of $g(\xi)$ and $\Gamma^E(\xi)$ arising in eq. (2.38) as an integral over time t of their Fourier transforms $g(-t)$ and $\Gamma^E(t)$. Technically, the Fourier transform of $g(\xi)$ does not exist because $g(\xi) \sim \xi$ for large ξ; we will deal with this fact rigorously in the Appendix. However, for the moment we will simply assume that the Fourier transform exists in some capacity and proceed. (As a convenient abuse of notation, ξ arguments will always denote functions in the frequency domain, and t arguments their Fourier transforms in the time domain.)

Taking advantage of the causality conditions ($\Gamma^E(t)$, $\Gamma^H(t) = 0$ for $t < 0$) yields the following expression for the force expressed purely in the time domain:

$$F_i = \Im \frac{\hbar}{\pi} \int_0^\infty dt\ g(-t) \left(\Gamma_i^E(t) + \Gamma_i^H(t)\right) \tag{2.22}$$

The advantage of evaluating the force integral in the time domain is that, due to the finite conductivity and lack of sources for $t > 0$, $\Gamma(t)$ will rapidly decay in time. As shown in Fig. 2-2 (and proved in the Appendix), $g(-t)$ also decays with time, in general as $1/t^2$. This allows us to pick a simulation time T such that, for times $t > T$, knowledge of the fields will not change the force result in eq. (2.22) beyond a predetermined error threshold. This approach is very general as it requires no precise knowledge of how the fields decay with time. We expect that, due to the finite σ, the fields should decay exponentially for sufficiently large times; in the interest of quantifying the temporal convergence of the force, we define the time dependent "partial force" $F_i(t)$ as:

$$F_i(t) \equiv \Im \frac{\hbar}{\pi} \int_0^t dt'\ g(-t') \left(\Gamma_i^E(t') + \Gamma_i^H(t')\right). \tag{2.23}$$

Letting $F_i(\infty)$ denote the $t \to \infty$ limit of $F_i(t)$, which is the actual Casimir force, we define the relative error $\Delta_i(t)$ in the i-th component of the force as:

$$\Delta_i(t) \equiv \left| \frac{F_i(t) - F_i(\infty)}{F_i(\infty)} \right|. \tag{2.24}$$

We plot $F_x(t)$ in Fig. 2-1 for the force between two one-dimensional, perfectly-conducting plates separated by a distance 1 (in units of a, where a is an arbitrary length scale), employing different values of σ. The inset plots $\Delta(t)$ for the same configuration. As expected, the asymptotic value of $F_x(t)$ is independent of σ, and $\Delta(t)$ converges exponentially to zero. A surprising fact in Fig. 2-1 is that *higher* σ leads to *slower* temporal convergence. This counter-intuitive fact is discussed in detail in Ref. 172. In general, we have found that picking σ on the order of the length scale of the problem (e.g., the plate separation) optimizes the temporal convergence

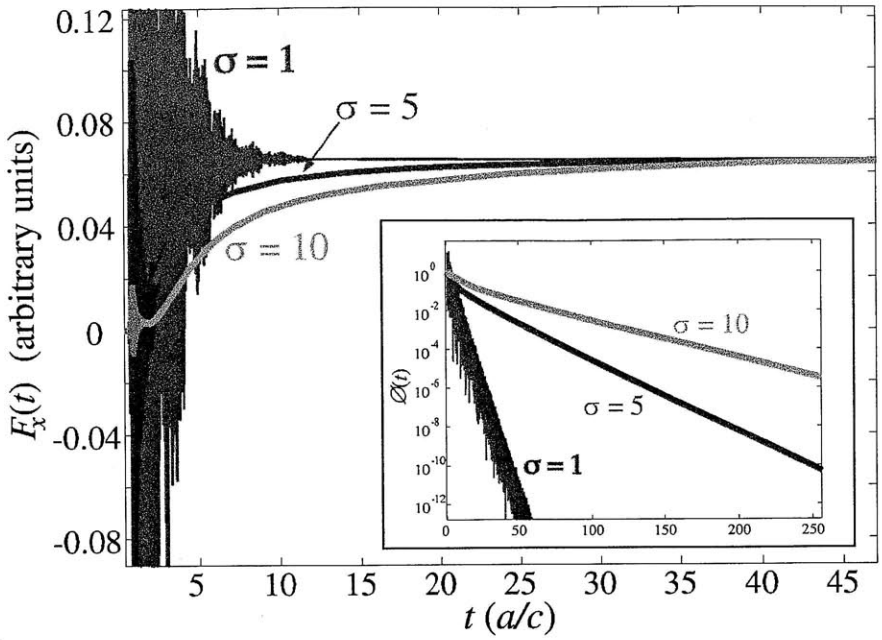

Figure 2-1: Partial force as defined in eq. (2.23) for one-dimensional parallel plates as a function of time t. (Inset): Relative error $\Delta(t)$ as a function of t on a semi log scale.

of $\Delta(t)$.

Since it is possible to employ strictly-real current sources in FDTD, giving rise to real Γ, and since we are only interested in analyzing the influence of $g(t)$ on eq. (2.22), it suffices to look at $\Im g(-t)$. Furthermore, $g(t)$ will exhibit rapid oscillations at the Nyquist frequency due to the delta-function current, and therefore it is more convenient to look at its absolute value. Figure 2-2 plots the envelope of $|\Im g(-t)|$ as a function of t, where again, $g(t)$ is the Fourier transform of eq. (2.20). As anticipated in the previous section, $g(t)$ decays in time. Interestingly, it exhibits a transition from $\sim t^{-1}$ decay at $\sigma = 0$ to $\sim t^{-1/2}$ decay for large σ. The slower decay at long times for larger σ arises from a transition in the behavior of eq. (2.21) from the singularity at $\xi = 0$.

It turns out that the strong Nyquist frequency oscillations in $g(t)$ lead to lower convergence in the force. This is because the Fourier transform $g(\xi)$ is not square integrable, and grows in magnitude as $\xi \to \infty$. It turns out, however, that $g(\xi)$ is well-behaved when viewed as a *distribution* [182], that is, it is only defined in terms of

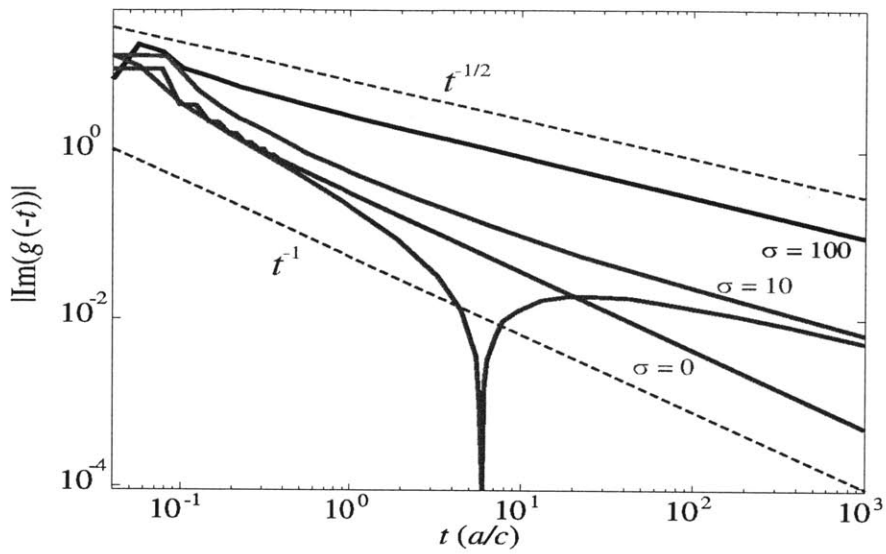

Figure 2-2: $|\Im g(t)|$ for various values of σ, illustrating the transition from t^{-1} to $t^{-1/2}$ power-law decay as σ increases. Because there are strong oscillations in $g(t)$ at the Nyquist frequency for intermediate σ, for clarity we plot the positive and negative terms in $g(t)$ as separate components.

its integrals against square-integrable functions. In Appendix 2A, we will show how this viewpoint allows us to analytically integrate the singular parts of $g(\xi)$ leading to a well-defined, smooth expression for $g(-t)$. In addition to leading to improved convergence in time of the Casimir force $F(t)$, this distributional viewpoint of $g(t)$ allows us to assign upper bounds to the convergence rate of the force $F(t)$: from the results of Appendix 2A, we will be able to prove that in general the FDTD force without the conductivity contour (i.e., $\sigma = 0$) converges as $1/T$; for the special case of z-invariant systems of perfect conductors, this convergence rate changes to $1/T^2$. By contrast, a non-zero σ will actually *reduce* the decay of $g(t)$ at long times (however, this reduction is countered by the exponential decay of the fields $\Gamma(t)$). In addition, we will see that the distributional viewpoint of $g(t)$ will be central to our extension of FDTD to finite temperature, discussed in Sec. 2.6.

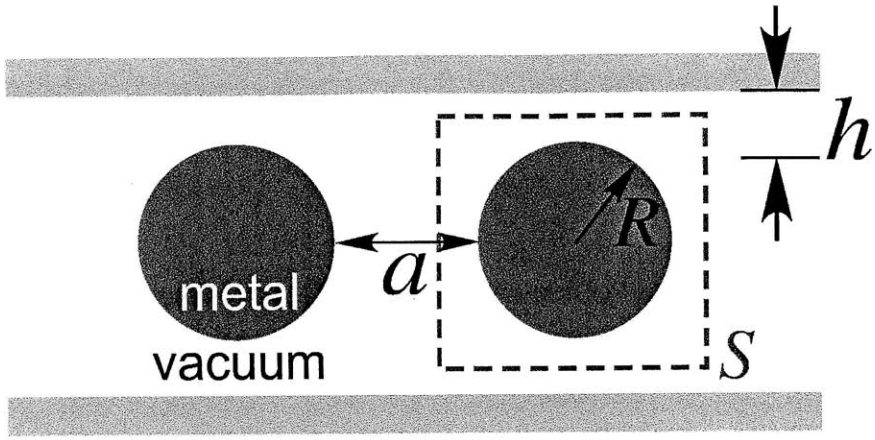

Figure 2-3: Schematic showing the two-dimensional piston-like configuration of [156]: Two perfectly conducting circular cylinders of radius R, separated by a distance a, are sandwiched between two perfectly conducting plates (the materials are either perfect metallic or perfect magnetic conductors). The separation between the blocks and the cylinder surface is denoted as h.

2.4 Harmonic Expansion

While each individual FDTD simulation can be performed very efficiently on modern computers, the surface S will, in general, consist of hundreds or thousands of pixels or voxels, each of which requires an independent FDTD simulation. This requires a large number of time-domain simulations, this number being highly dependent upon the resolution and shape of S, making the computations very costly in general.

We can dramatically reduce the number of required simulations by reformulating the force in terms of a harmonic expansion in $\Gamma^E(t;\mathbf{x},\mathbf{x})$, involving the distributed field responses to distributed currents. This is done as follows [an analogous derivation holds for $\Gamma^H(t;\mathbf{x},\mathbf{x})$]:

As S is assumed to be a compact surface, we can rewrite $\Gamma_{ij}(t;\mathbf{x},\mathbf{x})$ as an integral over S:

$$\Gamma^E_{ij}(t;\mathbf{x},\mathbf{x}) = \int_S dS(\mathbf{x}')\,\Gamma^E_{ij}(t;\mathbf{x},\mathbf{x}')\delta_S(\mathbf{x}-\mathbf{x}') \tag{2.25}$$

where in this integral dS is a scalar unit of area, and δ_S denotes a δ-function with respect to integrals over the surface S. Given a set of orthonormal basis functions $\{f_n(\mathbf{x})\}$ defined on and complete over S, we can make the following expansion of the

δ function, valid for all points $\mathbf{x}, \mathbf{x}' \in S$:

$$\delta_S(\mathbf{x} - \mathbf{x}') = \sum_n \bar{f}_n(\mathbf{x}) f_n(\mathbf{x}') \tag{2.26}$$

The $f_n(\mathbf{x})$ can be an arbitrary set of functions, assuming that they are complete and orthonormal on S [1].

Inserting this expansion of the δ-function into Equation (2.25) and rearranging terms yields:

$$\Gamma^E_{ij}(t; \mathbf{x}, \mathbf{x}) = \sum_n \bar{f}_n(\mathbf{x}) \left(\int_S dS(\mathbf{x}') \, \Gamma^E_{ij}(t; \mathbf{x}, \mathbf{x}') f_n(\mathbf{x}') \right) \tag{2.27}$$

The term in parentheses can be understood in a physical context: it is the electric-field response at position $\mathbf{x}$ and time t to a current source on the surface S of the form $J(\mathbf{x}, t) = \delta(t) f_n(\mathbf{x})$. We denote this quantity by $\Gamma^E_{ij;n}$:

$$\Gamma^E_{ij;n}(t, \mathbf{x}) \equiv \int_S dS(\mathbf{x}') \, \Gamma^E_{ij}(t; \mathbf{x}, \mathbf{x}') f_n(\mathbf{x}') \tag{2.28}$$

where the n subscript indicates that this is a field in response to a current source determined by $f_n(\mathbf{x})$. $\Gamma^E_{ij;n}(t, \mathbf{x})$ is exactly what can be measured in an FDTD simulation using a current $J(\mathbf{x}, t) = \delta(t) f_n(\mathbf{x})$ for each n. This equivalence is illustrated in Fig. 2-4.

The procedure is now only slightly modified from the one outlined in the previous sections: after defining a geometry and a surface S of integration, one will additionally need to specify a set of harmonic basis functions $\{f_n(x)\}$ on S. For each harmonic moment n, one inserts a current function $\mathbf{J}(\mathbf{x}, t) = \delta(t) f_n(\mathbf{x})$ on S and measures the field response $\Gamma_{ij;n}(\mathbf{x}, t)$. Summing over all harmonic moments will yield the total force.

[1] Non-orthogonal functions may be used, but this case greatly complicates the analysis and will not be treated here.

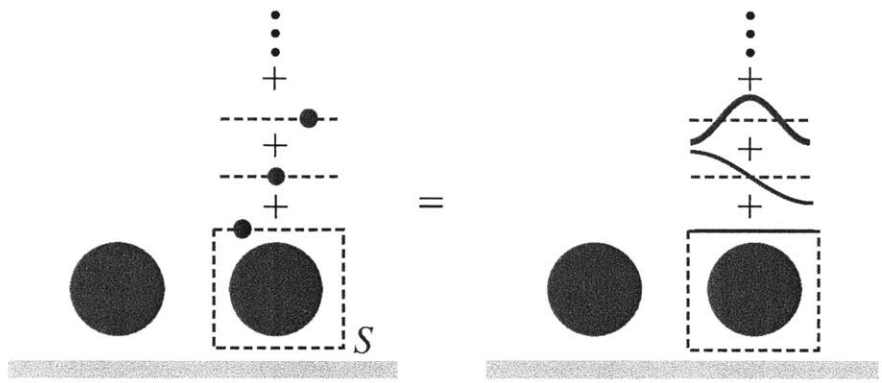

Figure 2-4: Differing harmonic expansions of the source currents (red) on the surface S. The left part shows an expansion using point sources, where each dot represents a different simulation. The right part corresponds to using $f_n(\mathbf{x}) \sim \cos(x)$ for each side of S. Either basis forms a complete basis for all functions in S.

2.4.1 Numerical Implementation

In principle, any surface S and any harmonic source basis can be used. Point sources are a simple, although highly inefficient, example. However, many common FDTD algorithms (including the one we use) involve simulation on a discretized grid. For these applications, a rectangular surface S with an expansion basis separately defined on each face of S is the simplest. In this case, the field integration along each face can be performed to high accuracy and converges rapidly. The Fourier cosine series on a discrete grid is essentially a discrete cosine transform (DCT), a well known discrete orthogonal basis with rapid convergence properties [158]. This in contrast to discretizing some basis such as spherical harmonics that are only approximately orthogonal when discretized on a rectangular grid.

2.5 Applications

We illustrate the application of the FDTD method to systems of perfect conductors and dielectrics in two and three dimensions. Three-dimensional systems with and without cylindrical symmetry are treated separately, as the harmonic expansion (as derived in Appendix 2B) becomes considerably simpler in the former case. We consider Casimir piston-like problems with non-monotonic and monotonic force de-

pendence on sidewall separation, both for previously solved geometries to validate our method and also for new geometries involving magnetic sidewalls and/or cylindrical pistons. We include realistic dielectric materials to calculate the force between suspended silicon waveguides or on a suspended membrane with periodic grooves, also demonstrating the application of PML absorbing boundaries and/or periodic boundaries. In addition we apply this method to a realizable three-dimensional system in which a silica sphere is stably suspended in a fluid above an indented metallic substrate.

2.5.1 Two-dimensional systems

Presently, we consider a variant of the piston-like configuration of Ref. 166, shown as the inset to Fig. 2-5. This system consists of two cylindrical rods sandwiched between two sidewalls, and is of interest due to the non monotonic dependence of the Casimir force between the two blocks as the vertical wall separation h/a is varied. The case of perfect metallic sidewalls ($\varepsilon(x) = -\infty$) [2] has been solved previously [156]; here we also treat the case of perfect magnetic conductor sidewalls ($\mu(x) = -\infty$) as a simple demonstration of the method using magnetic materials.

While three-dimensional in nature, the system is translation-invariant in the z-direction and involves only perfect metallic or magnetic conductors. As discussed in Ref. 167 this situation can actually be treated as the two-dimensional problem depicted in Fig. 2-4 using a slightly different form for $g(-t)$ in eq. (2.22), given by eq. (2.51) in Appendix 2B (interestingly, in this case $g(t)$ can be determined analytically, see eq. (2.51)). The reason we consider the three-dimensional case is that we can directly compare the results for the case of metallic sidewalls to the high-precision scattering calculations of Ref. 156 (which uses a specialized exponentially convergent basis for cylinder/plane geometries).

For this system, the surface S consists of four faces, each of which is a line segment

[2] Formally, in imaginary frequency, a perfect metal satisfies $\varepsilon(i\xi) = +\infty$. However, for a finite difference method either sign will give identical answers, and we find $\varepsilon(i\xi) = -\infty$ more suitable for our computational purposes.

of some length L parameterized by a single variable x. We employ a cosine basis for our harmonic expansion on each face of S. The basis functions for each side are then:

$$f_n(x) = \sqrt{\frac{2}{L}} \cos\left(\frac{n\pi x}{L}\right), \; n = 0, 1, \ldots \tag{2.29}$$

where L is the length of the edge, and $f_n(x) = 0$ for all points x not on that edge of S. These functions, and their equivalence to a computation using δ-function sources as basis functions, are shown in Fig. 2-4.

In the case of our FDTD algorithm, space is discretized on a Yee grid [194], and in most cases x will turn out to lie in between two grid points. One can run separate simulations in which each edge of S is displaced in the appropriate direction so that all of its sources lie on a grid point. However, we find that it is sufficient to place suitably averaged currents on neighboring grid points, as several available FDTD implementations provide features to accurately interpolate currents from any location onto the grid.

The force, as a function of the vertical sidewall separation h/a, and for both TE and TM field components, is shown in Fig. 2-5 and checked against previously known results for the case of perfect metallic sidewalls [156].[3] The agreement is excellent, providing a validation of our method. We also show the force (dashed lines) for the case of perfect magnetic conductor sidewalls. In the case of metallic sidewalls, the force is non-monotonic in h/a. As explained in Ref. 156, this is due to the competition between the TM force, which dominates for large h/a but is suppressed for small h/a, and the TE force, which has the opposite behavior, explained via the method of images for the conducting walls. Switching to perfect magnetic conductor sidewalls causes the TM force to be enhanced for small h/a and the TE force to be suppressed, because the image currents flip sign for magnetic conductors compared to electric conductors. As shown in Fig. 2-5, this results in a monotonic force for this case. In contrast, the dependence on h/R is reversed for a magnetic sidewall: the TE force increases and the TM force decreases as h/R increases. This is because the

[3]We are grateful to Jamal Rahi for sharing his scattering code with us, allowing us to make a direct comparison to our results.

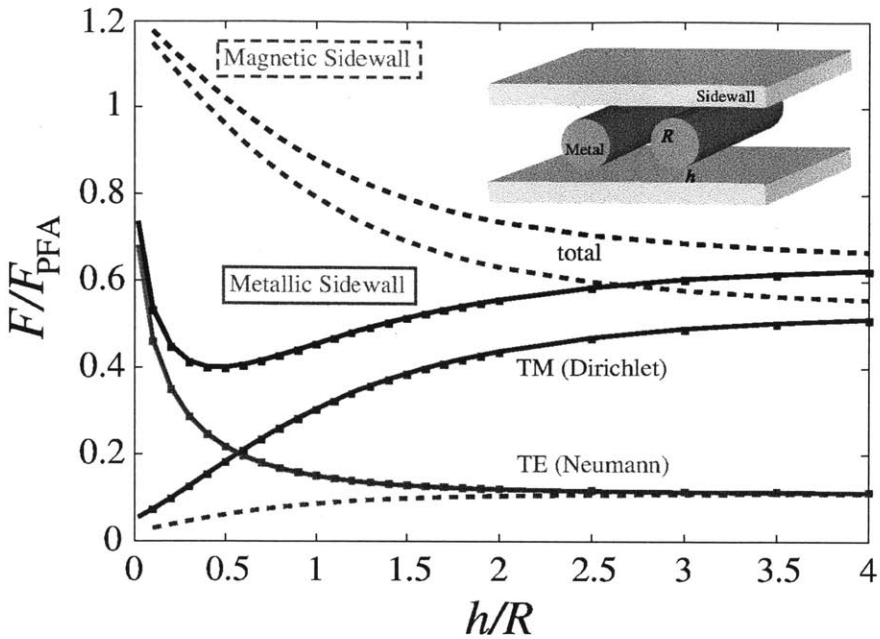

Figure 2-5: Force for the double cylinders of [156] as a function of sidewall separation h/a, normalized by the PFA force $F_{\mathrm{PFA}} = \hbar c\zeta(3)d/8\pi a^3$. Red/blue/black squares show the TE/TM/total force in the presence of metallic sidewalls, as computed by the FDTD method (squares). The solid lines indicate the results from the scattering calculations of [156], showing excellent agreement. Dashed lines indicate the same force components, but in the presence of perfect magnetic-conductor sidewalls (computed via FDTD). Note that the total force is non-monotonic for electric sidewalls and monotonic for magnetic sidewalls.

enhancement/suppression effects on the Green's function are reversed for a magnetic sidewall. Now the overall small contribution of the TE component for large h/R means that the TM force dominates and the net force is monotonic.

The result of the above calculation is a time-dependent field similar to that of Fig. 2-6, which when manipulated as prescribed in the previous section, will yield the Casimir force. As in Ref. 172, our ability to express the force for a dissipationless system (perfect-metal blocks in vacuum) in terms of the response of an artificial dissipative system ($\sigma \neq 0$) means that the fields, such as those shown in Fig. 2-6, rapidly decay away, and hence only a short simulation is required for each source term. In addition, Fig. 2-7 shows the convergence of the harmonic expansion as a function of n. Asymptotically for large n, an $n^{-1/4}$ power law is clearly discernible. The explanation

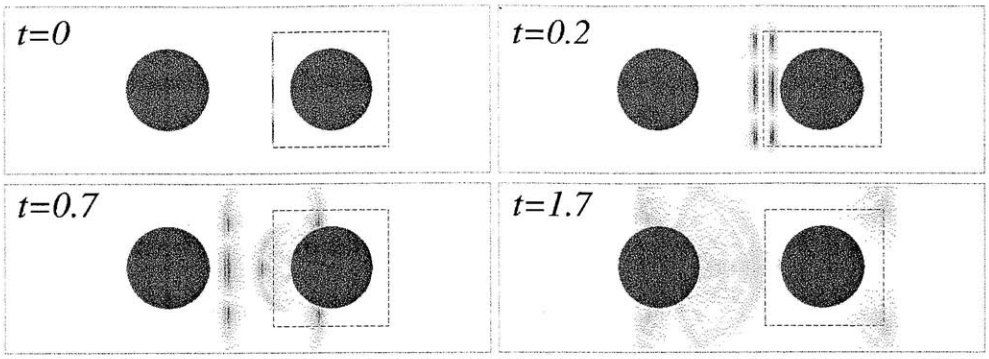

Figure 2-6: (Color Online) $\Gamma^E_{yy;n=2}(t, \mathbf{x})$ snapshots (blue/white/red = positive/zero/negative) for the $n = 2$ term in the harmonic cosine expansion on the leftmost face of S for the double blocks configuration of [166] at selected times (in units of a/c).

for this convergence follows readily from the geometry of S: the electric field $\mathbf{E}(\mathbf{x})$, when viewed as a function along S, will have nonzero first derivatives at the corners. However, the cosine series used here always has a vanishing derivative. This implies that its cosine transform components will decay asymptotically as n^{-2} [20]. As Γ^E is related to the correlation function $\langle \mathbf{E}(\mathbf{x})\mathbf{E}(\mathbf{x})\rangle$, their contributions will decay as n^{-4}. One could instead consider a Fourier series defined around the whole perimeter of S, but the convergence rate will be the same because the derivatives of the fields will be discontinuous around the corners of S. A circular surface would have no corners in the continuous case, but on a discretized grid would effectively have many corners and hence poor convergence with resolution.

2.5.2 Dispersive Materials

Dispersion in FDTD in general requires fitting an actual dispersion to a simple model (e.g., a series of Lorentzians or Drude peaks). Assuming this has been done, these models can then be analytically continued onto the complex conductivity contour.

As an example of a calculation involving dispersive materials, we consider in this section a geometry recently used to measure the classical optical force between two suspended waveguides [103], confirming a prediction [152] that the sign of the classical force depends on the relative phase of modes excited in the two waveguides. We now

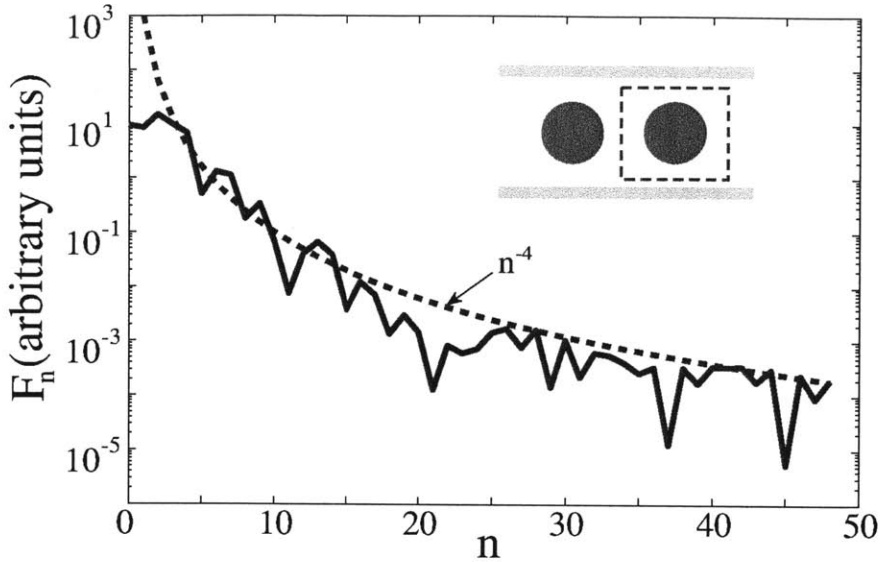

Figure 2-7: Relative contribution of harmonic moment n in the cosine basis to the total Casimir force for the double blocks configuration (shown in the inset)

compute the Casimir force in the same geometry, which consists of two identical silicon waveguides in empty space. We model silicon as a dielectric with dispersion given by:

$$\varepsilon(\omega) = \varepsilon_0 + \frac{\varepsilon_f - \varepsilon_0}{1 - \left(\frac{\omega}{\omega_0}\right)^2} \tag{2.30}$$

where $\omega_0 = 6.6 \times 10^{15}$ rad/sec, and $\varepsilon_0 = 1.035$, $\varepsilon_f = 11.87$. This dispersion can be implemented in FDTD by the standard technique of auxiliary differential equations [194] mapped into the complex-ω plane as explained in Ref. 172.

The system is translation-invariant in the z direction. If it consisted only of perfect conductors, we could use the trick of the previous section and compute the force in only one 2d simulation. However, dielectrics hybridize the two polarizations and require an explicit k_z integral, as discussed in Ref. 167. Each value of k_z corresponds to a separate two-dimensional simulation with Bloch-periodic boundary conditions. The value of the force for each k_z is smooth and rapidly decaying, so in general only a few k_z points are needed.

To simulate the infinite open space around the waveguides, it is ideal to have "absorbing boundaries" so that waves from sources on S do no reflect back from the

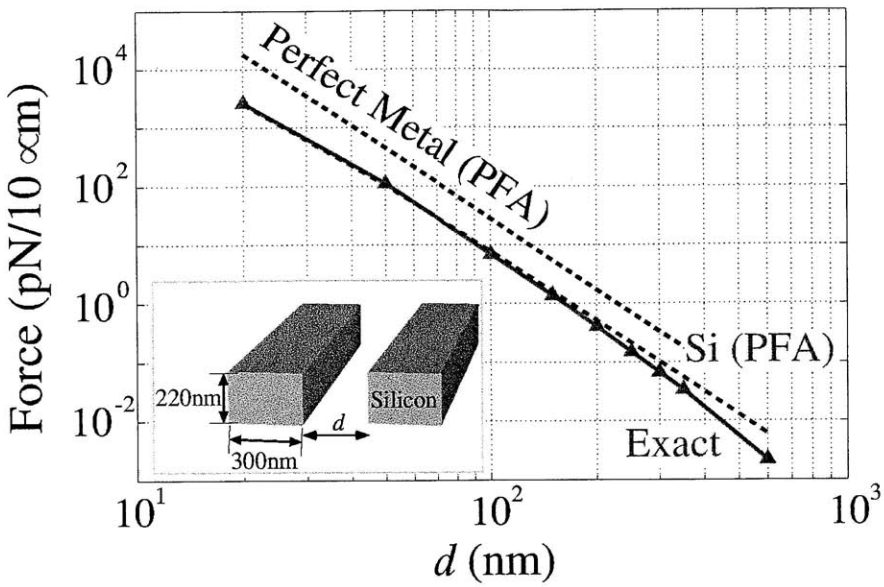

Figure 2-8: Force per unit length between long silicon waveguides suspended in air [103], determined by the FDTD method (red triangles). Also shown is the analogous one-dimensional computation assuming silicon plates of finite thickness (blue dashes), and the result $F = \pi^2/240d^4A$ for perfect metals (assuming plate area A equal to the interaction area of the waveguides).

boundaries. We employ the standard technique of perfectly matched layers (PML), which are a thin layer of artificial absorbing material placed adjacent to the boundary and designed to have nearly zero reflections [194]. The results are shown in red in Fig. 2-8. We also show (in blue) the force obtained using the proximity force approximation (PFA) calculations based on the Lifshitz formula [44, 104]. For the PFA, we assume two parallel silicon plates, infinite in both directions perpendicular to the force and having the same thickness as the waveguides in the direction parallel to the force, computing the PFA contribution from the surface area of the waveguide. As expected, at distances smaller than the waveguide width, the actual and PFA results are in good agreement, while as the waveguide separation increases, the PFA becomes more inaccurate. For example, by a separation of 300nm, the PFA result is off by 50%. We also show for comparison the force for the same surface between two perfectly metallic plates, also assuming infinite extent in both transverse directions.

2.5.3 Three dimensions with cylindrical symmetry

In the case of cylindrical symmetry, we can employ a cylindrical surface S and a complex exponential basis $e^{im\phi}$ in the ϕ direction. For a geometry with cylindrical symmetry and a separable source with $e^{im\phi}$ dependence, the resulting fields are also separable with the same ϕ dependence, and the unknowns reduce to a two-dimensional (r, z) problem for each m. This results in a substantial reduction in computational costs compared to a full three-dimensional computation.

Treating the reduced system as a two-dimensional space with coordinates (r, z), the expression for the force (as derived in Appendix 2B) is now:

$$F_i = \sum_n \int_0^\infty dt\, \Im[g(-t)] \int_S ds_j(\mathbf{x})\, \Gamma_{ij;n}(\mathbf{x}, t) \tag{2.31}$$

where the m-dependence has been absorbed into the definition of Γ above:

$$\Gamma_{ij;n}(x, t) \equiv \Gamma_{ij;n,m=0}(\mathbf{x}, t) + 2 \sum_{m>0} \Re[\Gamma_{ij;n,m}(\mathbf{x}, t)], \tag{2.32}$$

and $ds_j = ds\, n_j(\mathbf{x})$, ds being a one-dimensional Cartesian line element. As derived in Appendix 2B, the Jacobian factor r obtained from converting to cylindrical coordinates cancels out, so that the one-dimensional (r-independent) measure ds is the appropriate one to use in the surface integration. Also, the $2\Re[\cdots]$ comes from the fact that the $+m$ and $-m$ terms are complex conjugates. Although the exponentials $e^{im\phi}$ are complex, only the real part of the field response appears in eq. (2.32), allowing us to use $\Im[g(-t)]$ alone in eq. (2.31).

Given an $e^{im\phi}$ dependence in the fields, one can write Maxwell's equations in cylindrical coordinates to obtain a two-dimensional equation involving only the fields in the (r, z) plane. This simplification is incorporated into many FDTD solvers, as in the one we currently employ [51], with the computational cell being restricted to the (r, z) plane and m appearing as a parameter. When this is the case, the implementation of cylindrical symmetry is almost identical to the two-dimensional situation. The only difference is that now there is an additional index m over which

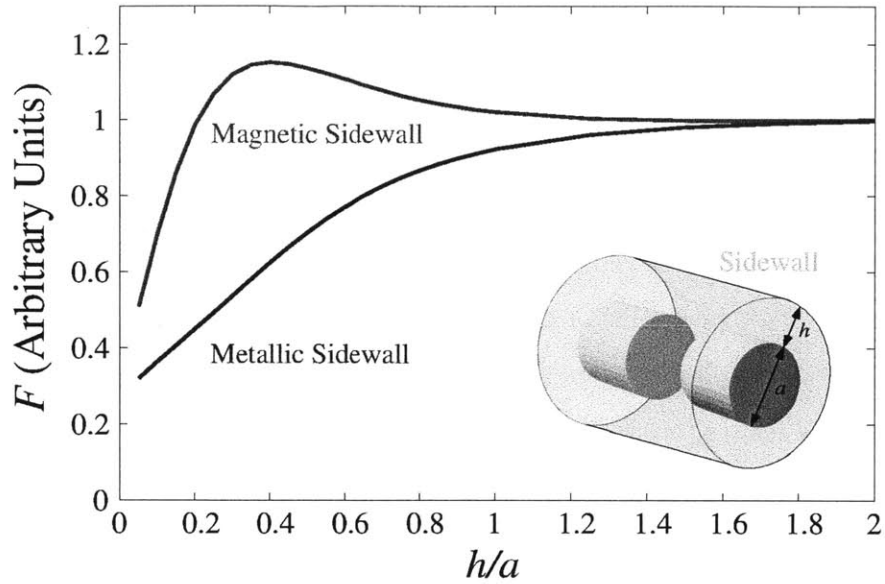

Figure 2-9: Force as a function of outer sidewall spacing h/a for the cylindrically-symmetric piston configuration shown in the figure. Both plates are perfect metals, and the forces for both perfect metallic and perfect magnetic conductor sidewalls are shown. Note that in contrast to Fig. 2-5, here the force is monotonic in h/a for the metallic case and non monotonic for the magnetic case.

the force must be summed.

To illustrate the use of this algorithm with cylindrical symmetry, we examine the 3d system shown in the inset of Fig. 2-9. This configuration is similar to the configuration of cylindrical rods of Fig. 2-5, except that instead of translational (z) invariance we instead impose rotational (ϕ) invariance. In this case, the two sidewalls are joined to form a cylindrical tube. We examine the force between the two blocks as a function of h/a (the $h = 0$ case has been solved analytically [117]).

Due to the two-dimensional nature of this problem, computation time is comparable to that of the two-dimensional double block geometry of the previous section. Rough results (at resolution 40, accurate to within a few percentage points) can be obtained rapidly on a single computer (about 5 minutes running on 8 processors) are shown in Fig. 2-9 for each value of h/a. Only indices $n, m \in \{0, 1, 2\}$ are needed for the result to have converged to within 1%, after which the error is dominated by the spatial discretization. PML is used along the top and bottom walls of the tube.

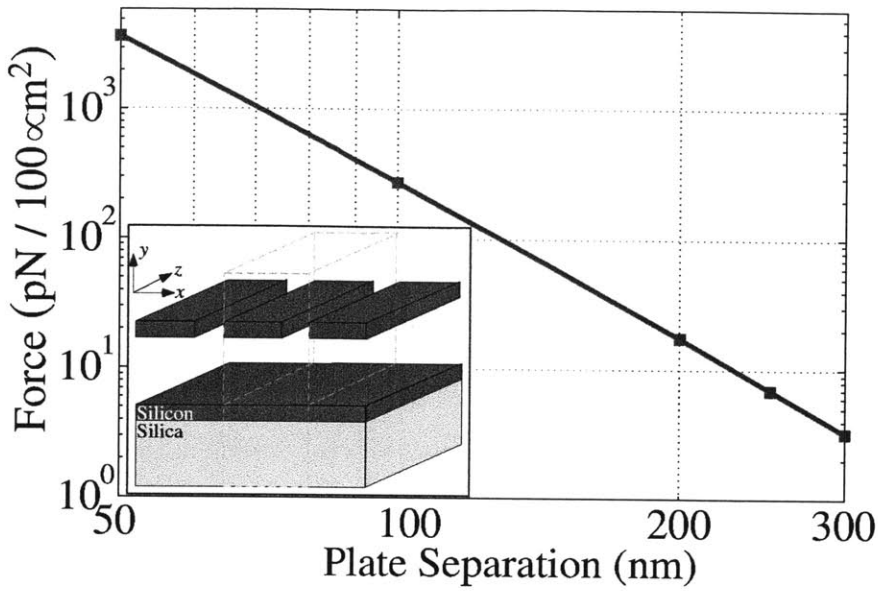

Figure 2-10: The Casimir force between a periodic array of Silicon waveguides and a Silicon/Silica substrate, as the array/substrate separation is varied. The system is periodic in the x-direction and translation-invariant in the z-direction, so the computation involves a set of two-dimensional simulations.

In contrast to the case of two pistons with translational symmetry, the force for metallic sidewalls is monotonic in h/a. Somewhat surprisingly, when the sidewalls are switched to perfect magnetic conductors the force becomes non monotonic again. This is due to the differing geometric effects of cylindrical symmetry compared to quasi-2d symmetry. Although the use of perfectly magnetic conductor sidewalls in this example is unphysical, it demonstrates the use of a general-purpose algorithm to examine the material-dependence of the Casimir force. If we wished to use dispersive and/or anisotropic materials (as we will in Chapter 5), no additional code would be required.

2.5.4 Periodic Boundary Conditions

Periodic dielectric systems are of interest in many applications. The purpose of this section is to demonstrate computations involving a periodic array of dispersive silicon dielectric waveguides above a silica substrate, shown in Fig. 2-10. We will employ FDTD with periodic boundary conditions for more complex systems in later chapters.

As discussed in Ref. 167, the Casimir force for periodic systems can be computed as in integral over all Bloch wavevectors in the directions of periodicity. Here, as there are two directions, x and z, that are periodic (the latter being the limit in which the period goes to infinity). The force is then given by:

$$\int_0^\infty \int_0^\infty F_{k_z,k_x} dk_z dk_x \tag{2.33}$$

where F_{k_z,k_x} is the force computed from one simulation of the unit cell using Bloch-periodic boundary conditions with wavevector $\mathbf{k} = (k_x, 0, k_z)$. In the present case, the unit cell is of period 1μm in the x direction and of zero length in the z direction, so the computations are effectively two-dimensional (although they must be integrated over k_z).

We use the dispersive model of eq. (2.30) for silicon, while for silica we use [166]

$$\epsilon(\omega) = 1 + \sum_{j=1}^{3} \frac{C_j \omega_j^2}{\omega_j^2 - \omega^2} \tag{2.34}$$

where $(C_1, C_2, C_3) = (0.829, 0.095, 1.098)$ and $(\omega_1, \omega_2, \omega_3) = (0.867, 1.508, 203.4) \times 10^{14}$ (rad/sec).

2.5.5 Full 3d computations: stable confinement in 3d

As a final demonstration, we compute the Casimir force for a fully three-dimensional system, without the use of special symmetries. The system used is depicted in Fig. 2-11. This setup demonstrates stable levitation with the aid of a fluid medium, which has been explored previously in Ref. 174 in the context of quasi-2d systems. With this example, we present a setup similar to that used previously to measure repulsive Casimir forces [134], with the hope that this system may be experimentally feasible. A silica sphere sits atop a perfect metal plane which has a spherical indentation in it. The sphere is immersed in bromobenzene. As the system satisfies $\varepsilon_{\text{sphere}} < \varepsilon_{\text{fluid}} < \varepsilon_{\text{plane}}$, the sphere feels a repulsive Casimir force upwards [134]. This is balanced by the downward force of gravity, which confines the sphere vertically. In addition, the

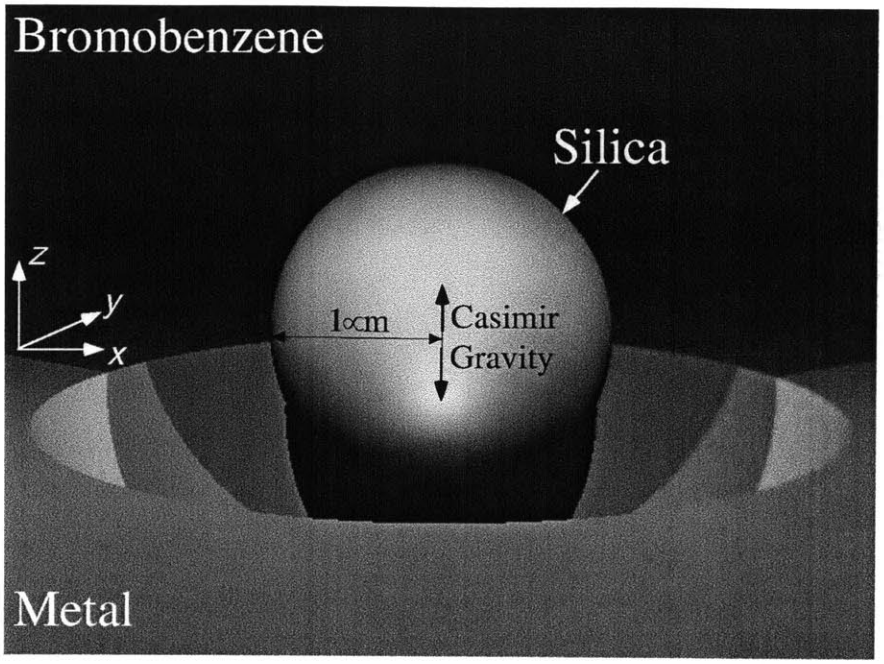

Figure 2-11: Three-dimensional configuration showing stable levitation. At the equilibrium point, the force of gravity counters the Casimir force, while the Casimir force from the walls of the spherical indentation confine the sphere laterally

Casimir repulsion from the sides of the spherical indentation confine the sphere in the lateral direction. The radius of the sphere is 500 nm, and the circular indentation in the metal is formed from a circle of radius 1μm, with a center 500 nmm above the plane. For computational simplicity, in this model we neglect dispersion and use the zero-frequency values for the dielectrics, as the basic effect does not depend upon the dispersion (the precise values for the equilibrium separations will be changed with dispersive materials). These are $\varepsilon = 2.02$ for silica and $\varepsilon = 4.30$ for bromobenzene. For the gravitational force we use densities of 1.49 g/cm^3 for bromobenzene and 1.96 g/cm^3 for silica.

An efficient strategy to determine the stable point is to first calculate the force on the glass sphere when its axis is aligned with the symmetry axis of the indentation. This configuration is cylindrically-symmetric and can be efficiently computed as in the previous section. Results for a specific configuration, with a sphere radius of 500 nm and an indentation radius of 1 μm, are shown in Fig. 2-12.

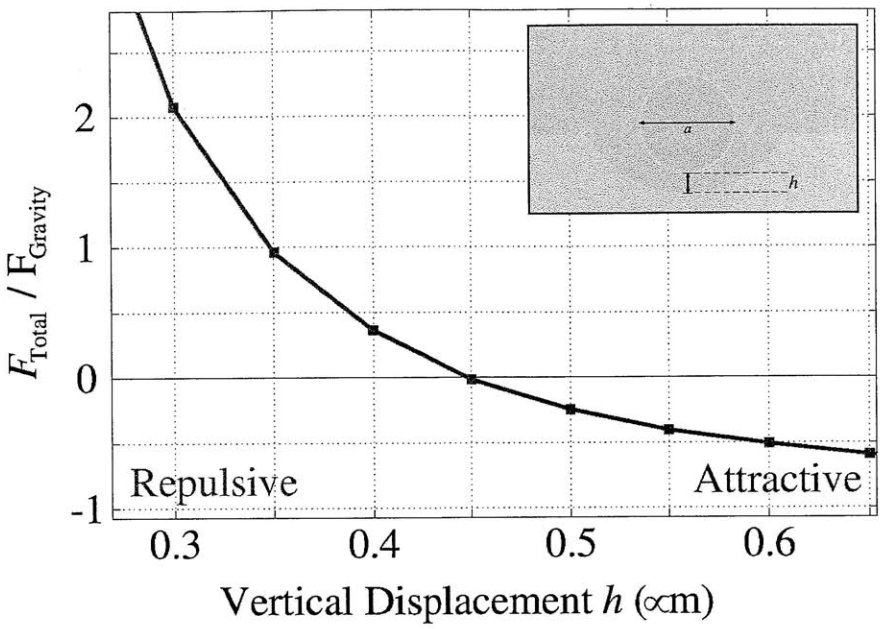

Figure 2-12: Total (Casimir + gravity) vertical (z) force on the silica sphere (depicted in the inset) as the height h of the sphere's surface above the indentation surface is varied. The point of vertical equilibrium occurs at $h \sim 450$ nm.

The force of gravity is balanced against the Casimir force at a height of $h = 450$ nm. To determine the strength of lateral confinement, we perform a fully three-dimensional computation in which the center of the sphere is displaced laterally from equilibrium by a distance Δ_x (the vertical position is held fixed at the equilibrium value $h = 450$nm). The results are shown in Fig. 2-13. It is seen that over a fairly wide range ($|\Delta x| < 100$ nm) the linear term is a good approximation to the force, whereas for larger displacements the Casimir force begins to increase more rapidly. Of course, at these larger separations the vertical force is no longer zero, due to the curvature of the indentation, and so must be re-computed as well.

The fully three-dimensional computations are rather large, and require roughly a hundred CPU hours per force point. However, these Casimir calculations parallelize very easily – every source term, polarization, and k-point can be computed in parallel, and individual FDTD calculations can be parallelized in our existing software – so we can compute each force point in under an hour on a supercomputer (with 1000+ processors). In contrast, the 2d and cylindrical calculations require tens of

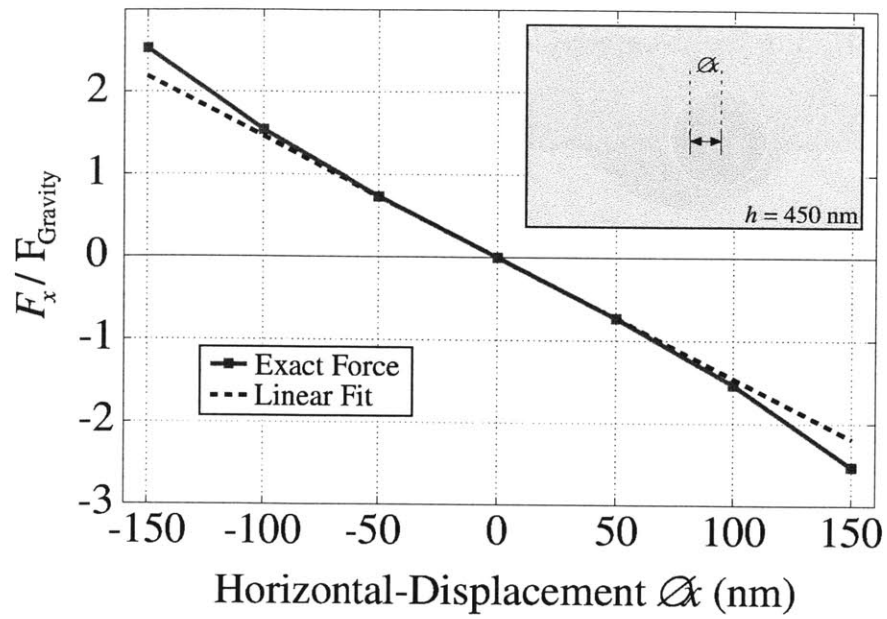

Figure 2-13: Casimir restoring force on the sphere as a function of lateral displacement dx, when the vertical position is fixed at $h = 450$ nm, the height at which gravity balances the Casimir force

minutes per force point. This method is usable in situations involving complex three-dimensional materials, e.g, periodic systems or systems with anisotropic materials; we will demonstrate the application to 3d periodic systems to chiral metamaterials in Chapter 3 and to 3d systems with anisotropic materials in Chapter 5 in order to examine Casimir repulsion in vacuum.

2.6 Finite temperature with FDTD

In this section we discuss how our FDTD method can be extended to finite-temperature Casimir forces; this work was done with Kai Pan. At a nonzero T, the integral for the Casimir force in imaginary frequency is replaced by a sum over "Matsubara frequencies" $\xi_n = n\pi\omega_T$ for integers n, where $\omega_T = 2k_B T/\hbar$ and k_B is Boltzmann's

constant [127]; this has the general form:

$$F(T) = \pi\omega_T \left[\frac{f(0^+)}{2} + \sum_{n=1}^{\infty} f\left(n\pi\omega_T\right) \right]. \tag{2.35}$$

At real frequency, the effect of $T > 0$ is simply to include an additional weighting factor $\coth\left[\frac{\omega(\xi)}{\omega_T}\right]$ in the definition of $g(\xi)$ in eq. (2.21). The obvious approach to incorporating finite T into the conductivity contour is to replace $g[\omega(\xi)]$ with:

$$\begin{aligned} g[\omega(\xi)] \to g[\omega(\xi)] \coth\left[\frac{\omega(\xi)}{\omega_T}\right] \\ = -i\xi \left(\sqrt{1+\frac{i\sigma}{\xi}}\right)(1+i\sigma/2\xi)\coth\left[\frac{\omega(\xi)}{\omega_T}\right], \end{aligned} \tag{2.36}$$

and then Fourier transform to yield the finite-temperature analogue of $g(t)$. However, when we tried this as a straightforward extension of the results of Sec. 2.5 we were unable to get the correct result for the simple case of 1d parallel plates; instead, the forces obtained would *decrease* as T increases (whereas the correct result, from eq. (2.35), should increase linearly in T). Thinking that the problem was simply implementation, Kai developed an independent implementation of eq. (2.36). However, he found the same puzzling results. After some thought, we realized that the problem stemmed from treating $g(t)$ as a *function*, whereas (see Appendix 2A) we should treat it as a *distribution*. For $T = 0$ computations this turned out to not be significant as we could get the correct answer by naively Fourier transforming $g(\xi)$ as a function (the spatial resolution imposed a high-frequency cutoff on the Fourier integral). In this case, the problem is that eq. (2.36) has a non-integrable $1/\xi$ singularity due to the $\coth(\omega/\omega_T)$ factor. The solution, we found, is to subtract the $\omega = 0$ contribution from eq. (2.35), integrate it analytically, and combine the result with the Fourier transform of the remaining non-singular term (which can be performed numerically without trouble). If we subtract the $n = 0$ pole from the coth, we obtain

$$g_{n>0}(\xi) = g[\omega(\xi)] \left\{ \coth\left[\frac{\omega(\xi)}{\omega_T}\right] - \frac{\omega_T}{\omega(\xi)} \right\}, \tag{2.37}$$

We found that the results from our previous "incorrect" implementations agreed with the forces computed using $g_{n>0}$. The task remains to correctly evaluate the $n = 0$ term. To handle the $n = 0$ contribution, we begin with the real-ω $T = 0$ expression for the Casimir force, which in our notation from the stress-tensor method is written schematically as:

$$F_i = \Im \frac{\hbar}{\pi} \int_0^\infty d\omega \; g_R(\omega)\Gamma_i(\omega), \tag{2.38}$$

From Eq. (2.35), the $\omega = 0$ contribution for $T > 0$ is then

$$\begin{aligned} F_{i,(n=0)} &= \lim_{\omega \to 0^+} \Im \left[\frac{\hbar}{\pi} \frac{1}{2} (-i\omega)\Gamma_i(\omega) \frac{2\pi k_{\mathrm{B}} T}{\hbar} \right] && (2.39) \\ &= \lim_{\omega \to 0^+} \Re \left[-\omega \Gamma_i(\omega) k_{\mathrm{B}} T \right]. && (2.40) \end{aligned}$$

To relate Eq. (2.40) to what is actually computed in the FDTD method requires some care because of the way in which we transform to the $\omega(\xi)$ contour. The quantity $\Gamma_i^E(\omega)$ is proportional to an integral of $E_{ij}(\omega) = -i\omega G_{ij}(\omega)$. The $\omega(\xi)$ transformed system computes $\tilde{\Gamma}_i(\xi) \sim \tilde{E}_{ij}(\xi) = -i\xi \tilde{G}_{ij}(\xi)$, where $\tilde{G}(\xi)$ involves $\omega^2 \varepsilon(\mathbf{r}) \to \xi^2 (1 + \frac{i\sigma}{\xi}) \varepsilon(\mathbf{r})$. However, what we actually want is $-i\omega G_{ij}(\omega)|_{\omega=\omega(\xi)} = -i\omega(\xi)\tilde{G}_{ij}(\xi)$. Therefore, the correct $\omega = 0$ contribution is given by

$$\lim_{\omega \to 0^+} \Gamma_i^E(\omega) = \lim_{\xi \to 0^+} \frac{\omega(\xi)}{\xi} \tilde{\Gamma}_i^E(\mathbf{r}, \xi) \tag{2.41}$$

Combined with $\omega(\xi) k_{\mathrm{B}} T$ from Eq. (2.40), this gives an $n = 0$ contribution of $\tilde{\Gamma}|_{\xi=0^+}$ multiplied by $-\omega(\xi)^2 k_{\mathrm{B}} T / \xi|_{\xi=0^+} = \sigma k_{\mathrm{B}} T$. This $\omega = 0$ term corresponds to a simple expression in the time domain, where $\tilde{\Gamma}|_{\xi=0^+}$ is simply the time integral of $\tilde{\Gamma}(t)$. Therefore, while we originally integrated $g_{n>0}(t)\tilde{\Gamma}(t)$ to obtain the $n > 0$ contributions, the $n = 0$ contribution is included if we instead integrate:

$$\left[g_{n>0}(t) + \sigma k_{\mathrm{B}} T \right] \tilde{\Gamma}(t). \tag{2.42}$$

The term $[g_{n>0}(t) + \sigma k_{\mathrm{B}} T]$ generalizes the original $g(t)$ function from to finite T. Kai has applied this formula to the extension of the 2d double block results to finite

temperature with FDTD (which we have cross-checked with BEM), and has found the interesting result that the non-monotonicity in the force vs. sidewall separation actually disappears for sufficiently high T. These results, along with a physical explanation of this effect, can be found in Ref. 143.

2.7 An alternative material transformation

In Sec. 2.2.3 we discussed how an analytic transformation $\omega \to f(\omega)\omega$ in frequency is mathematically equivalent to a transformation $\varepsilon(\omega) \to f^2(\omega)\varepsilon[f(\omega)\omega]$. In FDTD, dispersions in which $\varepsilon(\omega)$ and $\mu(\omega)$ are rational functions of ω are straightforward to implement via auxiliary equations [194]. Therefore, in real situations one takes data for the actual $\varepsilon(\omega)$ and fits it to a rational function, most commonly a sum of Lorentzians. Accurate fits for many common materials exist in the literature (e.g., Ref. 125 and Ref. 14). However, in order to get the conductivity contour we require that $f(\omega) = \sqrt{1 + \frac{i\sigma}{\omega}}$; in general, $\varepsilon[f(\omega)\omega]$ will not be a rational function, even if $\varepsilon(\omega)$ is.[4] To solve this $\varepsilon[f(\omega)\omega]$ in FDTD, we would need to first perform another fit to rational functions. This fit could be tedious, and would depend on the parameter σ used (this is very undesirable, as the underlying physics is independent of σ).

Here we discuss an idea for an alternative method in which the rationality of $\varepsilon(\omega)$ can be preserved after the complex frequency mapping. Consider the full Maxwell's equation eq. (2.6) for the electric Green's function:

$$\left[\nabla \times \frac{1}{\mu(\mathbf{r},\omega)}\nabla \times \; - \omega^2\varepsilon(\mathbf{r},\omega)\right] \mathbf{G}_j^E(\omega;\mathbf{r},\mathbf{r}') = \delta(\mathbf{r}-\mathbf{r}')\hat{\mathbf{e}}_j, \tag{2.43}$$

and consider the "pseudo-conductivity" mapping $f(\omega) = \left(1 + \frac{i\sigma}{\omega + i\alpha}\right)$ for a fixed, real $\alpha > 0$. The product $f(\omega)\omega$ still goes to zero as $\omega \to 0$ and remains confined to the upper half plane, so the integral along this contour will still correspond to the physical Casimir force (this is why we require $\alpha > 0$). This frequency mapping is

[4] A common exception is in Sec. 2.5.2 where this $f(\omega)$ plugged into a lossless Lorentzian will still yield another Lorentzian.

actually well-known in the context of perfectly-matched layers (PML) [13], known as complex frequency-shifted PML (CFS PML) [92]. $f(\omega)$ is now a rational function, and the mapping $\omega^2 \to f^2(\omega)\omega^2$ can be expressed in eq. (2.43) as:

$$\left[\nabla \times \frac{1}{f(\omega)\mu[\mathbf{r}, f(\omega)\omega]}\nabla \times \; - \omega^2 \left(f(\omega)\varepsilon[\mathbf{r}, f(\omega)\omega]\right)\right] \mathbf{G}_j^E(\omega; \mathbf{r}, \mathbf{r}') = \delta(\mathbf{r}-\mathbf{r}')\hat{\mathbf{e}}_j, \quad (2.44)$$

now, both quantities $f(\omega)\mu[f(\omega)\omega]$ and $f(\omega)\varepsilon[f(\omega)\omega]$ are rational functions of ω and can therefore be implemented via auxiliary differential equations for any σ and α; these correspond to the new permeability and permittivity in the computation, respectively. From the theory of CFS-PML we know that the resulting time-domain equations will be stable. Thus, once the real-frequency dispersion $\varepsilon(\omega)$ is fit to rational functions (e.g., a sum of Lorentzians), the same fit can be used for any choice of contour parameters σ and α. It remains to actually implement this idea to ensure that no subtle issues crop up (e.g., as was the case for finite temperatures discussed above).

2.8 Concluding Remarks

We have demonstrated a practical implementation of a general FDTD method for computing Casimir forces via a harmonic expansion in source currents. The utility of such a method is that many different systems (dispersive, anisotropic, periodic boundary conditions) can all be simulated with the same algorithm.

In practice, the harmonic expansion converges rapidly with higher harmonic moments, making the overall computation complexity of the FDTD method $O(N^{1+1/d})$ for N grid points and d spatial dimensions. This arises from the $O(N)$ number of computations needed for one FDTD time step, while the time increment used will vary inversely with the spatial resolution [194], leading to $O(N^{1/d})$ time steps per simulation. In addition, there is a constant factor proportional to the number of terms retained in the harmonic expansion, as an independent simulation is required for each term. For comparison, without a harmonic expansion one would have to run

a separate simulation for each point on S. In that case, there would be $O(N^{(d-1)/d})$ points, leading to an overall computational cost of $O(N^2)$ [172].

We do not claim that this is the most efficient technique for computing Casimir forces, as there are other works that have also demonstrated very efficient methods capable of handling arbitrary three-dimensional geometries, such as a recently-developed boundary-element method [162]. However, these integral-equation methods and their implementations must be substantially revised when new types of materials or boundary conditions are desired that change the underlying Green's function (e.g., going from metals to dielectrics, periodic boundary conditions, or isotropic to anisotropic materials), whereas very general FDTD codes, requiring no modifications, are available off-the-shelf.

As a final remark we comment on the application of this method to computing Casimir-Polder (CP) potentials involving atoms [24] and surfaces. In this approximation the relevant quantity is the spatial derivative of the electromagnetic Green's function for the surfaces in the absence of the atoms. While this quantity can be computed with the FDTD method, it is not an ideal setting because the full determination of the CP potential in all space requires a separate computation per grid point. We believe that boundary-element methods, which can determine this potential in all space from one calculation, offer a very promising method for CP potentials.

Appendix 2A: Functional treatment of $g(t)$

We now demonstrate how a well-defined Fourier transform $g(t)$ of $g(\xi)$ can be constructed by viewing g as a *distribution* rather than a function. Aside from simplifying our computation of $g(t)$ (and yielding analytic results in the particular case of z-invariant PEC systems), this provides us with an upper bound on the asymptotic convergence rate for the Casimir force with simulation time t and facilitates the extension of the FDTD method to nonzero temperatures.

The function $g(\xi)$ is given by:

$$g(\xi) = -i\xi\left(1 + \frac{i\sigma}{\xi}\right)\frac{1 + i\sigma/2\xi}{\sqrt{1 + i\sigma/\xi}}\Theta(\xi) \tag{2.45}$$

$g(\xi)$ has the behavior that it diverges in the high-frequency limit. For large ξ, $g(\xi)$ has the limit:

$$g(\xi) \to g_1(\xi) \equiv \frac{\xi}{i}\Theta(\xi) + \sigma\Theta(\xi) \quad \text{as } \xi \to \infty \tag{2.46}$$

Viewing $g_1(\xi)$ as a function, we could only compute its Fourier transform $g_1(t)$ by introducing a cutoff in the frequency integral at the Nyquist frequency, since the time signal is only defined up to a finite sampling rate and the integral of a divergent function may appear to be undefined in the limit of no cutoff.

Applying this procedure to compute $g(-t)$ yields a time series that has strong oscillations at the Nyquist frequency. The amplitude of these oscillations can be quite high, increasing the time needed to obtain convergence and also making any physical interpretation of the time series more difficult. These oscillations are entirely due to the high-frequency behavior of $g(\xi)$, where $g(\xi) \sim g_1(\xi)$. However, $g(t)$ and $g(\xi)$ only appear when when they are being integrated against smooth, rapidly decaying field functions $\Gamma(\mathbf{x}, t)$ or $\Gamma(\mathbf{x}, \xi)$. In this case, g can be viewed as a tempered distribution (in the same manner as the δ-function) [182]. Although $g(\xi)$ diverges for large ξ, this divergence is only a power law, so it is a tempered distribution and its Fourier transform is well-defined without any truncation. In particular, the Fourier transform of $g_1(\xi)$ in eq. (2.46) is given by:

$$g_1(-t) = \frac{i}{2\pi}\left(\frac{1}{t^2} + \frac{\sigma}{t}\right) \tag{2.47}$$

Adding and subtracting the term $g_1(\xi)$ from $g_(\xi)$, the remaining term decays to zero for large ξ and can be Fourier transformed numerically without the use of a high-frequency cutoff, allowing $g(-t)$ to be computed as the sum of $g_1(t)$ plus the Fourier transform of a well-behaved function. This results in a much smoother $g(-t)$ which will give the same final force as the $g(-t)$ used in Ref. 172, but will also have

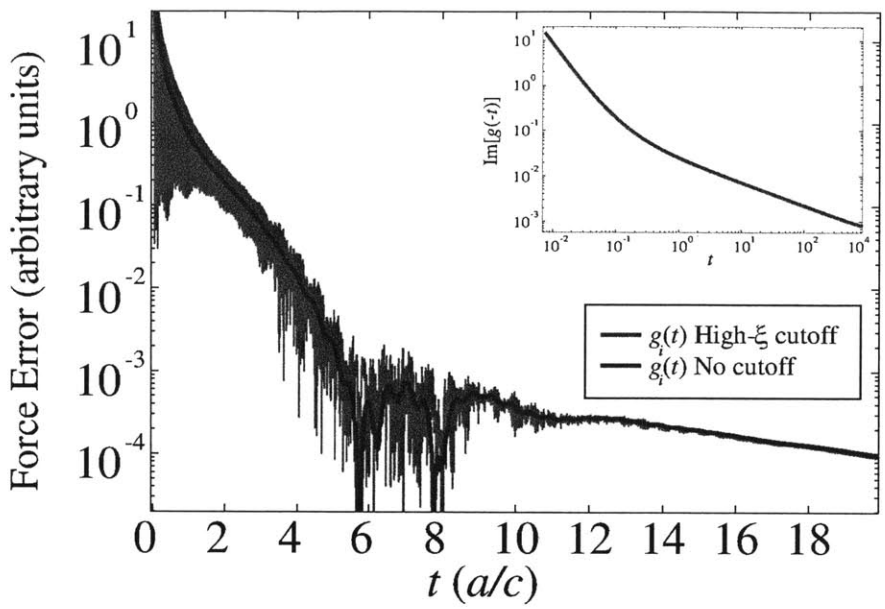

Figure 2-14: Plot of the force error (force after a finite time integration vs. the force after a very long run time) for $g(t)$ determined from a numerical transform as in Ref. 172 and from the analytic transform of the high-frequency components. Inset: $\Im[g(-t)]$ obtained without a cutoff, in which the high-frequency divergence is integrated analytically. Compare with Fig. 1 of Ref. 172.

a much more well-behaved time dependence.

In Fig. 2-14 we plot the convergence of the force as a function of time for the same system using the $g(-t)$ obtained by use of a high-frequency cutoff and for one in which $g_1(\xi)$ is transformed analytically and the remainder is transformed without a cutoff. The inset plots $\Im g(-t)$ obtained without using a cutoff (since the real part is not used in this paper) for $\sigma = 10$. If a complex harmonic basis is used, one must take care to use the full $g(t)$ and not only its imaginary part.

Further simplification

In addition to the treatment of the high-frequency divergence in the previous section, we find it convenient to also Fourier transform the low-frequency singularity of $g(\xi)$ analytically. As discussed in Ref. 172, the low-frequency limit of $g(\xi)$ is given by:

$$g(\xi) \to g_2(\xi) \equiv \frac{\sqrt{i}}{2}\frac{\sigma^{3/2}}{\xi^{1/2}}\Theta(\xi) \text{ as } \xi \to 0 \tag{2.48}$$

The Fourier transform of $g_2(\xi)$, viewed as a distribution, is:

$$g_2(-t) = \frac{i}{4\sqrt{\pi}} \frac{\sigma^{3/2}}{t^{1/2}} \tag{2.49}$$

After removing both the high- and low-frequency divergences of $g(\xi)$, we perform a numerical Fourier transform on the function $\delta g(\xi) \equiv g(\xi) - g_1(\xi) - g_2(\xi)$, which is well-behaved in both the high- and low-frequency limits.

In the present text we are only concerned with real sources, in which case all fields $\Gamma(\mathbf{x}, t)$ are real and only the imaginary part of $g(-t)$ contributes to the force in Equation (2.22). The imaginary part of $g(-t)$ is then:

$$\Im[g(-t)] = \Im(\delta g(-t)) + \frac{1}{2\pi}\left(\frac{1}{t^2} + \frac{\sigma}{t}\right) + \frac{1}{4\sqrt{\pi}} \frac{\sigma^{3/2}}{t^{1/2}} \tag{2.50}$$

In particular, setting $\sigma = 0$ (in which case $\delta g = 0$), we find that $\Im[g(-t)] \sim \frac{1}{t^2}$. Therefore, we have proven that (somewhat surprisingly) the Casimir force will always converge with time t even without conductivity present (since $\Gamma(t)$ is bounded in magnitude). However, the convergence rate of the time-integrated force is only $1/t$ and in practice can be quite slow for, e.g., two-dimensional systems. By contrast, with even a small $\sigma > 0$ we will have asymptotically exponential convergence.

Perfect conductors and z-invariance

As discussed in Ref. 167, the stress-tensor frequency integral for a three-dimensional z-invariant system involving only vacuum and perfect metallic conductors is identical in value to the integral of the stress tensor for the associated two-dimensional system (corresponding to taking a $z = 0$ crossection), with an extra factor of $i\omega/2$ in the frequency integrand. In the time domain, this corresponds to solving the two-dimensional system with a new $g(-t)$.

In this case the Fourier transform can be performed analytically. The result is:

$$\Im[g(-t)] = \frac{1}{2\pi}\left(\frac{2}{t^3} + \frac{3\sigma}{2t^2} + \frac{\sigma^2}{2t}\right) \tag{2.51}$$

Note that since S is a closed surface, the integral of $\Gamma(x,t)$ over S for very short times is always zero, so the $t \to 0$ divergence in $g(t)$ above will not play a role in the force. If we set $\sigma = 0$, we have $\Im[g(-t)] \sim 1/t^3$; therefore, without the conductivity contour the time-integrated force will decay faster than the generic $1/t$ law above.

Appendix 2B: Harmonic expansion in cylindrical coordinates

The extension of the derivation of the harmonic expansion to three dimensions and non-Cartesian coordinate systems is straightforward, as the only difference is in the representation of the δ-function. Because the case of rotational invariance has the computational advantage of reducing 3d simulations to 2d, we will explicitly derive the result for this case.

For cylindrical symmetry, we work in cylindrical coordinates (r, ϕ, z) and choose a surface S that is also rotationally invariant about the z-axis. S is then a surface of revolution, consisting of the rotation of a parameterized curve $(r(s), \phi = 0, z(s))$ about the z axis. The most practical harmonic expansion basis consists of functions of the form $f_n(x)e^{im\phi}$. Given a ϕ dependence, many FDTD solvers will solve a modified set of Maxwell's Equations involving only the (r, z) coordinates. In this case, for each m the problem is reduced to a two-dimensional problem where both sources and fields are specified only in the (r, z)-plane.

Once the fields are determined in the (r, z)-plane, the force contribution for each m is given by:

$$\int_0^{2\pi} d\phi \int_S ds_j(\mathbf{x})\, r(\mathbf{x}) e^{-im\phi} \int_0^{2\pi} d\phi' \int_S ds(\mathbf{x}')\, r(\mathbf{x}') e^{im\phi'} \delta_S(\mathbf{x}-\mathbf{x}') \Gamma^E_{ij;m}(t;\mathbf{x},\mathbf{x}') \tag{2.52}$$

where the values of $\mathbf{x}$ range over the full three-dimensional (r, ϕ, z) system. Here we introduce the Cartesian line element ds along the one-dimensional surface S in anticipation of the cancellation of the Jacobian factor $r(\mathbf{x})$ from the integration over S. We have explicitly written only the contribution for Γ^E, the contribution for Γ^H

being identical in form.

In cylindrical coordinates, the representation of the δ-function is:

$$\delta(\mathbf{x}-\mathbf{x}') = \frac{1}{2\pi r(\mathbf{x})}\delta(\phi-\phi')\delta(r-r')\delta(z-z') \tag{2.53}$$

For simplicity, assume that S consists entirely of $z =$ constant and $r =$ constant surfaces (the more general case follows by an analogous derivation). In these cases, the surface δ-function δ_S is given by:

$$\delta_S(\mathbf{x}-\mathbf{x}') = \frac{1}{2\pi r(\mathbf{x})}\delta(\phi-\phi')\delta(r-r'), \quad z = \text{constant}$$
$$\delta_S(\mathbf{x}-\mathbf{x}') = \frac{1}{2\pi r(\mathbf{x})}\delta(\phi-\phi')\delta(z-z'), \quad r = \text{constant}$$

In either case, we see that upon substitution of either form of δ_S into eq. (2.52), we obtain a cancellation with the first $r(\mathbf{x})$ factor. Now, one picks an appropriate decomposition of δ_S into functions f_n (a choice of $r =$ const or $z =$ const merely implies that the f_n will either be functions of z, or r, respectively). We denote either case as $f_n(\mathbf{x})$, with the r and z dependence implicit.

We now consider the contribution for each value of n. The integral over $\mathbf{x}'$ is:

$$\Gamma^E_{ij;nm}(t,\mathbf{x}) = \int_0^{2\pi} d\phi' \int_S ds(\mathbf{x}')r(\mathbf{x}')\Gamma^E_{ij;nm}(t,\mathbf{x},\mathbf{x}')f_n(\mathbf{x}')e^{im\phi'} \tag{2.54}$$

As noted in the text, $\Gamma^E_{ij;nm}(t,\mathbf{x})$ is simply the field measured in the FDTD simulation due to a three-dimensional current source of the form $f_n(\mathbf{x})e^{im\phi}$. In the case of cylindrical symmetry, this field must have a ϕ dependence of the form $e^{im\phi}$:

$$\Gamma^E_{ij;nm}(t,r,z,\phi) = \Gamma^E_{ij;nm}(t,r,z)e^{im\phi} \tag{2.55}$$

This factor of $e^{im\phi}$ cancels with the remaining $e^{-im\phi}$. The integral over ϕ then produces a factor of 2π that cancels the one introduced by δ_S. After removing these factors, the problem is reduced to one of integrating the field responses entirely in

the (r, z) plane. The contribution for each n and m is then:

$$\int_S ds_j(\mathbf{x})\, \bar{f}_n(\mathbf{x}) \Gamma^E_{ij;nm}(t, r, z) \tag{2.56}$$

If one chooses the $f_n(\mathbf{x})$ to be real-valued, the contributions for $+m$ and $-m$ are related by complex conjugation. The sum over m can then be rewritten as the real part of a sum over only non negative values of m. The final result for the force from the electric field terms is then:

$$F_i = \int_0^\infty dt\, \Im[g(-t)] \sum_n \int_S ds_j(r, z)\, f_n(r, z) \Gamma^E_{ij;n}(t, r, z) \tag{2.57}$$

where the m-dependence has been absorbed into the definition of $\Gamma_{ij;n}$ as follows:

$$\Gamma^E_{ij;n}(t, r, z) \equiv \Gamma^E_{ij;n,m=0}(t, r, z) + 2 \sum_{m>0} \Re[\Gamma^E_{ij;nm}(t, r, z)] \tag{2.58}$$

We have also explicitly included the dependence on r and z to emphasize that the integrals are confined to the two-dimensional (r, z) plane. The force receives an analogous contribution from the magnetic-field terms.

Chapter 3

Microstructure effects for Casimir forces in chiral metamaterials

3.1 Introduction

We examine a recent prediction for the chirality-dependence of the Casimir force in chiral metamaterials by numerical computation of the forces between the exact microstructures, rather than homogeneous approximations. We give background and definitions in Sec. 3.3, and compute the exact force for a chiral bent-cross pattern in Sec. 3.4. In Sec. 3.5 we turn our attention to a more idealized, but computationally more complex, "omega"-particle medium. The method we developed for this case involves a novel combination of the scattering-theory formulation for Casimir forces and the numerical boundary-element method (BEM) technique, which we discuss in Appendix 3. For the "omega"-particle medium (in the dilute approximation) we are able to unambiguously identify the effects of the microstructure (i.e. proximity forces and anisotropic effects) and isolate the "metamaterial" contribution to the force. We find that for both the crosses and omega-particles the microstructure effects dominate the force for separations where chirality was predicted to have a strong influence. At separations where the homogeneous approximation is valid, in even the most ideal circumstances the effects of chirality are less than 10^{-4} of the total force, making them completely irrelevant to experiments.

3.2 Background

3.2.1 Casimir forces and Metamaterials

A key step in the theory of Casimir forces has been the application of effective-medium theory to predict novel Casimir effects. In this context, effective-medium theory refers to any result predicted from the use of an effective-medium approximation (EMA), in which the optical properties of a complex microstructure are approximated as a uniform slab of material. These optical properties are described by a set of constitutive parameters (e.g., $\varepsilon(\omega)$ and $\mu(\omega)$), the idea being to choose these parameters so as to model the most important aspects of the optical response of the structure in as simple a way as possible. Usually these simplified equations can be solved analytically.

EMAs first made their appearance in Casimir forces in the 1970s, when in Ref. 21 Boyer predicted a repulsive Casimir force between a conventional material (one with $\varepsilon(i\xi) > 1$ and $\mu(i\xi) \sim 1$) and a "magnetic" material, which has $\mu(i\xi) > \varepsilon(i\xi)$. This observation remained an interesting curiosity until recent years, when it was realized that materials with complex microstructures could be engineered so that (e.g., near a structural resonance) they mimic the behavior of materials with exotic values of $\varepsilon(\omega)$ and $\mu(\omega)$, so-called "metamaterials" [216]. For example, microstructures can be engineered so as to have a negative refractive index [157]. With the success of EMAs applied to metamaterials, Boyer's idea was revived in the hope that a new route could be found towards Casimir repulsion between vacuum-separated objects. In this new form, it was proposed that dielectric metamaterials might have an effective $\mu(i\xi) > \varepsilon(i\xi)$, in order to exhibit repulsive Casimir forces in vacuum where conventional dielectric structures have only attraction [67, 99, 180]. However, these works treated the EMA terms as free parameters, inserting arbitrary values of $\varepsilon(i\xi)$ and $\mu(i\xi)$ into the Lifshitz formula and examining the conditions under which repulsion occurred. As with Boyer's original work, Casimir repulsion was predicted in a variety of circumstances; however, it was not known whether or not one could find physical microstructures composed of metallic/dielectric materials that are describable by such an $\varepsilon(i\xi)$ and $\mu(i\xi)$ over a sufficiently wide imaginary-frequency

bandwidth. On the contrary, although it is certainly possible to take a given structure and form and EMA from it (valid in some range of frequencies), it is far from clear if the inverse problem is possible. This is especially problematic in the Casimir setting, where the quantities of interest are the *broadband* responses of the materials in *imaginary* frequencies. As an example, although $\varepsilon(i\omega)$ can attain almost arbitrary values in the vicinity of a structural resonance, it is well known [97] that in imaginary frequency, $\varepsilon(i\xi) > 0$ always. A more recent example this is the case of split-ring resonators, which can form a magnetic metamaterial when placed in two-dimensional arrays [148]. If one takes a simple Lorentzian model for $\mu(\omega)$ in real frequency and then analytically continues to $\omega = i\xi$, Casimir repulsion can result for certain parameter ranges [180]. However, taking a more realistic model [148] for $\mu(\omega)$ [178] results in $\mu(i\xi) - \mu(0) \sim -\xi^2$ [178, 180, 197], where $\mu(0) < \varepsilon(0)$. Therefore, there is no repulsion or even force reduction in the EMA regime for this model (that is, the presence of $\mu \neq 1$ actually *increases* the attraction). Most importantly, a recent theorem [155] implies that one cannot have repulsion in the effective–medium (large separation) regime when the materials are vacuum-separated (although repulsion is possible outside of this regime – see Chapter 5). This implies that we cannot choose constitutive parameters arbitrarily, since by this theorem those parameters that predict Casimir repulsion cannot be physical. However, it is still possible that significant reduction or modulation of the Casimir force can occur as a result of metamaterial effects, and this issue requires further investigation.

3.2.2 Chiral Metamaterials

In this chapter, we examine a particular class of metamaterials known as *chiral* metamaterials, which, in addition to $\varepsilon(\omega)$ and $\mu(\omega)$, are described by a chirality term $\kappa(i\omega)$. The (source-free) EMA equations for a chiral metamaterial are:

$$\begin{aligned} \nabla \times \mathbf{H} &= -i\omega\varepsilon(\omega)\mathbf{E} + i\kappa(i\omega)\mathbf{H} \\ \nabla \times \mathbf{E} &= +i\omega\mu(\omega)\mathbf{H} - i\kappa(i\omega)\mathbf{E}. \end{aligned}$$

Chirality refers to the "handedness" of the microstructure; the chirality can be flipped (i.e., $\kappa \to -\kappa$) under a spatial inversion of the microstructure. A recent EMA analysis of chiral metamaterials [214] predicted Casimir repulsion assuming sufficiently large values of κ. We know this cannot be physically possible [155,188] and that some physical restrictions must apply to the parameter κ to prohibit repulsion in the EMA regime. However, a possibility not ruled out by Ref. 155 is that the magnitude of the Casimir force can be modulated by chirality [213]; that is, two materials of identical ε and μ but opposite chirality ($\kappa_1 = -\kappa_2$) are predicted within EMA to exhibit a stronger attractive Casimir force than for $\kappa_1 = \kappa_2$, regardless of whether or not the force is repulsive in the latter case. Part of the purpose of our investigation is to determine how large the difference in the force between these two cases is. Additionally, chirality effects may lead to repulsion outside of the EMA regime, e.g., repulsive forces for certain relative transverse positions between two chiral metamatmaterials and attraction for other separations (although in this case a description in terms of the EMA must be supplemented by information about the microstructure).

The case of chiral metamaterials is different than magnetic metamaterials in that there is no strict chiral effective-medium limit: chirality effects vanish at large separations where the EMA should be valid, and are strongest at small separations where the EMA is questionable. This is due to the fact that, for low frequencies, κ must have the limiting behavior $\lim_{|\omega|\to 0} \kappa(\omega) \sim \omega$ [197, 214]. In the limit that the separation d goes to infinity, only the $\omega \to 0$ behavior matters (due to the exponential suppression of high-frequency terms), in which case chirality effects vanish. Therefore, the question of whether chiral metamaterial effects can significantly reduce the Casimir force, at least in theory, remains open. Answering this question requires accurate calculations using the exact microstructure of the metamaterials, rather than a homogeneous EMA.

3.3 Definitions and Methodology

For any κ, the EMA predicts that the force between two media of the same chirality (SC) should be lower than for media of the opposite chirality (OC), with the size of this difference increasing with κ. Because in general $\kappa \sim \xi$ [197, 214], this effect is largest at short separations and goes to zero at large separations. Therefore, to get a useful prediction (e.g., force reduction due to chirality), we are forced to consider the predictions of the EMA at intermediate separations. However, not only does the EMA fail at sufficiently small separations, but the force in that limit is eventually described by the PFA [42] in which there are only pairwise attractions. An analysis based on pairwise attractions would find little effect due to chirality. Instead, the behavior would be dominated by small-scale features such as the shortest distance between two components of the microstructures. Unfortunately, it is quite possible that this shortest-distance metric also changes under a flip of chirality, with the force being larger for the mirror-symmetric (OC) case; this is in fact what happens for both systems studied here. A simple interpretation of the results would lead to a false attribution of force-reduction effects to chirality, whereas they are actually due to proximity forces. We make a rigorous distinction between proximity forces and chiral effects with the following argument: if the materials behave as homogeneous, chiral media, the relative chirality should be the only source of a force difference between the SC and OC cases, where $F_{OC} > F_{SC}$, independent of the transverse displacement x. However, if the force is governed by pairwise attraction, it should exhibit a strong x-dependence. We can therefore directly test the validity of the EMA by comparing the force for different values of x. If we compare the *ranges* of the force $F(x)$ and find that $\max_x F_{SC}(x,z) < \min_x F_{OC}(x,z)$ for a given z, we can state that this is proof of force reduction due to chirality. If for some value of x, $F_{SC}(x,z) < 0$ but $F_{OC} > 0\ \forall x$, this is evidence of Casimir repulsion due to chirality. If, on the other hand, there exist x, x' such that $F_{SC}(x,z) > F_{OC}(x',z)$, we are in the regime that proximity effects dominate.

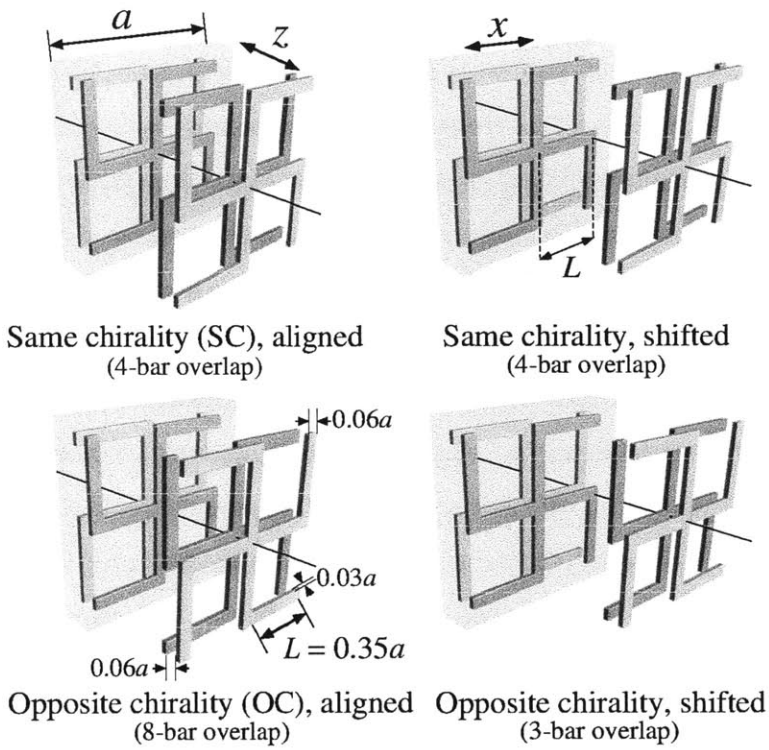

Figure 3-1: Interactions between two chiral metamaterials [213]. The shaded box indicates a unit cell; the structures are periodic in the transverse direction. Nearest neighbor bars on opposing structures are colored yellow. In the EMA, the forces should obey $F_{SC} < F_{OC}$. By contrast, in the pairwise-force approximation the force is determined by the number of overlapping nearest-neighbor bars, as indicated: $F_{OC} > F_{SC}$ when the centers are aligned (left column), but $F_{OC} < F_{SC}$ when they are displaced by $L/2$ (right column).

3.4 Bent-arm crosses

We first examine a chiral metamaterial structure proposed in Ref. 213 and shown in Fig. 3-1. A unit cell of each "medium" consists of a single bi-layer of two bent-arm crosses, one spiraling clockwise and the other counter-clockwise. Their ordering in the z-direction determines the chirality of the medium; that is, flipping the chirality reduces to flipping the direction of the crosses. Each unit cell is of side length a, where a represents our unit of length. We omit the dielectric polyimide in which the metal was embedded in Ref. 213, as this eliminates a chirality-independent attraction between the layers. Although this structure was not predicted to have repulsion, it was

determined on the basis of real-frequency simulations that, of all the chiral structures considered in Ref. 213, this bent-arm cross structure had the largest chirality. As shown in Fig. 3-1, we examine two values of x: $x = 0$ (in which case the centers of the crosses are aligned) and $x = L/2$, where L is the length of an individual straight segment of the crosses. We pick these two displacements of x because the PFA force (discussed below) is of a particularly simple form for $x = 0$ and smallest for $x = L/2$; this is because the individual nearest-neighbor flat segments on opposing slabs line up for these displacements, in which case PFA should be most accurate..

3.4.1 Computational Method

The exact Casimir force between the periodic structures of Fig. 3-1 is computed using the finite-difference time-domain (FDTD) method discussed in Chapter 2. For simplicity, we assume zero temperature (in the high-temperature limit, we expect the relative contributions of any chiral effects to go to zero, as the $\omega = 0$ term dominates). As discussed in Sec. 2.5.4, the FDTD method is well-suited to periodic systems; the total force is expressed as the integral:

$$F(x, z) = \int_{-\infty}^{\infty} \int_{-\infty}^{\infty} F_{k_x,k_y}(x, z) dk_x dy_y. \tag{3.1}$$

Each $F_{k_x,k_z}(x, z)$ requires one FDTD simulation. Unlike the periodic system of Sec. 2.5.4, in the present case we do not have inversion symmetry, so we must integrate k from $-\infty$ to ∞. For a given separation z, we find that that a range of integration $|k| \leq 2.6/z$ with 12 integration points is sufficient to compute the force at the 1% level. Ideally an infinite number of bi-layers in the z direction are used, however we must perform our computations with a finite number of layers. For our purpose, ten bi-layers in the z-direction on each side are sufficient; adding more layers does not change the results at the 1% level. We compute the force for two different material types: perfect electric conductors (PEC) and dispersive gold. For gold we take a plasma model with $\omega_p = 1.37 \times 10^{16}$rad/sec (neglecting the dissipative term from the Drude model has no effect on the force). The latter model requires a definite value

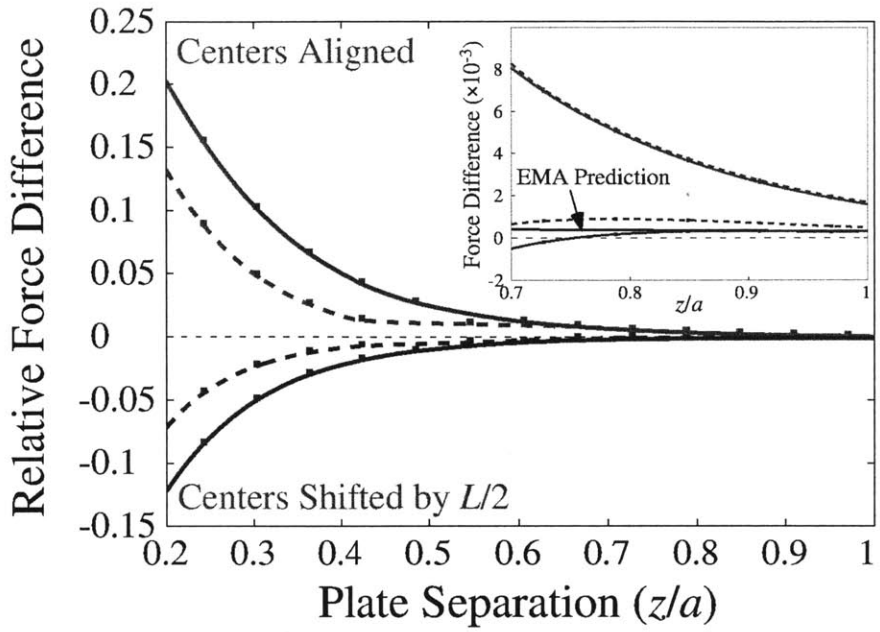

Figure 3-2: Relative force difference $(F_{OC} - F_{SC})/F_{OC}$ for the left (red) and right (blue) columns of Fig. 3-1 for PEC (solid) and dispersive gold for $a = 1\ \mu m$ (dashed). From Fig. 3-1, the sign difference is due to proximity effects. The inset shows a zoom of the large-z regime, along with the EMA prediction (black).

for the length scale a, which we take to be $a = 1\mu m$; this represents a reasonable lower limit on the range of practical experimental fabrication.

3.4.2 Results

The results of our computations are shown in Fig. 3-2; here, we plot the *relative* force difference (RFD) $[F_{OC}(x,z) - F_{SC}(x,z)]/F_{OC}(x,z)$. Normalizing by $F_{OC}(x,z) > 0$ will gives the RFD a much weaker z-dependence, making visualization simpler. In the chiral metamaterial/EMA limit, we expect the RFD to be greater than zero for all x at a given z. From Fig. 3-2, the RFD for PEC (solid lines) and gold (dashed lines) display similar qualitative behavior; the behavior of the exact RFD is not consistent with the EMA: even the sign of $F_{OC}(x) - F_{SC}(x)$ changes as a function of x for $z/a < 0.75$.

We now show how the results for low z/a can be qualitatively described by pairwise nearest-neighbor attractions. Consider, for instance, the two cases diagrammed

in Fig. 3-1. First, when the centers of the unit cells are aligned, there is approximately a 4-bar overlap in the SC case and an 8-bar overlap in the OC case. If the force is proportional to the number of overlapping nearest-neighbor bars (this is the case if the PFA is valid), we expect $F_{OC} > F_{SC}$. When the centers are displaced by $x = L/2$, SC has a 4-bar overlap and OC has a 3-bar overlap, so we expect $F_{OC} < F_{SC}$, and the relative force difference should be reduced by a factor of approximately 1/4. This prediction, based purely on pairwise attraction, captures the qualitative behavior of the RFD for $z/a < 0.75$.

Although at larger z/a the RFD is positive for both values of x, the force curves still exhibit a strong x-dependence. The inset to Fig. 3-2 shows a zoom of the $z/a \sim 1$ region; to compare these results to the EMA predictions, our collaborators Zhao et. al. re-ran their parameter retrieval computations (discussed in Ref. 214) for our configuration (using PEC material for simplicity). We then took their real-frequency results and put them into the Lifshitz formula, suitably modified to include chirality [214]. The predicted RFD is shown as the solid black line in the inset of Fig. 3-2. In this region it appears that the forces at $x = L/2$ for both gold and PEC have converged to the EMA prediction, but $x = 0$ is still off by quite a bit (although it does appear to be converging slowly). Although EMA qualitatively predicts the correct behavior of the RFD, for these values of z the chiral effects are very small: they account for only 0.1% of the total force. Furthermore, as the force difference is still highly x-dependent, it is possible that other transverse displacements may still switch the sign of the force difference. We therefore cannot determine if this is really an "ideal" chiral effect or not, and even if this is the case, it is an effect too small to be relevant in experiments.

The predictions of Ref. 213 were based on *isotropic*, chiral media; however, the bent-arm crosses of Fig. 3-1 are highly anisotropic. It is possible that the effects of this anisotropy dominate those of chirality, even at large separations. Additionally, these crosses are composed of many wide, flat metallic segments, which give large pairwise attractive forces; this reduces the relative contribution of any chiral effects. In the next section, we will consider a more idealized chiral system in which both

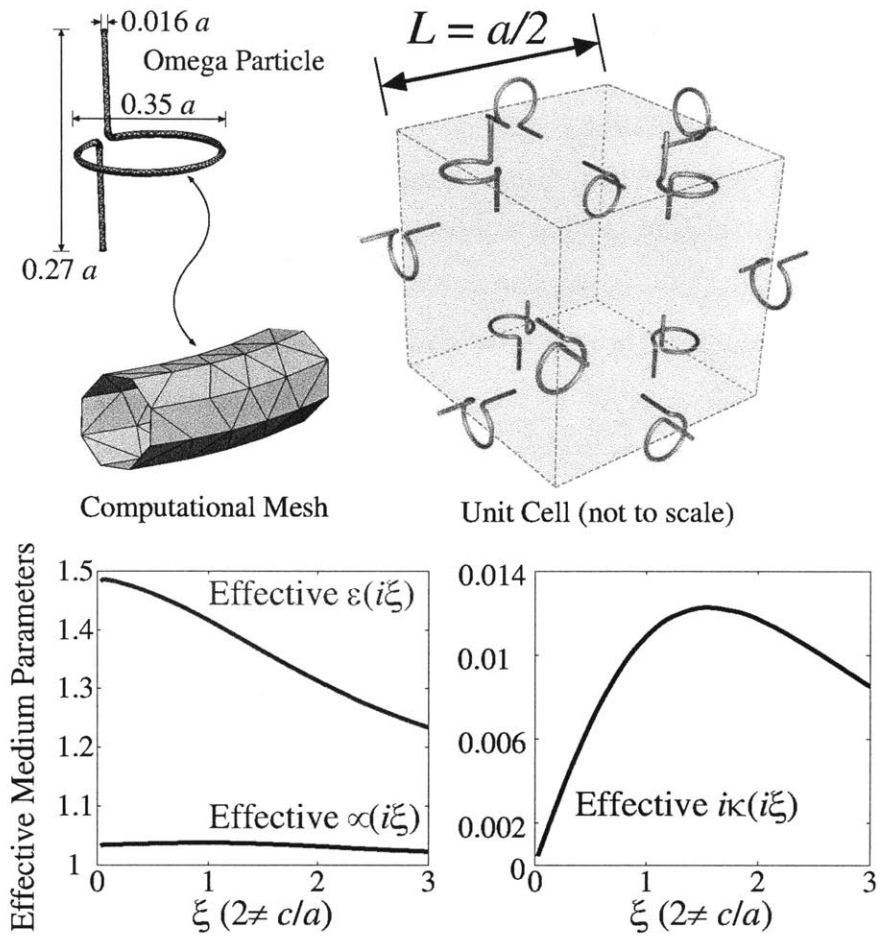

Figure 3-3: *Top:* Unit cell of isotropic chiral metamaterial: PEC "omega" particles in vacuum. Shaded cube indicates relative positions in unit cell. *Bottom:* Effective-medium parameters, as a function of imaginary frequency $\omega = i\xi$, deduced directly from imaginary-ω scattering data. $\mu(0) \neq 1$ because the particles are PEC.

proximity and anisotropy effects are minimized.

3.5 Omega particles

We have seen that at small separations, where the chirality of the microstructure is predicted by EMA to have a large effect, the force is instead dominated by pairwise interactions. To obtain a chiral effect with minimal pairwise/anisotropic contributions, we consider in this section a more idealized microstructure composed of so-called "omega" particles [197, 213], shown in Fig. 3-3. Each individual particle is predicted

to have a strong chiral response (as determined by the cross coupling of **E** and **H** in the dipole polarizability [197]). When assembled into a period-a unit cell of high symmetry these particles should form a nearly ideal isotropic chiral metamaterial. The unit cell configuration is shown in Fig. 3-3 (top). We have found that, by picking a unit cell of lower symmetry (see below), the anisotropy quickly dominates chiral metamaterial effects. Therefore, we examine only force results for the 12-fold symmetric case of Fig. 3-3(top). To make the medium as homogeneous as possible, the omega particles are relatively closely packed, and as material dispersion had little qualitative role in the previous results, we take the particles to be PEC for simplicity. We compute the EMA parameters using a hybrid boundary-element scattering method (discussed in Sec. 7.3). In the dipole limit, we find that this unit cell exhibits high symmetry in the polarizability, making the material well-described by a set of EMA parameters $\varepsilon(i\xi), \mu(i\xi), \kappa(i\xi)$. Fig. 3-3 (bottom) shows the computed values for these EMA parameters (see Sec. 7.3 for details); ε is close to 1 while $|\kappa| \sim 0.01$. Although the chirality is still only a small fraction of the permittivity, this fraction is an order of magnitude higher than the EMA parameters retrieved by Zhao et. al. for the bent-arm crosses of the previous section. Therefore, we believe this to be an idealized system to study chiral effects.

3.5.1 Computational Method

Presently, we outline the computational method used to compute Casimir forces between the omega particles of Fig. 3-3. Force computations for a structure as complex as Fig. 3-3 are very difficult for finite-difference methods, because of the disparity of size between the periodicity a and the wire diameter $0.016a$. Instead, we develop a hybrid boundary-element/scattering theory technique. This technique combines the theoretical formulation of Casimir forces discussed in Ref. 154 (for precursors, see Refs. [50, 84, 113]) with the numerical boundary-element method of Ref. 162. This will be our first use of scattering theory and the boundary-element method, both of with will play key roles in later chapters.

Ref. 154 gives a detailed derivation of the process by which the Casimir en-

ergy/force between several objects can be expressed in terms of the classical electromagnetic scattering matrices of individual objects. The precursors to this formulation can be found dating back to the 1960s for non-retarded van der Waals forces between molecules [70]; the modern formulation applies to retarded forces between bodies of arbitrary shape. For our purposes, we will only need the simplified case of the energy/force between two bodies a and b. Here, the energy can be expressed in the following form:

$$E = \int_0^\infty \frac{d\omega}{2\pi} \log\det\left(1 - \mathbb{F}_a \mathbb{U}_{ab} \mathbb{F}_b \mathbb{U}_{ba}\right). \tag{3.2}$$

$\mathbb{F}_j$ is the scattering matrix [123] for object j, which we now define. Assume that we have a complete, orthogonal basis of fields $\{\mathbf{E}_\alpha^s\}$ for a (discrete or continuous) index α and a binary index $s = \pm$. The index s represents "incoming" and "outgoing" waves [154]; for example, if the basis represents spherical waves, outgoing waves represent radiation from a source. For planewaves, incoming/outgoing represent waves propagating, e.g., in the $\pm z$ direction. If a particular incoming wave $\mathbf{E}_\alpha^-(\mathbf{x})$ is incident on object j in isolation, the *total* electric field $\mathbf{E}^{\text{tot}}(\mathbf{x})$ is given by:

$$\mathbf{E}^{\text{tot}}(\mathbf{E}) = \mathbf{E}_\alpha^-(\mathbf{x}) + \sum_\beta (\mathbb{F})_{\beta\alpha} \mathbf{E}_\beta^+(\mathbf{x}) \tag{3.3}$$

The *translation matrices* $\mathbb{U}_{ab}$ in eq. (3.2) represent a change of coordinates from the origin of the coordinate system of object b to the origin of object a. These are simply unitary matrices that give an appropriate change of basis (e.g., from planewaves to spherical waves) and are known analytically. See Ref. 154 for further discussion.

The main obstacle to a direct application of eq. (3.2) is that the matrices $\mathbb{F}$ are known for only a small class of shapes for which the Helmholtz equation is separable [191]: examples include spheres, plates, and cylinders of arbitrary material [154], and PEC cones [111]. In order to apply these scattering techniques to our omega particles we must apply a general numerical method for the computation of the $\mathbb{F}_j$. To accomplish this, we incorporate the boundary-element method (BEM) [159] to compute the scattering matrices. The BEM implementation we use, developed by Homer

Reid, had previously been applied to the computation of Casimir forces between objects [162], details of which can be found in [161]. In general, this BEM formulation does not make explicit reference to a coordinate system; instead, the coordinate system is implicit in the nature of the surface mesh discretization of the objects [161], shown in Fig. 3-3. However, in its present form the BEM of [161] cannot be applied to our problem because it does not accommodate periodic boundary conditions. Unlike FDTD, it is very difficult to modify the boundary conditions of BEM as the method is intimately tied to the nature of the free-space Green's function. We can overcome this limitation for our purposes by numerically computing the scattering matrices $\mathbb{F}$ for a single omega particle explicitly in a spherical multipole basis, and then using the analytic properties of this basis to build analytically the full scattering matrix of the array of omega particles in Fig. 3-3; this procedure is detailed in Appendix 3. In addition, we use a dilute approximation (justified in Sec. 3.5.3) in which multiple scattering events within a given structure are neglected. This simplifies our analytic construction (although multiple scattering can be incorporated - we will do precisely this for periodic arrays of cylinders in Chapter 4).

At this point we have a matrix of scattering amplitudes $F_{l',m',P';l,m,P}$ for the individual omega particles, where l, $-l \leq m \leq l$ and l', $-l' \leq m' \leq l'$ are the respective multipole moments of the incident and scattered spherical waves, and $P, P' \in \{M, E\}$ their polarization. In the above notation, our basis index is $\alpha = \{l, m, P\}$. These matrices are converted to a planewave basis [154], where for each ω the planewave has transverse wavevector $\mathbf{k}_\perp$ and polarization $P = s,\ p$. In the planewave basis, we obtain the scattering from the unit cell of Fig. 3-3 from the scattering matrices of the twelve individual omega particles, each rotated and displaced appropriately and subject to periodic boundary conditions. Finally, to simulate a semi-infinite omega medium in z, we concatenate multiple layers of omega particle unit cells displaced by integer multiples of a in the z direction. With this method, we can quickly compute forces for many configurations, e.g., many $x - z$ displacements. This has a substantial advantage over FDTD, where a separate computation is required for every (x, z) pair.

3.5.2 Results

To demonstrate that we have an isotropic, chiral medium in the EMA, we extract the effective-medium parameters $\varepsilon(i\xi)$, $\mu(i\xi)$, and $\kappa(i\xi)$ [Fig. 3-3 (bottom)] from the scattering matrix at $\mathbf{k}_\perp$. Parameter retrieval [213] from reflection and transmission at normal incidence cannot be used, because for imaginary ω the transmission decreases exponentially with the thickness of the medium. Instead, we compute the specular reflection coefficients $R_{\mathrm{ss}}(\omega, \mathbf{k}_\perp)$ and $R_{\mathrm{sp}}(\omega, \mathbf{k}_\perp)$ in the planewave basis. For each frequency $\omega = i\xi$, these quantities (given in Ref. 214) can be expanded to quadratic order in $|k_\perp| \ll \xi$ and κ:

$$\begin{aligned} R_{\mathrm{ss}} &= \frac{\eta - 1}{\eta + 1} + \frac{\eta}{(1+\eta)^2}\left(1 - \frac{1}{n^2}\right)\left(\frac{k_\perp}{\xi}\right)^2 + O\left(\frac{k_\perp}{\xi}\right)^4 \\ R_{\mathrm{sp}} &= -i\kappa \frac{2\eta}{n^3\,(1+\eta)^2}\left(\frac{k_\perp}{\xi}\right)^2 + O\left(\frac{k_\perp}{\xi}\right)^4 \end{aligned} \tag{3.4}$$

where $\eta(i\xi) \equiv \sqrt{\mu(i\xi)/\varepsilon(i\xi)}$, $n(i\xi) \equiv \sqrt{\varepsilon(i\xi)\mu(i\xi)}$. The coefficients of each term are determined by a fit (with the restriction that $|\mathbf{k}_\perp| < \xi/10$, for which this expansion is accurate). Due to the high isotropy of the unit cell (the EMA parameters, which depend only on the dipole moment of the omega particles, will not depend on their relative positions within the unit cell), the results of the fit do not depend on the direction of the vector $\mathbf{k}_\perp$. As discussed earlier, the results for the EMA parameters indicate a strong chiral response when compared to the bent-arm crosses.

The results of the computations for the relative force difference are shown in Fig. 3-4 and are similar in form to Fig. 3-2. We examine the RFD at each z/a—in this case, for each (x, z) the force is taken relative to the minimum force for each z (which turns out to always be attractive); this is convenient to obtain a positive difference that can be plotted on a log scale. The shaded areas of each color represent the range of values that the force assumes for all transverse (x) displacements. Their spread (the x-dependence) indicates the extent of the breakdown of the EMA, and for $z \lesssim 3.1a$ it is so severe that the red and blue force curves overlap. When these curves separate, but before they sharpen (the blue (SC) curve goes to zero due to our convention: the

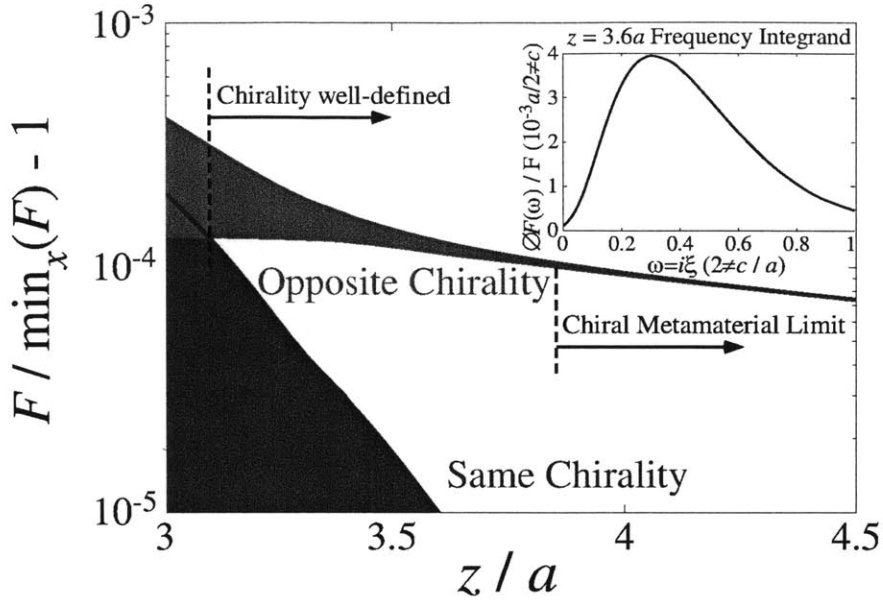

Figure 3-4: Forces (in dilute approximation) between chiral media from Fig. 3-3, for the SC (blue) and OC (red) cases. The range of the force across all transverse (x) displacements is shaded, and normalized by the minimum of the force over all x. For $z \lesssim 3.1a$, chirality is not well-defined (curves overlap). Only when curves are distinct and x-independent can the systems be described as chiral metamaterials. *Inset:* Frequency integrand of the relative force difference at $z = 3.6a$. The smallness of the $\omega = 0$ term is an indicator that this difference is due to chirality and not anisotropy (see text).

SC configuration should always be the minimum force for each z in the EMA limit), we have an intermediate regime where chiral effects compete with proximity effects. Only when the curve thickness is much less than the relative force difference ($\lesssim 10\%$ for $z \gtrsim 3.6a$) is EMA accurate. Unfortunately, this suffers from the same problem as the bent-arm crosses: the EMA is only strong when chiral effects are very small. In this case, the chiral dependence is approximately 10^{-4} of the total force.

For a less isotropic unit cell (e.g., only one omega particle per unit cell), the relative force difference can be made much larger, but the source of this difference is ambiguous, as in Fig. 3-2, because the EMA parameters are now tensors. We can examine the frequency integrand of the force to rigorously differentiate between chirality and proximity/anisotropy effects. Although somewhat of an academic exercise given the minor contribution of chirality to the overall force, it is important because

the RFD in the anisotropic case can be orders of magnitude larger, and we need to know whether this is really due to anisotropy rather than chirality. For two purely chiral materials in the EMA regime, the zero-frequency component of the force difference is exactly zero [214]. On the other hand, proximity and anisotropy forces will, in general, have a large zero-frequency component. Therefore, the magnitude of the zero-frequency component, relative to the $\omega > 0$ terms, is an indication of the contribution of chirality effects relative to proximity/anisotropy forces, and indicates whether the force difference arises from chirality alone. In Fig. 3-4(Inset) we display the frequency integrand at $z = 3.6a$ (well into the EMA limit). The force difference is very nearly zero at $\omega = 0$ and follows a profile similar to $\kappa(i\xi)$ in Fig. 3-3, indicating that the force difference in the isotropic case is indeed due to chirality. By contrast, frequency integrands at smaller z have a large $\omega = 0$ component, indicating the presence of proximity effects. Additionally, for less isotropic unit cell configurations we have found that the frequency integrands have a large zero-frequency component even in the large-z limit, indicating that anisotropy is responsible for the larger RFD in that case. This could also explain the results of Fig. 3-2 for larger z at $x = 0$.

3.5.3 Validity of EMA and the dilute approximation

To simplify the computation of the scattering matrices for our omega particle medium, we employed a dilute approximation that neglected multiple scattering events. In this section, we briefly examine the validity of this approximation, as well as that of the effective medium picture. As mentioned in Sec. 3.4.2, one can compute the Casimir force and the force difference from the EMA parameters using a modified Lifshitz formula. For the range of z/a in Fig. 3-4, we find that the results give the correct force between the two media but overestimates the force difference by roughly 30 percent. This is because the error terms in the expansion of eq. (3.4) above are $O(k_\perp^4)$, the same order as the chirality contributions to the force, which are $\sim R_{\rm sp}^2$ [214]. Therefore, it is not surprising that there is a significant quantitative error in the EMA prediction for the RFD even at large separations. However, we see that the EMA can give qualitatively correct predictions at this range. This is useful because it allows us to

employ the EMA to check the accuracy of the dilute approximation. To do this, we employ the Clausius–Mossotti (C–M) equation [197] to the dipole moments. C–M relates the dipole polarizabilities $\alpha_{P',P}$ of individual particles to the bulk effective-medium parameters (including multiple scattering between particles) in the dipole approximation [30, 197]:

$$\begin{aligned}
\varepsilon^{CM} &= 1 + n\frac{3\alpha_{EE} - n(\alpha_{EE}\alpha_{MM} + \alpha_{EM}^2)}{3D} \\
\kappa^{CM} &= -in\frac{\alpha_{EM}}{D} \\
\mu^{CM} &= 1 + n\frac{3\alpha_{MM} - n(\alpha_{EE}\alpha_{MM} + \alpha_{EM}^2)}{3D}
\end{aligned} \tag{3.5}$$

where

$$D \equiv 1 - n\left(\frac{\alpha_{EE} + \alpha_{MM}}{3} + n\frac{\alpha_{EE}\alpha_{MM} + \alpha_{EM}^2}{9}\right) \tag{3.6}$$

and n is the number density (in our case $12/a^3$) of omega particles. The dilute case corresponds to discarding all terms nonlinear in α; we compute the polarizabilities from eq. (3.5) assuming this dilute limit, working backwards from the effective-medium parameters of Fig. 3-3. We then re-insert these dilute polarizabilities back into C–M to compute lowest-order non-dilute correction. Doing this, we find that the RFD of Fig. 3-4 is changed by $< 15\%$. We therefore expect the non-dilute approximation to not appreciably change the results we have obtained in the large-z regime. For smaller z, the RFD is dominated by pairwise interactions and multiple scattering between different omega particles on the same slab is again expected to be irrelevant. On a technical note, C–M is obtained in the static ($\omega \to 0$) limit, whereas at finite imaginary ω the exponential field decay tends to reduce interaction between particles; therefore, we believe the error estimate of 15 % obtained for the dilute approximation is an overestimate.

3.6 Conclusions

Based on numerical calculations involving the exact microstructure of possible chiral metamaterials, we find that to observe an unambiguous effect of chirality in isotropic, chiral metamaterials, one must measure the total force to 4 digits of accuracy. Given that it is controversial whether even 1% accuracy can be obtained in Casimir measurements for simple geometries [94], combined with the restrictions on lengthscales that are imposed by the need to fabricate a complex microstructure, detecting such a 10^{-4} effect is most likely impossible. Although these calculations are for specific metamaterial structures, they are for two of the most promising known chiral structures, for idealized perfect metals, and moreover we find that two radically different structures yield similarly small chiral effects. While this does not preclude the possibility of observing other interesting Casimir effects in metamaterials (especially if they rely on the $\omega \to 0$ response of the metamaterial, which is the case we will treat in Chapter 4), it suggests serious limitations for finite-ω effects. Further, this analysis highlights the importance of accounting for the exact microstructures involved, as they can have an important effect on the conclusions reached.

Appendix 3: Computing Multipole Moments in BEM

In this Appendix we give more details about our hybrid method for computing the scattering matrices of omega particle slabs. We first discuss how we utilize the BEM implemented by Homer Reid in [162] to compute spherical-wave scattering matrices. Details of the BEM itself can be found in Ref. 161.

The main output of the BEM computations is a "BEM matrix" $\mathbb{M}_j$ for object j [1]. For Casimir forces, this matrix can be directly inserted into a trace formula analogous to eq. (3.2) [161]. However, in the more traditional application of BEM this matrix is used to compute (real-frequency) scattering amplitudes [159]. This is

[1] $\mathbb{M}$ can be thought of as a generalization of the electrostatic capacitance matrix for different objects [71], both in the sense that $\mathbb{M}$ applies to $\xi > 0$ and that it relates to interactions between different mesh elements on the *same* object

done as follows: assume that surface of object j is discretized into a set of panels $\{\alpha\}$; each panel has a set of vector surface current basis functions f_α defined on it (for explicit representations of these panels and the basis functions $\mathbf{f}_\alpha$, see Ref. 159 and Ref. 161). Any surface current distribution $\mathbf{j}(\mathbf{x})$ can be approximately represented as a linear combination of currents on individual panels (this representation becomes exact as the panel size goes to zero):

$$\mathbf{j}(\mathbf{x}) = \sum_\alpha j_\alpha \mathbf{f}_\alpha(\mathbf{x}). \tag{3.7}$$

The effect of any scattering process can be fully described by using effective electric and magnetic surface currents [191] confined to the surface of j, and therefore expressed as a linear combination of the $\mathbf{f}_\alpha$ above. Given the BEM matrix $\mathbb{M}_j$ and an incident composite field $\mathbf{F}^{\text{inc}}(\mathbf{x}) = (\mathbf{E}^{\text{inc}}(\mathbf{x}), \mathbf{H}^{\text{inc}}(\mathbf{x}))$, these surface currents are given by (for simplicity we leave implicit an index distinguishing electric from magnetic surface currents):

$$\mathbf{j}^{\text{out}} \equiv \sum_\alpha j_\alpha^{\text{out}} \mathbf{f}_\alpha = \mathbb{M}_j \left(\sum_\alpha \mathbf{f}_\alpha \langle \mathbf{f}_\alpha | \mathbf{F}^{\text{inc}} \rangle \right) \tag{3.8}$$

here the inner product is defined as an integral over all space. The function $\mathbf{f}_\alpha(\mathbf{x})$ is only non-zero on panel α, so this integral is over a compact domain and can be performed by two-dimensional Gaussian quadrature. Therefore, the scattered current $\mathbf{j}^{\text{out}}$ can be found via matrix multiplication once the inner product of $\mathbf{F}^{\text{inc}}$ over the surface mesh is formed. Details of the computation of this inner product can be found in [161].

Once $\mathbf{j}^{\text{out}}$ is determined, we compute the scattered field $\mathbf{E}^{\text{out}}(\mathbf{x})$ by performing a surface integral over S_j of the current $\mathbf{j}^{\text{out}}$ against the dyadic Green's function[2] $\mathbb{G}_0(\mathbf{x}, \mathbf{x}')$ [198]:

$$\mathbf{E}^{\text{out}}(\mathbf{x}) = \int_{S_j} d^2\mathbf{x}' \, \mathbb{G}_0(\mathbf{x}, \mathbf{x}') \, \mathbf{j}^{\text{out}}(\mathbf{x}'). \tag{3.9}$$

For our purpose, $\mathbf{E}^{\text{inc}}$ and $\mathbf{H}^{\text{inc}} = \frac{1}{i\omega} \nabla \times \mathbf{E}^{\text{inc}}$ are given by a single multipole moment

[2]Only the scattering coefficients for the electric fields are required for Casimir force computations [154].

α, e.g., $\alpha = \{l, m, P\}$ for spherical multipoles, and we desire the multipole components of the scattered field $\mathbf{E}^{\text{out}}_{l',m',P'}$. The result will be the scattering matrix element $\mathbb{F}_{l',m',P';l,m,P}$. Rather than the direct approach, which would involve taking the multipole moments of $\mathbf{E}^{\text{out}}(\mathbf{x})$ in eq. (3.9), we can extract these moments directly by using the mulitpole representation of the dyadic Green's function [198]. For spherical multipoles, the result is:

$$\mathbb{F}_{l',m',P'} = \omega^2(-1)^{m'} \int_{S_j} d^2\mathbf{x}' \, \mathbf{E}_{l',-m',P'} \cdot \mathbf{j}^{\text{out}}(\mathbf{x}'), \tag{3.10}$$

where the (regular) spherical multipole moment basis functions are given by [154]:

$$\begin{aligned} \mathbf{E}_{l,m,M} &= \nabla \times [j_l(\omega r) Y_{lm}(\theta, \phi)\hat{\mathbf{r}}] \\ \mathbf{E}_{l,m,N} &= \frac{1}{\omega} \nabla \times \mathbf{E}_{l,m,N}. \end{aligned} \tag{3.11}$$

$j_l(x)$ are the spherical Bessel functions, and $Y_{lm}(\theta, \phi)$ the spherical harmonics.[3] For our computations, we find that $l \leq 3$ is sufficient for 1% convergence of the force (and force difference). Lower surface-surface separation would require additional values of l.

We now show how to build (in the dilute limit) the scattering matrix for an entire slab of omega particles. This involves applying both translation and rotation operations to the single-particle scattering matrices to describe scattering from the different constituents of a unit cell in Fig. 3-3. The rotations are applied in the spherical multipole basis; the scattering matrix $\mathbb{F}$ is a spherical tensor constructed from basis elements $|l', m'\rangle \otimes \langle l, m|$[4]. A rotation is specified by a set of Euler angles α, β, γ [62]. The transformation operator for a spherical basis element $|l, m\rangle$ is given in the Z-Y-Z convention by [4]:

$$\mathbb{R}(\alpha, \beta, \gamma) = e^{i\alpha \hat{L}_z} e^{i\beta \hat{L}_y} e^{i\gamma \hat{L}_z} \tag{3.12}$$

[3]In eq. (3.9) we have implicitly assumed *outward* scattering, for which $r > r'$

[4]Since the rotations are diagonal in the polarization basis, we suppress this index.

where L_k are the angular momentum operators (these matrices are given for each l by the $2l+1$-dimensional representation of $SU(2)$). In the Z-Y-Z convention for the Euler angles, the explicit matrix elements of $\mathbb{R}$ are:

$$\langle l', m' | \mathbb{R}(\alpha, \beta, \gamma) | l, m \rangle = e^{-im'\alpha} e^{-im\gamma} d(l, m', m, \beta) \delta_{l',l} \tag{3.13}$$

where $d(l, m', m, \beta)$ is the "little" Wiger matrix, which can be expressed in terms of hypergeometric functions [3]:

$$\begin{aligned} d(l, m', m, \beta) &= (-1)^q \sqrt{\frac{\binom{2l-k}{k+a}}{\binom{k+b}{b}}} \binom{a+k}{k} [\sin(\pi\beta/2)]^a [\cos(\pi\beta/2]^b \\ &\times \; {}_2F_1[-k, (1+a+b+k), (1+a), 1-\cos(\pi\beta/2)] \end{aligned} \tag{3.14}$$

where

$$\begin{aligned} k &= K_j, q = Q_j, a = A_j \\ K &= \{l+m, l-m, l+m', l-m'\} \\ Q &= \{m'-m, 0, 0, m'-m\} \\ A &= \{m'-m, m-m', m-m', m'-m\} \\ j &= \{j \,|K_j \leq K_i \; \forall i\}. \end{aligned} \tag{3.15}$$

The transformation of the $(1,1)$ spherical tensor $|l', m'\}\{l, m|$ is then:

$$\begin{aligned} \mathbb{F}^R_{l',m',P';l,m,P} &\equiv \mathbb{R} \otimes \mathbb{R}[\mathbb{F}_{l',m',P';l,m,P}] \\ &= \sum_{M,M'} e^{i\alpha(m-m')} e^{i\gamma(M-M')} d(l', M', m', \beta) d^*(l, M, m, \beta) \, \mathbb{F}_{l',M',P';l,M,P} \end{aligned}$$

This is done for each angle of rotation given in the unit cell of Fig. 3-3. To finish the construction of the unit cell scattering matrix, the particles must also translated by a set of basis vectors within the unit cell. However, it is mathematically more convenient to first convert the scattering matrices to a planewave basis. This conversion is accomplished by multiplication by the wave conversion matrices $D(\mathbf{k}_\perp, p; l, m, P)$,

which are given explicitly in Ref. 154. Once the scattering matrices are expressed in the planewave basis, translation by a vector $\mathbf{X} = (\mathbf{X}_\perp, z)$ amounts to multiplication by the (diagonal) matrix [154]:

$$\mathbb{U}(\mathbf{X})_{\mathbf{k}'_\perp,p';\mathbf{k}_\perp,p} = (2\pi)^2\delta^{(2)}(\mathbf{k}_\perp - \mathbf{k}'_\perp)e^{i\mathbf{k}_\perp\cdot\mathbf{X}_\perp}e^{-\sqrt{\omega^2+|\mathbf{k}_\perp|^2}z} \tag{3.16}$$

This gives the full scattering matrix, in the planewave basis, for a single unit cell. Now we must incorporate the two-dimensional periodicity of the lattice: for scattering from a unit cell in the planewave basis, one computes the scattering coefficients between planewaves of arbitrary $\mathbf{k}_\perp$ and $\mathbf{k}'_\perp$, P and P'. When the scattered fields are summed over all unit cells of a periodic structure (in two dimensions), the scattering matrix gains a factor $\sum_{\mathbf{G}}(2\pi)^2\delta^{(2)}(\mathbf{k}_\perp - \mathbf{k}'_\perp + \mathbf{G})/a^2$, where $\{\mathbf{G}\}$ are the reciprocal lattice vectors $\mathbf{G} \in \{\frac{2\pi}{a}n_x\hat{\mathbf{x}} + \frac{2\pi}{a}n_y\hat{\mathbf{y}} \,|\, (m,n) \in \mathbb{Z}^2\}$. Therefore, only scattering processes between planewaves where $\mathbf{k}_\perp - \mathbf{k}'_\perp = \mathbf{G}$ are required. However, the scattering matrix acquires an additional (continuous) index $\mathbf{k}_\perp$ that lies in the first Brillouin zone; $\mathbf{k}_\perp$ is simply the Bloch vector corresponding to the periodic boundary conditions on the fields. Finally, we sum the scattering matrices over multiple layers in z to get a semi-infinite omega medium; this amounts to applying the operator $\sum_{n=0}^{\infty}\mathbb{U}(0,0,na)$; in practice, we truncate this sum to $n_{\max} = 30$. The total Casimir energy between objects 1 and 2, separated by a distance d, is expressed as:

$$E = \int_0^\infty \frac{d\omega}{2\pi}\int_{-\pi/a}^{\pi/a}\frac{dk_x}{2\pi}\int_{-\pi/a}^{\pi/a}\frac{dk_y}{2\pi}\log\det\left(1 - \mathbb{U}(0,0,d)\mathbb{F}^{(1)}_{\mathbf{k}_\perp}\mathbb{U}(0,0,d)\mathbb{F}^{(2)}_{\mathbf{k}_\perp}\right). \tag{3.17}$$

The matrices $\mathbb{F}^{(1,2)}_{\mathbf{k}_\perp}$ have discrete indices indexed by the Brillouin zone $(n_x, n_y) \in \mathbb{Z}^2$. [5] For computation, we must restrict the range of n_x and n_y to make the matrices finite-dimensional. For the present computations, we find that $|n_x|, |n_y| \leq 3$ suffice. Lower separations would require higher values of n. The integration over $d^2\mathbf{k}_\perp$ is performed with a simple trapezoidal rule using 11 points in each dimension.

[5]Discreteness of the matrix indices is not actually required for numerical computation; in Chapter 6 we will use a basis in which the matrix indices are continuous variables.

Chapter 4

Structural anisotropy and orientation-induced Casimir repulsion in fluids

4.1 Introduction

In chapter we consider the Casimir force between two periodic arrays of nanowires (both in vacuum, and on a substrate separated by a fluid) at separations comparable to the period. We compute the dependence of the exact Casimir force between the arrays under both lateral translations and rotations. Although typically the force between such structures is well-characterized by the Proximity Force Approximation (PFA), we find that in the present case the microstructure modulates the force in a way qualitatively inconsistent with PFA. In contrast to the previous chapter, we find instead that effective-medium theory, in which the slabs are treated as homogeneous, anisotropic dielectrics, gives a surprisingly accurate picture of the force, down to separations of half the period. This includes a situation for identical, fluid-separated slabs in which the exact force changes sign with the orientation of the wire arrays, whereas PFA predicts attraction. We discuss the possibility of detecting these effects in experiments, concluding that this effect is strong enough to make detection possible

in the near future.

4.2 Preliminary Discussion

We examine the configuration shown in Fig. 4-1, consisting of two identical microstructured slabs consisting of periodic arrays of dielectric nanowires. We compute the exact Casimir force for this geometry using a combination of existing scattering theory techniques [91, 154, 208], to be described below. We find that the microstructure of the slabs leads to a number of interesting qualitative effects: the force between the slabs can be dramatically modulated by rotating the two slabs at fixed surface-surface separation. In vacuum, the force between the slabs can be significantly reduced (more than halved as the rotation angle changes), and if the slabs are immersed in a fluid, the sign of the force can flip. It turns out that, even at moderate separations $d/a \sim 1$, PFA cannot capture either of these effects. Specifically, consider the behavior of the Casimir force between the slabs as they undergo lateral translations y (at $y = 0$ the slabs are mirror-symmetric) and rotations θ. At $\theta = 0$, the slab microstructures are aligned as in Fig. 4-1 (upper), while for $\theta = \pi/2$ the slabs are crossed, as in Fig. 4-1 (lower). As y and θ are varied, the slab surface-surface separation d is kept fixed. From a simple geometric argument, it is clear that for vacuum-separated wires PFA predicts the following bound on the Casimir force between two identical slabs:

$$F_{\text{aligned},y=a/2} \leq F_{\text{crossed}} \leq F_{\text{aligned},y=0} \tag{4.1}$$

(a positive force is attractive). Here F_{crossed} denotes the force when $\theta = \pi/2$. This bound is insensitive to the details of the exact PFA used, and simply relies on the fact that the wire surface-surface separations are minimized at $\theta = 0, y = 0$ and maximized when $\theta = 0, y = a/2$. Although a PFA prediction must be valid as $d/a \to 0$, for the systems examined in this work we find that the bound eq. (4.1) is violated even at moderate distances $d/a \sim 1$. For vacuum-separated metallic/dielectric (e.g., gold or silica) nanowires and no substrate, this implies that changing the orientation of the wire arrays (i.e., their geometry) plays a stronger role in reducing the force than simply

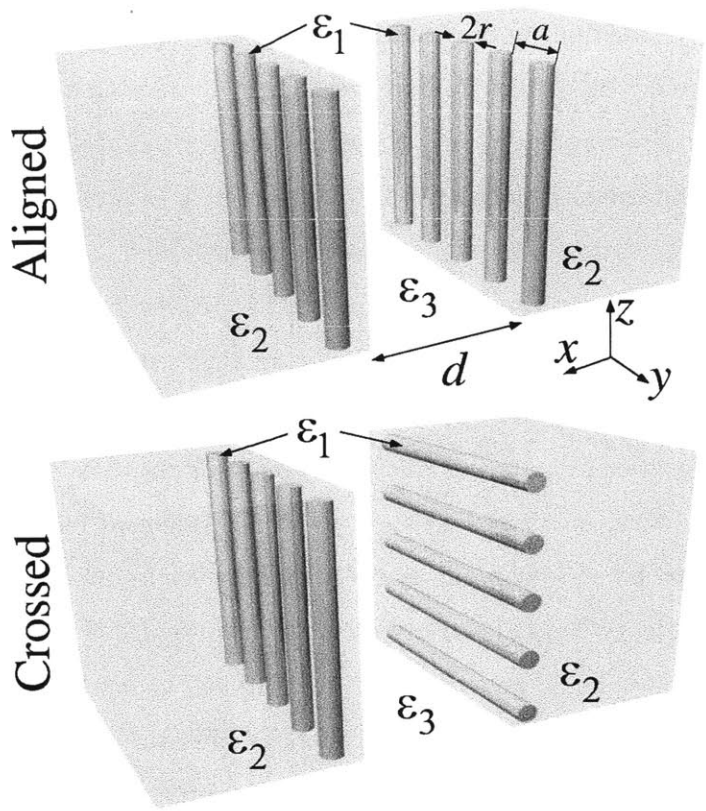

Figure 4-1: Configuration examined in the text. Each slab consists of a single periodic array of cylindrical wires embedded in a semi-infinite substrate; the goal is to create for each slab an effective anisotropic medium. Of interest here is the change in the force from when the wires are aligned (Top) and when they are crossed (Bottom). When the medium between the plates is a properly chosen fluid, we show that the force switches sign as a function of orientation for certain separations.

reducing the pairwise surface-surface separation between the slabs. In another case to be discussed, in which the wires are gold, the substrate silica, and the fluid ethanol, the bound eq. (4.1) is also valid. However, we find from exact calculation that while PFA predicts $F_{y=a/2} < 0$ and $F_{\text{crossed}} > 0$, the opposite is in fact true, i.e., aligned slabs are always attracted to each other, while crossed slabs are *repelled.* Therefore, in our case at $d/a \sim 1$ the sign of the force can therefore be modulated by rotating the slabs (but not translating them), an interesting possibility for experiments that we discuss later.

To understand these effects qualitatively, we find that a much more suitable frame-

work is the effective medium approximation (EMA), in which the microstructured slabs of Fig. 4-1 are describable as an homogeneous medium with a given anisotropic permittivity tensor $\overleftrightarrow{\varepsilon} = \mathrm{diag}\left(\varepsilon_{||}, \varepsilon_{\perp}, \varepsilon_{\perp}\right)$ (here and below, $\overleftrightarrow{\varepsilon}$, $\varepsilon_{||}$ and $\varepsilon_{\perp}$ will be used to denote effective, homogenized permittivities). We are able to compute the effective ε tensor for this configuration from our scattering method [179], and we find that for the gold-silica-ethanol configuration, the deduced effective-medium parameters follow an ascending sequence $\varepsilon_{\perp} < \varepsilon_{\text{fluid}} < \varepsilon_{||}$. This ascending sequence is known to lead to repulsion [44] for uniform, isotropic materials, and we find below that the effect is also present for anisotropic materials and individual polarizations (although in this case, as discussed below, an ascending sequence is not sufficient for repulsion). One expects the EMA to be strictly valid as $d \to \infty$, however in our case it turns out, somewhat surprisingly, to be qualitatively accurate down to $d/a \lesssim 1$ (a mathematical proof of why the EMA holds at such short separations, at least for crossed slabs, is given in Appendix 4B. Further, we find that for realistic materials (gold wires, silica substrate, immersed in an ethanol fluid) and geometry parameters, this orientation induced repulsion at fixed surface-surface separation between the two slabs holds down to separations $d/a \sim 0.5$.

In Chapter 3, we discussed how attempts to predict novel Casimir effects on the basis of effective-medium theory have either (1) not lead to interesting effects, or (2) been contradicted by exact calculations, the latter case being the subject of the previous chapter. Therefore, while in some circumstances EMA can be a useful qualitative guide (and rigorously accurate in certain limits), it must be used with caution—ideally, as a supplement to exact calculations. By the use of EMA, orientation dependence (and the resulting Casimir torque) between slabs has previously been considered for two birefringent plates with weak anisotropy [133, 185, 199]; exact calculational techniques have been applied to corrugated metallic plates [165]. Although the torques in these systems are in principle measurable, the change in the force with orientation is small, and the forces are always attractive. Based on an EMA analysis, Ref. 82 showed a large orientation dependence for theoretical uniaxial conductors, and suggested a possible realization via nanowire arrays, but without calculation in

the latter case and without changing the sign of the force.

In the present chapter, we analyze this effect for periodically-patterned, vacuum-separated suspended membranes (which form a potentially promising medium for Casimir force measurements [175]) and for gold wires on silica substrate, immersed in ethanol. In both cases, we find eq. (4.1) is violated down to $d/a \sim 1$. In the former case, we find that the force is 70% lower for crossed slabs compared to aligned slabs (for any y) at large separations, while at separations comparable to the unit cell (e.g., 100 nm) there is a more modest, but still significant, 30% reduction. For the latter system, we find that aligned slabs are attractive for all y down to $d/a \sim 0.5$ while crossed slabs are repulsive in this range. These examples demonstrate a system in which effective-medium theory is correct and gives predictions that differ from PFA in a highly nontrivial way. Given that nanowire arrays below 15 nm can be fabricated with current technology [131] and that for these dimensions the predicted effects occur down to sub-100 nm length-scales, these effects should be experimentally accessible. After presenting these results, we argue how they may be experimentally detectable (assuming suitable fabrication techniques) and estimate force magnitudes in the hypothetical case where one of the slabs is replaced by either a sphere or cylinder with a wire pattern stamped on its surface.

4.3 Method

In this chapter, we perform our Casimir force calculations with a semi-analytic scattering method using a combination of results from Ref. 91, 154, 208, which efficiently computes the exact Casimir force between periodic arrays with one dimensional of translation-invariance. Our implementation differs somewhat from previous scattering methods (e.g., Refs. [35,93]) in that it is particularly well-suited to unit cells with objects of compact cross-section, such as the wires in Fig. 4-1 (rather than, e.g., extended rectangular gratings). While we are primarily interested in objects of circular cross-section in the current work, the present method can be extended in a straightforward manner to treat unit cells with arbitrarily shaped compact objects using the

hybrid technique discussed in Sec. 6.4 (adapted to the cylindrical multipole basis). In addition, we have checked the results with FDTD and found good agreement, and additional FDTD computations show similar results for square wires. Also, the effects are not significantly different at zero temperature and 300 K, so we work exclusively in the zero-temperature limit.

The two plates are separated from each other by a distance d in the x direction, and the slab is termed y-directed if the wires are along the y axis (similarly for z). The slabs are aligned if both slabs are y- or z-directed, and crossed if they are not. The zero-temperature Casimir interaction energy for a q-directed slab displaced by $\mathbf{x}$ from a q' directed slab ($q, q' = y, z$) is:

$$E = \frac{\hbar c}{2\pi} \int_0^\infty d\xi \int \frac{d^2\mathbf{k}_{yz}}{4\pi^2} \log\det\left(\mathbb{I} - \mathbb{R}_1^{(q')}\mathbb{U}^\dagger\mathbb{R}_2^{(q)}\mathbb{U}\right) \tag{4.2}$$

where $\mathbb{R}_{1,2}$ are the scattering matrices of planewaves for the two slabs, $\mathbb{U}(\mathbf{x})$ is the planewave translation matrix for relative displacement $\mathbf{x}$ between the slabs, and the integral of transverse wavevector components k_y, k_z is over the first Brillouin zone. See Ref. 154 for a detailed derivation and a partial review of precursors [50, 84, 113]. For the present work, we require an efficient method of computing the scattering matrices from periodic arrays, which we describe in more detail in Appendix 3A.

For sufficiently large distances, the relevant frequencies and wave-vectors are unable to probe the structure of the arrays and consequently an effective medium approximation should produce good results. In our case, such an effective medium should have a much larger conductivity in the direction of the wires as compared to the other orthogonal directions even in the static limit (this being one of the motivations for the current configuration), so it is clear that an anisotropic EMA is called for. Fortunately, Casimir interactions between anisotropic homogeneous media have been studied by several authors [7, 8, 145, 149, 179], allowing us to build upon their results. We use the method of Ref. 179 (outlined in Appendix 4A) to obtain the scattering matrices assuming a known permittivity $\overleftrightarrow{\varepsilon}$. In the subsequent analysis, we also require the inverse procedure: given the scattering matrices (computed using

the method of Ref. 179) of the exact structure, retrieve the best-fit EMA $\overleftrightarrow{\varepsilon}$. This procedure quickly becomes intractable if arbitrary $\overleftrightarrow{\varepsilon}$ and $\overleftrightarrow{\mu}$ are allowed. Instead, we assume $\mu_{ij} = \delta_{ij}$ and $\overleftrightarrow{\varepsilon}_{xx}=\overleftrightarrow{\varepsilon}_{yy}$ exhibit no dependence on $\mathbf{k}_\perp$ aside from its polarization. For $|\mathbf{k}_\perp| \to 0$ the scattering matrices for each polarization reduce to the standard Fresnel formula for reflection off isotropic interfaces. Their inversion then yields the effective dielectric tensor:

$$\varepsilon_{||}(i\xi) = \varepsilon_{\text{fluid}} \left(\frac{1-R_{||}}{1+R_{||}}\right)^2, \quad \varepsilon_{\perp}(i\xi) = \varepsilon_{\text{fluid}} \left(\frac{1+R_{\perp}}{1-R_{\perp}}\right)^2 \tag{4.3}$$

4.4 Results

In the configuration of Fig. 4-1, the wires have radius $r = 0.3\,a$ and period a; we take the wire centers to be in the substrate and the wire surface to be tangent to the substrate surface to maximize the wire-wire interactions. The permittivities of wires, substrate, and fluid are respectively $\varepsilon_1(i\xi)$, $\varepsilon_2(i\xi)$ and $\varepsilon_3(i\xi)$ for imaginary frequency ξ. The materials used for the wires, substrate, and fluid are gold, ethanol, and silica, respectively. For gold, we use a plasma model with $\xi_p = 1.36 \times 10^{16}\,\text{rad/sec}$ (the addition of a small loss term does not change the results significantly). For silica and ethanol we use standard oscillator models [14, 125].

4.4.1 Vacuum-separated slabs

We first compute the Casimir forces when the intervening medium is vacuum ($\varepsilon_3 = 1$), comparing the force $F_{\text{aligned}}(y)$ for aligned slabs with the force F_{crossed} for crossed slabs. In the aligned case, the force can depend on y (leading to a lateral component of the force), and in this case F_{aligned} refers only to the *normal* component of this force. In the crossed case $\theta = \pi/2$ there is no y-dependence. Although there is no sign change for vacuum-separated slabs, this configuration is of interest because it can be fabricated as a single suspended-membrane structure for each orientation [175], and may be easier to work with than a fluid system. Figure 4-2 shows results for wires composed of perfect metal, gold, and heavily doped silicon, the latter being more

conventional for fabrication. We plot the ratio $F_{\text{crossed}}/F_{\text{aligned}}(y)$ (the shaded regions indicate the full range of this ratio as y is varied), which serves two purposes. First, it indicates the required relative accuracy in a force measurement needed to discern the orientation-dependence of the force in an experiment. Second, it indicates the transition from the PFA to the EMA regimes via eq. (4.1): if the force is determined as a sum of pairwise interactions, then the total force is maximized when the pairwise surface-surface distances are minimized. A simple geometric argument shows that the net distance is maximized for $\theta = 0, y = a/2$. On the other hand, this distance is minimized for $\theta = 0, y = 0$. The bound eq. (4.1) then follows. It turns out that the force is always attractive in this situation, so we have the further bound $F_{\text{aligned}}(y = a/2) > 0$. Therefore, PFA predicts that there is a range of y such that $F_{\text{crossed}}(y)/F_{\text{aligned}} > 1$. By contrast, EMA predicts the inequality $F_{\text{crossed}} < F_{\text{aligned}}$ (there is no y-dependence in this approximation). This inequality stems from the following scattering-theory argument: for $d/a \gg 1$, the exponential suppression of $k_y, k_z \neq 0$ in $\mathbb{U}$ [154] implies that the force is dominated by the scattering of planewaves at normal incidence ($k_y = k_z = 0$). For normal incidence, the reflection matrix $\mathbb{R}^{(z)}$ is anisotropic but diagonal in polarization, and can be computed from an effective anisotropic dielectric tensor: $\overleftrightarrow{\varepsilon}\,(i\xi)$:

$$\overleftrightarrow{\varepsilon}\,(i\xi) = \text{diag}\left(\varepsilon_{xx}, \varepsilon_{yy}, \varepsilon_{zz}\right) \Rightarrow \mathbb{R} \approx \text{diag}\left(R_{||}, R_{\perp}\right) \tag{4.4}$$

where $R_{||}$ and $R_{\perp}$ are the matrix elements for incident light polarized parallel and perpendicular, respectively, to the wires. For normal incidence, ε_{xx} does not contribute, and we define $\varepsilon_{||} = \varepsilon_{zz}$ and $\varepsilon_{\perp} = \varepsilon_{yy}$. Due to the high permittivity of the wires and the low permittivity of the substrate, we expect $|R_{\perp}| \ll |R_{||}|$ and $R_{\perp}R_{||} \geq 0$ [note that $R(i\xi)$ is real]. When the wires are aligned, the relevant product of scattering matrices in the energy integrand is $\left(R_{||}^2 + R_{\perp}^2\right) \approx R_{||}^2$, and when they are crossed the term is $2R_{||}R_{\perp}$, implying $F_{\text{crossed}} < F_{\text{aligned}}$. From Fig. 4-2, this bound is clearly violated in doped Si for $d/a < 0.6$, and for other materials at smaller d. Note that this includes a region $d/a < 2$ for which there is still a strong y-dependence of this ratio,

indicating that while EMA is not strictly valid, it still has more predictive power than PFA.

As $d/a \to \infty$, the force ratios should approach a constant determined by $\overleftrightarrow{\varepsilon}$ ($\xi \to 0$): this ratio is ≈ 0.29 for all three materials. However, this limit is approached very slowly ($O(d^{-1/2})$ for perfect metal/gold wires). The EMA d-dependence is due both to constituent material dispersion and an effective geometric dispersion in $\overleftrightarrow{\varepsilon}$ ($i\xi$) induced by the geometry of the wires. As $\xi \to 0$, $\varepsilon_{||} \to \varepsilon_1(i\xi)$ and $\varepsilon_\perp \to \varepsilon_2(i\xi)$. The former limit follows from the $1/\xi^2$ divergence of ε_1 as $\xi \to 0$ (if we add a dissipative term to ε_1, the divergence is only $1/\xi$ but this crossover occurs at frequencies too low to affect the present results). The latter limit follows from the fact that the static polarizability of the wires in the transverse direction is finite, implying that their contribution to the scattering amplitude vanishes as $\xi \to 0$. Therefore, as $\xi \to 0$, $\varepsilon_\perp$ depends only on the substrate, which has semi-infinite extent; we have checked this relation numerically and found good agreement. $\lim_{d\to\infty} F_{\text{crossed}}/F_{\text{aligned}}$ can then be obtained by computing the force between two anisotropic plates, with $\varepsilon_{||} = \infty$ and $\varepsilon_\perp = \varepsilon_2(0)$.

For all $d/a \gg 1.5$, the orientation-dependence of the force is quite strong ($\gg 30\%$). In this range, the absolute pressure is approximately 2% of the corresponding pressure between two homogeneous perfect metal plates. As differences of this magnitude between vacuum-separated plates have been measured on the $100-$ nm length scale, we are hopeful that this departure from PFA can be detected experimentally.

4.4.2 Fluid-separated slabs and tunable repulsion

In the previous example the force is always attractive, because $\varepsilon_1(i\xi), \varepsilon_2(i\xi) \geq \varepsilon_3(i\xi)$ for all ξ [155]. However, if the medium between the slabs is a fluid such that $\varepsilon_1(i\xi) > \varepsilon_3(i\xi) > \varepsilon_2(i\xi)$, the above EMA analysis predicts that the force in the crossed configuration should be repulsive as $d/a \to \infty$ since by the Fresnel formula at $\xi = 0$, $R_\perp R_{||} < 0$, leading to the well-known Casimir repulsion for an ascending sequence of ε for each polarization [134]. By contrast, in the aligned configuration the force is attractive when $y = 0$ due to mirror symmetry [83], and the intuition

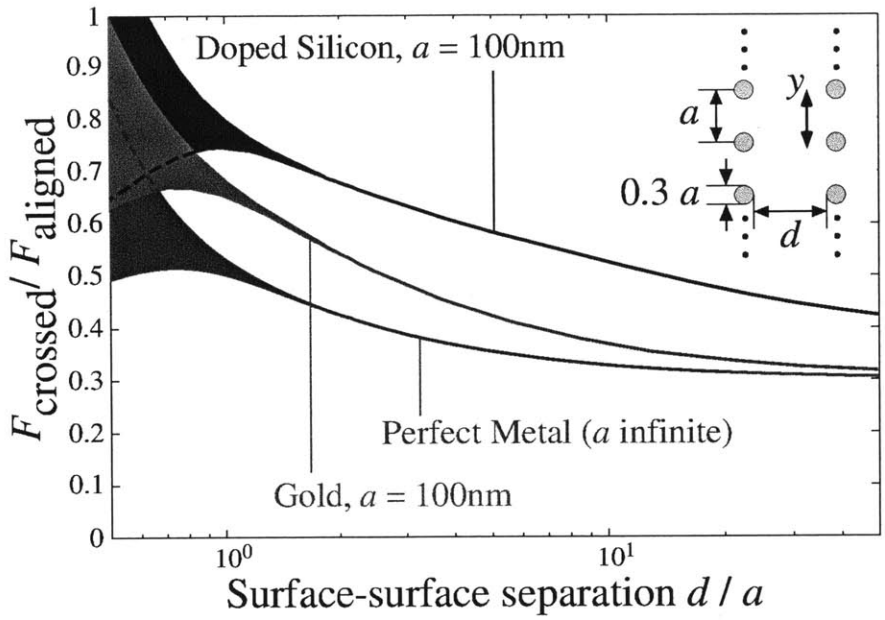

Figure 4-2: Ratio of the Casimir force between crossed wire arrays (F_{crossed}) over aligned wires ($F_{\text{aligned}}(y)$) between vacuum-separated nanowires of perfect metal, gold, and doped silicon (dopant density $10^{20}/\text{cm}^3$). $a \to \infty$ corresponds to using non-dispersive $\varepsilon(i\xi \to 0)$ for all materials (because ξ is in units of c/a). Shaded regions indicate the range of values that F_{aligned} takes over all relative lateral displacements y of the wire centers, with their higher (lower) boundary indicating the force for $y = 0$ ($y = a/2$). PFA predicts, via eq. (4.1), that the maximum of this ratio should exceed 1, which is only true for Si at $d/a \sim 0.6$, and for gold/perfect metal at lower separations. Inset: details of the configuration examined.

that this attraction holds for non-zero y is confirmed by calculation. However, strong corrections to this argument occur at finite separations: waves with nonzero k_y and k_z contribute, and are not in general polarized along the y or z axes. These waves will couple to both $\varepsilon_{||}$ and $\varepsilon_{\perp}$ on each reflection. The sign of the resultant reflection coefficient will usually be the same for both z- and y-directed slabs, leading to attractive contributions. Further, as seen in Chapter 3 the microstructure can also lead to significant corrections, possibly eliminating the effect for separations comparable to the unit cell. As such separations are necessarily required for experiments, we require exact results to verify that this effect persists in experimentally accessible regions.

The exact results are shown in Fig. 4-3; as in Fig. 4-2, shaded regions show the y-dependence. The results show a clear attractive-repulsive transition as the slab

orientation is varied between the aligned and crossed configurations. This effect persists for both the ideal case of perfect metals ($a \to \infty$) and dispersive materials at $a = 100\,\text{nm}$; both show qualitatively similar behavior. For crossed slabs, the repulsion is fairly flat over a $\sim 40\,\text{nm}$ range. At first sight, it is temping to ascribe the repulsive force observed for crossed wires to PFA-line interactions between opposing areas where metallic wires face dielectric substrate and thus feel a repulsive force. However, if this were the case, then by the same argument (and eq. (4.1)), $F_{\text{aligned}}(y = a/2)$ should exhibit an even stronger repulsion. This is clearly not the case in Fig. 4-3 for $d/a > 0.5$; rather, the results for repulsion are consistent with the EMA argument given above. To estimate the magnitude of this repulsion, for $a = 100\,\text{nm}$ the repulsive pressure is approximately 1% of the pressure between parallel perfectly-conducting plates separated by a comparable distance d in vacuum, e.g, $\sim 0.13\,\text{pN}/\mu\text{m}^2$. Repulsive forces in fluids on this order of magnitude have been measured [134], therefore these forces are potentially within reach of current or near-future measurement techniques (the force in more realistic sphere-plate and cylinder-plate geometries will be considered in Sec. 4.4.4 below). Interestingly, when the wires are crossed and d varies there is an attractive-repulsive transition at a critical separation $d = d_c$. This leads to an unstable equilibrium with respect to d. (The crossed configuration is always unstable with respect to orientation.) This transition, as mentioned above, is attributed to the eventual dominance of attractive forces as separation goes to zero. However, we will see below that such a transition is predicted by EMA as well, and is therefore not due entirely to proximity effects.

Before continuing, it is interesting to see what the PFA prediction for the force in this system is. We simplify matters by computing the PFA assuming instead wires of square $r \times r$ cross-section, with centers a distance $r/2$ beneath the substrate surface (by minimizing the amount of curved surface, we expect this to maximize the range of separations for which PFA is accurate). Using FDTD computations, we have found that this system exhibits behavior qualitatively similar to that of Fig. 4-3. The results for $a = 100\,\text{nm}$ are shown in Fig. 4-4 (taking $a \to \infty$ yields a qualitatively similar curve). Inspection reveals that the PFA prediction exhibits the *opposite* behavior for

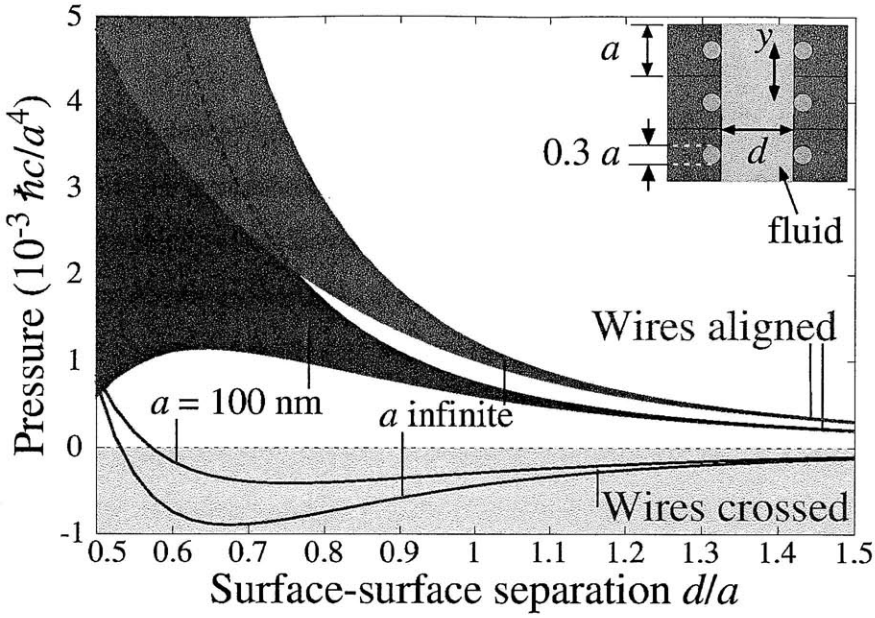

Figure 4-3: Casimir pressure for the same parameters as the inset to Fig. 4-2, with a silica substrate and ethanol between the two slabs. Positive values indicate an attractive force, negative values (shaded) repulsive. Both $a \to \infty$ and $a = 100\,\text{nm}$ are shown. As in Fig. 4-2, shaded regions denote the range of y-displacements. When the wires are aligned (blue), the force is always attractive, but when the wires are crossed (red), the force turns repulsive at a critical separation $d > d_c$, which depends on a.

the sign of the force as the full numerical calculations: the PFA force is exclusively *attractive* for crossed wires, but for aligned wires shifted by $y = a/2$ the force becomes *repulsive.*

Although PFA fails qualitatively and quantitatively to predict the results of Fig. 4-2 and Fig. 4-3, we have not yet examined the quantitative accuracy of EMA. In the next section, we will examine a description of the force in terms of the EMA, rigorously valid in the regime ($d/a \to \infty$). We will see that EMA gives qualitatively correct predictions for the magnitude and sign of the forces down to separations comparable to the unit cell size.

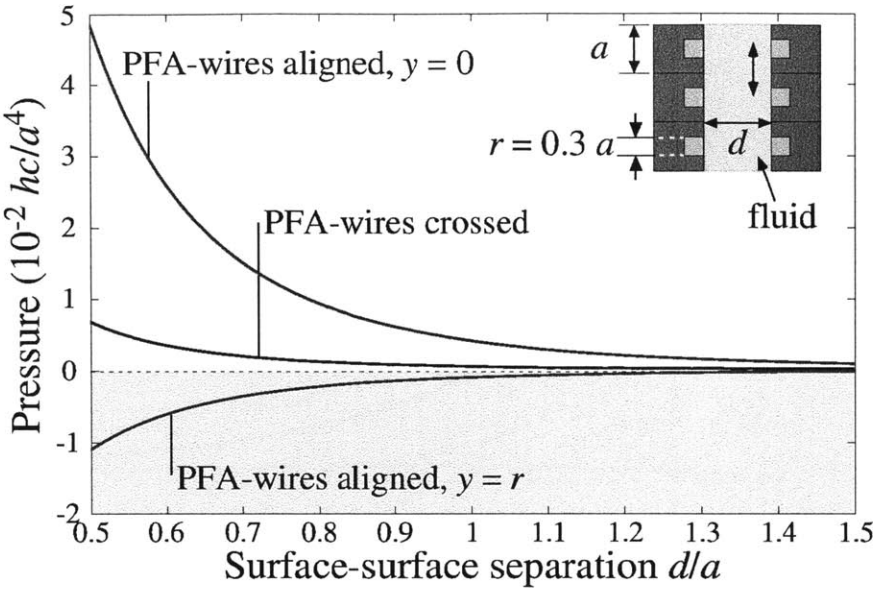

Figure 4-4: Forces computed for the configuration of Fig. 4-3 using the Proximity Force Approximation (PFA), for $a = 100\,\text{nm}$. For convenience in applying the PFA, square wires of width r are used instead of circular wires (the exact results are not qualitatively changed). We see that the behavior of Fig. 4-3 is not qualitatively captured: the force is always attractive for crossed wires, and the bound eq. (4.1) is strictly satisfied. Similar results are obtained for $a \to \infty$.

4.4.3 Comparison with EMA

In this section, we examine the extent to which the EMA analysis given above in Sec. 4.4.1 predicts the correct results, using the method of Ref. 179. We use a simplified EMA, assuming that $\overleftrightarrow{\mu}\,(i\xi) = 1$ and $\overleftrightarrow{\varepsilon}\,(i\xi)$ is isotropic in the plane perpendicular to the wires. In this case, $\varepsilon_{||}$ and $\varepsilon_{\perp}$ are the only EMA parameters involved; these are retrieved by applying eq. (4.3) to the scattering matrices computed from the exact structure. The EMA-predicted force is then computed from the method of Ref. 179. A plot of the retrieved parameters for $a = 100\text{nm}$ is shown in Fig. 4-5. Shown for reference in Fig. 4-5 are $\varepsilon(i\xi)$ of the constituent materials ethanol, silica, and gold. As expected, $\varepsilon_{\perp}$ approaches $\varepsilon_{\text{silica}}$ for low ξ, while for higher ξ the wires increase the effective permittivity. In $\varepsilon_{||}$, we see a significant geometric dispersion: in fact, at low ξ, $\varepsilon_{||}(i\xi) \sim 1 + \left(\xi_p'/\xi\right)^2$, where $\xi_p' \sim 0.36\,\xi_p$ is a new, effective plasma frequency for the gold wires. This is similar to an argument presented in Ref. 148,

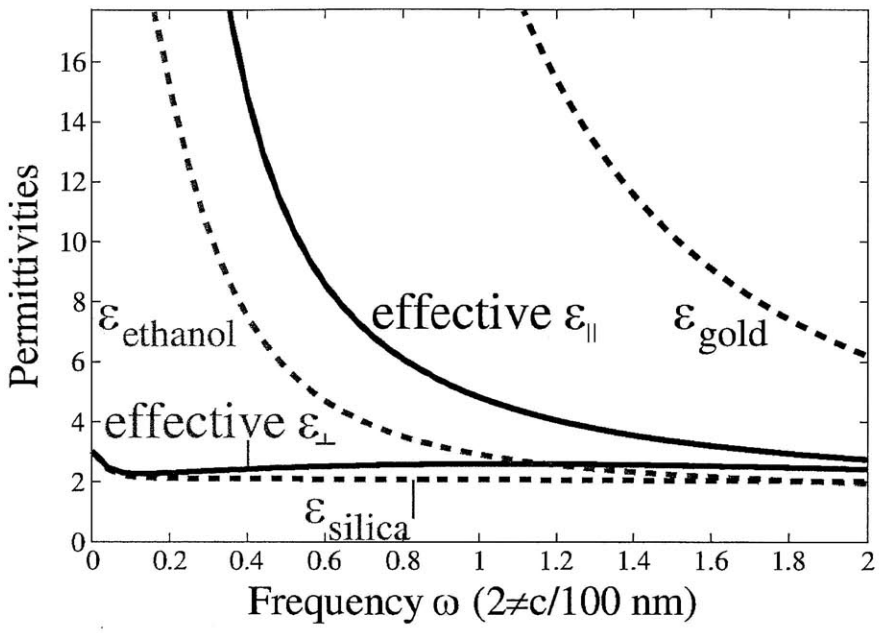

Figure 4-5: Effective-medium parameters for the system of Fig. 4-3 derived from scattering data for a length scale $a = 100\,\text{nm}$. $\varepsilon_{||}$ is the effective dielectric parallel to the wires (black), and $\varepsilon_{\perp}$ the effective dielectric perpendicular to the wires (blue). The dielectrics of the constituent materials gold, silica, and ethanol are shown for reference. These dispersions will be used to compute the Casimir force in the effective-medium approximation below.

where the effective dielectrics of square arrays of wires along the wire axis can be described by a plasma model with a reduced plasma frequency (as we have only included a single row of wires, Ref. 148's result cannot be directly applied, but its basic idea remains). A similar effect holds when the wires are perfect conductors, where $\xi_p' = 7.9$. This accounts for the d-dependence in the EMA regime of Fig. 4-2: the geometry introduces an effective length scale into the system, given by ξ_p.

We use the retrieved $\varepsilon_{||}$ and $\varepsilon_{\perp}$ to compute $\mathbb{R}$ and hence the Casimir force for the fluid-separated geometry. Computation of the force with the EMA parameters for the vacuum-separated slabs in the limit $d \to \infty$ gives agreement with the results of Fig. 4-2. The results for the fluid-separated case are shown in Fig. 4-6. We find that, as opposed to PFA, EMA gives qualitatively accurate (i.e., the same order of magnitude) predictions for both the magnitude and sign of the force. In particular, EMA predicts attractive-repulsive transitions at some $d = d_c$, where for $d < d_c$ the

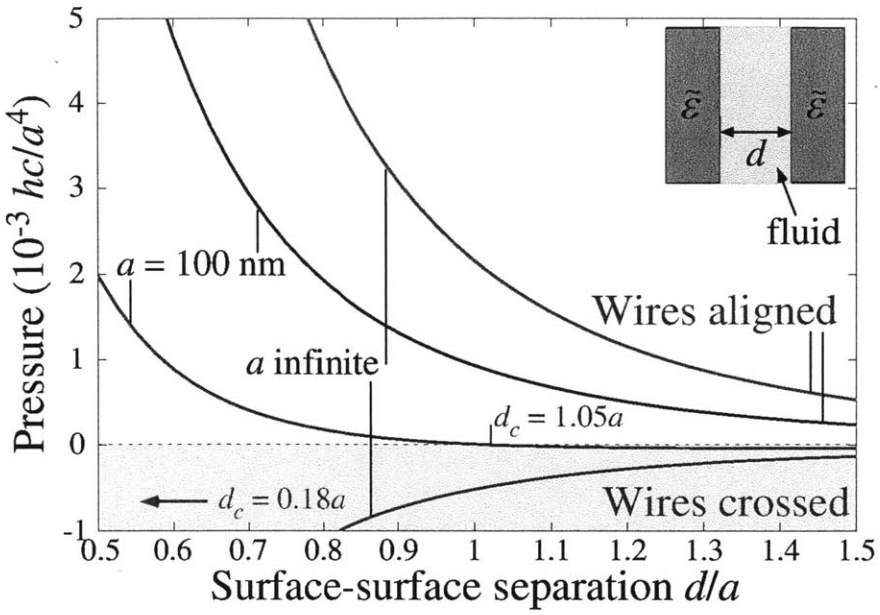

Figure 4-6: Results for the force computed in the Effective-medium Approximation (EMA) using an effective homogeneous, anisotropic permittivity tensor $\overleftrightarrow{\varepsilon}$, via the method described in Appendix 4A. As in Fig. 4-3, results for both a infinite (i.e., non-dispersive materials) and $a = 100\,\text{nm}$ are shown, for both crossed and aligned configurations. Although quantitatively inaccurate over the range plotted, the EMA does qualitatively capture the behavior of the force a opposed to PFA. Also shown are d_c, the location of the attractive-repulsive transitions for the crossed wires ($d_c = 0.18a$ for $a \to \infty$ and is not shown).

force for crossed slabs is attractive. The fact that $\varepsilon_{||}(\xi)$ is a rapidly decreasing function of ξ, while $\varepsilon_{\perp}$ increases, indicates that within the EMA the force should receive attractive contributions from higher ξ (which dominate at small separations). Further, the decrease of both $\varepsilon_{||}$ and ε_2 with decreasing a also contributes to a reduction in repulsion. This explains why the repulsion for $a = 100\,\text{nm}$ is lower than for $a \to \infty$. With our simplified EMA the predicted values of d_c are very inaccurate: $d_c \approx 0.18\,a$ for $a = \infty$ and $d_c \approx 1.05\,a$ when $a = 100\,\text{nm}$. However, the y-independent regimes of Figs. 2–3 suggests that some EMA must be valid in those regimes, and in this case a more accurate EMA would involve both $\varepsilon_{xx} \neq \varepsilon_{\perp}$ as well as an anisotropic effective $\overleftrightarrow{\mu}$. A more general model of dispersion would allow for a translation-invariant but $\mathbf{k}$-dependent permittivity. Fitting an effective $\overleftrightarrow{\varepsilon}$ $(\mathbf{k})$ is somewhat complicated in this framework; rather, to explore the validity of this "specular" approximation

we compute the force with all non-specular (i.e., terms not conserving $\mathbf{k}_\perp + \mathbf{G}_\perp$, where $\mathbf{G}_\perp$ is a reciprocal lattice vector) terms in the scattering matrix $\mathbb{R}$ removed. We find the surprising result that, while this specular approximation does not give significantly different predictions for the force for aligned wires, it gives much more accurate predictions for d_c and the magnitudes of the force for crossed wires. This indicating that non-specular scattering events are suppressed when the wires are crossed, even at relatively small separations $d/a \sim 0.5$. We give a rigorous proof of this result in Appendix 4B, using a recently-developed diagrammatic expansion for the Casimir energy [110].

4.4.4 Forces for other geometries

Parallel-plate configurations involving suspended membrane structures show potential for new sets of experimental Casimir force measurements for vacuum-separated geometries [175]; such measurements detect the Casimir force (or force gradient) through a shift in either the optical spectrum or the resonance frequency of the upper membrane. However, to measure the sign change in the force predicted here a measurement between fluid-separated objects must be performed, where fluid damping is prohibitive. Instead, a force measurement involving an object (e.g., a sphere) mounted on an atomic force microscope (AFM) tip [134] is more realistic. In this case, alignment issues favor the use of one spherical and one planar object [95, 130], rather than the two planes considered here. For our purpose, a pattern of wires similar to Fig. 4-1 would be need to be stamped on the surface of the object. In this section, we give force predictions both sphere-plate and cylinder-plate geometries. The latter case has more difficult alignment issues, but still simpler than plate-plate alignment, and in this case the Casimir force is much larger than for sphere-plate setups [22]. For both cases, the radius of curvature R is many orders of magnitude larger than the surface-surface separation d (e.g., $R = 200\,\mu\text{m}$ and $d \sim 100\,\text{nm}$). Because $d, a \ll R$, it is appropriate to use a hybrid PFA/exact method in which each unit of surface on the sphere/cylinder feels the *exact* pressure (as computed in Sec. 4.4.2) between a plate-plate configuration of the same surface-surface separation. The result is asymp-

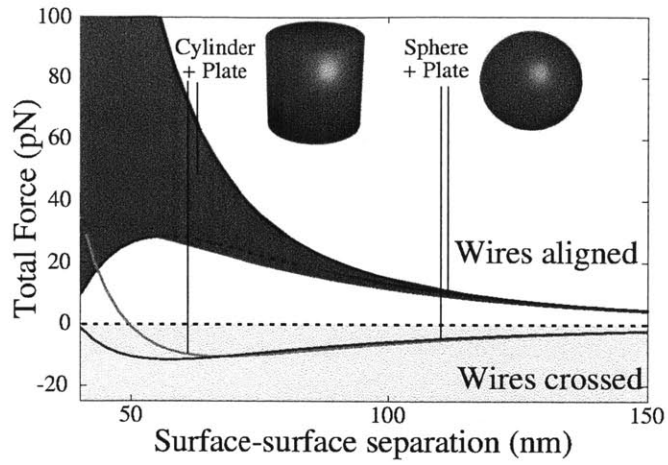

Figure 4-7: Forces for sphere-plate (red) and cylinder-plate configurations, for $a = 100\,\text{nm}$. In both cases, the wire pattern of Fig. 4-1 is stamped onto the surface of both objects, which have radii of curvature $R = 200\,\mu\text{m}$. The cylinder length is chosen to be $L = 16\,\mu\text{m}$ so that the two force curves have comparable magnitude; however the cylinder-plate force is proportional to L and so will be much larger in magnitude for a more realistic $L \sim R$.

totically exact in the limit $R \to \infty$ for fixed d and a.

Results are shown in Fig. 4-7 for $R = 200\,\mu\text{m}$, and are plotted in units of pico-Newtons. The sphere-plate force has a peak repulsion of $\sim 10\,\text{pN}$, which although below the detection limit of current measurement techniques in fluids, may be observable in the near future. We also note that, although the presence of Casimir repulsion may be experimentally challenging, eq. (4.1) can be verified with much less sensitivity (e.g., $\sim 50\,\text{pN}$ at $d = 50\,\text{nm}$). For the cylinder-plate, we take a length $L = 16\,\mu\text{m}$ in order for the force to be comparable in magnitude to the sphere-plate force. However, it is clear that if we instead take $L \sim R$, we can obtain both repulsive and attractive forces on the order of $10^3\,\text{pN}$, well within current experimental detection ranges. Therefore, this system seems most attractive for detection of an attractive-repulsive transition with orientation in a fluid if techniques similar to those of Ref. 204 to align the long axis of the cylinder relative to the plane can be extended to fluid-separated objects.

4.5 Conclusions

We have presented an example system, consisting of microstructured slabs, in which PFA fails at relatively small separations. Instead, EMA qualitatively describes the behavior of the Casimir force, including the case in which the force can be switched from attractive to repulsive as the slabs are rotated. We have discussed the prospects for detecting these forces in experiments. One issue arising in an experiment, not discussed here, is the increased complexity of the electrostatic calibrations. Conceivably, these complications can be eliminated in the fluid-separated case by the addition of electrolytes to the fluid. This should also reduce or eliminate the effect of accumulated surface charges on the gold-silica interface, due to contact potentials [37,38]. For the case of vacuum-separated doped silicon, a more involved calibration procedure is required.

Although not examined here, we also note that orientational attractive-repulsive transitions may also occur using naturally anisotropic materials. We have confirmed this for the case of lithium niobate slabs immersed in ethanol at zero temperature; although here $d_c > 7\,\mu$m (implying that finite-temperature effects must be taken into account), transitions at smaller separations may be possible with appropriate materials.

Appendix 4A: Details of Computational Methods

Scattering from periodic arrays

There are numerous computational and semi-analytic methods from classical electromagnetic scattering that can be adapted to Casimir calculations [75]. For example, there are computational techniques based on generic grids/meshes, e.g. finite-difference methods [119,146,167,172]. There are also Casimir methods [35,93] based on classical cross-section methods (rigorous coupled-wave analysis [129], also called eigenmode expansion [15]), which divide the geometry into slices with constant cross-sections and match modal expansions between slices. Alternatively, there are spec-

tral integral-equation methods tracing their roots to classic Mie scattering and related problems [191]: one divides the geometry into high-symmetry objects like spheres and cylinders, computing the scattering matrix for each object in a specialized basis (e.g. spherical waves), and then combining the matrices from different objects to match the boundary conditions. These methods have been adapted to Casimir problems for geometries consisting of a finite number of isolated objects [50, 84, 113, 154] and corrugated surfaces [23]. Here, we adapt similar methods to periodic arrays of isolated objects (cylinders) by exploiting classical lattice-sum scattering methods [208]. For completeness, and because our formulation is directly in imaginary frequency and our normalization conventions differ from other applications [91, 208], we outline the derivation in this section.

The scattering matrix $\mathbb{T}_0$ from a single circular cylinder can be computed analytically in the basis of cylindrical multipoles, using the basis functions [154]:

$$|\mathbf{E}\rangle_{k_z,n}^{p,\text{reg/out}}(i\xi,\mathbf{x}) = \mathbb{L}^p\left[\phi_{k_z,n}^{\text{reg/out}}(i\xi,\mathbf{x}-\mathbf{x}_j)\,\hat{\mathbf{z}}\right] \tag{4.5}$$

where the linear differential operators $\mathbb{L}^p$ ($p = M, N$ are the transverse electric and transverse magnetic polarizations, respectively) are:

$$\begin{aligned}\mathbb{L}^M &= \frac{1}{\sqrt{k_z^2+\xi^2}}\nabla\times \\ \mathbb{L}^N &= \frac{1}{\xi\sqrt{k_z^2+\xi^2}}\nabla\times\nabla\times\end{aligned}$$

and the cylindrical wave functions are:

$$\begin{aligned}\phi_{k_z,n}^{\text{reg}}(i\xi,\mathbf{x}) &= I_n\left(\sqrt{k_z^2+\xi^2}\sqrt{x^2+y^2}\right)e^{ik_z z+in\theta} \\ \phi_{k_z,n}^{\text{out}}(i\xi,\mathbf{x}) &= K_n\left(\sqrt{k_z^2+\xi^2}\sqrt{x^2+y^2}\right)e^{ik_z z+in\theta}\end{aligned}$$

I_n and K_n are the modified cylindrical Bessel functions, and $\mathbf{x}_j$ gives the coordinate origin. The calculation of $\mathbb{T}_0$ is straightforward and we omit it here. We note that although the present method is simplified by the semi-analytic calculation of the scattering from circular cylinders, methods exist that can compute the scattering matrices of non-circular cylinders of arbitrary cross-section [163]; such a hybrid method allows for efficient scattering computations from general two-dimensional arrays of compact objects.

We now derive the scattering matrix $\mathbb{T}$ for a periodic array of cylindrical scatters in a uniform medium (the fluid interface will be added later). $\mathbb{T}$ is defined to be the scattering matrix from each cylinder j in the basis given by eq. (4.5) with origin $\mathbf{x}_j = ja\hat{\mathbf{y}}$, in the presence of the entire array of cylinders. This array has period a in the y-direction and is translation-invariant in z, and only a single layer in the x-direction. In other words, for an incident field $|\mathbf{E}\rangle^{\text{in}}$, the scattered field emitted by currents on cylinder j is:

$$|\mathbf{E}^{(j)}\rangle^{\text{scatt}} = e^{ik_y ja}\mathbb{T}|\mathbf{E}\rangle^{\text{in}} \tag{4.6}$$

Here we have assumed that the incident field $|\mathbf{E}\rangle^{\text{in}}$ is a planewave with transverse wavevector components k_y and k_z, and have normalized it with respect to the origin. Then using the translation matrices [154] for the basis functions of eq. (4.5), the scattered field from object j, converted to the basis at the origin ($j = 0$), is given by:

$$\underset{k_z,n}{\overset{p,\text{reg}}{}}\langle\mathbf{E}^{(j=0)}|\mathbf{E}^{(j)}\rangle = \sum_{n'',n'} \mathbf{S}^{(j)}_{n-n'} e^{ik_y ja}(-1)^{n'}\mathbb{T}^{p,p'}_{n',n''}\,\underset{n''}{\overset{p'}{}}\langle\mathbf{E}|\mathbf{E}\rangle^{\text{in}} \tag{4.7}$$

where the elements of the lattice sum $\mathbf{S}$ are given by:

$$S^{(j)}_m = K_m\left(|\mathbf{x}|\sqrt{k_z^2 + \varepsilon_2\xi^2}\right)e^{-im\theta_j} \tag{4.8}$$

and $\theta_j = \text{sign}(j)\frac{\pi}{2}$; and this transformation is diagonal in polarization p. Using linearity of the scattering process to sum over all incident cylindrical waves, the total incoming field at the origin x_0 for a planewave $|\mathbf{E}\rangle^{\text{in}}$ is obtained by summing the

incident fields and the scattered fields from all cells $j \neq 0$:

$$
\begin{aligned}
|\mathbf{E}\rangle^{\text{in,total}} &= \left[1 + \left(\sum_{j\neq 0} e^{ik_y ja}\mathbb{S}^{(j)}\right)\mathbb{A}\mathbb{T}\right]|\mathbf{E}\rangle^{\text{in}} \\
&= (1 + \mathbb{S}\mathbb{A}\mathbb{T})\,|\mathbf{E}\rangle^{\text{in}}
\end{aligned}
$$

The matrix $\mathbb{S}$ is formally defined as the infinite sum of all $\mathbb{S}^{(j)}$ (in imaginary frequency this sum is well-defined due to the exponential decay of K_n), and $\mathbb{A}_{n,n'} = (-1)^n \delta_{n,n'}$. The field scattered from the cylinder at $\mathbf{x} = \mathbf{x}_0$, in the presence of the array of cylinders, is then:

$$
\begin{aligned}
|\mathbf{E}^{(j=0)}\rangle^{\text{scatt}} &= \mathbb{T}_0\,(1 + \mathbb{S}\mathbb{A}\mathbb{T})\,|\mathbf{E}\rangle^{\text{in}} \\
&= \mathbb{T}|\mathbf{E}\rangle^{\text{in}}
\end{aligned}
$$

where the last equality follows by the definition of $\mathbb{T}$. Because this equation holds for arbitrary incident field vectors $|\mathbf{E}\rangle^{\text{in}}$, the equation holds for the operators as well, allowing us to solve for $\mathbb{T}$:

$$
\mathbb{T} = [1 - \mathbb{T}_0\mathbb{S}\mathbb{A}]^{-1}\,\mathbb{T}_0 \tag{4.9}
$$

Although both $\mathbb{S}$ and $\mathbb{A}$ are diagonal in polarization p, in general $\mathbb{T}_0$ is not and different polarizations will couple to the periodicity via eq. (4.9). The scattering matrix from the entire array is a sum of $\mathbb{T}$ over all unit cells. This sum is more naturally expressed in a planewave basis, using the wave conversion matrices $\mathbb{D}$ for cylindrical waves [154] (here we have absorbed the normalization factors C_p, defined in Appendix B. of Ref. 154, into the definition of $\mathbb{D}$), from which we find the planewave scattering matrix:

$$
\mathbb{R}_{\mathbf{k}} = \mathbb{D}_{\mathbf{k}}^{\dagger}\mathbb{T}\mathbb{D}_{\mathbf{K}} \tag{4.10}
$$

Here $\mathbf{k}$ is the reduced Bloch vector, and the matrix $\mathbb{R}_{\mathbf{k}}$ couples all vectors $\mathbf{k} + m\pi\hat{\mathbf{y}}$ for all integer m.

The incorporation of multiple interfaces in the x-direction is achieved via a standard transfer matrix approach, e.g., Ref. 208. For the case of a uniform medium ε_3 outside of the plates, the Fresnel formula are combined in a straightforward manner with the matrix $\mathbb{T}$ above to finally give the full scattering matrix $\mathbb{R}$ for the objects of Fig. 4-1.

For numerical computations, ten cylindrical multipole moments in the single-cylinder scattering matrix, $10/\xi$ terms in the lattice sum of eq. (4.9), and a simple exponential extrapolation from only 7×7 Brillouin zones for eq. (4.10) were sufficient for $< 1\%$ error.

Effective-Medium Approximation

In this section we outline the method used to predict the scattering matrices $\mathbb{R}$ from a specified $\overleftrightarrow{\varepsilon}$. The method is given in full detail in Ref. 179.

In an anisotropic EMA, we assume that the i-th object is described by a homogeneous (position-independent) permittivity tensor

$$\overleftrightarrow{\varepsilon} = \begin{bmatrix} \varepsilon_{xx} & \varepsilon_{xy} & \varepsilon_{xz} \\ \varepsilon_{xy} & \varepsilon_{yy} & \varepsilon_{yz} \\ \varepsilon_{xz} & \varepsilon_{yz} & \varepsilon_{zz} \end{bmatrix}, \tag{4.11}$$

where the frequency dependence is left implicit and we used the fact that the permittivity tensor is symmetric on its spatial indices [96]. The relatively symmetric character of our setup leads to a very useful simplification in eq. (4.11) that becomes apparent in a coordinate system with its x-axis perpendicular to the slabs interfaces: it is clear that regardless of the in-plane orientation of the wires there is no mixing with the x-component, and so

$$\varepsilon_{xy} = \varepsilon_{xz} = 0. \tag{4.12}$$

In addition, for our simplified EMA we make the further approximation that $\varepsilon_{xx} =$

$\varepsilon_{yy} \equiv \varepsilon_\perp$. This symmetry implies that the ε tensor is diagonal in the x, y, z coordinate system of Fig. 4-1 (top) and is of the form:

$$\overleftrightarrow{\varepsilon} = \begin{bmatrix} \varepsilon_\perp & 0 & 0 \\ 0 & \varepsilon_\perp & 0 \\ 0 & 0 & \varepsilon_{||} \end{bmatrix} \tag{4.13}$$

Consider a planewave of transverse wavevector $\mathbf{k}_\perp = (k_y, k_z)$ impinging on the slab, and let ϕ be the angle $\mathbf{k}_\perp$ makes with the z-axis. For our purpose, the scattering problem is best solved in the coordinate system (x', y', z') of the plane wave, where $x' = x$ and z' is parallel to $\mathbf{k}_\perp$. In this basis, the $\overleftrightarrow{\varepsilon}$ tensor becomes:

$$\overleftrightarrow{\varepsilon} = \begin{bmatrix} \varepsilon_\perp & 0 & 0 \\ 0 & \varepsilon_\perp c^2 + \varepsilon_{||} s^2 & (\varepsilon_{||} - \varepsilon_\perp) sc \\ 0 & (\varepsilon_{||} - \varepsilon_\perp)\, sc & \varepsilon_{||} c^2 + \varepsilon_\perp s^2 \end{bmatrix}$$

where $c = \cos\phi$ and $s = \sin\phi$.

We can now proceed to determine the scattering matrices of planewaves for the isotropic-anisotropic flat interface. After a considerably long algebraic calculation (for details see Ref. 179, but note the change in coordinate systems between our Fig. 4-1 and their Fig. 3, and that for us $c = \cos\phi$ and the speed of light is set to 1), it is possible to show that the four reflected/incident amplitude ratios are given by

$$\begin{aligned}
r^{\mathrm{TE,TE}}(i\xi, \mathbf{k}_\perp) &= \left.\frac{\det \mathbb{M}_1}{\det \mathbb{M}}\right|_{\substack{\omega \to i\xi \\ k_{z'} \to k_\perp}} \\
r^{\mathrm{TM,TE}}(i\xi, \mathbf{k}_\perp) &= \left.\frac{\det \mathbb{M}_2}{\det \mathbb{M}}\right|_{\substack{\omega \to i\xi \\ k_{z'} \to k_\perp}} \\
r^{\mathrm{TE,TM}}(i\xi, \mathbf{k}_\perp) &= \left.\frac{\det \mathbb{M}_3}{\det \mathbb{M}}\right|_{\substack{\omega \to i\xi \\ k_{z'} \to k_\perp}} \\
r^{\mathrm{TM,TM}}(i\xi, \mathbf{k}_\perp) &= \left.\frac{\det \mathbb{M}_4}{\det \mathbb{M}}\right|_{\substack{\omega \to i\xi \\ k_{z'} \to k_\perp}}
\end{aligned}$$

where

$$\mathbb{M} = \begin{bmatrix} -1 & 0 & \alpha^{(1)} & \alpha^{(2)} \\ q_{\text{in}}/\omega & 0 & -\beta^{(1)} & -\beta^{(2)} \\ 0 & q_{\text{in}}/\omega & 1 & 1 \\ 0 & -1 & \gamma^{(1)} & \gamma^{(2)} \end{bmatrix}$$

$$\mathbb{M}_1 = \begin{bmatrix} 1 & 0 & \alpha^{(1)} & \alpha^{(2)} \\ q_{\text{in}}/\omega & 0 & -\beta^{(1)} & -\beta^{(2)} \\ 0 & q_{\text{in}}/\omega & 1 & 1 \\ 0 & -1 & \gamma^{(1)} & \gamma^{(2)} \end{bmatrix}$$

$$\mathbb{M}_2 = \begin{bmatrix} -1 & 1 & \alpha^{(1)} & \alpha^{(2)} \\ q_{\text{in}}/\omega & q_{\text{in}}/\omega & -\beta^{(1)} & -\beta^{(2)} \\ 0 & 0 & 1 & 1 \\ 0 & 0 & \gamma^{(1)} & \gamma^{(2)} \end{bmatrix}$$

$$\mathbb{M}_3 = \begin{bmatrix} 0 & 0 & \alpha^{(1)} & \alpha^{(2)} \\ 0 & 0 & -\beta^{(1)} & -\beta^{(2)} \\ q_{\text{in}}/\omega & q_{\text{in}}/\omega & 1 & 1 \\ 1 & -1 & \gamma^{(1)} & \gamma^{(2)} \end{bmatrix}$$

$$\mathbb{M}_4 = \begin{bmatrix} -1 & 0 & \alpha^{(1)} & \alpha^{(2)} \\ q_{\text{in}}/\omega & 0 & -\beta^{(1)} & -\beta^{(2)} \\ 0 & q_{\text{in}}/\omega & 1 & 1 \\ 0 & 1 & \gamma^{(1)} & \gamma^{(2)} \end{bmatrix}$$

Here $q_{\text{in}} \equiv \sqrt{\omega^2 - \mathbf{k}_\perp^2}$; the coefficients in the matrices above are defined by

$$\begin{aligned} \alpha^{(p)} &= \frac{(q^{(p)})^2 - \omega^2 A}{\omega^2 C_1} \\ \beta^{(p)} &= -\omega \frac{L_{31}}{q^{(p)}} - \omega \frac{L_{32}}{q^{(p)}} \alpha^{(p)} \\ \gamma^{(p)} &= -\omega \frac{L_{41}}{q^{(p)}} - \omega \frac{L_{42}}{q^{(p)}} \alpha^{(p)} \end{aligned} \tag{4.14}$$

where $p = 1, 2$ and also

$$q^{(p)} = q^{(\pm)} = \omega \frac{1}{\sqrt{2}} \sqrt{A + B \pm \sqrt{(A-B)^2 + 4C}} \tag{4.15}$$

with

$$\begin{aligned} A &= L_{14} L_{41} \\ B &= L_{23} L_{32} \\ C &= L_{14} L_{42} L_{23} L_{31} \end{aligned}$$

Finally, the elements L_{ij}, are defined in terms of the permittivity tensor as

$$\begin{aligned} L_{14} &= \frac{k_{z'}^2}{\omega^2 \varepsilon_\perp} - 1 \\ L_{23} &= 1 \\ L_{31} &= -L_{42} = (\varepsilon_\perp - \varepsilon_{||}) sc \\ L_{32} &= -\frac{k_{z'}^2}{\omega^2} + \varepsilon_\perp c^2 + \varepsilon_{||} s^2 \\ L_{41} &= -\varepsilon_{||} c^2 - \varepsilon_\perp s^2 \end{aligned}$$

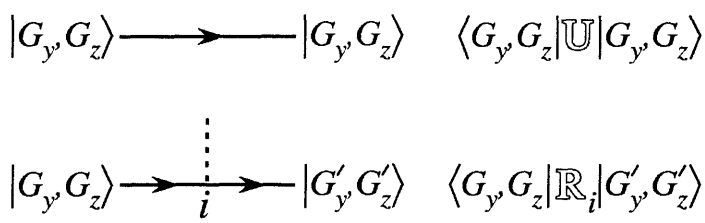

Figure 4-8: Feynman rules for the diagrammatic expansion of the Casimir energy, following Ref. 110. In our notation, planewave states are indexed by their reciprocal lattice vector $\mathbf{G}_\perp = (G_y, G_z)$; frequency, polarization, and the conserved reduced Bloch vector $\mathbf{k}_\perp$ are suppressed as our focus is on non-specular (i.e., $\mathbf{G}_\perp$ not conserved) reflections. Here $\mathbb{U}$ is the free-space translation matrix, and $\mathbb{R}_i$ the scattering matrix for object i (= 1, 2 for our case). Primes on the polarizations (e.g., y') denote distinct wavevectors.

A careful analysis shows that the equations eq. (4.14) become singular at $\phi = n\frac{\pi}{2}$ for integer n. In this case, we take the limit $\phi \to n\frac{\pi}{2}$ numerically.

Appendix 4B: Suppression of non-specular scattering

In this section we give a proof that non-specular scatterings (i.e., those not conserving the perpendicular wavevector $\mathbf{k}_\perp + \mathbf{G}_\perp$) are greatly suppressed for crossed slabs relative to aligned slabs. This explains the wide range of validity for the specular-reflection approximation for crossed slabs. The proof is a straightforward application of a recently-developed diagrammatic expansion for the Casimir force [110]. In this framework, the log det expression of eq. (4.2) is re-expressed as Tr log and expanded in a power series. Each term in the power series can be computed via a set of Feynman rules, shown in Fig. 4-8. For sufficiently large separations, this series is rapidly convergent.

Each scattering event is represented as the process $|G_x, G_z\rangle \to |G'_x, G'_z\rangle$, where G_x, G_z represent the perpendicular wavevector of the planewave. We suppress both the frequency and reduced Bloch vector $\mathbf{k}_\perp$ (which are both conserved in the scattering process), and the polarization p (which is not relevant to our analysis of non-specular

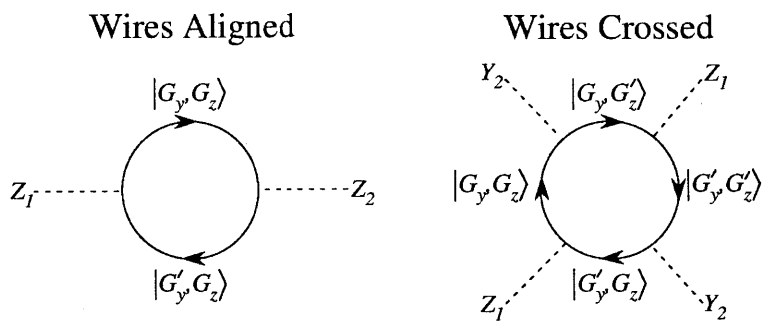

Figure 4-9: Lowest-order diagrams representing the contribution of non-specular scattering events to the Casimir energy, constructed using the rules of Fig. 4-8. Because we are measuring the energy of interaction between two objects, successive interaction vertices must involve different objects. On the left, when both objects 1 and 2 are directed along the z-axis, a non-specular event can occur in a 2-vertex diagram. However, when the wires are crossed, the lowest-order allowed non-specular process involves a 4-vertex diagram.

reflection). Each object is represented as a pair indicating the object alignment (Y, Z) and object index $(1, 2)$. The key point is that, due to translation-invariance, the scattering matrix for a Z object is proportional to $\delta\left(G_z - G'_z\right)$, and for a Y object is proportional to $\delta\left(G_y - G'_y\right)$. Further, the free-space propagator is diagonal in the planewave basis and thus conserves both G_y and G_z. Successive interaction vertices in a diagram must involve distinct objects as external insertions; therefore, for the crossed configuration, a planewave must scatter twice as many times to return to its original state in the lowest-order diagram relative to the aligned configuration. Example lowest-order diagrams are shown in Fig. 4-9. We find that for aligned (e.g., ZZ) slabs, the lowest order diagram involving non-specular reflection involves two vertices, while for crossed slabs it involves four vertices. Since each propagator represents an exponential attenuation, and each scattering event multiplication by a number of magnitude less than unity, this implies that non-specular interactions are greatly suppressed for crossed slabs.

Chapter 5

Casimir repulsion between metallic objects in vacuum

5.1 Introduction

In Chapter 3 we discussed attempts to use geometry to modulate the Casimir force, either by reducing its magnitude or switching it from attractive to repulsive. We explicitly demonstrated that neither of these were possible to any significant degree in the case of chiral metamaterials, and argued that in general metamaterials were a dead-end route towards these goals. In Chapter 4 we discussed how geometry can be used to switch the sign of the Casimir force, but only if the objects are separated by an appropriate fluid medium. The question remains: can the force between vacuum-separated metallic/dielectric bodies ever be repulsive? In this chapter, we demonstrate that the answer is *yes* by showing that *anisotropy*, in the form of an elongated particle above a plate with a hole, shown schematically in Fig. 5-1(a). The particle is unstable to displacements in the transverse direction and to rotations and therefore does not support stable levitation, consistent with Ref. 155. The result, originally concerned with the idealized case (in which the plate is perfectly thin, perfectly conducting, and the particle of infinitesimal size) follows from an elegant symmetry argument due to Michael Levin, which we briefly summarize in Sec. 5.2.1. This repulsive force is interesting in that it can neither be interpreted as arising (qualitatively)

from pairwise-additive forces [29,48,49,93,113] or from an effective-medium interpretation [99,133,176,178,214] (for other such exceptions, see Ref. 168); it is therefore truly *geometric* in origin.

We will demonstrate via numerical computations using both the FDTD and BEM that this effect extends to plates with finite thickness and non-ideal conductivity (e.g., gold) and particles of finite size in both dimensions, and obtain estimates for the strength of the repulsive force in these cases. We will examine in detail the effects of these non-ideal properties on the repulsive force, and we will find that under realistic assumptions on both the materials and the object dimensions this repulsive effect persists, but is very small in magnitude (on the order of 10 aN).

In Sec. 5.3 we will examine a modified system in which the particle is replaced by an anisotropic Rydberg atom, and the "repulsive" effect is manifest as an unusual level shift in the excitation spectrum of this atom, an idea that was proposed to our group by Simen Ellingsen. These level shift experiments are of much greater sensitivity to experimental measurements and are likely to detect effects of this magnitude. However, we will show that at present we cannot engineer a Rydberg atom with sufficient anisotropy to observe this effect, although this may be possible in the future.

To enhance the repulsive force (and demonstrate the power of our numerical techniques), in Sec. 5.4 we extend our analysis beyond the "dipole-regime" to systems in which the particle cannot be treated as a single dipole, looking at, e.g., rings of multiple particles and anisotropic cylindrical capsules (which can be thought of as composites of many individual anisotropic particles). In these cases, analytic dipole arguments can not be applied as they would not lead to a sensible upper bound on the force; for example, a simple additive approximation would predict an unbounded repulsive force as more particles were added, because a finite force results from a particle of infinitesimal transverse dimension. Therefore, accurate numerical techniques are crucial in order to obtain useful results. We find that under the same physical restrictions as Sec. 5.2 we can engineer a thousand-fold enhancement of the repulsive force. This enhancement, although quite significant, still only yields a net force of $\approx 10\,\mathrm{fN}$, which is still well over an order of magnitude below the current threshold of

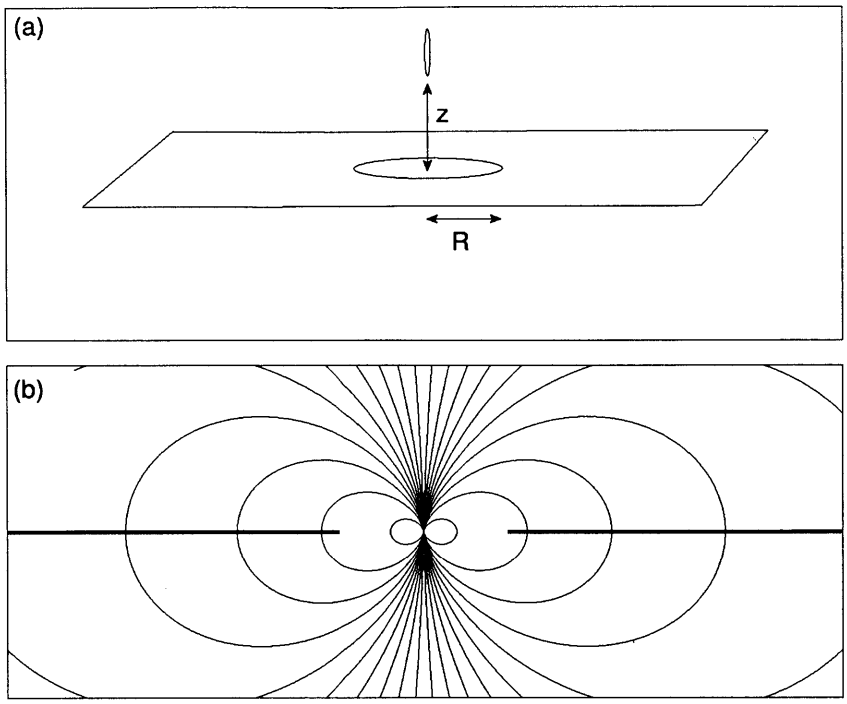

Figure 5-1: (a): Schematic (not to scale) of the idealized plate-particle configuration. An elongated metallic particle is centered above a perfectly thin metallic plate with a hole of radius R and width $W = 2R$. The particle is constrained to only move along the z axis and cannot rotate. (b): The key to the symmetry argument is that at $z = 0$, the electric field $\mathbf{E}$ of a z-directed dipole cannot couple to the thin plate, as $\mathbf{E}(z = 0) \cdot \hat{\mathbf{z}} = 0$.

detectability from AFM measurements [58]. Therefore, this effect remains primarily of theoretical, rather than experimental, interest.

5.2 Repulsion in the dipole regime

5.2.1 Symmetry Argument

In this section we briefly describe the symmetry argument that originally predicted a repulsive effect in the "dipole" regime of Fig. 5-1 (that is, when the plate is perfectly thin, and the particle an anisotropic point dipole). This argument is due to Michael Levin, which he had originally used to present an example in electrostatics in which a point charge can be *attracted* to its image on a non-planar conducting surface [100].

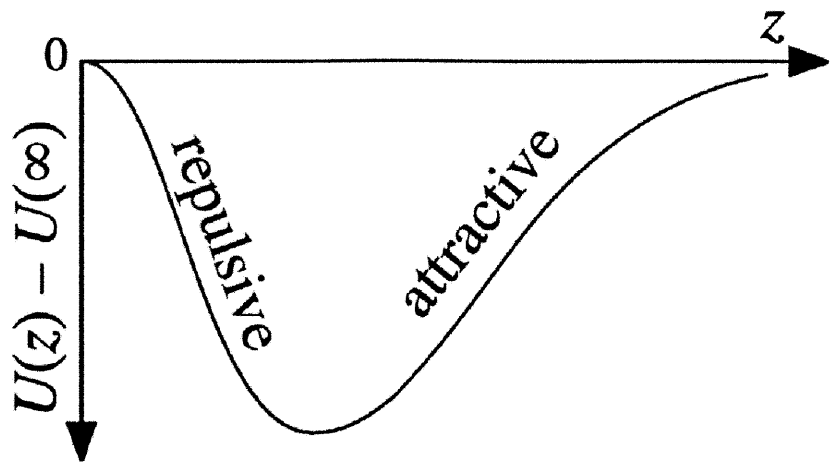

Figure 5-2: Schematic of the potential energy $U(z)$ relative to the energy at infinite separation $U(\infty)$ for the particle of Fig. 5-1. From Fig. 5-1(b), this quantity must be zero at $z = 0$. Furthermore, the force for $z \to \infty$ must be attractive, implying that $U(z \to \infty) - U(\infty) < 0$ with positive slope. The simplest behavior for such a function is shown here, implying a repulsive region around $z = 0$.

Applied to the Casimir context, the argument is as follows: assume that the particle in Fig. 5-1(a) is electrically polarizable only in the z direction (and has no magnetic polarizability) and is confined to the line $r = 0$ centered above the plate (so that the total force is parallel to the z-axis); the plate itself is perfectly conducting and perfectly thin. The Casimir energy $U(z)$ of the particle above the plate is due to charge fluctuations of the particle coupling to induced charge fluctuations of the plate. If the particle is removed to $z \to \infty$, we have $U(z \to \infty) = 0$ (we use this to set the zero of the energy). However, due to the symmetry of the dipole field at all frequencies ω [see Fig. 5-1(b)], the charge fluctuations of the particle at $z = 0$ cannot induce charges on the plate, implying $U(0) = 0$. Since the energy is a continuous function of z, and since the force for large z is attractive (implying that $\frac{dU}{dz} > 0$), $U(z)$ must have the behavior, illustrated in Fig. 5-2, in which its derivative changes sign at least once. Therefore, there is some region in z for which the force is repulsive[1].

The this prediction can be understood on more physically intuitive grounds from

[1]It is mathematically possible that, while for each frequency there exists a repulsive region, these regions are distinct for different ω and the net integral of the force over ω, for each z, gives a positive result. However, this turns out not to be the case.

an argument based on charge fluctuations in electrostatics, where we examine explicitly the $\omega = 0$ contribution to the Casimir force. This contribution is proportional to the classical electrostatic energy of a z-directed permanent electric dipole. This dipole induces charges in the plate; in the limit that the plate is infinitesimally thin, we can combine the charges on the two sides of the plate into a single surface charge density σ. On a qualitative level, we expect σ to be of the form shown in Fig. 5-3(a), with $\sigma > 0$ for small r and negative for large r. In particular, σ can be constructed as a superposition of dipoles in the $z = 0$ plane, oriented radially inward about the z axis. A simple calculation shows that the vertical force on a dipole at $(0, 0, z)$ from a horizontal dipole a distance r from the z axis is repulsive if $r > 2z$ and attractive if $r < 2z$. Thus, if the hole is circular with diameter W and $z < W/4$, all the dipoles will exert a repulsive force, resulting in a net repulsive force. On the other hand, if $z \gg W$, most of the dipoles will exert an attractive force, so the total force is attractive. In contrast, a dipole oriented *parallel* to the plate is always attracted, as can be seen from Fig. 5-3(b). This explains why an elongated shape is required for the repulsive effect (see Fig. 5-5 and Fig. 5-6): dipole fluctuations parallel to the plate give rise to an attractive Casimir force.

5.2.2 Non-ideal geometric effects

Moving beyond the idealized geometry of Fig. 5-1, we have a number of non-ideal effects to consider. The first is the finite size of the dipole particle: although repulsion must occur for some range of z, any elongated object must be displaced by half its length along z before we can genuinely claim a repulsive effect ("repulsive" effects have been previously examined for interleaved structures [170], however here we are only interested in the case of a separating plane between the two objects [2]). Second, any real particle will have a non-zero transverse (parallel to the plate) polarizability which, from the argument in Sec. 5.2.1, will always give an attractive contribution

[2]In order to maximize the repulsive effect, in Sec. 5.4 we will drop the requirement of a separating plane, but at this point we will have already placed the ideas behind the repulsive force on a firm footing

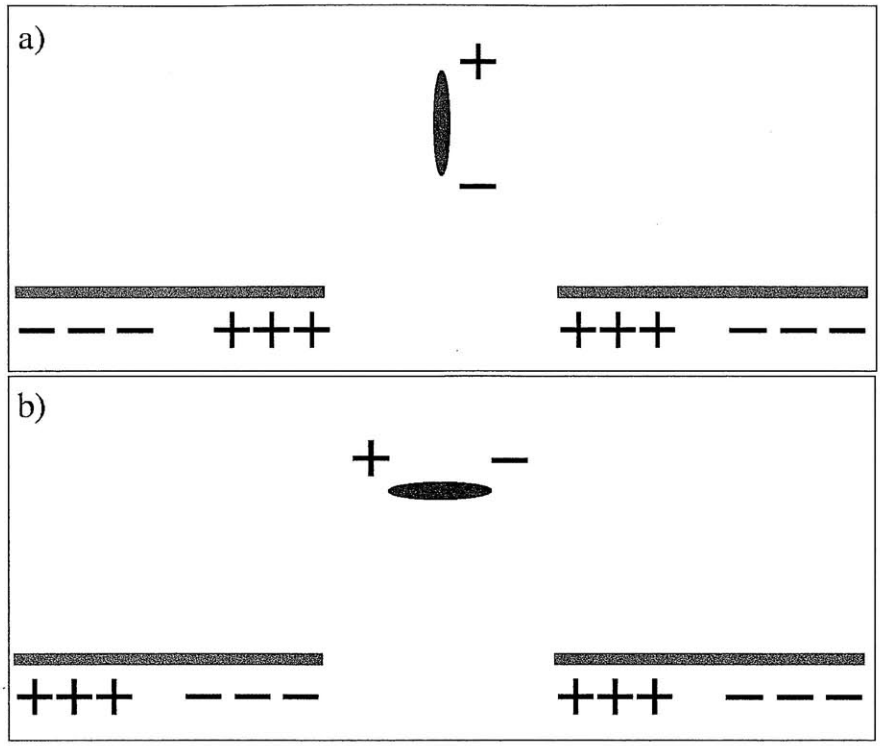

Figure 5-3: (a): Induced charges on a two-dimensional plate due to a permanent electric dipole (red) normal to the plate. Positive charges will cluster at the points closest to the dipole, attracted to the negative charge. This leaves a negative charge excess farther away from the center. (b): Induced charges when the dipole is parallel to the plate. Now the induced charges on the plate are antisymmetric, and it is clear that the energy of the dipole is lowest at $z = 0$, leading to an attractive force.

to the force. Third, any real plate will have a finite thickness, the effect of which is not obvious at this point (we will see in our numerics that this is in fact the most important non-ideal factor to consider). Finally, the symmetry argument applied to perfect conductors; the effect will have to be verified for objects with realistic material dispersion. In this section, we examine the effects of the first three non-idealities in two dimensions, using the boundary-element method (BEM) [161]. In our case, the 2d system corresponds to the transverse-electric (TE), $k_z = 0$ solution of the 3d field equations in a z-invariant geometry. The advantage of working with 2d-BEM is that this allows us to rapidly explore the parameter space, while giving qualitative insight into the physics of the system. We will incorporate all of these non-idealities into a full 3d calculation in Sec. 5.2.3.

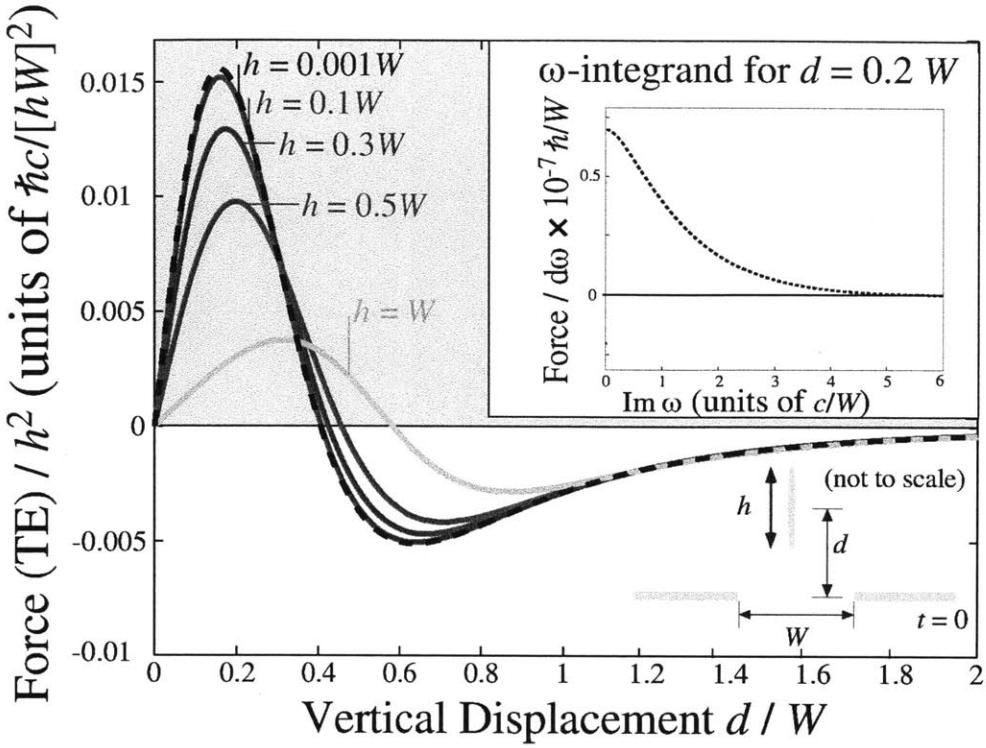

Figure 5-4: 2d force between a thin PEC plate and a perfectly anisotropic particle (i.e., no transverse dimension), scaled by the particle height h, as a function of vertical displacement d for a range of h. The shaded region in the main panel denotes a repulsive force. The scale-invariance of the force curve holds for $h < 0.1W$, but deviations become significant for $h \sim 0.5W$. Inset: force frequency integrand for $h = 0.001W$ at a fixed $d = 0.2W$, demonstrating that the repulsive effect holds at all frequencies for an idealized geometry.

We first examine the effect of a finite particle length h on the repulsive force, assuming zero transverse width, so that the particle is a perfect z-directed dipole in the $h \to 0$ limit. In the limit that h is much smaller than any length scale of the system (for a thin, perfectly conducting plate, the only length scale is W), we can describe the charge fluctuations of the object in terms of an effective point dipole. This is because higher-wavelength fluctuations must have wavelengths on the order h and will therefore couple to frequencies on the order of $1/h$; these frequencies will decay exponentially away from the dipole and therefore not couple to the plate in the $h \to 0$ limit. For a finite h, the polarizability of the effective dipole in 2d, $\omega \to 0$ limit is proportional to h^2. As the Casimir force couples linearly to the polarizability,

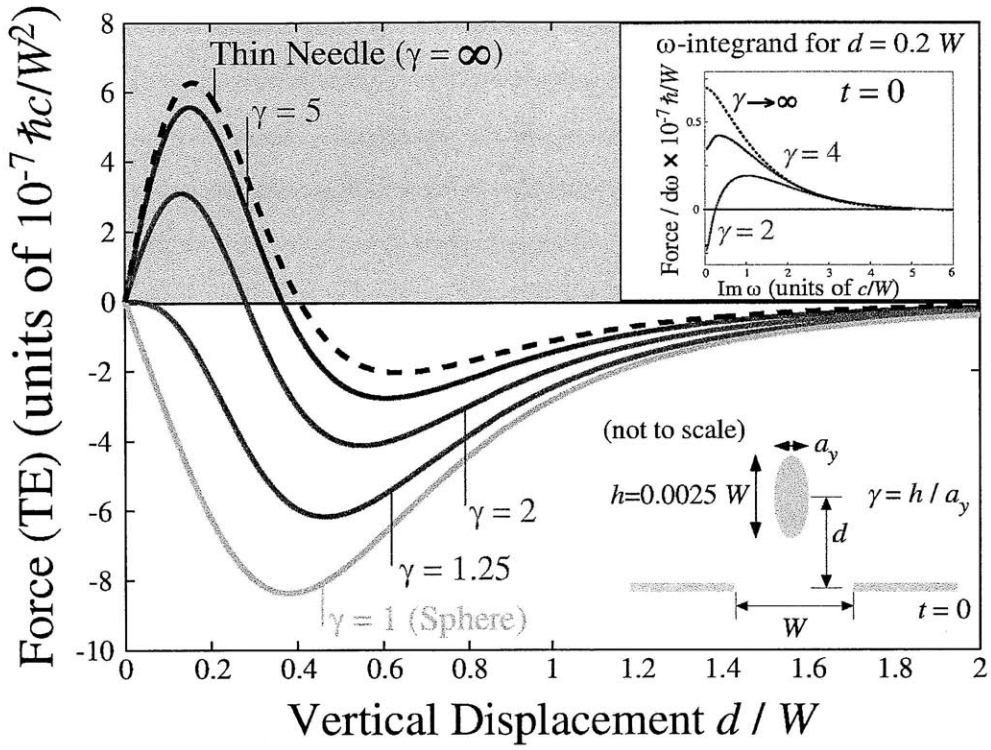

Figure 5-5: Dependence of the force on aspect ratio γ for a fixed particle height $h = 0.0025W$ and a perfectly thin plate $t = 0$. Decreasing γ always decreases the force. Inset: frequency integrand for three values of the force at a fixed $d = 0.2W$.

the entire force must be proportional to h^2. Therefore, for $h \ll W$ the force curve $F_h(d/W)(W/h)^2$ should be invariant. Numerical results for a range of h are shown in Fig. 5-4. As this is our first encounter with a repulsive force curve, we will pause for a few brief remarks. We first note that the repulsive region extends from $d = 0$ to $d \sim W/2$, which is in line with the prediction of Sec. 5.2.1. There is a point where the force changes sign from repulsive to attractive; this implies a stable equilibrium in z for a certain d. This is not in contradiction to the predictions of [155] as the force is unstable in other directions; we will examine this explicitly in Sec. 5.2.4. In Fig. 5-4, for $h/W < 0.1$, the force curve has collapsed to the point-dipole limit. As h increases, the relative repulsive force decreases until the effect finally disappears. As the actual force is scaled by h^2, there is some intermediate value (outside of the scale-invariant $h \ll W$ limit) for which the magnitude of the repulsive force is maximized; we will make use of this observation later in Sec. 5.4.2.

We now consider the effect of a finite transverse dimension a, varying the aspect ratio $\gamma \equiv h/a$ while fixing $h/W = 0.0025$. $\gamma \to \infty$ corresponds to the ideal anisotropic limit of Fig. 5-4. We show results in Fig. 5-5 for a number of values of γ ranging from $\gamma = 5$ to $\gamma = 1$ (corresponding to a sphere). For all values of the displacement d, decreasing γ decreases the repulsive effect, as would be expected from the argument of Sec. 5.2.1; by $\gamma \sim 1.25$ the repulsive force disappears entirely. The argument of Sec. 5.2.1 strictly applies only to the electrostatic case; it is interesting to examine the effect of finite γ on the force as a function of frequency ω. This is shown in the inset of Fig. 5-5, which compares the frequency integrand of the force for $\gamma = \infty, 4, 2$ with d fixed at $0.2W$. It can clearly be seen that the primary reduction in the repulsive force occurs at low frequencies, with higher frequencies unaffected. This can be understood by realizing that for a given wavelength, the transverse polarizability of the particle is strong whenever the particle is shorter than that wavelength, but is cut off when the particle is above that wavelength. Therefore, the value of a introduces a high-wavelength (low-frequency) cutoff on the attractive contributions of transverse dipole fluctuations.

Finally, we examine the effect of a finite plate thickness $t > 0$ in Fig. 5-6. In contrast to the dependence on γ above, we see a very strong dependence of the repulsive effect on t; for $t/W = 0.025$ the peak repulsive force is already cut in half, while for $t/W = 0.1$ the force is attractive at all separations. This has important implications for the design of repulsive forces below in Sec. 5.2.3 and Sec. 5.4, as it highlights the finite plate thickness as a critical geometric parameter for preserving the repulsive effect. We plot the frequency integrand of the force Fig. 5-6(Inset) with a fixed $\gamma = 4$ and $d = 0.2W$. In contrast to the finite aspect ratio case of Fig. 5-5, here we see the finite thickness acts as a *low*-frequency cutoff for attractive effects; that is, the non-ideal effects for $t > 0$ are strongest at high frequencies. Below in Sec. 5.2.3, we will see that this observation has the interesting consequence that gold materials with $t > 0$ can have a stronger repulsive force than PEC materials for the same geometry.

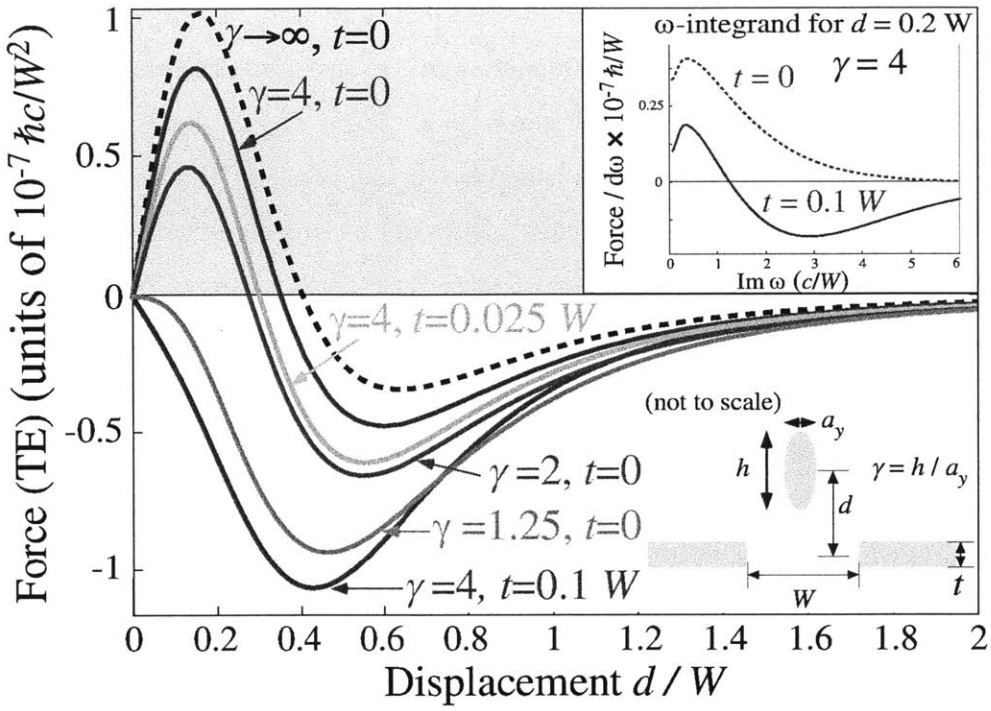

Figure 5-6: Combined thickness and aspect ratio effects on the repulsive force for fixed $h = 0.0025W$. Inset: frequency integrands for a perfectly thin $t = 0$ plate and a finite $t = 0.1W$ thickness plate, for fixed separation $d = 0.2W$ and aspect ratio $\gamma = 4$.

5.2.3 3d force predictions

We now examine the combined effects of the geometric factors of the previous section and non-ideal material dispersion, and make predictions on the repulsive effect for a reasonable 3d geometry. As the Casimir force increases with a decrease in the overall length scale, we would like to use the smallest dimensions possible to obtain an upper limit on the repulsive force; the minimal value of these dimensions will depend on both fabrication and material constraints. From Sec. 5.2.2, we see that the most important factor is the minimal value of t. We choose gold as our "non-ideal" material; for gold thin films, a reasonable minimal thickness (for which the film can be described by bulk models) is $t = 20\,\text{nm}$. Taking $W = 1\,\mu\text{m}$, we have $t/W = 0.02$; from Fig. 5-6, we expect that at this value of W finite-thickness effects will not dominate. We take the particle to be a cylinder of diameter $a = 20\,\text{nm}$ and height $h = 320\,\text{nm}$, giving $\gamma = 16$, which Fig. 5-5 indicates will not give significant attractive contributions; this

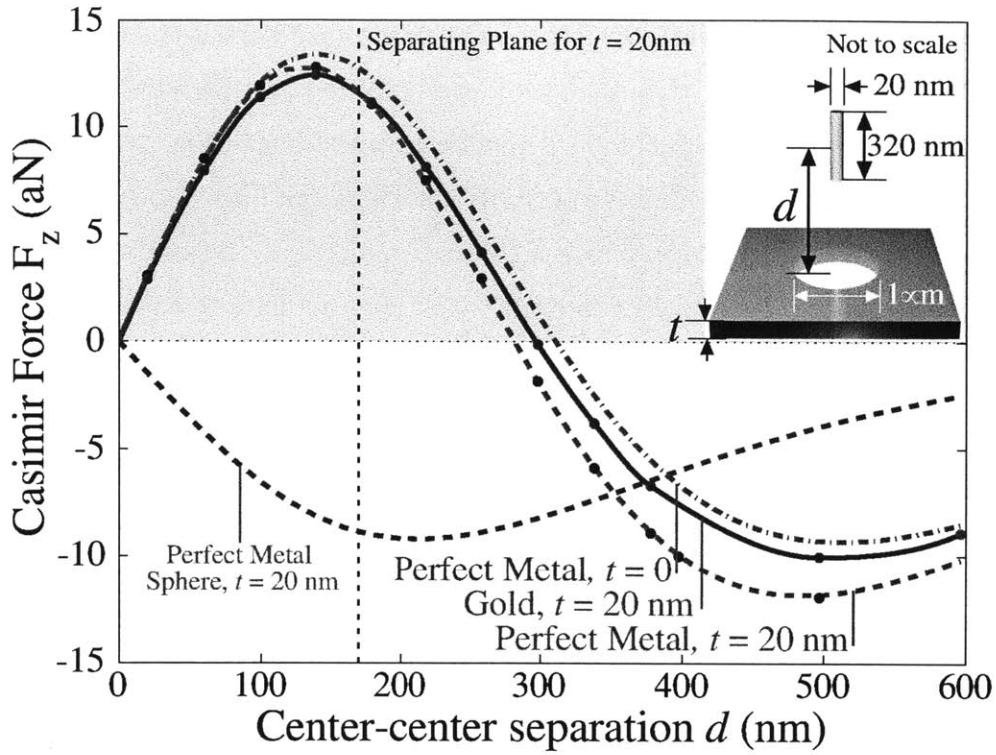

Figure 5-7: Repulsive forces in a three-dimensional geometry. The repulsive force holds for both $t = 0$ and $t = 20\,\text{nm}$ for both PEC and gold. The vertical dashed line at $d = 170\,\text{nm}$ indicates the location of a separating plane for all configurations. Interestingly, gold has a slightly stronger repulsive force, which is explained in the text. Shown for reference is the force for a 30 nm radius PEC sphere, which is always attractive. Inset: geometry used for the force computations.

plate-particle configuration is shown in Fig. 5-7(inset). For the permittivity of gold we use a plasma model[3] $\varepsilon(i\xi) = 1 + \omega_p^2/\xi^2$, where $\omega_p = 1.37 \times 10^{16}\,\text{rad/sec}$.

Fig. 5-7 shows the forces (in units of aN) for the configurations in this case. Also shown is the force for PEC materials with the same dimensions, as well as $t = 0$ for comparison. For reference, the force on a sphere (i.e., $\gamma = 1$) of diameter 60 nm is also included. The PEC configurations are computed using BEM, while the gold configuration is computed using FDTD, taking advantage of the optimization for cylindrical symmetry Sec. 2.5.3. We also repeat the PEC computations for $t = 20\,\text{nm}$ with FDTD as a check on both methods. As expected, the force for the sphere is

[3]A Drude model for gold is more realistic; however, the omission of the loss term, which is convenient for FDTD, does not significantly affect our results.

attractive for all d. By contrast, the forces for all anisotropic particles exhibit a region of d with a repulsive force. Because $h > 0$, the tip of the particle intrudes into the hole for $d < h/2 = 170\,\text{nm}$, denoted by a vertical dashed line in Fig. 5-7. However, there is a range of about 130 nm for $d > 170\,\text{nm}$ where the force is unambiguously repulsive: the two objects lie on opposite sides of an imaginary separating plane. As anticipated from Fig. 5-6, the PEC objects with $t = 20\,\text{nm}$ have a reduced repulsive effect compared to the $t = 0$ cases. Surprisingly, the gold objects exhibit a *stronger* repulsive force than the PEC case with the same geometry. This can be understood by recalling the behavior of the thick-plate frequency integrand for the force, from Fig. 5-6(Inset). The attractive contributions due to $t > 0$ come from high ξ; however the plasma frequency of gold acts as a high-frequency cutoff, implying that these attractive contributions are absent while the low-frequency repulsive contributions (which are not as sensitive to $t > 0$) are preserved.

The most significant feature of Fig. 5-7, however, is the scale of the y-axis - the repulsive forces are on the order of 10 aN. This presents a significant obstacle to the experimental detection of the repulsive force as most Casimir experiments have detection thresholds on the order of 1 pN [58]. The subjects of Sec. 5.3 and Sec. 5.4 below will examine possible avenues by which our setup can be modified to make experimental detectability more feasible.

5.2.4 Stability

Ref. 155 proved the impossibility of stable equilibria between vacuum-separated metallic/dielectric objects via Casimir forces alone. We had previously mentioned that the "stable" equilibrium in z of Fig. 5-7 at $d_0 \sim 300\,\text{nm}$ is not in conflict with this proof. The reason is that the point d_0 is actually a *saddle point* when embedded in the full phase space, which includes both transverse displacements r and rotations θ of the cylinder. We explicitly show this instability by plotting the *transverse* force as a function of r in Fig. 5-8 and the energy at $r = 0, d/W = 0.15$ as a function of θ in Fig. 5-9. In Fig. 5-8, it is clear that there is a strong lateral force for all $r > 0$; if the particle is displaced from the $r = 0$ line, this force will pull the particle further

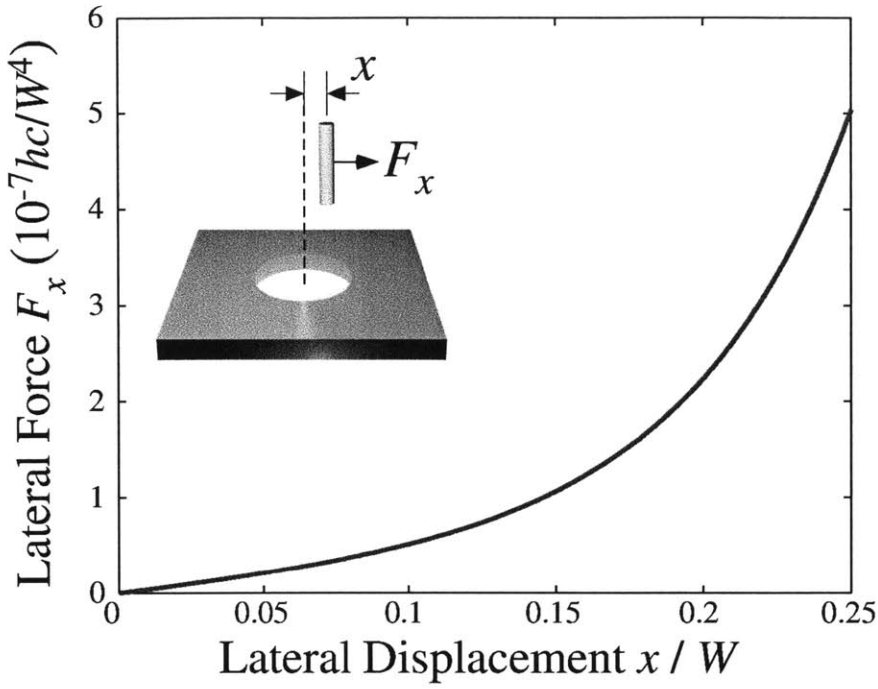

Figure 5-8: Transverse force on a small cylinder as a function of the lateral displacement r. For $r \neq 0$ the force is always away from the $r = 0$ axis, indicating instability in the transverse direction.

away. The instability in angular orientation (which is not guaranteed by Ref. 155) is due to the fact that the transverse component of charge fluctuations on the particle will couple more strongly to charge fluctuations of the plate. This is demonstrated in Fig. 5-9 by the fact that there is a potential minimum for $\theta = \pi/2$ (the particle is parallel to the plate), in which case the transverse polarizability of the particle is maximized. In this orientation, the particle will always feel an attractive force (since this corresponds to Fig. 5-5 with $a \ll 1$). Therefore, for the repulsive effect to become a true "repulsive" force, we must have confinement for both the transverse and rotational degrees of freedom of the particle. This is not unreasonable, since most actual measurements of Casimir forces between objects (which involve, e.g., an object mounted on a cantilever [27, 95, 130] or voltage-gated MEMS [219]) employ such confinements for their force measurements [4].

[4]Notable exceptions include the measurement of Casimir-Polder forces on a Bose-Einstein condensate [138], and measurements of *critical* Casimir forces [68] using total internal reflection microscopy

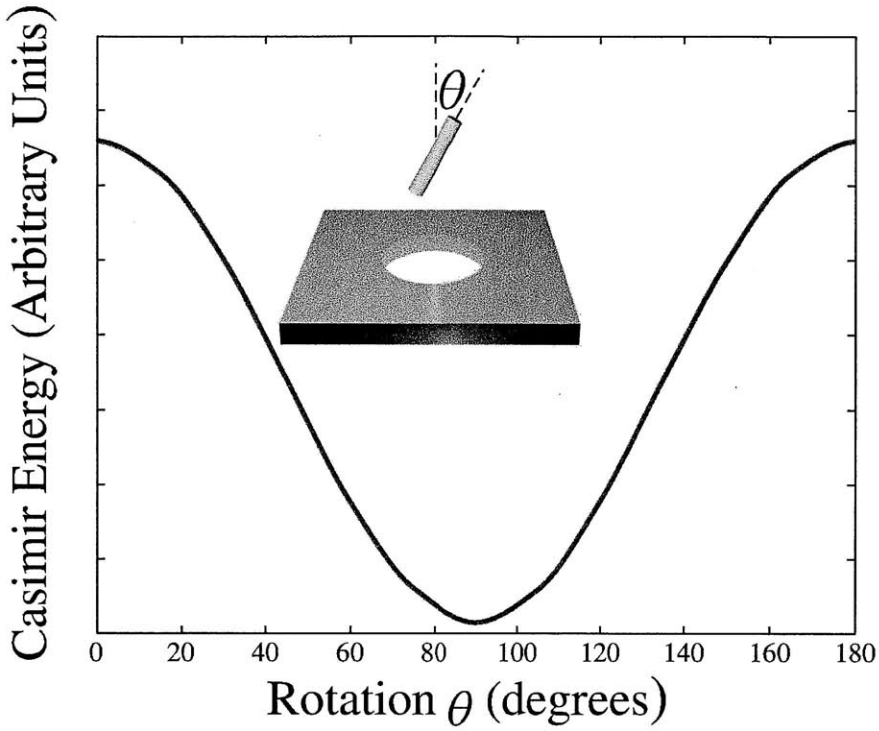

Figure 5-9: Energy as a function of rotation angle θ of the cylinder; the energy is at a relative maximum for $\theta = 0$, indicating that there is also an instability in θ. The energy minimum occurs at $\theta = 90°$ for which the dipole is parallel to the plate.

5.3 Casimir-Polder forces

As mentioned in Sec. 5.2.3, the forces in Fig. 5-7 are extremely small in magnitude; typical Casimir force thresholds are on the order of piconewtons. In the next section we will examine how the force can be raised closer to the level of detectability. However, before doing this we mention another possibility of observing a related case in which the PEC/gold particle is replaced by a Rydberg atom, an idea that was proposed to us by Simen Ellingsen, who has theoretically studied related effects. The basic physics revolves around the Casimir-Polder force, which is a specialization of the Casimir force to atoms [24]. In this case, the effect of quantum fluctuations is to alter the energy levels of the atom; as the spectrum of fluctuations depends on the position of the atom (e.g., the distance to a conducting plate), the energy levels of the atom will shift as it is moved. This implies a geometry- and position-dependent potential, termed the *Casimir-Polder* potential. The utility of this idea in our context is that

there exist highly sensitive spectroscopic methods to measure energy level shifts in atoms [46], and these can potentially detect much smaller perturbations than, e.g., AFM setups measuring Casimir forces. In fact, a recent theoretical proposal [16] claims to be able to realize *yocto*-Newton sensitivity in the near future. Therefore, it is worth examining the applicability of these techniques to the present system.

For the case at hand, Simen's work [32, 46] showed that the Casimir-Polder potential is given by:

$$U^{CP}(\mathbf{x}) = -\frac{1}{2}\sum_k \mathbf{d}_k \cdot \overleftrightarrow{\Gamma}(\mathbf{x}) \cdot \mathbf{d}_k = -\frac{1}{2}\sum_k \mathrm{Tr}\left[(\mathbf{d}_k \otimes \mathbf{d}_k) \cdot \overleftrightarrow{\Gamma}(\mathbf{x})\right] \equiv -\frac{1}{2}\mathrm{Tr}\left[\overleftrightarrow{\alpha} \cdot \overleftrightarrow{\Gamma}\right] \tag{5.1}$$

where $\{|k\rangle\}$ represent all atomic states, $\mathbf{d}_k$ is the dipole polarizability $\langle k|\mathbf{E}|\phi\rangle$, $|\phi\rangle$ the initial state (for a Rydberg atom this will not in general be the ground state), and the tensor $\overleftrightarrow{\Gamma}$ is related to the Green's tensor $\mathbb{G}$ via:

$$\overleftrightarrow{\Gamma}(\mathbf{x}) = \lim_{\omega\to 0} \omega^2 \mathbb{G}(\mathbf{x}, \mathbf{x}; \omega) = -\lim_{\xi\to 0} \xi^2 \mathbb{G}(\mathbf{x}, \mathbf{x}, i\xi). \tag{5.2}$$

Here $\mathbb{G}$ is the scattering part of the Green's function in the absence of the atom (e.g., for a single metallic plate). Note that although T does not appear in eq. (5.1), we have not assumed the zero-temperature limit; rather, these equations hold for both zero temperature and temperatures comparable to 300 K [46, 47].

Going back to Fig. 5-1, the interesting physics involves the decoupling of the thin plate from particle/atom dipole fluctuations along z. If, in the present case, we have $\overleftrightarrow{\alpha} \sim \mathrm{diag}(0, 0, 1)$, we will have the interesting effect that the energy shift due to $U^{CP}(\mathbf{x}) = U^{CP}(r, z)$ will vary non-monotonically in z, such that $U^{CP}(0, 0) = 0$. However, "natural" atoms are not particularly anisotropic; using an isotropic $\overleftrightarrow{\alpha}$ would yield the same effect as an $\gamma = 1$ aspect ratio in Fig. 5-5, implying a monotonic energy shift. A possible way around this difficulty, suggested by Simen, is to employ Rydberg atoms excited into anisotropic states [46]. Rydberg atoms are excited atoms of very high quantum number (e.g., Rb^{90}); as such, the spatial extent of their outermost electron orbitals is much larger than normal atoms, typically on

the order of microns [32]. This means that (1) the atom can interact with other objects over long ranges, and (2) the atomic polarizability is very large (being well-approximated by the free-electron polarizability). Finally, although Rydberg atoms are normally isotropic, they can be excited to angular momentum states that have an anisotropic polarizability [46]. Although these states are not long-lived, the level shift itself can be probed dynamically by examining the excitation spectrum of the atom using an incident laser. Therefore, both the excitation and measurement could be performed simultaneously. After some calculation, Simen found that the most promising excited state would be

$$\begin{aligned} |\phi\rangle &= |n, l=1, m=0\rangle \otimes |\uparrow\rangle \\ &= -\sqrt{\frac{1}{3}}|n, l=1, j=\frac{1}{2}, m_j=\frac{1}{2}\rangle + \sqrt{\frac{2}{3}}|n, l=1, j=\frac{3}{2}, m_j=\frac{1}{2}\rangle, \end{aligned} \tag{5.3}$$

where we have explicitly specialized to a spin-$\frac{1}{2}$ atom (e.g., Rb). For this state, the net dipole matrix $\overleftrightarrow{\alpha}_\phi$ is:

$$\overleftrightarrow{\alpha}_\phi \approx |\mathbf{d}_n|^2 \frac{1}{5} \begin{pmatrix} 1 & 0 & 0 \\ 0 & 1 & 0 \\ 0 & 0 & 3 \end{pmatrix}. \tag{5.4}$$

In this section we will present a preliminary study of this effect, in particular determining the feasibility of observing anything interesting using $\overleftrightarrow{\alpha}_\phi$. We compute the Green's function for the isolated plate-with-hole using the method discussed in Sec. 6.4 to extract scattering coefficients using BEM; the results are shown in Fig. 5-10. We plot the components Γ_{rr} and Γ_{zz} for $r = 0$ as a function of d for both a thin plate ($t = 0$). As expected, Γ_{zz} first increases as d decreases, and then goes back down to zero at $d = 0$, while Γ_{rr} increases monotonically as $d \to 0$. For comparison, the result for Γ_{zz} with no hole (which diverges as $d \to 0$ is shown - for $d/R < 1$ this is much larger than the plate with a hole.

We examine the effect of a nonzero plate thickness in Fig. 5-11; $t > 0$ attenuates the non-monotonic effect in Γ_{zz} while increasing the "attractive" Γ_{rr} component. It

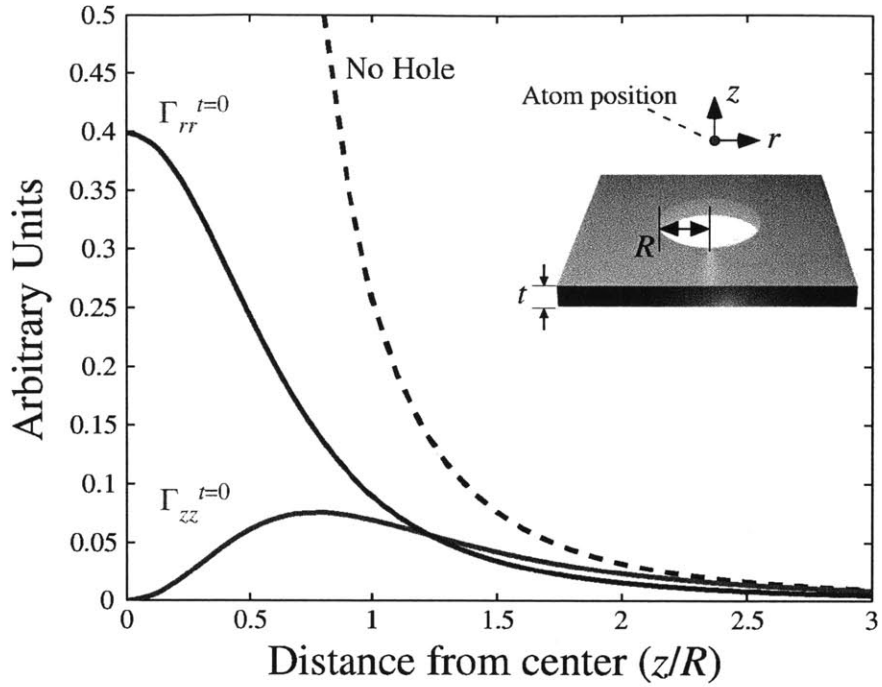

Figure 5-10: Different components to the Casimir-Polder energy: Γ_{zz} and Γ_{rr} of the tensor defined in eq. (5.2) as a function of vertical displacement d for the zero-thickness plate-with-hole. The Casimir-Polder energy is proportional to a weighted trace of the Γ tensor. For comparison, Γ_{zz} is shown for a metallic plate without a hole (black dashed line).

is clear that $t/R < 0.5$ is required (regardless of α) to observe any effect qualitatively different from a uniform plate.

Unfortunately, it is easy to see from the results of Fig. 5-10 that a 3:1 contrast in the polarizability (e.g., $\overleftrightarrow{\alpha}_\phi$) is not large enough for the non-monotonic effect of Γ_{zz} to overcome the monotonic effect of Γ_{rr}, this being due to its large magnitude relative to Γ_{zz}. Approximately twice this level of anisotropy is required before non-monotonic effects start to emerge. However, this may be possible in the future if more anisotropic excited states can be designed.

5.3.1 More Directions of Anisotropy

The main obstacle preventing us from observing a non-monotonic Casimir-Polder potential is the insufficient anisotropy of $\overleftrightarrow{\alpha}_\phi$. Due to the rotational symmetry

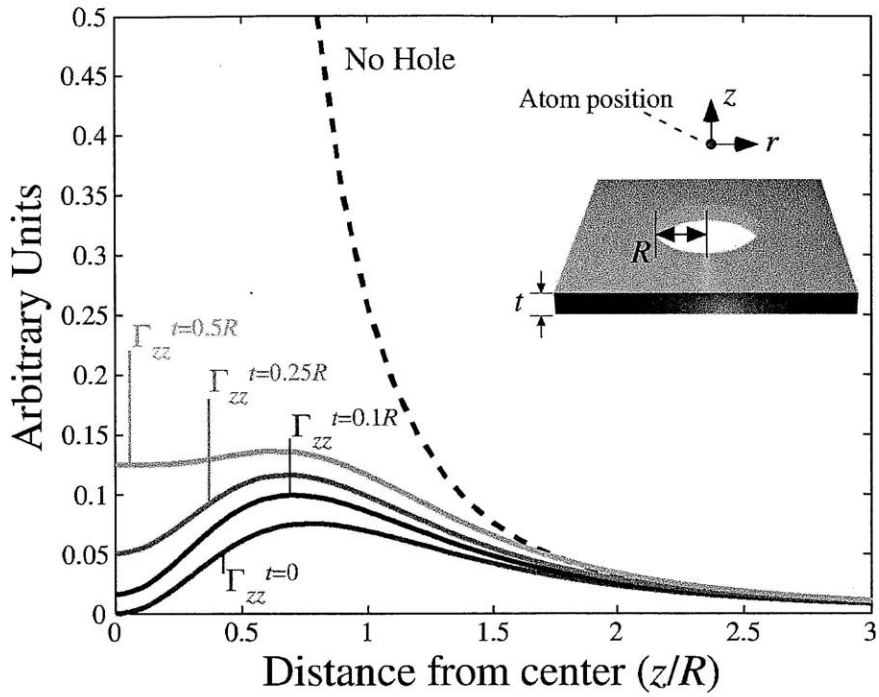

Figure 5-11: Casimir-Polder energy for an anisotropic atom: Γ_{zz} for different plate thickness t as a function of vertical displacement d. Finite thickness attenuates the non-monotonic effect on the Casimir-Polder energy. Shown for reference is the energy for a solid plate.

of the plate-particle geometry, the effective anisotropy of the particle is only 2:3. From Fig. 5-5, it is not surprising that an anisotropy this low should not contribute a strong "repulsive" effect. In order to investigate a possible route around this problem, we examined a configuration in which the effective anisotropy can be enhanced by breaking the rotational symmetry of the geometry. This new geometry is shown in the inset of Fig. 5-12; here the plate-with-hole is replaced by a thin cylinder with a gap along the z-axis. We examine this geometry using a symmetry argument similar to Sec. 5.2.1: assume that the cylinders have vanishing radius, and consider a particle that has only fluctuations in the y-direction. In this case, analogous to Fig. 5-3, the dipole symmetry of the system means that the particle can only couple to symmetric charge fluctuations of the cylinder (illustrated in Fig. 5-12[inset]). The nature of the electric field gradient is then analogous to Fig. 5-3, and we expect a repulsive force, implying a non-monotonic Casimir-Polder potential.

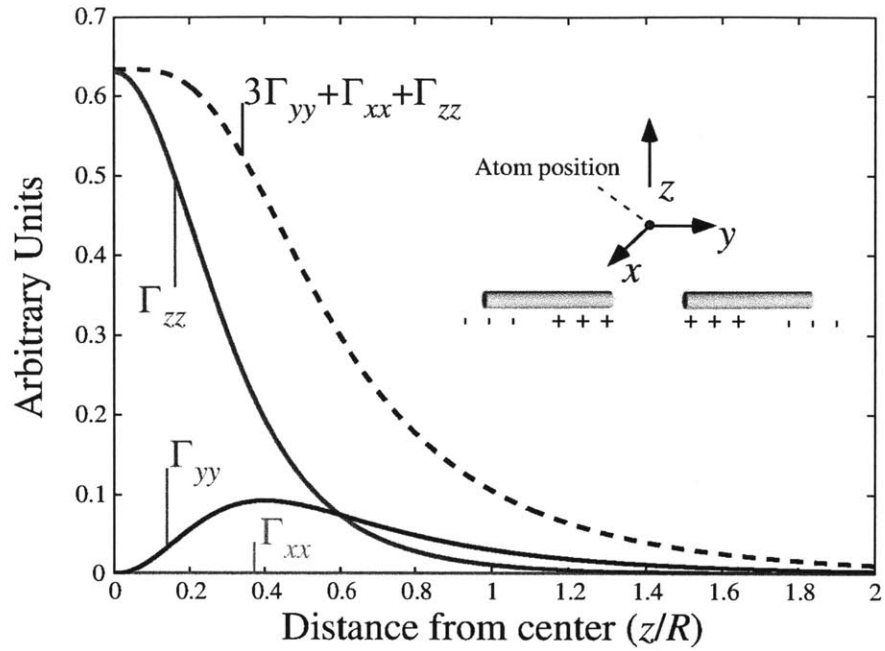

Figure 5-12: A more isotropic repulsive effect due to two cylinders: similar to Fig. 5-3, the induced charge density due to an electrostatic dipole polarized along the z-direction will yield a repulsive force for small z. In contrast to a plate-with-hole, one component (Γ_{xx} is zero, leading to a flattening of the total energy for a $(1,1,3)$ dipole.

The potential advantage of this geometry is that charge fluctuations of the cylinders in the x/y-plane will be strongly suppressed; this implies a greatly reduced coupling to the x-component of the particle's polarizability. Therefore, instead of a 2:3 effective polarizabilty, the suppression of one direction of transverse fluctuations implies, to a first approximation, a 1:3 effective polarizability. We plot exact results for the Casimir-Polder potential in the main part of Fig. 5-12; it is clear that the "repulsive" contribution Γ_{yy} in Fig. 5-12 has the same approximate form as the "repulsive" contribution from Γ_{zz} in Fig. 5-10, and similarly for the "attractive" contribution Γ_{zz}. However, the new feature is that the remaining transverse fluctuation term, Γ_{xx}, is much less than the other two terms and is effectively zero. The net Casimir-Polder potential is then proportional to $3\Gamma_{yy} + \Gamma_{zz}$, which is also shown in Fig. 5-12. As predicted by our symmetry argument, there is a more pronounced "flattening" feature of the Casimir-Polder potential near the origin in comparison to the plate-with-hole case (this flattening is not due to the finite width of the cylin-

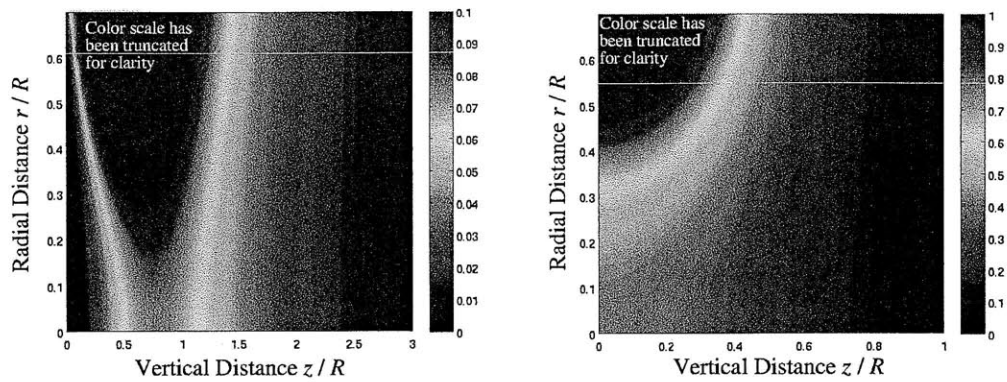

Figure 5-13: Casimir-Polder energy for off-axis displacements. Left: $\Gamma_{zz}(r,z)$ as both z and r are varied, for a $t=0$ plate. Right: $\Gamma_{rr}(r,z)$ for the same case. The striking feature is that Γ_{zz} is enhanced for off-axis displacements. This leads to an instability for an atom, but below we will see how this can lead to a genuine increase in the repulsive force.

ders, which is $0.02W \ll 0.2W$). However, the full Casimir-Polder potential remains monotonic.

5.3.2 Off-axis displacement

Before concluding our investigation of novel Casimir-Polder effects in our repulsive geometry, we take a moment to examine the full two-dimensional behavior $\Gamma_{jj}(r,z)$ of the Casimir-Polder terms in the plate-with-hole geometry; this behavior will be of great importance in the next section. Fig. 5-13 shows a 2d plot of $\Gamma_{zz}(r,z)$ on the left and $\Gamma_{rr}(r,z)$ on the right, both assuming a perfectly thin ($t=0$) plate. The primary difference is that, although $\Gamma_{rr}(r,z)$ increases monotonically as the particle-plate distance decreases [this distance is measured with respect to the point $(z,r)=(0,1)$], $\Gamma_{zz}(r,z)$ exhibits a relative maximum for each $r<1$ as z is varied. For $r=0$ this clearly corresponds to the relative maximum of Fig. 5-10. However, the surprising feature of $\Gamma_{zz}(r,z)$ is that this maximum is more pronounced for $r \neq 0$, implying that the "repulsive" effect is *enhanced* when the particle is displaced off-axis.

This enhancement does not strictly correspond to an enhancement of the repulsive force. From Fig. 5-13, it is clear that the derivative $\frac{\partial}{\partial r}\Gamma_{zz}(r,z) > 0$, implying an insta-

bility towards off-axis displacement; this is consistent with the discussion of Sec. 5.2.4. Furthermore, the attractive coupling to the lateral polarizability also becomes greatly enhanced for off-axis displacements. In the next section we will explore how to translate the enhanced repulsive effect into an actual repulsive force. We will combine this idea with the use of a "particle" that can no longer be well-approximated as a dipole, in order to determine how much the repulsive effect can be enhanced under physically reasonable circumstances.

5.4 Repulsion beyond the dipole regime

We now examine the repulsive effect when the anisotropic object can no longer be thought of as a point dipole. We show through numerical calculations that as the distance between the plate and central object decreases, there is an intermediate regime in which the repulsive force increases dramatically. Beyond this, the force rapidly switches over to attraction as the separation decreases further to zero, in line with the proximity force approximation. We demonstrate that this effect can be understood as a competition between an increased repulsion due to a larger polarizability of the central object interacting with increased fringing fields near the edge of the plate, and attractive forces due primarily to the nonzero thickness of the plate. In contrast to the previous results, it is essential to use a finite plate thickness from the beginning, because otherwise we will obtain divergent forces in certain cases. It is also essential to take interactions between, e.g., different cylinders into account (as otherwise we could fit an infinite number of perfectly thin cylinders into the hole and get an infinite repulsive force). We find that by replacing the single cylindrical particle with a ring of cylinders, or more generally an extended uniaxial conductor, the repulsive force can be enhanced by a factor of approximately 10^3.

We will address two questions: first, is repulsion limited to systems where one particle is very small or can it be obtained for two objects of length scales comparable to their separation; and second, is this repulsion necessarily weak (10 aN for a single particle) or can it theoretically be made stronger in comparison with other Casimir

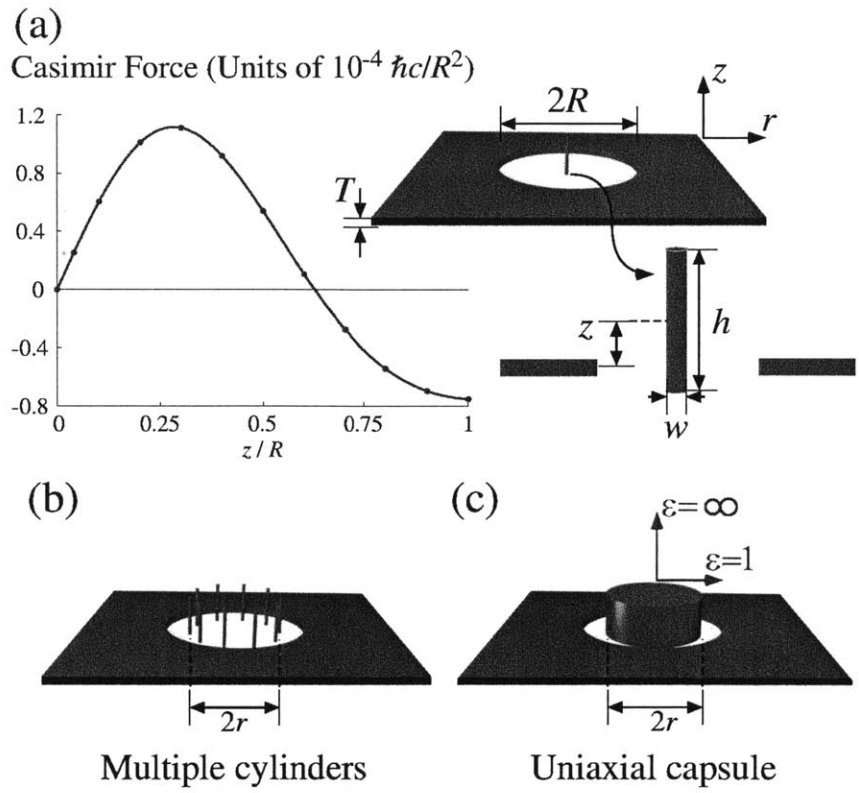

Figure 5-14: Configurations used in Sec. 5.4. *Top*: Reference configuration for comparison. *Top Left*: Geometry illustrating the single plate-needle configuration. *Top Right*: Casimir force vs. vertical height z for the configuration in the top left panel. Positive forces denote repulsion. *Bottom*: The two generalizations considered here: *Bottom Left*: Replacing a single cylinder with a ring of N (in the figure, $N = 10$) cylinders, each of which is more closely spaced to the edge of the hole. *Bottom Right*: An idealized version of the cylinder ring configuration, consisting of a cylinder of uniaxial conductance in the vertical (z) direction.

forces without simply shrinking the entire system (for perfect conductors, multiplying all dimensions by a scale factor a changes the force by a factor of $1/a^2$, but in actual systems there is a limit to the minimum achievable length scales). To answer these questions, we replace the single particle of Fig. 5-14(a) (in this case a circular cylinder of high aspect ratio) with a macroscopic array of identical particles [Fig. 5-14(b)], effectively forming a capsule of uniaxial conducting material [Fig. 5-14(c)]. To understand the mechanism behind this enhancement, we separately consider the repulsion as a single cylinder is displaced off-axis as well as the screening interaction when multiple cylinders are combined. For a single cylinder we find that there is

an optimal off-axis position where the repulsion is enhanced (up to 50 times) due to the presence of strong fringing fields. The presence of this optimal position is a consequence of the competing repulsive and attractive effects of fringing fields and proximity-force approximation (PFA) [41] interactions, respectively. As the cylinder is brought closer to the plate, the PFA forces take over and the repulsion vanishes. The Casimir force is non-additive, and the total force between the array of cylinders and the plate will not simply be a sum of the forces between the individual cylinders and the plate. However, we find that the non-additive contributions (or screening effects) associated with the presence of multiple cylinders are surprisingly small: the enhancement does not saturate until there are dozens of cylinders with separation significantly smaller than the cylinder length. We furthermore find that this repulsion persists when realistic conductivities are included, and when the capsule is anchored to a substrate by via a long oxide post. Although substantial experimental challenges remain in fabricating this particular structure, these results, combined with previous work on effective uniaxial/anisotropic media [82, 121, 133, 165, 185, 199] suggests that strongly anisotropic metamaterials offer new opportunities to achieve exotic Casimir interactions.

An obvious way to increase the absolute magnitude of the force would be to shrink all dimensions of the system uniformly by a scaling factor a—for perfect conductors, the force will scale as $1/a^2$ by dimensional analysis. However, for real materials there is a lower limit to the dimensions that can be achieved before material effects (e.g., the skin depth for gold) become important. For the present case, the most important geometric parameter is the thickness T of the plate, which must be nonzero for any physical configuration—we expect that T should be larger than the skin depth of gold in order for our analysis to be valid. As in Sec. 5.2, setting, e.g., $T \sim 20\,\mathrm{nm}$ as an optimistic lower bound on a real plate thickness constrains the minimal value for R, and hence the overall force magnitude.

The basic principle of repulsion in this system lies in the charge fluctuations of the plane decoupling from fluctuations of the needle at $z = 0$. Then when considering more general geometries we should have in mind a cylindrically-symmetric object of

conductivity primarily along the z-axis, which is our motivation for considering the configurations of Fig. 5-14 (c,d). In both cases, due to the close contact between the center object and the edge of the plate, it is essential to account for finite-size effects, making analytic or semi-analytic calculation difficult. Furthermore, in the presence of a thick plate we cannot rely on a general symmetry argument to guarantee repulsion for any range of parameters. As a result, the results of this work are entirely numerical; we employ both BEM and FDTD for our results. For simplicity, we primarily assume perfectly-conducting materials, and we further drop the requirement of a separating plane between the two objects (while still requiring that the cylindrical object be more than halfway out of the plane, so that the "repulsion" is not due to a trivial redefinition of coordinates). Additionally, to make a fair definition of "enhancement", we work within geometric constraints for the plate similar to Sec. 5.2.

5.4.1 Enhancement of fringing fields

The repulsive forces arise from fringing fields due to the sharp edges around the hole of the plate; this holds for both perfectly thin ($t = 0$) and thicker plates. Drawing on our intuition from electrostatics, for any fixed plate geometry we suspect that these fields are greatly enhanced as the plate edges are approached (i.e., $r = |\mathbf{r}| > 0$); we saw a confirmation of this in the Casimir-Polder regime in Fig. 5-13. If the plate thickness is *a priori* fixed, it is possible that this enhancement of the fringing fields leads to an enhanced repulsive effect for some range of r. Because the repulsive force is unstable in the transverse direction, a single cylinder displaced by $r > 0$ will experience a strong (attractive) radial force; to compensate for this, we would need to include, e.g., multiple cylinders displaced symmetrically about $r = 0$ to make the net radial force zero. However, to understand the effects of the fringing fields alone it is more illuminating to first consider the z-component $F_z(r, z)$ of the Casimir force, as a function of r and z, between a *single* cylinder at position (r, z) and a *thin* ($t = 0$) plate, as depicted in Fig. 5-15 (Inset). For definiteness, the cylinder is taken to have height $h = 0.64R$ and width $w = 0.04R$ (the same units as in Fig. 5-7). In this case, the plate is taken to be a circular annulus of inner radius R and outer radius $8R$, the

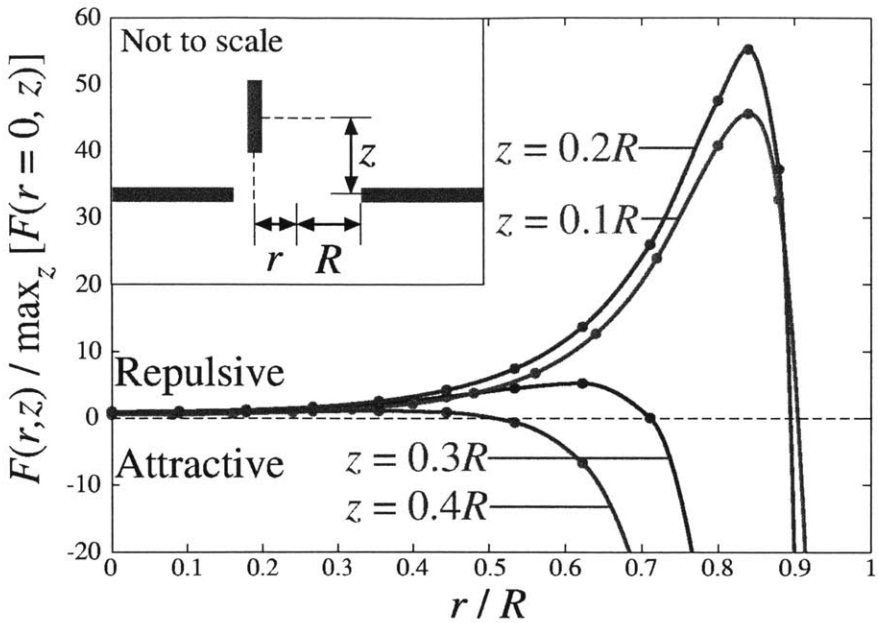

Figure 5-15: The effect of fringing fields on F_z, the z-component of the Casimir force for a single metallic cylinder: for a fixed z, F_z is enhanced as r increases. Plotted above is F_z for several values of z/R, normalized by the maximum of the repulsive force ($0.0278\,\hbar c/R^2$) for $x = 0$. As $r \to R$, F_z undergoes a very strong enhancement, peaking at approximately 55 for $r \sim 0.8R$ and $z = 0.2R$. For every z, as x increases pairwise attractive forces take over and F_z switches sign (note that for $r \neq 0$ there is an attractive force F_x between the cylinder and the plate edge, so the total Casimir force is not strictly repulsive in this case). Shown for reference in the inset is F_z (in units of $\hbar c/R^2$) at $r = 0$.

latter being large enough to eliminate finite-size effects on the force.

The results, computed with BEM, are shown in Fig. 5-15, where all dimensions are given in units of R. As our goal is to examine the force relative to the $r = 0$ case, we normalize the force results by the peak repulsive force along the z-axis, i.e., $F(r,z)/\max_z[F(r = 0, z)]$. Moving away from $r = 0$, we find that this ratio is consistently larger than 1 for all z plotted. This increase can be quite large (up to 55 times larger) before the force rapidly switches sign to attraction. We propose the following explanation for this effect: as $r \to R$, the fringing fields of the thin plate, which are induced by dipolar charge/current fluctuations of the cylinder, grow without bound. This leads to an enhanced plate-dipole coupling with increasing r, which for fixed z should lead to an enhanced repulsion if the force at that z is repulsive

for $r = 0$. However, when the cylinder-plate separation becomes comparable to the cylinder height h, higher-order (i.e., non-dipolar) currents on the cylinder will begin to contribute to the energy. As these higher-order multipole currents are not bound by the dipolar symmetry argument of Sec. 5.2.1, we expect their contribution to the force to be attractive in general. With this interpretation, the force curves of Fig. 5-15 show a competition between the contribution of dipole currents on the cylinder, which is repulsive for certain z and grows without bound as $r \to R$, and the contributions of higher-order cylinder currents which are attractive and grow more rapidly than the dipole term as $r \to R$.

This argument is supported by the results of Fig. 5-15, and raises a further interesting theoretical question: is it possible to *increase* the repulsive effect by *decreasing* the size of the cylinder (while keeping its aspect ratio constant)? The motivation for this is that a smaller cylinder can be brought closer to the edge of the plate before higher order currents contribute (attractively) to the force, therefore taking greater advantage of the increased fringing fields and leading to a larger repulsive net force. (Note that this does not violate PFA, because whenever we have repulsion we are assuming h is always comparable to the surface-surface separation.) Numerical computations (see below) support this argument; however, a rigorous analysis is of course required to confirm this. As this is of course an unphysical limit, we will not perform such an analysis here. Rather, we simply use this observation to illustrate that it is crucial to account for the finite thickness t of the plate: once $R - r \sim t$, a cylinder of any size will induce higher-order currents on the plate, which will also lead to attraction. A non-zero value of t must therefore be set in order to obtain physically meaningful force bounds.

We now consider the more realistic case of the force between a cylinder an a finite thickness ($t > 0$) plate in Fig. 5-16. In light of the argument presented above, we also study the effect for several values of h. On a technical note, use of the boundary-element method requires that the size of the mesh used to discretize the surfaces be smaller than any characteristic separation. However, now that $t > 0$, we must place two copies of the annulus used above within a distance t of each other. As $t \ll R$,

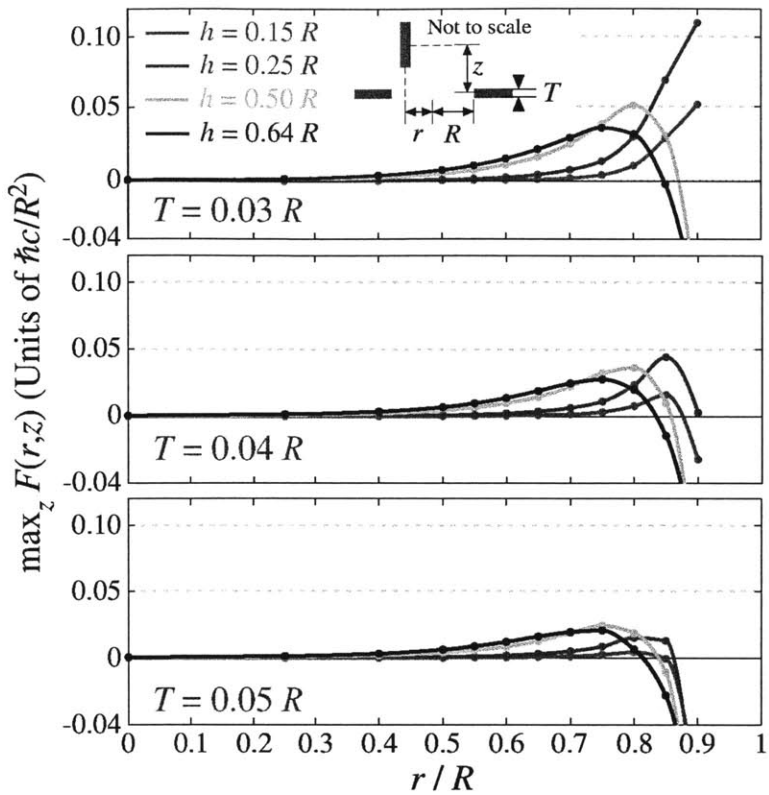

Figure 5-16: The effect of plate thickness on the Casimir force on a single cylinder. For each panel, the plate thickness is fixed and the Casimir force (maximized over $z > 0$) on a single cylinder is plotted as a function of x. The force for different values of cylinder height h are shown (for each h, the aspect ratio of the cylinder is fixed). For small t (Top), decreasing the cylinder size can actually lead to an increased repulsion for $x \sim R$. Increasing t (Middle and Bottom) leads to a decreased repulsion for all cylinders at all x, but the effect is strongest for small h cylinders.

this requires a much denser mesh than used above in the thin plate case. Roughly, the number of surface mesh elements will scale as t^{-2}, so that the overall spatial and temporal resource requirements scale as $\sim t^{-4}$ and $\sim t^{-6}$, respectively [162]. Due to this rather steep scaling, we find that for the range of t considered here an annulus with outer radius of $8R$ proves too computationally demanding. To reduce the overall number of surface mesh elements, we truncate the outer radius at $1.6R$ instead; although there will now be finite-size effects, we estimate their effect at well below 10% of the total force in all cases. We examine three plate thicknesses $t/R = 0.03, 0.04, 0.05$ and five different values of h/R. For each cylinder value of h,

the corresponding cylinder width is chosen to as to keep a constant cylinder aspect ratio. The results are shown in Fig. 5-16; to simplify the presentation, for each t we plot only the maximum repulsive force force $\max_{z>0} F_z(r, z)$ for each r. The top panel of Fig. 5-16 supports the argument given in the previous paragraph: although for most values of r, $h = 0.64R$ gives the largest repulsive force, as $r/R \to 1$, cylinders of progressively smaller size exhibit a stronger repulsion. (Although we expect that the limits $h \to 0$, $r/R \to 1$ and $t \to 0$ can be taken in such a way as to make the peak repulsion unbounded, numerical limitations make computation of forces with $r/R > 0.9$ difficult.) On the other hand, as t increases the attractive contributions of higher-order plate currents turn on at progressively smaller r. Further, this effect is strongest for the small-h cylinders, as shown by successive panels of Fig. 5-16. For example, by $t/R = 0.04$ the force curves for $h < 0.25R$ now show attraction by $r = 0.9R$, and for $t/R = 0.05$, the cylinders with $h/R \sim 0.5$ now show the strongest repulsive effect when maximized over all r. In contrast to the strong t-dependence of the force for small h, for $h = 0.64R$ the results are quantitatively altered (approximately 50%), but the order of magnitude of the repulsive effect remains. On the basis of this, we conclude that for the range of thicknesses we are interested in, the best value of h/R is in the range $h/R \sim 0.5$.

5.4.2 Multiple cylinders and uniaxial capsules

Previously, we found that the repulsive force is greatly enhanced as a cylinder is brought close to the edge of a plate—how close depended on both the cylinder height h and the plate thickness t. It is reasonable to assume that this effect should be enhanced if multiple cylinders are now added, bearing aside non-additive cylinder-cylinder interactions. In particular, if N cylinders are spread about a ring of radius r, one expects that for N not too large the repulsive force should scale linearly with N. As N increases, cylinder-cylinder interactions will take over. In Sec. 5.4.2, we will examine this behavior in detail. We find that the non-additive cylinder-cylinder interactions simply lead to a saturation of the repulsive effect, and that the value of N at which this occurs is quite high, leading to a large force enhancement. In

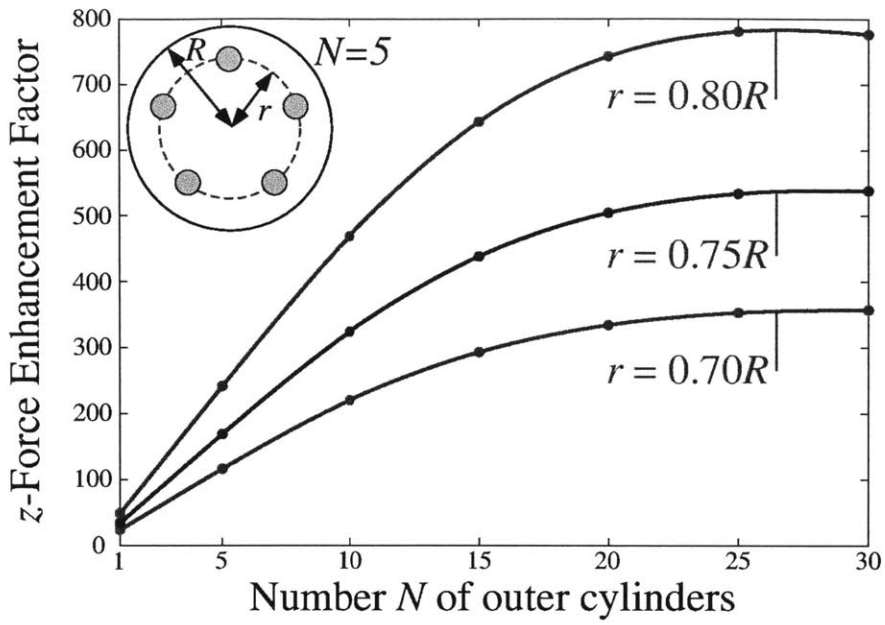

Figure 5-17: Enhancement of Casimir repulsion with a a realistic geometry (Fig. 5-14, Bottom Left): in place of a single cylinder, a ring of N cylinders is placed at radius r (shown for $N = 5$ in the inset). The cylinders have height $h/R = 0.64$, and for computational tractability the plate thickness t is zero. For small N the force increases linearly, with slope corresponding approximately to the magnitude of enhancement of Fig. 5-15. As N increases, the effect saturates. As in previous figures, the force is maximized over z.

the limit of large N, it is appropriate to replace the ring of cylinders with a homogeneous cylindrical capsule of uniaxial conductivity Fig. 5-14(d). This is examined in Sec. 5.4.2, and allows us to obtain an upper bound for the repulsive force in our system. In addition, as these systems have rotational symmetry, the net force is along the z-axis and there is no longer an attractive radial component.

Multiple cylinders

We examine the effect of multiple cylinders with BEM simulations. Due to the computational limitations in BEM for a plate of finite thickness, we cannot directly simulate multiple cylinders next to a thick plate. Instead, we utilize the fact (see Fig. 5-16) that a cylinder of $h = 0.64R$ is not strongly affected by a finite but small slab thickness and perform BEM simulations for a thin plate instead. We expect that these

results will still be approximately valid for plate thicknesses $t \lesssim 0.05R$. The results of these computations are shown in Fig. 5-17 for three values of ring radius r/R. For small N, the z-force increases approximately linearly, with the slope roughly corresponding to the size of the enhancement factor for a single cylinder in Fig. 5-15 (red curve) for the value $x \sim r$. As N increases, non-additive cylinder-cylinder interactions become important, and this linear enhancement eventually saturates. However, it is interesting that this saturation does not occur until fairly large N, at which point the peak enhancement factor is $\sim$ 800 for $r = 0.8R$ (larger r exhibit weaker repulsion, in line with Fig. 5-15). Further, it is interesting to observe that increasing N past this saturation point does not have an appreciable effect on the force: the additional cylinders are simply screened, and net repulsive force is practically unchanged. Additional calculations (not shown) for thinner cylinders show very similar values for the peak repulsion, with saturation after this peak. This leads us to believe that the ideal uniaxial capsules, shown in Fig. 5-14 (d), are actually a fairly good approximation to the more realistic configuration of many cylinders considered here. The advantage of the uniaxial capsules, examined in the next section, is that we can easily simulate them in FDTD and incorporate the thick plate, which as stated before is crucial for obtaining a realistic bound on the repulsion.

Uniaxial capsules

The basic mechanism of the repulsive effect relies on combining fringing fields with objects of high, anisotropic conductivity. Until this point, this anisotropy has been realized via the shape of the objects. However, as argued in the previous section, the limit in which the cylinders are allowed to become arbitrarily narrow and densely packed is well-defined and furthermore seems to be a good approximation to the finite-sized cylinder configurations considered previously. In this limit, the cylindrical ring is replaced by a cylindrical capsule of homogeneous material with uniaxial conductivity along the z axis: $\varepsilon(i\xi) = \mathrm{diag}(1, 1, \infty)$. The capsule has a height h, outer radius r, and (for generality) inner radius r'; see Fig. 5-14 (d). Although we cannot simulate anisotropic materials with our boundary-element method, they can easily be treated

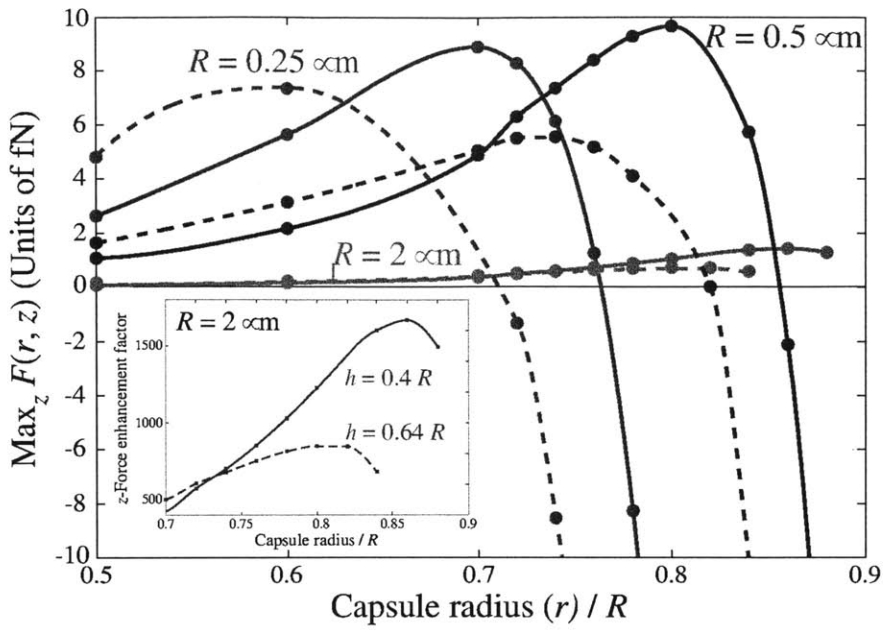

Figure 5-18: Forces (maximized over z) for a thick cylindrical capsule composed of uniaxial conductor (Fig. 5-14, Bottom Right). In contrast to previous figures, here the plate thickness is fixed to $t = 20\,\text{nm}$ and the hole radius R is varied to three different values. For each R, the force is computed, as a function of capsule radius r, for capsule heights $h = 0.5R$ (solid lines) and $h = 0.64R$ (dashed lines). *Inset*: z-force enhancement factors as a function for both values of h for $R = 2\,\mu\text{m}$, which approximates a thin plate. The maximum force is approximately 10 fN.

with FDTD [119, 172]. This has the advantage that finite-thickness plates can be incorporated with no additional computational cost, and we can also exploit the cylindrical symmetry of the configuration to make the problem two-dimensional. In general the inner radius r' can be non-zero. However, we examined the difference in the force on a capsule as the inner radius r' is varied, and it turned out that this has almost no effect (less than 1%) on the force - the inner conducting material is almost, if not entirely, screened from the field of the plate. Therefore, without loss of generality in the following we set $r' = 0$ and consider solid cylinders only.

In the previous sections, we argued that the enhancement of Casimir repulsion in between the point dipole and PFA regimes is due to two effects - the increased size of the center object, and the increase in the fringing fields of the plate. We did this by separately examining each effect in turn. We are now in a position to examine the full

combination of these effects, primarily to obtain an approximate upper bound on the possible strength of the repulsive effect assuming a fixed plate thickness t. To preserve contact with our previous work Ref. 101, in this section we fix our units so that $t = 20\,\text{nm}$ in all cases. From the results of previous sections, maximizing the repulsion over the remaining parameters (hole radius R, capsule radius r, capsule height h–here it is understood that we have already maximized over vertical displacement $z > 0$) will yield a finite peak repulsion. To simply the presentation, we will write both h and r in units of the hole width R, so that only the radios h/R and r/R are relevant. Then for fixed h/R and r/R, as R is varied (keeping $t = 20\,\text{nm}$ always) we expect the force to scale as R^{-2} for $R \gg t$; as R decreases further, we expect the effect of $t > 0$ to overwhelm the R^{-2} scaling at some point, leaving an optimal value of R for each h/R and r/R. From the results of the previous section, we expect that examining both $h/R = 0.4$ and $h/R = 0.64$ will give a good estimate for the maximum force enhancement. For these two values, we consider three values of R, such that $t/R = 0.0025, 0.01$, and 0.02 (corresponding to $R = 2\,\mu\text{m}, 0.5\,\mu\text{m}, 0.25\,\mu\text{m}$, respectively). In Fig. 5-18 we plot the force for these six configurations as a function of capsule radius r. The case $R = 2\,\mu\text{m}$ is nearly indistinguishable from the thin plate case. To make contact with the results presented in previous sections, we plot the enhancement factor in the force for this case in the inset of Fig. 5-18. For $h/R = 0.64$, we get an enhancement similar to the previous section with multiple cylinders, while for $h/R = 0.4$ this factor is ~ 1600. Of course we know from previous results that this value can be made arbitrarily large; if we are to fix the plate thickness, we should consider instead the absolute magnitude of the repulsive force. When this is done, we see that going from $R = 2\,\mu\text{m}$ to $R = 0.5\,\mu\text{m}$ yields a further enhancement factor of 6, whereas for the $t = 0$ case it should be 16. When R is further decreased we see a decrease in the force for $h/R = 0.5$, and only a slight increase for $h/R = 0.64$. Further decreases in R (not shown) lead to a decrease in the force for both h. We see that although the enhancement factor for $R = 2\,\mu\text{m}$ is much larger for $h/R = 0.4$ than $h/R = 0.64$, the actual peak magnitudes for the forces are fairly similar for both values of h, and peak at approximately 10 fN. This is to be contrasted with the

peak repulsive force found in Ref. 101, which was approximately 10 aN, and gives our quoted enhancement factor of $\sim 10^3$.

Additionally, we can use the uniaxial capsule configuration to examine the importance of our assumption of perfect conductors. Replacing the conducting plate with gold (plasma frequency 1.37×10^{16} rad/s) and the capsule with a material that has permittivity $\varepsilon(\omega) = \mathrm{diag}(1, 1, \varepsilon_{\mathrm{gold}}(\omega))$, we find that the peak repulsive force for $R = 2\,\mu$m is reduced by 50%, but that for $R = 500$ nm it is only reduced by 20%, while for $R = 250$ nm it is *increased* by 10%. The increase in the repulsive force for smaller R can be understood from the fact that the attractive forces from finite-thickness plates come from high-ω components, which are cutoff by the plasma frequency in the gold permittivity. Therefore, using gold actually helps to attenuate some of the attractive effects introduced by using finite-thickness plates, and implies that our force bounds remain valid for imperfect conductors. Finally, we examined the effect of introducing a long dielectric column attached to the capsule (this would serve as both an anchor for the capsule and a means of detecting the force on it). We find that a column made of silica (modeled as constant permittivity $\varepsilon = 2.25$) and of half the width of the capsule does not significantly modify the repulsive force. However, taking the column width equal to the capsule width reduces the peak repulsive force by a factor of 10.

5.5 Conclusions

We have shown that it is possible to achieve repulsive Casimir forces between metallic objects in vacuum. Using numerics we have shown this effect to be robust to both geometric and material nonidealities. However, the repulsive force itself is quite small. We have investigated a Casimir-Polder version of this effect, and similarly concluded that the effect is too weak to be easily measured. Finally, we have shown that Casimir repulsion is not limited to the small-particle dipole-interaction regime of our previous paper, and can in fact be enhanced a thousandfold by considering interactions between macroscopic materials with highly anisotropic microstructures. However,

this force is still below the detection threshold of atomic force microscopy [58]. If this hole/capsule geometry were arranged in a periodic array with period twice the hole diameter (our numerical calculations indicate that this is sufficient to prevent interactions across holes), the repulsive pressure would be approximately 2 mPa for $R = 500\,\mu$m, comparable to the attractive force between metal plates at 900 nm separation, but the fabrication and alignment of such a structure appears extremely difficult. As a more general point, however, we believe that one route to obtaining a number of exotic Casimir effects would be to exploit effective uniaxial conductors formed by, e.g., vertical arrays of nanowires [195]. Even if the repulsive regime cannot be achieved, our results suggest that significant modifications to the Casimir force may result.

Chapter 6

Modeling near-field radiative heat transfer from sharp objects using a general 3d numerical scattering technique

We examine the non-equilibrium radiative heat transfer between a plate and finite cylinders and cones, making the first accurate theoretical predictions for the total heat transfer and the spatial heat flux profile for three-dimensional compact objects including corners or tips. We find qualitatively different scaling laws for conical shapes at small separations, and in contrast to a flat/slightly-curved object, a sharp cone exhibits a local *minimum* in the spatially resolved heat flux directly below the tip. The method we develop, in which a scattering-theory formulation of thermal transfer is combined with a boundary-element method for computing scattering matrices, has many similarities with the methods we used for computing Casimir forces, especially in Chapter 3. Our method can be applied to three-dimensional objects of arbitrary shape.

6.1 Introduction

The exchange of heat between non-touching bodies at different temperatures is accomplished by the absorption and emission of radiation. Radiative heat transfer has many applications to technology, including thermal-photo-voltaics (TPV), nano-patterning, and imaging [10, 142, 181]. At the simplest level, the radiative heat flow out of a body is simply proportional to the surface area of that body, the proportionality constant being bounded from above the Stefan-Boltzmann result for blackbody radiation σT^4 [164]. However, we have spent several chapters examining how the spectrum of zero-point electromagnetic fluctuations due to one body can be modified by the presence of another body, and by now we should suspect that a similar phenomenon applies to the thermal fluctuations of the electromagnetic field. In fact, theory has predicted [151] that the blackbody limit to thermal transfer between two bodies can be greatly exceeded when the two bodies approach each other to within a distance smaller than the thermal wavelength $\lambda_T = hc/k_B T$. For normal temperatures $T \sim 300K$ this enhancement occurs at sub-micron separations. This is due to the tunneling of thermally-excited evanescent modes tunneling across the barrier between the two objects; the amplitude of this tunneling is strongly position-dependent [10,78,108,147,150,151,200]. Recent experiments have confirmed [181,187] this enhancement over the blackbody limit. These experiments have generated great interest, including the hope that near-field enhancement effects can be tailored for, e.g., TPV applications.

Until the last few years, the only rigorous theoretical results for thermal transfer concerned parallel plates; however, very recently rigorous theoretical predictions been made for sphere-sphere [136] and sphere-plate [89, 140] geometries. Although in principle capable of handling arbitrary shapes, these theoretical techniques (along with others [17, 124]) were previously implemented only when the scattering matrices are expressed analytically (e.g., spheres and plates in 3d). As an alternative, stochastic finite-difference time-domain methods have been used to examine heat transfer for periodic structures [169], but this method is not computationally well-suited for

compact objects in three dimensions. Our technique extends the formalism of Ref. 89 directly to arbitrary compact objects, and allows us to make the first accurate theoretical predictions for near-field thermal transfer from 3d compact objects of arbitrary shape (including corners or tips) to a dielectric substrate. Our work is motivated by studies of non-contact thermal writing with a hot, sharp object [115,206], which have previously only been treated by either proximity or dipole approximations [132,147]. To do this, we use a hybrid boundary-element/scattering technique similar to what we used in Chapter 3, in which we numerically compute the scattering matrices of this object in a multipole basis; for our study, we employ a cylindrical-wave basis. Unlike the usual spherical-wave basis, this allows us to concentrate our resolution on the surfaces adjacent to the substrate, but requires a new quadrature approach to discretize the scattering matrix. In addition to sphere-plate heat transfer, we study both cylinder-plate and cone-plate configurations (see sketch in Fig. 6-1), for which no known analytic solution exists. Our results exhibit clear scaling laws for the total heat transfer that distinguish locally flat structures (e.g., cylinders and spheres), from locally sharp structures (cones). In addition, we study the spatial distribution of heat-flux over the substrate, a topic that has been treated previously using a point-dipole approximation for the heat source [132]. Our results show that the heat flux pattern depends strongly on the shape of the tip. Cones in particular have a flux pattern exhibiting an unusual feature: a local *minimum* in the heat flux directly below the tip, which we can explain with a modified dipole picture.

6.2 Method

6.2.1 Fluctuational Electrodynamics

Our starting point is the theory of fluctuational electrodynamics (FE), as formulated by Rytov [183]. Under Rytov's framework we examine a collection of objects, indexed by α, in which each object is locally in thermal equilibrium at temperature T_α (this includes the environment in which all of the other objects reside). The justification for

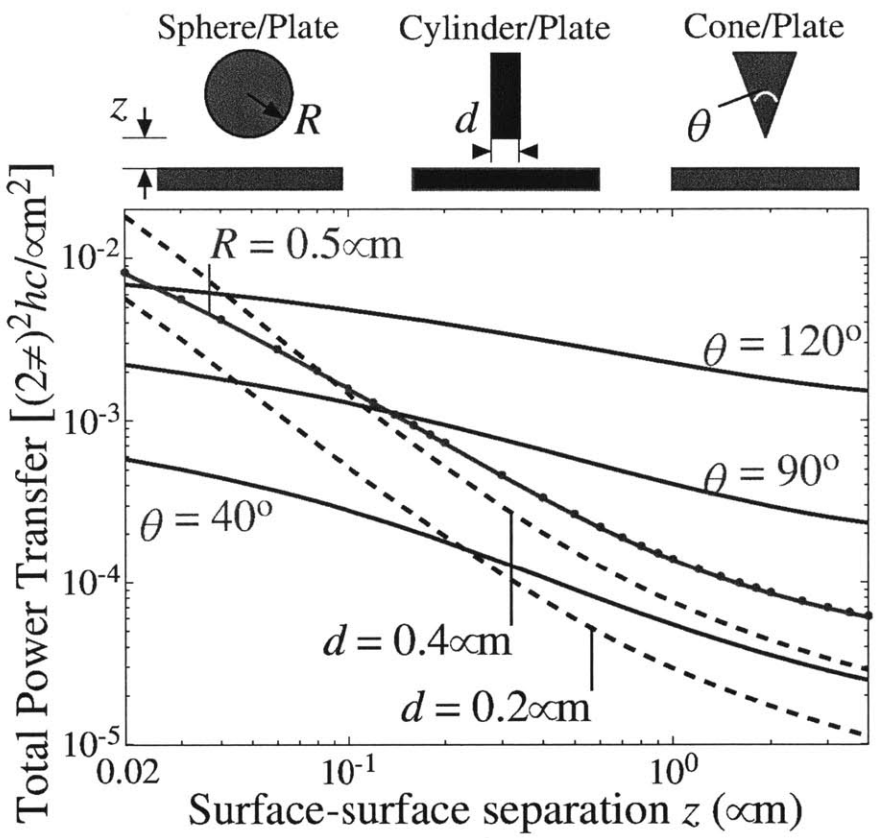

Figure 6-1: Total thermal transfer between a silica plate and doped silicon objects of various shapes. The plate is semi-infinite, and the objects all have height equal to $1\,\mu$m in the z-direction. The plate/environment temperature is $T_P = 300\,$K and the objects are at temperature $T_A = 600\,$K. Red dots denote results with the sphere scattering matrix determined analytically, the only case in which we have an analytic solution for the scattering matrix.

this is that the time for equilibration within a single object (which is usually achieved via phonons [5]) is much shorter than the timescale for radiative heat exchange between two disconnected objects. The actual thermal radiation is due to local current sources $\mathbf{J}_\alpha(\omega;\mathbf{x})$ on each object; a key assumption in FE is that these current sources are completely uncorrelated with respect to both α and $\mathbf{x}$:

$$\langle \mathbf{J}_\alpha(\omega;\mathbf{x}) \otimes \mathbf{J}_{\alpha'}(\omega';\mathbf{x}')\rangle = \Im\left[\varepsilon(\omega;\mathbf{x})\right]\Theta(\omega,T_\alpha)\delta(\omega-\omega')\delta^{(3)}(\mathbf{x}-\mathbf{x}')\delta_{\alpha,\alpha'}\overleftrightarrow{J}_\alpha(\omega;\mathbf{x}), \quad (6.1)$$

where $\Theta = \omega^4 \left(\exp\left(\hbar\omega/k_B T\right) - 1\right)^{-1}$ [45, 183], $\hbar$ is Planck's constant and k_B the Boltzmann constant. Here $\overleftrightarrow{J}_\alpha(\omega;\mathbf{x})$ depends on the local anisotropy of object α; here we will assume all objects are locally isotropic, in which case $\overleftrightarrow{J}_\alpha(\omega;\mathbf{x})_{ij} = \delta_{ij}$. We have also assumed linearity of all materials involved, which allows us to treat each frequency independently, as with Casimir forces [1].

With this model for the current sources, we can build up the following phenomenological picture for the physics of radiative thermal transfer: each object α independently emits radiation, determined by current sources local to object α from eq. (6.1) alone and independent of the geometry and configuration of all other objects $\alpha' \neq \alpha$. This emitted radiation will then undergo both multiple-scattering and absorption processes; these processes will depend on both the geometries and configurations of all objects α', but will be independent of the radiation from all other objects $\alpha' \neq \alpha$. Therefore, the total flow of energy can be determined by considering in turn the flow of energy from each object α to all other objects $\alpha' \neq \alpha$ [2].

For a given configuration of fields, the energy flow F_S through a surface S is given by the total flux of the Poynting vector $\mathbf{E} \times \mathbf{H}^*$ through S:

$$F_S = \Re \int_S [\mathbf{E} \times \mathbf{H}^*] \cdot d\mathbf{S}. \tag{6.2}$$

Schematically, we then have the following setup for computing the total heat flow through a surface S:

$$F_S = \Re \sum_\alpha \int_0^\infty \frac{d\omega}{2\pi} \Theta(T_\alpha, \omega) \sum_{\mathbf{J}_\alpha} \int_S \left[\mathbf{E}_{J_\alpha}(\omega;\mathbf{x}) \times \mathbf{H}^*_{J_\alpha}(\omega;\mathbf{x})\right] \cdot d\mathbf{S}. \tag{6.3}$$

Here $\{\mathbf{J}_\alpha\}$ represents a complete set of independent volume current sources on object α. The most obvious such set is a δ-function basis: $\{\mathbf{J}_\alpha\} = \{\hat{\mathbf{e}}_j(\mathbf{x}) \,|\, \mathbf{x} \in \alpha, j \in \{\hat{\mathbf{x}}, \hat{\mathbf{y}}, \hat{\mathbf{z}}\}\}$. The fields $\mathbf{E}_{J_\alpha}, \mathbf{H}_{J_\alpha}$ are simply the solutions to Maxwell's equations with

[1] Strictly speaking, FE does not require a locality condition [i.e., $\delta(\mathbf{x} - \mathbf{x}')$], similar to how this is not required for Casimir forces [154]. However, we will assume locality throughout for simplicity

[2] As the environment is one such object, this includes the case of a single object radiating into free space.

sources $\mathbf{J}_\alpha$:

$$\left[\nabla \times \nabla - \omega^2 \varepsilon(\omega; \mathbf{x})\right] \mathbf{E}_{\mathbf{J}_\alpha} = -i\omega \mathbf{J}_\alpha(\mathbf{x}) \tag{6.4}$$

6.2.2 Computation

The most straightforward approach is a direct solution, in which for each frequency ω and object α, eq. (6.4) is solved for every point $\mathbf{x} \in \alpha$. A requirement is that the volume of α be discretized, e.g., by a uniform grid of sufficiently high spatial resolution. The solution would then be analogous to the first numerical solutions to Casimir problems for generic geometries [166]. Such a method has been explored for quasi-two-dimensional gratings using stochastic current sources in the time domain [169] (see also Ref. 25 as a precursor for computing the radiation of an object in isolation), however the computations are extremely expensive, even in two dimensions. Additionally, it does not take advantage of the uncorrelated nature between currents on different objects. Our goal will be to compute this the thermal transfer eq. (6.3) by replacing volume current sources with *surface* current sources, which has the clear advantage of a large gain in efficiency.

In a very real sense, the physics of radiative thermal transfer is the same as the physics of Casimir forces: the statistical average of uncorrelated, fluctuating current sources gives rise to a nontrivial electromagnetic stress-energy tensor; for Casimir forces we were interested in the components of $\langle \mathbf{E} \otimes \mathbf{E} \rangle$ and $\langle \mathbf{H} \otimes \mathbf{H} \rangle$ when all objects were at thermal equilibrium. Here, we have only local equilibrium, and the components are $\langle \mathbf{E} \otimes \mathbf{H}^* \rangle$ [3]. While the scattering-theory viewpoint for Casimir forces is best arrived at though a path-integral derivation [154, 160], the solution to the thermal transfer problem is actually more physically intuitive [89, 90]. In this work we will consider the simplified case of only three "objects" - a uniform dielectric half-space P, an arbitrary compact object A, and the environment E. The derivation of the thermal transfer is simplified in this case; for the more general case, see Ref. 90.

[3]The complex conjugate of $\mathbf{H}$ gives another crucial difference with equilibrium Casimir forces: the frequency integrand is non-analytic and cannot be Wick-rotated. This is manifest in the physics of thermal transfer in, e.g., the resonant enhancement of heat transfer due to surface plasmons [201]

In the problem studied here, an object A at temperature T_A faces a dielectric plate B at temperature T_B, in an environment E that is also at temperature T_B. Under the assumptions of Rytov's theory, all sources emit radiation independently, and therefore the source currents do not depend on the relative position/orientation of objects A and B. In the actual physical system, objects A, B, and the environment are all sources of radiation – the radiation from A is at temperature T_A and the radiation from B and E is at temperature T_B. However, we can eliminate the sources from A by the following argument: if $T_A = T_B$, the system is in thermal equilibrium and the expectation value of the Poynting vector vanishes at all points $\mathbf{x}$ and at every frequency due to detailed balance [45]. Therefore, the Poynting vector due to radiation solely from object A at temperature T_A is exactly the negative of the Poynting vector due to radiation from B and E at temperature T_A with object A at zero temperature. The full non-equilibrium Poynting vector can therefore be computed with radiative sources from B and E only.

To compute the power flux, we first compute the electric field correlator $\langle \mathbf{E}(\mathbf{x}) \otimes \mathbf{E}(\mathbf{x}')\rangle_j$, $j = P, E$, for general $\mathbf{x} \neq \mathbf{x}'$ (the Poynting vector will be obtained at the end by taking $\lim_{x' \to x} \nabla_{x'} \langle E(\mathbf{x}) \otimes E^*(\mathbf{x}')\rangle$ [4]. This correlator has the general form:

$$\langle \mathbf{E} \otimes \mathbf{E}'^*\rangle_j = \int_0^\infty \frac{d\omega}{2\pi} \Theta(\omega, T_j) \langle \mathbf{E} \otimes \mathbf{E}'^*\rangle_{j,\omega}; \tag{6.5}$$

unless otherwise noted, we consider each frequency ω separately and drop the ω subscript below. The correlator takes on a simple form in an orthogonal basis $\mathbf{E}_\alpha(\omega; \mathbf{x})$ for the field degrees of freedom, indexed by a (discrete or continuous) index α. In our case, these waves will be cylindrical waves propagating in the $\pm z$ direction (described below). For computation, it is convenient to first express the correlator as a matrix $\mathbb{D}$; in matrix notation (with implied summation over repeated indices):

$$\langle \mathbf{E}(\mathbf{x}) \otimes \mathbf{E}^*(\mathbf{x}')\rangle = (\mathbb{D})_{\alpha',\alpha} \mathbf{E}_{\alpha'}(\mathbf{x}) \otimes \mathbf{E}^*_\alpha(\mathbf{x}'). \tag{6.6}$$

[4]There is an additional zero-temperature term in the $\langle EE\rangle$ correlator that results in the Casimir force at thermal equilibrium; this shows up as a modification of Θ. However, this term does not contribute to heat transfer and will be ignored throughout

$\mathbb{D} = \mathbb{D}_P + \mathbb{D}_E$ due to statistical independence of the thermal fluctuations, where $\mathbb{D}_{P/E}$ involve sources only from P / E. The correlators $\mathbb{D}_{P/E}$ are obtained from the "unperturbed" correlators $\mathbb{D}^0_{P/E}$; $\mathbb{D}^0_P$ involves the plate sources without A and $\mathbb{D}^0_E$ involves the environment sources with neither A nor P present. The $\mathbb{D}^0_j$ are known analytically; we will give their expressions in the cylindrical-wave basis below. Each component of the operator $\mathbb{D}^0_j$, e.g, the quantity $\mathbf{E}_{\alpha'} \otimes \mathbf{E}_\alpha$, represents a tensor product of two solutions to the vacuum Maxwell's equations, while the matrix element $(\mathbb{D})_{\alpha',\alpha}$ represents the relative contribution of this term to the correlator. The nice thing about FE is that now we can forget all about the statistical nature of the current sources - once the $\mathbb{D}^0_j$ are known, the full correlators $\mathbb{D}_j$ can be determined from them by use of the Lippmann-Schwinger equation [89, 154]. In our notation, the solution is expressed as:

$$\mathbb{D}_j \;=\; \mathbb{O}_j \mathbb{D}^0_j \mathbb{O}^\dagger_j, \quad j = P, E \tag{6.7}$$

The $\mathbb{O}_j$ are matrices that describe the scattering of incoming and outgoing fields with the allowance for sources in between. The $\mathbb{O}_j$ are constructed from the more conventional incoming/outgoing scattering matrices $\mathbb{F}_{P/A}$ [123, 154] for objects P and A individually. In Appendix 5 we will derive the form for $\mathbb{O}$ explicitly for parallel plates (the generalization to arbitrary objects follows a similar process), which will clarify the meaning of the operators $\mathbb{O}_j$ in eq. (6.7).

In general, any multipole basis used will break up into two sets of "incoming" and "outgoing" waves (for some examples, see Ref. 154). These will be referred to by the index $s = \pm 1$. For the cylindrical multipole basis (described below), the expressions for the $\mathbb{O}_j$ in the Lippmann-Schwinger equation decompose into 2×2 block matrices, where each block index represents a single value of the propagation direction $(s', s = \pm)$:

$$\mathbb{O}_P = \begin{pmatrix} 0 & \mathbb{U}_{PA}\left(\mathbb{F}_A\right)_{-+}\mathbb{U}_{AP}\mathbb{M}_P^{-1} \\ 0 & \mathbb{U}_{AP}\mathbb{M}_P^{-1} \end{pmatrix}, \qquad \mathbb{M}_P = 1 - \mathbb{U}_{AP}\left(\mathbb{F}_P\right)_{+-}\mathbb{U}_{PA}\left(\mathbb{F}_A\right)_{-+}$$

$$\mathbb{O}_E = \begin{pmatrix} \mathbb{M}_E^{-1} & 0 \\ \mathbb{U}_{AP}\left(\mathbb{F}_P\right)_{+-}\mathbb{M}_E^{-1}\mathbb{U}_{PA}\left(\mathbb{F}_A\right)_{--} & 0 \end{pmatrix}, \quad \mathbb{M}_E = 1 - \mathbb{U}_{PA}\left(\mathbb{F}_A\right)_{-+}\mathbb{U}_{AP}\left(\mathbb{F}_P\right)_{+-} \tag{6.8}$$

Here $\mathbb{U}(\mathbf{x}' - \mathbf{x})$ is the (real-frequency) translation matrix for the waves from $\mathbf{x}$ to $\mathbf{x}'$. The subscript $\mathbb{U}_{PA}$ is shorthand for $\mathbb{U}(z_P - z_A)$ (similarly for $\mathbb{U}_{AP}$). The $\mathbb{U}$ are known analytically; the important quantities are $\mathbb{F}_{P/A}$, the scattering matrices [123, 154] for objects P and A, respectively. As object P is a plate, $\mathbb{F}_P$ is known analytically. However, as was the case for Caimir forces, $\mathbb{F}_A$ cannot be determined analytically for a general object A. Instead, the computation of the scattering matrix elements is accomplished via a boundary-element method [159], described below. The z-component of the Poynting flux at position $\mathbf{x}$, $S_{\mathbf{x}}$, and the total power flux S_T through the $z = 0$ plane can both be expressed as operator traces:

$$S_{\mathbf{x}/T} = \Re\,\mathrm{Tr}\left[\mathbb{S}_{\mathbf{x}/T}\mathbb{D}_T\right], \tag{6.9}$$

with

$$\left(\mathbb{S}_{\mathbf{x}}\right)_{\alpha',\alpha} = -\frac{i}{\omega}\hat{\mathbf{z}} \cdot \left[\mathbf{E}_\alpha(\mathbf{x}) \times \left(\nabla \times \mathbf{E}_{\alpha'}(\mathbf{x})\right)^*\right] \tag{6.10}$$

and $\left(\mathbb{S}_T\right)_{\alpha',\alpha}$ given below.

To actually compute these quantities, we must specialize to a specific multipole basis. When considering the interaction of, e.g., a sphere and a plate, most studies [50, 89, 113, 140] have employed a spherical multipole basis in which the scattering matrix for the sphere is known analytically. A direct numerical extension to non-spherical objects entails computing the scattering matrices in a spherical multipole basis along the lines of our work in Chapter 3 for omega particles. However, at close separations many more multipoles of increasingly higher order must be retained. Higher-order multipole moments have rapid oscillations, and therefore any numerical

discretization (surface or volume) of the objects must be comparably increased. Due to the spherical symmetry of the multipoles, this discretization must occur uniformly across the object, despite the intuitive expectation that only a high discretization near the interfaces is required. Instead, in this study we employ a cylindrical-wave basis of fields $\mathbf{E}_{s,m,k_\rho,p}(\mathbf{x})$ in which the waves (also known as Bessel beams) propagate in the $\pm z$ direction [198]. These can be expressed as azimuthal Fourier transforms of ordinary planewaves as follows:

$$\mathbf{E}_{s,m,k_\rho,p} = i^{\delta_{p,M}}(-1)^n k_\rho \int_0^{2\pi} \frac{d\phi_{\mathbf{k}_\perp}}{2\pi} e^{im\phi_{\mathbf{k}_\perp}} \mathbf{E}_{\mathbf{k}_\perp,p}(x); \tag{6.11}$$

The variable $s = \pm$ refers to the direction of propagation; m is the (integer) angular moment of the field, $0 \leq k_\rho < \infty$ the radial wavevector, and $p = M, N$ the polarization. The composite index in this case is $\alpha = \{s, m, k_\rho, p\}$. This basis is especially well-suited to the case considered here in which objects have rotational symmetry about the z-axis, as different values of m are decoupled; this does not change our formulation but does simplify our numerical implementation

To compute the elements of $\mathbb{F}_A$, we again employ the boundary-element method (BEM) [159] implemented by Homer Reid [161]. In contrast to the Casimir case of Chapter 3, we now desire the scattering matrices in real frequency; fortunately, Homer's code is able to handle both real and imaginary frequency equally well [5]. Along the same lines as Chapter 3, A is discretized into a mesh; our numerical method then computes the induced currents from an incident multipole field $\mathbf{E}_\alpha(\mathbf{x})$ (here $\alpha = \{s, m, k_\rho, p\}$). The multipole moments of this current distribution are then computed in a straightforward manner analogous to Chapter 3. Only two changes need to be made: the first is the dyadic Green's function in the cylindrical-wave basis,

[5]The real-frequency case involves the additional complication of complex $\varepsilon(\omega)$; we are grateful to Homer for modifying his code to allow for this case.

given explicitly by [198]:

$$\begin{aligned}\mathbb{G}(\omega;\mathbf{x},\mathbf{x}') &= \sum_{n=-\infty}^{\infty}(-1)^n\sum_{p=M,N}\int_0^\infty \frac{dk_\rho}{2\pi}\frac{-\omega}{2qk_\rho}\mathbf{E}_{+1,k_\rho,n,p}(\mathbf{x})\otimes\mathbf{E}_{-1,k_\rho,-n,p}(\mathbf{x}')\theta(z-z') \\ &+ \mathbf{E}_{-1,k_\rho,n,p}(\mathbf{x})\otimes\mathbf{E}_{+1,k_\rho,-n,p}(\mathbf{x}')\theta(z'-z) \qquad (6.12)\end{aligned}$$

(here $\theta(x)$ is the Heaviside step function, not to be confused with the Planck factor Θ) and the explicit expression for the cylindrical multipole waves [198]:

$$\begin{aligned}\mathbf{E}_{s,m,k_\rho,M}(x,y,z) &= e^{isqz+im\phi}\left(\frac{in}{\rho}J_n(k_\rho r)\,\hat{\rho}-k_\rho J_n'(k_\rho r)\,\hat{\phi}\right) \\ \mathbf{E}_{s,m,k_\rho,N}(x,y,z) &= e^{isqz+im\phi}\left(\frac{ik_\rho}{\omega}J_n'(k_\rho r)\,\hat{\rho}-\frac{n}{\omega\rho}J_n(k_\rho r)\,\hat{\phi}\right), \qquad (6.13)\end{aligned}$$

where $q=\sqrt{\omega^2-k_\rho^2}$, J_n are the cylindrical Bessel functions, (ρ,ϕ,z) denote cylindrical coordinates, and J_n' denotes differentiation with respect to the argument.

Because the cylindrical-wave basis distinguishes between waves in the $\pm z$ direction (unlike a spherical wave basis), and because the near-field thermal transport mostly depends on reflections from adjacent surfaces, we are able to concentrate most of our BEM mesh resolution on the part of the surface of A nearby the plate, greatly improving computational efficiency [6] For example, in the mesh for a cone, shown in the center of Fig. 6-2 we use ~ 250 times more resolution at the tip than at the base, which allows us to compute thermal transfer down to separations 1% of the cone height.

One complication of cylindrical multipoles (compared to spherical multipoles) is that k_ρ is a continuous index and matrix multiplication is turned to integration. For computational purposes, this integration must be approximated as a discrete sum by numerical quadrature. We approximate the integral over k_ρ using a Gaussian quadrature scheme [3] for high accuracy. To illustrate this, consider the scattering matrix $\mathbb{F}_A$ of object A; its action on an incident electric field can be discretized as

[6] One limitation, however, is that now (similar to [17]) we must assume a separating plane between the two objects in order for the expression eq. (6.12) to be valid. However, this is the case for most realistic situations.

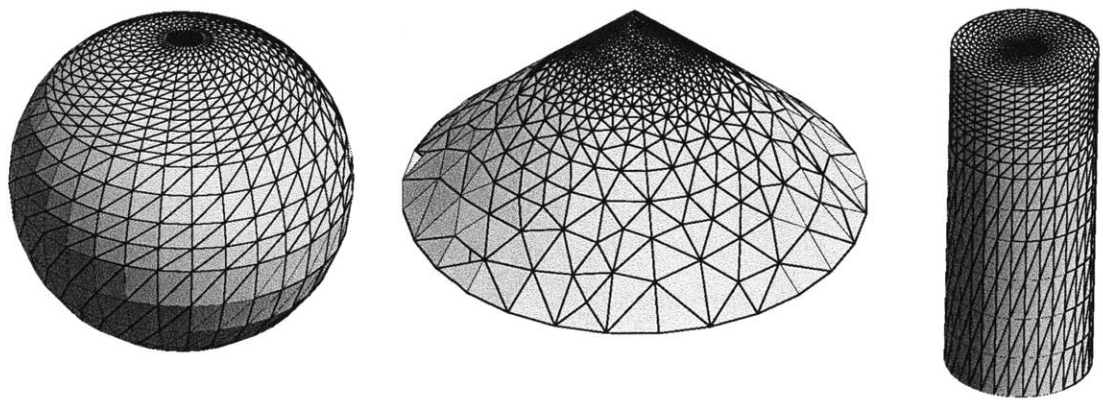

Sphere Cone Cylinder

Figure 6-2: Cone meshes used in the present section. The points at the tops of these objects are those nearest to the plate, and thus require the highest mesh density.

(for simplicity, summation over m and p is suppressed):

$$\mathbb{F}_A \mathbf{E}_{k_{\rho,i}} = \int_0^\infty \frac{dk'_\rho}{2\pi} \left(\mathbb{F}_A\right)_{k'_\rho;k_{\rho,i}} \mathbf{E}_{k'_\rho} \approx \sum_{j=0}^{N} w_j \left(\mathbb{F}_A\right)_{j,i} \mathbf{E}_{k_{\rho,j}} \tag{6.14}$$

where the sets $\{w_j, k_{\rho,j}\}$ form a set of one-dimensional quadrature weights and points, respectively, and $(\mathbb{F}_A)_{j,i} = (\mathbb{F}_A)_{k_{\rho,j},k_{\rho,i}}$ are the elements of the continuous scattering matrix sampled at the discrete quadrature points. The sampling density will depend on how smooth the variation of $\mathbb{F}_A$ is with k_ρ for each ω and m, as well as the region of k_ρ which contributions (this is determined by the exponential cutoff in $\mathbb{U}$; as a general rule, this cutoff varies as $k_\rho \sim 1/z$). We have found that the propagating sector can have a strong k_ρ-dependence, which is not surprising due to, e.g., the presence of Mie resonances for spheres. However, in this work we are primarily interested in the near-field evanescent enhancement of thermal transfer, in which the dominant contributions come from the evanescent sector. We have observed that in the region $k_\rho > \omega$, the matrix elements of $\mathbb{F}$ tend to be smoothly-varying with k_ρ, allowing for a sparse quadrature sampling.

The analytic expression for the non-equilibrium electric field correlator of a plate at temperature T_P and environment at $T = 0$ expressed in the planewave basis is well-known [90, 183]. Since eq. (6.11) relates planewaves to cylindrical waves, it is a

simple exercise to re-express this correlator in the basis of cylindrical multipoles [198]:

$$\left(\mathbb{D}_P^0\right)_{\alpha',\alpha} = \delta_{\alpha',\alpha}\delta_{s,+}\left(\frac{1-\left|r_{k_\rho,p}\right|^2}{4qk_\rho}\chi_p + \frac{\Im r_{k_\rho,p}}{2|q|k_\rho}\chi_e\right) \tag{6.15}$$

Here $r_{k_\rho,p}$ are the Fresnel coefficients for a dielectric plate, $\chi_{p(e)} = 1$ for $k_\rho < \omega$ ($k_\rho > \omega$) and zero otherwise, $q = \sqrt{\omega^2 - k_\rho^2}$, and $\delta_{i,j}$ is the Kronecker (Dirac) delta function on discrete (continuous) indices; the $\delta_{s,+}$ reflects the fact that only waves propagating in the $+z$ direction are emitted by the plate, which occupies the $z < 0$ plane. The expression for the environment correlator $\mathbb{D}_E^0$ is given by the same expression as $\mathbb{D}_P^0$ with $r = 0$ and $\delta_{s,+}$ replaced with $\delta_{s,-}$. [7]. Finally, the matrix elements for the total power flux are $(\mathbb{S}_T)_{\alpha',\alpha} = \frac{2\pi q k_\rho}{\omega}\delta_{k_\rho,k'_\rho}\delta_{p,p'}(-s')^{\delta_{p',N}}([\chi_p - \chi_e]s)^{\delta_{p,M}}$.

For the surface meshes, we use approximately 2,500 panels (discretized surface elements) to get 1% convergence, with the panels highly concentrated on the area of the objects nearest to the plate. We retain angular moments up to $|m| = 10$, and for each m we perform the ω and k_ρ integrations using 28 and 48 Gaussian quadrature points, respectively. For our study, object A is composed of doped silicon while the substrate B is silica. For the doped silicon dispersion we use a standard Drude-Lorentz model [43] with a dopant density of $1.4 \times 10^{19}\text{cm}^{-3}$, while for silica we use measured optical data [187].

6.3 Results

We examine the thermal transfer properties for three types of configurations (shown at to top of Fig. 6-1): sphere-plate, cylinder-plate, and cone-plate. The objects are chosen to all have length h in the z direction. Although the first configuration has previously been solved semi-analytically [89, 140], our use of cylindrical multipoles represents a new semi-analytic method for computing the sphere-plate transfer, one that we believe is orders of magnitude more efficient than semi-analytic methods based

[7] Technically, there is another source of fields from the environment originating from $z = -\infty$. However, assuming $\Im(\varepsilon_P) > 0$ these will be fully absorbed once the semi-infinite plate P is added to the system.

on spherical multipoles [88]. The other two configurations have not been previously calculated without approximation, as analytic expressions for the scattering matrices do not exist for the finite cylinder or the dielectric cone [8]. We focus on cases with rotational symmetry as these simplify our computations - only matrix elements for which $m' = m$ need be computed. We present results for the total radiative thermal transfer (the quantity most directly accessible to experiments) and the spatially-resolved Poynting flux (which is of interest for nanolithography applications).

6.3.1 Total Power Transfer

Figure 6-1 shows the geometry-dependence of the total heat transfer rate between different compact objects and a dielectric plate, over surface-surface separations z from several microns down to 20 nm. In addition to the expected near-field enhancement, we observe several crossings as, e.g., the broader surface area of the $R = 0.5\,\mu$m radius sphere competes with the smaller but flatter surface of the $d = 0.4\,\mu$m diameter cylinder. For smaller z, the ratio of the transfer between the $d = 0.4\,\mu$m and $d = 0.2\,\mu$m cylinders approaches the ratio of their surface areas (within 6% at $z = 20$ nm), as would be expected from a proximity approximation (PA) [89,135]. The sphere-plate exhibits the $1/z$ power law as predicted by PA [89, 181, 187] to within 10% for $z < 0.1\,\mu$m, while the cylinder-plate exhibits agreement to within approximately 10% over this range using a PA based on the integral of the plate-plate heat transfer rate over the cylinder front face and vertical sidewalls. The contribution from the sidewalls can be ignored (leading to a $\sim 1/z^2$ transfer rate [200]) for $z/d \lesssim 0.01$. The convergence to PA is not as strong as would be expected from our intuition from Casimir forces: although both quantities decay as a power law for two flat surfaces, the Casimir force has a z^{-4} decay rate for parallel plates and a z^{-3} decay for a sphere-plate. Therefore, we expect that much smaller separations are required to get a sub-1% agreement with PA. In contrast to the sphere and cylinders, the cones

[8] Analytic expressions do exist for a perfectly-conducting, infinite-length cone [111] because the vacuum Helmholtz equation is separable in cylindrical coordinates [191]; however, perfect conductors have zero thermal emission and thus are of no interest here

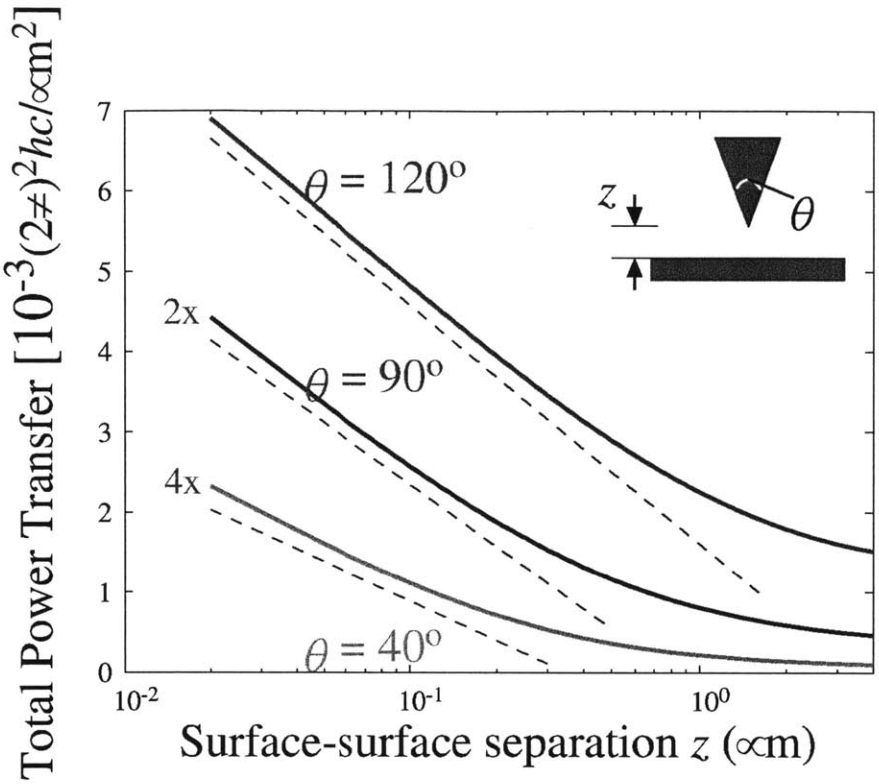

Figure 6-3: Heat transfer for the cone-plate systems from Fig. 6-1, plotted on a semilog scale to suggest that the total power transfer diverges logarithmically for small z. For clarity, data for $\theta = 90°$ is scaled by a factor of 2, and $\theta = 40°$ by a factor of 4. Dashed lines so a linear fit to the data for $20\,\text{nm} \leq z \leq 200\,\text{nm}$, shifted downwards for clarity.

do not seem to be asymptoting to a power law, and may even have a *logarithmic* divergence as $z \to 0$, a fact which we attribute to the scale-invariance of the plate-cone configuration when $z \ll 1\mu\text{m}$ and $z \ll \hbar c/k_B T$ (the latter eliminating material dispersion effects), which we discuss below. To check the accuracy of our numerical scattering method, we also plot the results for the sphere where $\mathbb{F}_A$ is calculated semi-analytically [89], shown as red dots, which agrees to within 1%.

Logarithmic divergence of cone heat flux

Above we mentioned that the heat transfer rates for cones appeared to diverge logarithmically as $z \to 0$. We re-plot these data in Fig. 6-3 on a semilog scale; the resulting curves are clearly linear for small z. We will now give a scaling argument

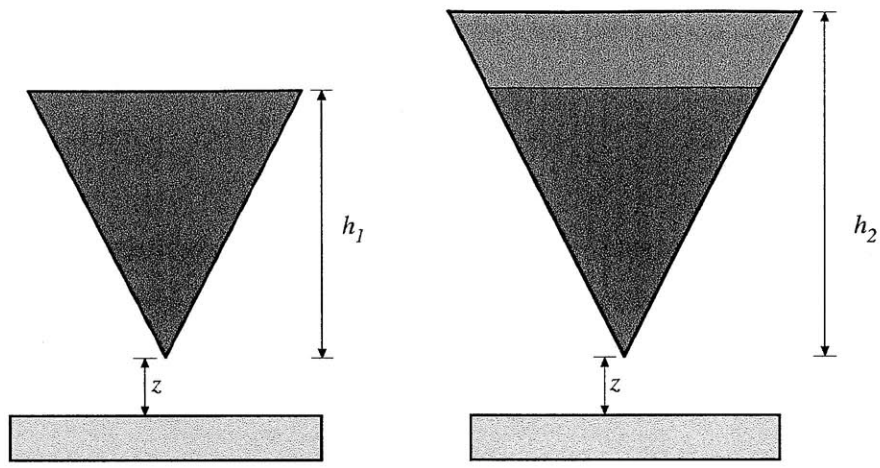

Figure 6-4: Schematic used to derive eq. (6.16). In the text, we consider fixing z and varying the cone height from h_1 to h_2; the heat transfer from the pink region in the right-hand cone varies as $\log(h_2/h_1)$.

to explain why this is the case.

The logarithmic divergence in the heat transfer between a plate and an *finite* cone as $z \to 0$ can be understood from a simple proximity-approximation argument (an infinite cone would have a divergent contribution to the heat transfer from propagating modes). Consider a first a cone of tip-plate separation z, and consider varying the cone height from h_1 to h_2 (see Fig. 6-4). Assuming that both $z \ll h_1, h_2 \ll \lambda_T$, we can ignore the effects of both material dispersion and heat transfer from purely propagating modes. A crude proximity argument would then predict that the change in total heat transfer in varying from h_1 to h_2 (see the pink region in Fig. 6-4) is:

$$S(h_2) - S(h_1) \approx \int_{h_1}^{h_2} dh \frac{2\pi h \sin\frac{\theta}{2}}{h^2} \approx \log\frac{h_2}{h_1}. \tag{6.16}$$

Therefore, PA predicts a logarithmic divergence in the cone height for a fixed z. Of course, for sufficiently large h we will no longer have $h \ll \lambda_T$ and the total heat flux will switch to an area law, which in our geometry translates to a quadratic divergence $S(h) \sim h^2$. The case of interest currently is the case of fixed h and variable z. However, with the exception of the finite h the plate-cone geometry is scale-invariant; therefore, we expect that the heat flux profile (which we will confirm in the next

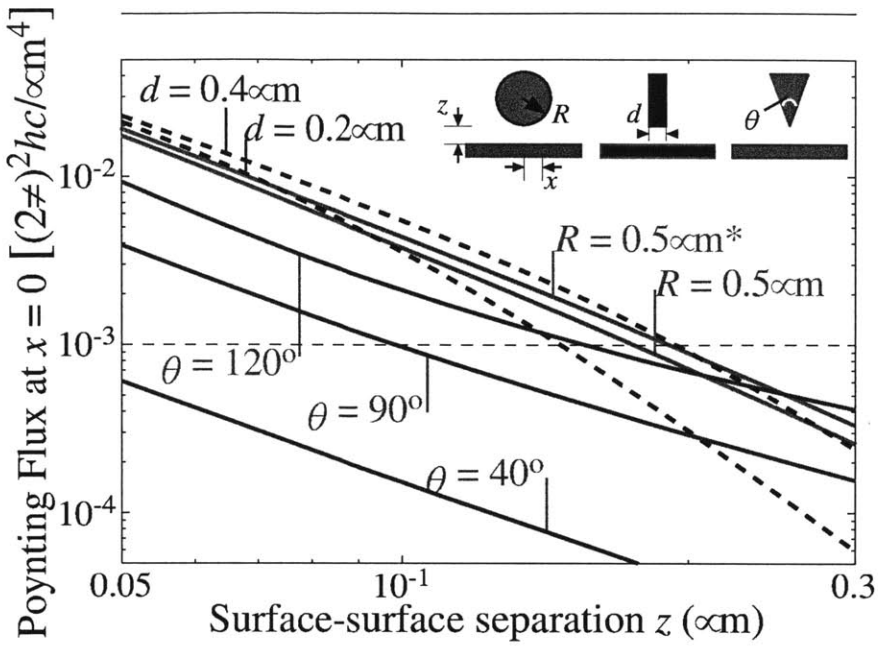

Figure 6-5: Poynting flux at the origin for the geometries of Fig. 6-1 with plate/environment temperature $T_P = 300\,\mathrm{K}$ and object temperature $T_A = 600\,\mathrm{K}$, using the single-polarization approximation (SPA) for the sphere and cylinders. The magenta line denotes the sphere-plate without the SPA, and the horizontal dashed line denotes the threshold used for the crossectional flux profiles of Fig. 6-6.

section) $S(\rho; z)$ at the plate surface will, for sufficiently small ρ, follows a simple scaling law:

$$S(\rho, z) = \frac{1}{\alpha^2} S(\alpha\rho, \alpha z) \tag{6.17}$$

where the prefactor α^{-2} comes from the fact that the heat flux has units of 1/Area. If this scale-invariance were to hold for all ρ, this would imply that the total heat transfer is a constant. However, the finite size of h implies that at some point ρ_* this scaling can no longer hold; for lack of any other units, we must have $\rho_* \sim h$. Therefore, if ρ_* remains constant, the effect of decreasing z by a factor of α amounts to *increasing* h by a factor of $1/\alpha$. Because the total heat flow diverges as $\log h$, we therefore have $S(z) \sim \log z$.

6.3.2 Spatially-resolved Poynting flux

For thermal writing applications, an important factor to consider is not only the total power delivered to the plate, but also the spatial extent over which this delivery occurs. In order to examine this, we envision a scenario in which a critical magnitude of the z-directed Poynting flux is required in order for some change to occur on the plate, for example, the patterning of a thermal mask for later etching [206]. Figure 6-5 plots the Poynting flux at $x = 0$ as a function of z, which will tell us how far away the object must be before it can effect this patterning. The cylinders and spheres converge to the same $\sim 1/z^2$ profile for small z (as expected from a PA), whereas the cones all follow $1/z^2$ profiles with different coefficients. This $1/z^2$ dependence follows from the scale-invariance of the scattering problem for small z, combined with the fact that there is a $1/z$ cutoff in the range of k_ρ that contributes to the transfer, so that the total number of modes that contribute is proportional to $\int_0^{1/z} dk_\rho k_\rho \sim 1/z^2$. In this calculation we have found that the result for nearly flat surfaces is dominated by the N polarization ($\mathbf{E} \perp \hat{\mathbf{z}}$), mirroring similar phenomena in other near-field cases [212], that results from the behavior of the Fresnel coefficients $R^{M/N}$ for high k_ρ:

$$\begin{aligned} R^M(\omega, k_\rho) &= \frac{\varepsilon(\omega) - 1}{4}\frac{\omega^2}{k_\rho^2} + O\left[\frac{1}{k_\rho^4}\right] \\ R^E(\omega, k_\rho) &= \frac{\varepsilon(\omega) - 1}{\varepsilon(\omega) + 1} + O\left[\frac{1}{k_\rho^2}\right]. \end{aligned} \tag{6.18}$$

This is fortunate because we have found that the M contribution to the Poynting flux requires much higher mesh resolution to converge. We can achieve this mesh resolution for the cones using a much finer mesh of approximately 12,000 panels (shown in Fig. 6-7), but such a fine mesh for the sphere or cylinders is computationally intractable due to the large amount of surface area close to the plate. Therefore, we must use the single-polarization approximation (SPA) for the sphere and cylinders. To check the SPA for a sphere we also plot the full results using the semi-analytic formulation, finding that the error from the SPA is $< 20\%$ at the largest z, decaying to $< 10\%$ at smaller z; SPA for a cone is discussed below.

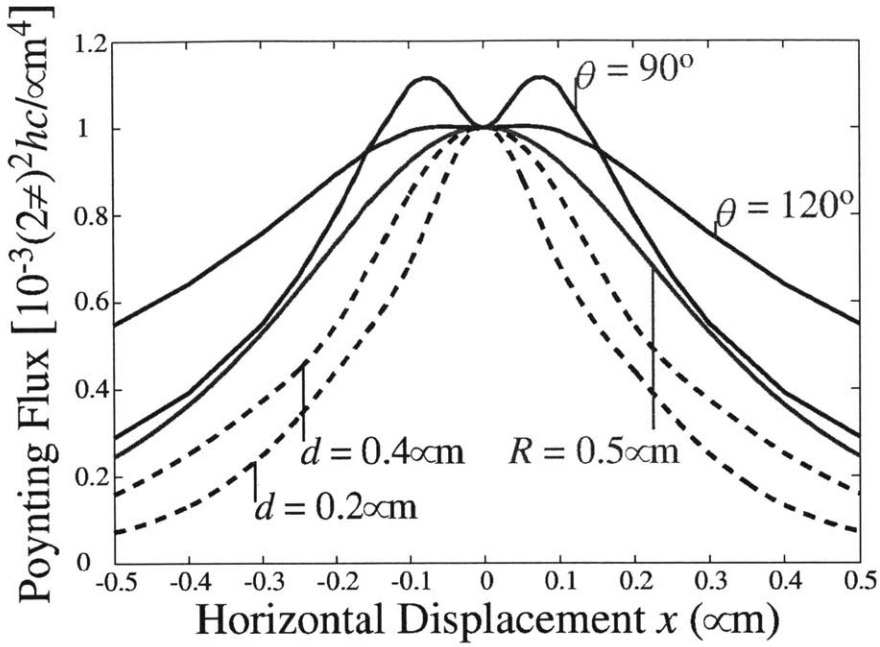

Figure 6-6: Spatially-resolved heat flux profiles at the substrate surface. z is chosen to fix Poynting flux at $x = 0$ at $10^{-3}(2\pi)^2hc/\mu m^4$. For the sphere and cylinders we have used the SPA (see text).

Figure 6-6 plots the Poynting flux as a function of x showing the heat transfer profile. For each object, we chose z to have the same $x = 0$ Poynting flux of $10^{-3}(2\pi)^2hc/\mu m^4$ (horizontal dashed line in Fig. 6-5), corresponding to a sphere-plate separation of $\approx 200\,\text{nm}$. The cylinders and 120° cone all reach this threshold at comparable separations, whereas the 90° cone is at less than half the separation, and the 40° cone does not even reach this threshold within the range considered.

To examine the near-field flux profile for different shapes, the relevant comparison point is the magnitude of the Poynting flux; from Fig. 6-6, different shapes must be placed at different separations from the plate in order to achieve the same Poynting flux. We take our measure to be the value of the Poynting flux at the origin $\rho = 0$ for simplicity. Fixing the Poynting flux at $\rho = 0$ to $10^{-3}(2\pi)^2hc/\mu m^4$, in Fig. 6-6 we plot the Poynting flux profiles for these shapes as a function of ρ. The widths for the cylinders are narrower than the sphere, implying that the cylinders can write higher spatial resolution. For both spheres and cylinders, the Poynting vector peaks at $\rho = 0$ and falls off monotonically. Surprisingly, the cones do not exhibit this simple

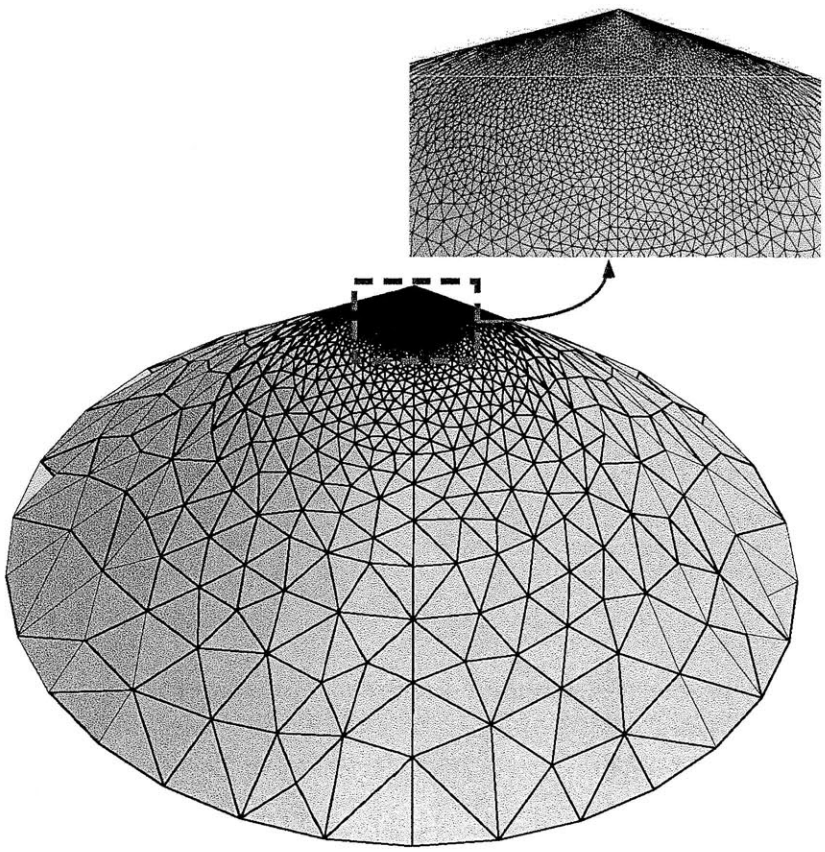

Figure 6-7: Extra-fine mesh used to compute the spatially-resolved Poynting flux for a $\theta = 90°$ cone, in which the mesh is highly concentrated at the tip. In total, approximately 12,000 mesh elements are used. This mesh illustrates the advantage of using a cylindrical-wave basis: spherical waves would have requires a much more uniform meshing of the cone surface, whereas here we can concentrate our mesh points near the tip.

behavior. Rather, the Poynting flux profiles for the two cones are *non*-monotonic in x, with a local minimum at $x = 0$.

It appears from Fig. 6-6 that the flux minimum at $x = 0$ becomes deeper as the cone opening angle becomes sharper. To verify this, we include the flux profile for $\theta = 40°$ as well, examining the Poynting flux profiles for all three cones at a fixed $z = 70\,\text{nm}$. The results are shown in Fig. 6-8; for ease of comparison, all curves are scaled to have a maximum of 1. We also show the $d = 0.2\,\mu\text{m}$ cylinder (using the SPA) for comparison. The dip is very prominent for $\theta = 40°$, where the Poynting flux at $x = 0$ is less than half of its peak value; the relative strength of the dip clearly

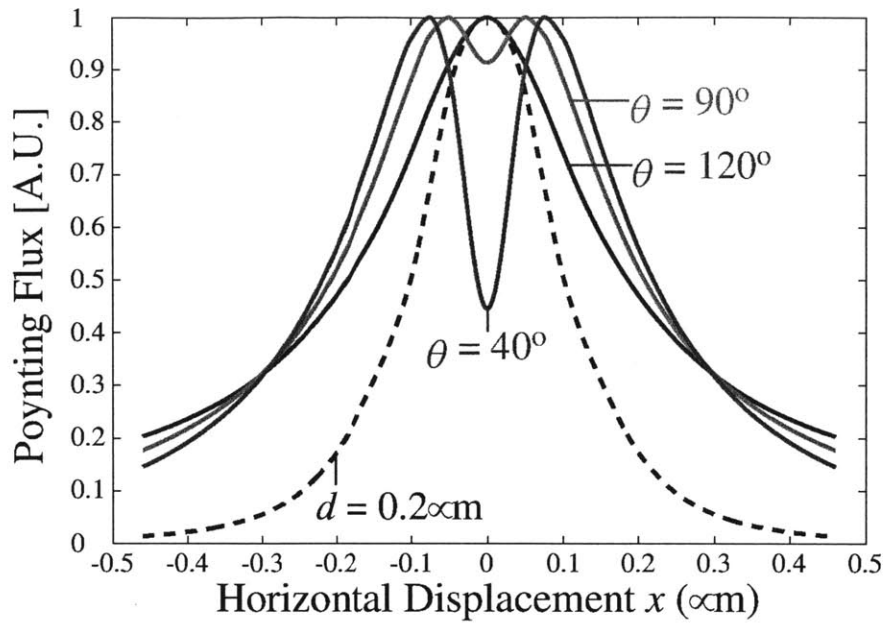

Figure 6-8: Spatially-resolved heat flux profiles (arbitrary units) at the substrate surface for three cones. The profiles are normalized so that their maximal value is equal to 1. For comparison, the profile for a cylinder of radius $d = 400\,\text{nm}$ (using the SPA) is shown as well.

decreases as θ increases.

We believe the explanation for the dip in the Poynting flux is that as the cone tip becomes sharper, its radiation pattern approaches that of a dipole with axis normal to the plate, which has zero Poynting flux at $x = 0$. This explanation predicts that a very thin cylinder with $d \ll z$ should also have a dip in the Poynting flux at $x = 0$, which we have also confirmed numerically. It is interesting to compare this result with the predictions of repulsive Casimir forces from Chapter 5 - there as here, a simple symmetry argument based on dipole fields can predict counter-intuitive results.

6.4 Conclusions

In this Chapter, we have presented the first exact calculations for thermal transfer between a plate and three-dimensional compact objects with sharp features. We achieved this by building on our techniques from Chapter 3 for computing Casimir

forces in chiral metamaterials, demonstrating the broad range of applicability for these methods. We have found that an approximately scale-invariant geometry can lead to qualitatively new behavior - a logarithmic scaling of the total thermal transfer, a property that could potentially be measured. Further, we have found that sharp tips can lead to surprising effects for the near-field thermal heat flux. This is in contrast to the case of Casimir forces, where PFA tends to hold for most regimes (a partial exception was found for the crossed wires in Chapter 4, but even there PFA eventually takes over). It is possible that other interesting effects for this field remain to be discovered.

Appendix 5: Derivation of the $\mathbb{O}$ Operators

In this section we will explicitly derive the operators $\mathbb{O}_j$ in eq. (6.8) for the case of two parallel plates, one plate being of finite thickness. We will do so in a form sufficiently general as to allow generalization to non-planar structures, while still being sufficiently transparent to illustrate the physical meaning behind the $\mathbb{O}$ operators given in eq. (6.7). The physics behind the $\mathbb{O}$ operators is illustrated in Fig. 6-9, and can be summarized as follows: in panel (a), an incident right-propagating field E^{inc} scatters off object 1 in isolation. The scattered field is $\mathbb{F}_1\left[E^{\text{inc}}\right]$. The effect of introducing another object 2 on this scattered field is shown in panel (b) [the incident field is unchanged and directly interacts with object 1]: now, the outgoing field $\mathbb{F}_1 E^{\text{inc}}$ undergoes multiple-scattering events, so that the net scattered field is a sum of left- and right-propagating waves. These fields are linearly dependent on the initial scattered field E^{inc}; O defines the operation connecting E^{inc} to the net scattered field in the presence of objects 1 and 2, and is shown in panel (c).

Assume that the semi-infinite parallel plate P has of permittivity ε_P and reflection coefficient r_P (given by the Fresnel formula) with right-most edge at $z_P = 0$. Plate A has permittivity ε_A and thickness h, with interfaces at z_A and $z_A + h$. For parallel plates, it is best to work in the planewave basis, where the electric field functions are

given by:

$$\begin{aligned}
\mathbf{E}_{s,\mathbf{k}_\perp,M} &= \nabla \times \left(e^{isqz+i\mathbf{k}_\perp\cdot\mathbf{x}_\perp}\hat{\mathbf{z}}\right) \\
\mathbf{E}_{s,\mathbf{k}_\perp,N} &= \frac{1}{\omega|\mathbf{k}_\perp|}\nabla \times \nabla \times \left(e^{isqz+i\mathbf{k}_\perp\cdot\mathbf{x}_\perp}\hat{\mathbf{z}}\right) \qquad (6.19)
\end{aligned}$$

$$(6.20)$$

Because of the two directions of translation-invariance and the isotropy of the plate dielectrics, both the initial field correlator $\mathbb{D}^0$ and the scattering matrices $\mathbb{F}_P$, $\mathbb{F}_A$ are diagonal in $\mathbf{k}_\perp$ and p. Therefore, we may focus on only one value of each. The scattering matrices for A are expressed in terms of the reflection and transmission coefficients r_A and t_A, respectively (these can be expressed in terms of the Fresnel coefficients; see, e.g., Ref. 19).

First consider the radiation from the plate P: the correlator for each component α in the absence of A is given by eq. (6.15), with $k_\rho = |\mathbf{k}_\perp|$ and $r = r_A$. The current sources that create this radiation remain unchanged when we introduce A. The radiative field, however, becomes modified by reflection/transmission through the thin plate. It is a simple matter to see that if the initial field radiating from the plate is $\mathbf{E}_P^0(z) = \mathbf{E}_+(z)$ (here we simplify to $\rho = 0$ and drop explicit reference to $\mathbf{k}_\perp$

and p), the solution $\mathbf{E}_P(z)$ for the field in the region $0 \leq z \leq z_A$ is given by:

$$
\begin{aligned}
\mathbf{E}_P(z) &= U^{(+)}(z,0)\mathbf{E}_+(0) \\
&+ \left[U^{(-)}(z,z_A)r_A U^{(+)}(z_A,z_P)\right]\mathbf{E}_-(0) \\
&+ U^{(+)}(z,z_P)\left[r_P U^{(-)}(z_P,z_A)r_A U^{(+)}(z_A,z_P)\right]\mathbf{E}_+(z) \\
&+ U^{(-)}(z,z_A)r_A U^{(+)}(z_A,z_P)\left[r_P U^{(-)}(z_B,z_A)r_A U^{(+)}(z_A,z_P)\right]\mathbf{E}_-(0) + \ldots \\
&= \left(\sum_{n=0}^{\infty}\left[r_P U^{(-)}(z_P,z_A)r_A U^{(+)}(z_A,z_P)\right]^n\right)U^{(+)}(z,0)\mathbf{E}_+(0) \\
&+ \left(\sum_{n=0}^{\infty}U^{(-)}(z,z_A)r_A U^{(+)}(z_A,z_P)\left[r_P U^{(-)}(z_B,z_A)r_A U^{(+)}(z_A,z_P)\right]^n\right)\mathbf{E}_-(0) \\
&= U^{(+)}(z,0)\left[1 - r_P U^{(-)}(z_P,z_A)r_A U^{(+)}(z_A,z_P)\right]^{-1}\mathbf{E}_+(0) \\
&+ U^{(-)}(z,z_A)r_A U^{(+)}(z_A,z_P)\left[1 - r_P U^{(-)}(z_B,z_A)r_A U^{(+)}(z_A,z_P)\right]^{-1}\mathbf{E}_-(0) \\
&\equiv (\mathbb{O}_P)_{++}\mathbf{E}_+(0) + (\mathbb{O}_P)_{-+}\mathbf{E}_-(0)
\end{aligned}
\tag{6.21}
$$

here we have defined $U^{(\pm)}(z_f,z_i) \equiv e^{\pm iq(z_f - z_i)}$ and included operator notation in the last line to make the correspondence with the general non-planar case more evident. Explicitly, in the planewave basis we have:

$$
\mathbf{E}_P(z) = \frac{1}{1 - r_P r_A e^{2iq(z_A - z_P)}}e^{iqz}\mathbf{E}_+(0) + \frac{e^{2iqz_A}r_A}{1 - r_P r_A e^{2iq(z_A - z_P)}}e^{iq(z - z_P)}\mathbf{E}_-(0) \tag{6.22}
$$

For the environmental sources, the final field is scattered off the combined $P - A$ system. If the incoming field (for a single $(\mathbf{k}_\perp, p)$) is $\mathbf{E}_-$, the solution for the full field

$\mathbf{E}_E(z)$ in the presence of P and A in the region $z_P \leq z \leq z_A$ is:

$$
\begin{aligned}
\mathbf{E}_E(z) &= U^{(-)}(z, z_A) t_A \mathbf{E}_-(z_A) \\
&+ U^{(+)}(z, z_P) r_P U^{(-)}(z_P, z_A) t_A \mathbf{E}_+(z_A) \\
&+ U^{(-)}(z, z_A) r_A U^{(+)}(z_A, z_P) r_P U^{(-)}(z_P, z_A) t_A \mathbf{E}_-(z_A) \\
&+ U^{(+)}(z, z_P) r_P U^{(-)}(z_P, z_A) r_A U^{(+)}(z_A, z_P) r_P U^{(-)}(z_P, z_A) t_A \mathbf{E}_+(z_A) \\
&+ \ldots \\
&= \sum_{n=0}^{\infty} U^{(-)}(z, z_A) \left[r_A U^{(+)}(z_A, z_P) r_P U^{(-)}(z_P, z_A) \right]^n t_A \mathbf{E}_-(z_A) \\
&+ \sum_{n=0}^{\infty} U^{(-)}(z, z_A) \left[r_P U^{(-)}(z_P, z_A) r_A U^{(+)}(z_A, z_P) \right]^n U^{(+)}(z, z_P) r_P U^{(-)}(z_P, z_A) t_A r_A U^{(+)}(z_A, z_P) r \\
&= U^{(-)}(z, z_A) \left[1 - r_A U^{(+)}(z_A, z_P) r_P U^{(-)}(z_P, z_A) \right]^{-1} t_A \mathbf{E}_-(z_A) \\
&+ \left[1 - r_P U^{(-)}(z_P, z_A) r_A U^{(+)}(z_A, z_P) \right]^{-1} U^{(+)}(z, z_P) r_P U^{(-)}(z_P, z_A) t_A \mathbf{E}_+(z_A) \\
&\equiv (\mathbb{O}_E)_{+-} \mathbf{E}_+(0) + (\mathbb{O}_E)_{--} \mathbf{E}_-(0)
\end{aligned}
$$

Explicitly, for planewaves we have:

$$
\mathbf{E}_P(z) = \frac{1}{1 - r_A r_P e^{2iq(z_A - z_P)}} t_A e^{iq(z - z_A)} \mathbf{E}_-(z_A) + \frac{r_P e^{iq(z_A - z_P)}}{1 - r_A r_P e^{2iq(z_A - z_P)}} t_A e^{iq(z - z_P)} \mathbf{E}_+(z_A) \tag{6.24}
$$

If we make the replacement $r_A \to (\mathbb{F}_A)_{-+}$ and $r_P \to (\mathbb{F}_P)_{+-}$ and take $(\mathbb{O}_P)_{--} = (\mathbb{O}_P)_{+-} = 0$ (there are no waves in the region $z > 0$ propagating in the $-z$ direction due to sources on E), we arrive at the expression for $\mathbb{O}_P$ in eq. (6.8). Similarly, setting $T_A = (\mathbb{F}_A)_{--}$ and $(\mathbb{O}_E)_{++} = (\mathbb{O}_E)_{-+} = 0$ (there are no waves in the region $z < \infty$ propagating in the $+z$ direction due to sources from E [9]) we arrive at the expression for $\mathbb{O}_E$ in eq. (6.8). We see now that the Lippmann-Schwinger equation eq. (6.7) is simply the statement that the solution for the correlator $\mathbf{E} \otimes \mathbf{E}$ in the full system $(P + A)$ is obtained by taking the tensor product of the field solution eq. (6.21); for

[9] Assuming, as before, that we can ignore the environmental sources from $z = -\infty$, as they are completely absorbed by P

example for P, we have:

$$\mathbf{E} \otimes \mathbf{E}^* = \left[(\mathbb{O}_P)_{++}\,\mathbf{E}_+(0) + (\mathbb{O}_P)_{-+}\,\mathbf{E}_-(0)\right] \otimes \left[(\mathbb{O}_P)_{++}\,\mathbf{E}_+(0) + (\mathbb{O}_P)_{-+}\,\mathbf{E}_-(0)\right]^* \tag{6.25}$$

with a similar result holding for sources from the environment. Multiplying by the initial weights $\mathbb{D}_j^0$ gives the result eq. (6.7).

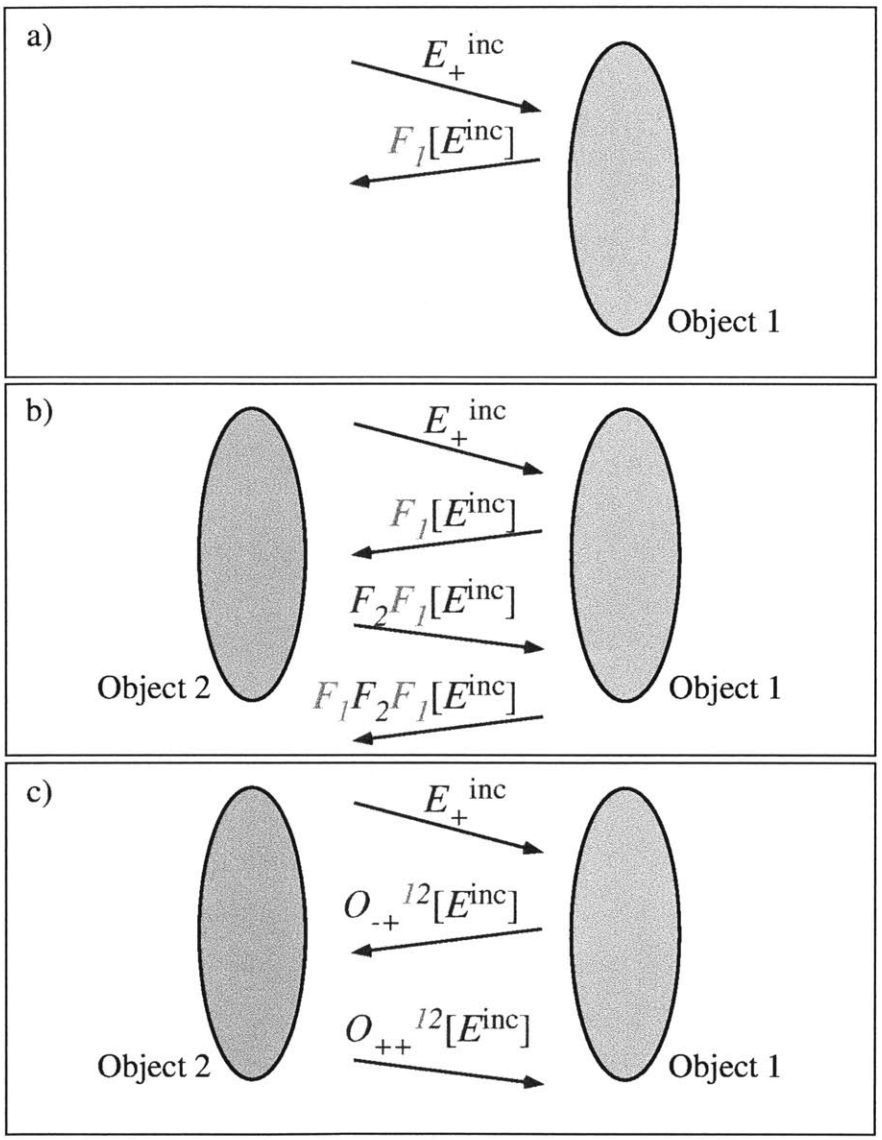

Figure 6-9: Schematic showing the physical meaning behind the $\mathbb{O}$ matrices; the processes are discussed in more detail in the text.

Chapter 7

Computation and visualization of photonic quasicrystal spectra via Bloch's theorem

In this chapter, we examine photonic *quasi*-crystals (PQCs), dielectric structures that, while lacking periodicity, still possess long-range order. We present a method by which the energy spectrum and the eigenstates of a PQC can be obtained by solving Maxwell's equations in higher dimensions for any PQC defined by the standard cut-and-project construction, to which a generalization of Bloch's theorem applies. This is in contrast to previous methods, which have relied on the use of rational approximates in large supercells to compute the eigenfrequencies and/or local density of states (LDOS) to an approximation of the true aperiodic structure. We validate our technique by examining the one-dimensional Fibonacci quasicrystal and the two-dimensional octagonal lattice. In addition, we demonstrate how one can compute band structures with defect states in the same higher-dimensional superspace. We find that by smoothing the structure in its native superspace one can obtain exponential convergence of the bandstructure, something that is impossible to do using a supercell. Finally, we investigate the application of this method to two-dimensional PQCs.

7.1 Introduction and Background

We propose a computational method to solve for the spectra and eigenstates of quasicrystalline electromagnetic structures by directly solving a periodic eigenproblem in a higher-dimensional lattice. Such photonic quasicrystals (PQCs) have a number of unique properties compared to ordinary periodic structures [2, 26, 28, 34, 39, 52, 53, 55, 57, 85, 87, 107, 128, 137, 144, 177, 203, 205, 207, 209, 211, 217, 218], especially in two or three dimensions where they can have greater rotational symmetry and therefore offer some hope of complete photonic band gaps with lower index contrast [66, 80, 210, 218] than the roughly 2:1 contrast currently required for periodic structures [114]. However, the study of photonic quasicrystals has always been indirect, in which the aperiodicity of the exact structure is only approached in the limit in which a large "supercell" calculation captures a sufficiently large portion of the aperiodic lattice. In contrast, the present method captures the entire infinite aperiodic structure in a single higher-dimensional unit cell. The idea that many quasicrystals can be constructed by an irrational slice of a higher-dimensional lattice is well known [72, 189, 192], and in fact is the most common formulation of quasicrystals in two and three dimensions [98, 116, 202], but the possibility of direct numerical calculations within the higher-dimensional space seems to have been little explored outside of some tight-binding calculations in one-dimensional quantum systems [36, 109]. There have been several previous numerical approaches to simulating quasicrystal structures in electromagnetism and quantum mechanics, but all have involved either a periodic approximate or a large supercell with absorbing/radiating boundary conditions.

In one dimension, a typical quasicrystal is an aperiodic sequence of two or more materials, determined either by a slice of a higher-dimensional lattice [189] or by some "string concatenation" rule [72]. In either case, efficient 2×2 transfer-matrix methods are available that allow one to quickly compute the transmission spectra and density of states for supercells consisting of many thousands of layers [59, 69]. Two- and three-dimensional quasicrystals are almost always defined as an irrational slice (i.e., incommensurate Miller indices) of a higher-dimensional lattice; for exam-

ple, the famous Penrose tiling can be viewed as a two-dimensional slice of a five-dimensional cubic lattice or of a four-dimensional root lattice A_4 [192]. In such cases, supercell computations of a finite portion of the infinite aperiodic structure (or a rational approximate thereof [59, 189]) require slower numerical methods, most commonly finite-difference time-domain (FDTD) simulations [55,56,85] or planewave expansions [40,79]. Unfortunately, these methods become very expensive for large supercells, nearly prohibitively so for three-dimensional quasicrystals—there have been experiments for 3D PQCs [98, 116], but as yet few theoretical predictions [190, 215]. With FDTD methods, for example, the PQC local density of states is typically integrated in Monte-Carlo fashion via random sources or initial conditions [2, 128, 203], but many simulations are required to sample all possible modes in a large supercell. Also, the finite domain of a supercell becomes even more significant in higher dimensions where a tractable supercell is necessarily smaller, as there can be localized states [39, 55, 85, 128] whose presence is dependent on the particular region of the PQC considered. Our method of computing the spectrum directly in the higher-dimensional unit cell, on the other hand, requires no supercell to capture the infinite aperiodic structure—it uniformly samples (up to a finite resolution) every possible supercell of the infinite quasicrystal, rather than any particular subsection. The influence of finite-resolution on the convergence of the spectrum can be systematically understood: one is not "missing" any part of the quasicrystal, so much as resolving the entire quasicrystal with lower resolution.

The structure of this chapter is as follows: in Sec. 7.1.1 we review the "cut-and-project" method for defining a PQC as a slice of a higher-dimensional lattice, followed in Sec. 7.2 by a description of our computational method in the higher-dimensional lattice. There, we describe the extension of Maxwell's equations to higher dimensions and also describe its solution in terms of a higher-dimensional Bloch planewave expansion. As a proof of concept, we present a sequence of one-dimensional examples in Sec. 7.3. First, we compare results for a one-dimensional "Fibonacci sequence" with standard one-dimensional transfer-matrix techniques. Second, as mentioned above, we demonstrate how one can use the same technique to study defects in the quasicrys-

tal, as demonstrated in the one-dimensional "Fibonacci" example. We demonstrate the ease with which one can construct and explore different quasicrystals by continuously varying the cut angle, and how exponential convergence with resolution can be obtained from smoothing the superspace structure. We then turn to optimizing the superspace dielectric structure, in order to obtain the largest fractional bandgap, and find that in all cases the optimal structure is actually a *periodic* quarter-wave stack. Finally, we discuss extension of the method to higher-dimensional structures.

7.1.1 Quasicrystals via cut-and-project

Given a periodic lattice, any lower dimensional cross-section of that lattice may be either periodic or quasi-periodic, depending upon the angle of the cross-section. For example, the periodic 2D cross-sections of a 3D crystal are the lattice planes, defined in crystallography by integer Miller indices. If the Miller indices have irrational ratios, on the other hand, the cross-section is aperiodic but still has long-range order because of the underlying higher-dimensional periodicity. This is what is known as a "cut-and-project" method of defining a quasicrystalline structure: as a slice of a periodic structure in a higher-dimensional "superspace" [72, 189]. (For a thorough discussion of quasicrystals via cut-and-project, see Ref. 72.) Cut-and-project defines a specific class of quasicrystals; equivalently, and more abstractly, cut-and-project corresponds to structures whose Fourier transform has support spanned by a finite number of reciprocal basis vectors (the projection of the reciprocal lattice vectors from higher dimensions) [72, 202]. This class includes most commonly considered quasicrystals in two or three dimensions, including the Penrose tiling [192], as well as many one-dimensional quasicrystals including a version of the Fibonacci structure.

For example, consider the Fibonacci PQC in one dimension formed from two materials $\varepsilon_A = 4.84$ and $\varepsilon_B = 2.56$ in layers of thickness A and B, respectively, similar to a recent experimental structure [34]. The Fibonacci structure S is then defined by the limit $n \to \infty$ of the string-concatenation rule $S_n = S_{n-2}S_{n-1}$ with starting strings $S_0 = B$ and $S_1 = A$ [34], generating a sequence $BABAABABAABA\cdots$. In the case where B/A is the golden ratio $\tau = (1+\sqrt{5})/2$, exactly the same structure

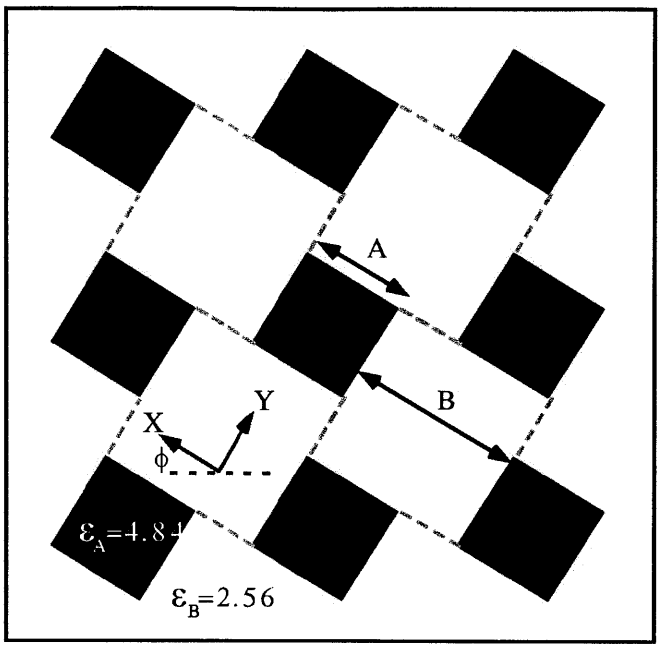

Figure 7-1: Unit cell of the Fibonacci superspace dielectric. The physical dielectric is obtained by taking a slice at an angle $\tan\phi = \tau$. Black/white are the dielectric constants of the structure factor material and air, chosen to be $\varepsilon = 4.84$ and $\varepsilon = 2.56$, respectively.

can be generated by a slice of a two-dimensional lattice as depicted in Fig. 7-1 [72]. The slice is at an angle ϕ with an irrational slope $\tan\phi = 1/\tau$, and the unit cell of the 2D lattice is an $A \times A$ square at an angle ϕ in a square lattice with period $(A + B)\sin\phi = a$. Because the slope is irrational, the offset/intercept of the slice is unimportant: any slice at an angle ϕ intercepts the unit cell at infinitely many points, filling it densely.

For thickness ratios $B/A \neq \tau$, the Fibonacci structure cannot be constructed by cut-and-project, and in general string-concatenation rules can produce a different range of structures (such as the Thue-Morse PQC [33]) than cut-and-project[1]. This is partly a question of definition—some authors reserve the term "quasicrystal" for cut-and-project structures [192]. In any case, cut-and-project includes a wide variety of aperiodic structures, including most of the structures that have been proposed in two

[1]Similarly, there are two-dimensional structures defined by analogous rules that cannot be formed by cut-and-project, and some structures such as the 2D Fibonacci crystal where it is unclear whether a cut-and-project construction is possible [106]

or three dimensions (where they can be designed to have n-fold rotational symmetry for any n), and are the class of quasicrystals that we consider in this paper.

In general, let $d \leq 3$ be the number of physical dimensions of a quasicrystal structure generated by a d-dimensional "slice" of an n-dimensional periodic structure ($n > d$). Denote this slice by X (the physical space) with coordinates $\mathbf{x} \in \mathbb{R}^d$, and denote the remaining $n - d$ coordinates by $\mathbf{y} \in \mathbb{R}^{n-d}$ in the "unphysical" space Y (so that the total n-dimensional superspace is $Z = X \oplus Y$). The primitive lattice vectors $\mathbf{R}_i \in Z$ define the orientation of the lattice with respect to the slice (rather than vice versa), with corresponding primitive reciprocal vectors $\mathbf{G}_i$ defined by the usual $\mathbf{R}_i \cdot \mathbf{G}_j = 2\pi\delta_{ij}$ [72]. (The concept of an "irrational slice" is commonly used in the quasicrystal literature. However, a general definition of what is meant by an "irrational slice" seems difficult to find, and less evident in dimensions $d > 2$. A more precise definition of "irrational slice" in general dimensions and a proof that it is dense in the unit cell is given in Appendix 6.)

The physical dielectric function $\varepsilon(\mathbf{x})$ is then constructed by starting with a periodic dielectric function $\varepsilon(\mathbf{x}, \mathbf{y})$ in the superspace and evaluating it at a fixed $\mathbf{y}$ (forming the slice). Because an irrational slice is dense in the unit cell of the superspace [72], it doesn't matter what value of $\mathbf{y}$ one chooses, as discussed below. In principle, one could define the unit cell of ε in the superspace to be any arbitrary n-dimensional function, but in practice it is common to "decorate" the higher-dimension unit cell with extrusions of familiar d-dimensional objects [72, 192]. More precisely, "cut-and-project" commonly refers to constructions where a set of lattice points within a finite window of the cut plane are projected onto the cut plane, and this is equivalent to a simple cut where objects at the lattice points are extruded in the y direction by the window width [72]. In particular, the extrusion window is commonly an inverted projection (shadow) of the unit cell onto the y directions [72], although this is not the case for the Fibonacci construction of Fig. 7-1. Note that the higher-dimensional lattice need not be hypercubic. For example, the Penrose tiling can be expressed as a two-dimensional slice of either a five-dimensional hypercubic lattice or of a non-orthogonal four-dimensional root lattice A_4 [192]. For computational purposes, the

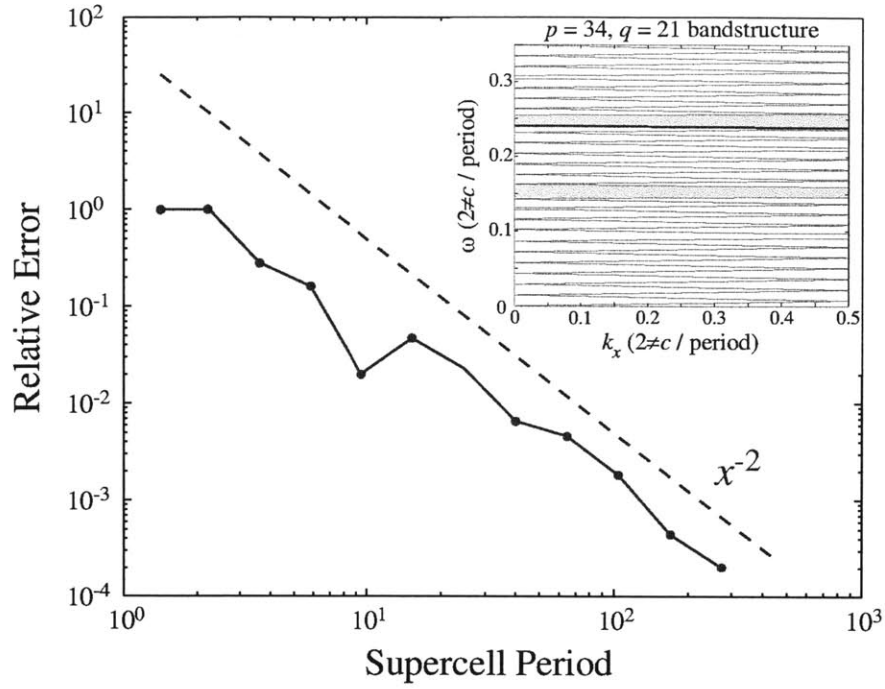

Figure 7-2: Error in the lower band edge as a function of the supercell period, which is $\sqrt{p^2+q^2}$, where p/q is a rational approximate to $\tau = \frac{1+\sqrt{5}}{2}$. The dashed black line indicates quadratic convergence, consistent with the fact that $|p/q - \tau| \sim \frac{1}{p^2+q^2}$. Inset: bandstruture for the $p = 34$, $q = 21$ approximate. The $k_x = 0$ point of the red band indicates the frequency points used for the convergence.

lower the dimensionality the better.

7.1.2 Supercell approach

Before proceeding to the superspace method, we present an example of a supercell calculation for the Fibonacci quasicrystal. In the supercell approach, the exact quasicrystal is replaced with a *rational approximate*, in which the structure of Fig. 7-1 is constructed from a cut angle of $\tan\phi = \frac{p}{q}$, where $\frac{p}{q}$ is a rational number close to τ. For example, the first few rational approximates to τ are $1/1, 2/1, 3/2, 5/3\ldots$. As the cut line has a rational slope, the cut-and-project construction will yield a periodic structure with period $\sqrt{p^2+q^2}$. As p and q increase, the period of the structure diverges, while the error $\left|\frac{p}{q} - \tau\right|$ goes to zero. These successively larger periodic structures therefore approximate the exact aperiodic structure. To examine

how rapidly the bandstructure of these rational approximates converges to the exact bandstructure, we examine the lower band edge of a bandgap at $\omega \approx 0.235$, shown in the inset to Fig. 7-2. Fixing the Bloch vector of the periodic structure to be $k_x = 0$, we plot the error of this band edge for successive rational approximates in the main part of Fig. 7-2. Although the convergence isn't exact, the error generally goes as the inverse square of the structure period.

This dependence can be understood from the convergence of the rational approximates p/q to τ: for any real number x, the error in the rational approximate is bounded by $\left|\frac{p}{q} - x\right| < \frac{1}{\sqrt{5}q^2}$ [65]. Since $p \sim q$, this bound goes as the inverse-square of the period. Therefore, we see that rate of convergence of the rational approximates to the exact bandstructure is intimately related to how "rational" the cut angle is. This makes sense, since if $\tan\phi$ is a rational number, the error will be exactly zero for a sufficiently large period. τ happens to be the most "irrational" number, which can be seen from its continued-fraction expansion [31]:

$$\tau = 1 + \frac{1}{1 + \frac{1}{1+\ldots}}. \tag{7.1}$$

Successive rational approximates simply correspond to truncating this expansion. Less "irrational" numbers have numbers larger than 1 appearing in the continued-fraction expansion, so we expect that in general the convergence is must faster than $\frac{1}{q^2}$ for other values of $\tan\phi$; τ is special in that it nearly saturates this bound. However, in Sec. 7.3.4 we will see that our superspace method can yield *exponential* convergence in the bandstructure for a smoothed version of Fig. 7-1, regardless of the value of ϕ.

7.2 Computations in Higher Dimensions

Although the cut-and-project technique is a standard way to *define* the quasicrystal structure, previous computational studies of photonic quasicrystals then proceeded to simulate the resulting structure only in the projected (d-dimensional) physical space. Instead, it is possible to extend Maxwell's equations into the periodic n-dimensional

superspace, where Bloch's theorem applies to simplify the computation. By looking at only the unit cell in n dimensions one can capture the infinite d-dimensional quasicrystal. Our development of this technique was inspired by earlier research on analogous electronic quasicrystals that applied a tight-binding method in two dimensions to compute the spectrum of a one-dimensional electronic quasicrystal [36, 109].

Let us start with Maxwell's equations in the physical space X for the quasicrystal $\varepsilon(\mathbf{x}, \mathbf{y})$ at some fixed $\mathbf{y}$ (that is, $\mathbf{y}$ is viewed as a parameter, not a coordinate). Maxwell's equations can be written as an eigenproblem for the harmonic modes $\mathbf{H}(\mathbf{x}, \mathbf{y})e^{-i\omega t}$ [73], where again $\mathbf{y}$ appears as a parameter.

$$\nabla_{\mathbf{x}} \times \frac{1}{\varepsilon(\mathbf{x}, \mathbf{y})} \nabla_{\mathbf{x}} \times \mathbf{H} = (\omega/c)^2 \mathbf{H}, \tag{7.2}$$

where $\nabla_{\mathbf{x}} \times$ denotes the curl with respect to the $\mathbf{x}$ coordinates. Assuming that the structure is quasicrystalline, i.e. that X is an irrational slice of the periodic superspace Z, then ω should not depend upon $\mathbf{y}$ [36]. The reason is that $\mathbf{y}$ only determines the offset of the "initial" slice of the unit cell (for $\mathbf{x} = 0$), but as we reviewed above the slice (considered in all copies of the unit cell) fills the unit cell densely. Therefore, any change of $\mathbf{y}$ can be undone, to arbitrary accuracy, merely by offsetting $\mathbf{x}$ to a different copy of the unit cell. An offset of $\mathbf{x}$ doesn't change the eigenvalues ω, although of course it offsets the eigenfunctions $\mathbf{H}$.

The fact that ω is independent of $\mathbf{y}$ allows us to re-interpret eq. (7.2), without actually changing anything: we can think of $\mathbf{y}$ as a coordinate rather than a parameter, and the operator on the left-hand side as an operator in d-dimensional space. Note that $\mathbf{H}$ is still a three-component vector field, and $\nabla_{\mathbf{x}} \times$ is still the ordinary curl operator along the $\mathbf{x}$ directions, so this is not so much a higher-dimensional version of Maxwell's equations as an extension of the unmodified ordinary Maxwell's equations into a higher-dimensional parameter space. The $\mathbf{y}$ coordinate appears in the operator only through ε. Because ω is independent of $\mathbf{y}$, i.e. it is just a number rather than a function of the coordinates, the equation (7.2) in higher dimensions is still an eigenproblem, and its spectrum of eigenvalues ω is the same as the spectrum of the

d-dimensional quasicrystal, since the equations are identical. The physical solution is obtained by evaluating these higher-dimensional solutions at a fixed $\mathbf{y}$, say $\mathbf{y} = 0$ (where a different $\mathbf{y}$ merely corresponds to an offset in $\mathbf{x}$ as described above).

For a real, positive ε, both the physical operator and the extended operator in in eq. (7.2) are Hermitian and positive semi-definite, leading to many important properties such as real frequencies ω [73].

7.2.1 Bloch's theorem and numerics for quasicrystals

Because the superspace eigenproblem is periodic, Bloch's theorem applies: the eigenfunctions $\mathbf{H}(\mathbf{x}, \mathbf{y})$ can be written in the Bloch form $\mathbf{h}(\mathbf{z})e^{i\mathbf{k}\cdot\mathbf{z}}$, where $\mathbf{h}$ is a *periodic* function defined by its values in the unit cell, and $\mathbf{k}$ is the n-dimensional Bloch wavevector [73].

Here, $\mathbf{k}$ determines the phase relationship between $\mathbf{H}$ in different unit cells of the superspace, but it does not have a simple interpretation once the solution is projected into physical space. The reason is that $\mathbf{h}$, viewed as a function of $\mathbf{x}$, is again only quasiperiodic: translation in $\mathbf{x}$ "wraps" the slice into a different portion of the unit cell, so both $\mathbf{h}$ and $e^{i\mathbf{k}\cdot\mathbf{z}}$ change simultaneously and the latter phase cannot be easily distinguished. This prevents one from defining a useful phase or group velocity of the PQC modes.

The key point is that Bloch's theorem reduces the eigenproblem to a finite domain (the n-dimensional unit cell), rather than the infinite domain required to describe the quasicrystal solutions in physical space. This means that standard numerical methods to find the eigenvalues of differential operators are immediately applicable. For example, since the solution $\mathbf{h}$ is periodic, one can apply a planewave expansion method [76] for $\mathbf{h}$:

$$\mathbf{h}(\mathbf{z}) = \sum_{\mathbf{G}} \tilde{\mathbf{h}}_{\mathbf{G}} e^{i\mathbf{G}\cdot\mathbf{z}}, \tag{7.3}$$

where the summation is over all n-dimensional reciprocal lattice vectors $\mathbf{G}$. Because the curl operations only refer to the $\mathbf{x}$ coordinates, $\nabla_{\mathbf{x}} \times \mathbf{h}$ is replaced by a summation over $\mathbf{g}_{\mathbf{x}} \times \tilde{\mathbf{h}}_{\mathbf{G}}$, where $\mathbf{g}_{\mathbf{x}}$ denotes $\mathbf{G}$ projected into X. The resulting eigenproblem for

the Fourier coefficients $\tilde{\mathbf{h}}$ (once they are truncated to some wavevector cutoff) can be computed either by direct dense-matrix methods [63] or, more efficiently, by iterative methods exploiting fast Fourier transforms [76]. In the present paper, we do the former, which is easy to implement in higher dimensions. We should also remind the reader that there is a constraint $\nabla_{\mathbf{x}} \cdot \mathbf{H} = 0$ on the eigenfunctions, in order to exclude unphysical solutions with static magnetic charges. In a planewave method, this leads to a trivial constraint $(\mathbf{k_x} + \mathbf{g_x}) \cdot \tilde{\mathbf{h}} = 0$, again with $\mathbf{k}$ and $\mathbf{G}$ projected into X.

7.2.2 The spectrum of the quasicrystal

With a familiar eigenproblem arising from Bloch's theorem, such as that of a periodic physical structure, the eigenvalues form a band structure: discrete bands $\omega_n(\mathbf{k})$ that are continuous functions of $\mathbf{k}$, with a finite number of bands in any given frequency range [6]. For a finite-resolution calculation, one obtains a finite number of these bands ω_n with some accuracy that increases with resolution, but even at low resolutions the basic structure of the low-frequency bands is readily apparent. The eigenvalues of the higher-dimensional quasicrystal operator of eq. (7.2), on the other hand, are quite different.

The underlying mathematical reason for the discrete band structure of a physical periodic structure is that the Bloch eigen-operator for a periodic physical lattice, $(\nabla + i\mathbf{k}) \times \frac{1}{\varepsilon}(\nabla + i\mathbf{k}) \times$, is the inverse of a compact integral operator corresponding to the Green's function, and hence the spectral theorem applies [60]. Among other things, this implies that the eigenvalues at any given $\mathbf{k}$ for a finite unit cell form a discrete increasing sequence, with a finite number of eigenvalues below any finite ω. The same nice property does not hold for the operator extended to n dimensions, because along the $\mathbf{y}$ directions we have no derivatives, only a variation of the scalar function ε. Intuitively, this means that the fields can oscillate very fast along the $\mathbf{y}$ directions without necessarily increasing ω, allowing one to have infinitely many eigenfunctions in a finite bandwidth. More mathematically, an identity operator is not compact and does not satisfy the spectral theorem [60], and since the operator of eq. (7.2) is locally the identity along the $\mathbf{y}$ directions the same conclusion applies.

This means that, when the $\mathbf{y}$ direction is included as a coordinate, it is possible to get an infinite number of bands in a finite bandwidth at a fixed $\mathbf{k}$.

In fact, as we shall see below, this is precisely what happens, and moreover it is what *must* happen in order to reproduce the well-known properties of quasicrystal spectra. It has been shown that quasicrystal spectra can exhibit a fractal structure [72], with infinitely many gaps (of decreasing size) in a finite bandwidth, and such a structure could not arise from an ordinary band diagram with a finite number of bands in a given bandwidth. Of course, once the unit cell is discretized for numerical computation, the number of degrees of freedom and hence the number of eigenvalues is finite. However, as the resolution is increased, not only do the maximum frequency and the accuracy increase as for an ordinary computation, but also the number of bands in a given bandwidth increases. Thus, as the resolution is increased, more and more of the fractal structure of the spectrum is revealed.

7.3 One-dimensional results

As a proof of concept implementation of cut-and-project, we construct a Fibonacci quasicrystal in Sec. 7.3.1 using the projection method described above, compute the band structure as a function of the projected wave-vector k_d and compare to a transfer-matrix calculation of the same quasicrystal structure. We also demonstrate the field visualization enabled by the projection method, both in the superspace (n dimensions) as well as in the physical space (d dimensions). In Sec. 7.3.2, we demonstrate how this method can accommodate systems with defects. Finally, we explore several one-dimensional quasicrystal configurations in Sec. 7.3.3 by varying the cut angle ϕ.

7.3.1 Fibonacci quasicrystal

Spectrum

We solved eq. (7.2) numerically using a planewave expansion in the unit cell of the 2D superspace, as described above, for the 1D Fibonacci quasicrystal structure depicted

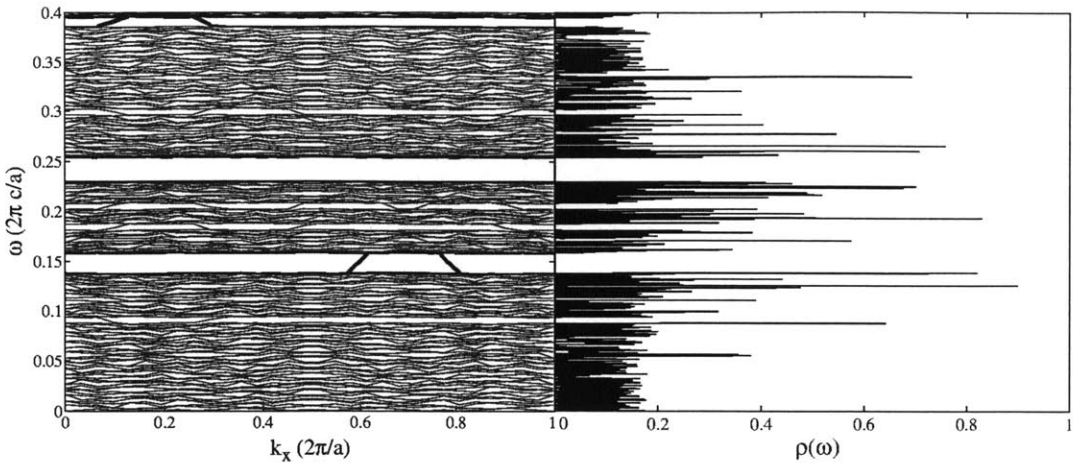

Figure 7-3: *Left:* Frequency spectrum ω of the Fibonacci quasicrystal vs. "wave-vector" k_x. The blue lines indicate spurious states which arise due to finite resolution effects (see text). *Right:* Corresponding density of states $\rho(\omega)$ computed using a transfer-matrix technique with a supercell of 10^4 layers.

in Fig. 7-1. The resulting band diagram is shown in Fig. 7-3(left), along with a side-by-side comparison of the local density of states in Fig. 7-3(right) calculated using a transfer-matrix approach with a supercell of 10^4 layers [102]. The two calculations show excellent agreement in the location of the gaps, except for one or two easily-identified spurious bands inside some of the gaps, which are discussed in further detail below. The most important feature of Fig. 7-3(left) is the large number of bands even in the finite bandwidth $\omega \in [0, 0.4]$, with the number of bands increasing proportional to the spatial resolution (planewave cutoff). This is precisely the feature predicted abstractly above, in Sec. 7.2.2: at a low resolution, one sees only the largest gaps, and at higher resolutions further details of the fractal spectrum are revealed as more and more bands appear within a given bandwidth, very different from calculations for periodic physical media. The important physical quantity is not so much the band structure, since $\mathbf{k}$ has no simple physical meaning as discussed previously, but rather the density of states formed by projecting the band structure onto the ω axis. In this density of states, the small number of spurious bands within the gaps, which arise from the discretization as discussed below, plays no significant role: the density of states is dominated by the huge number of flat bands (going to infinity as the

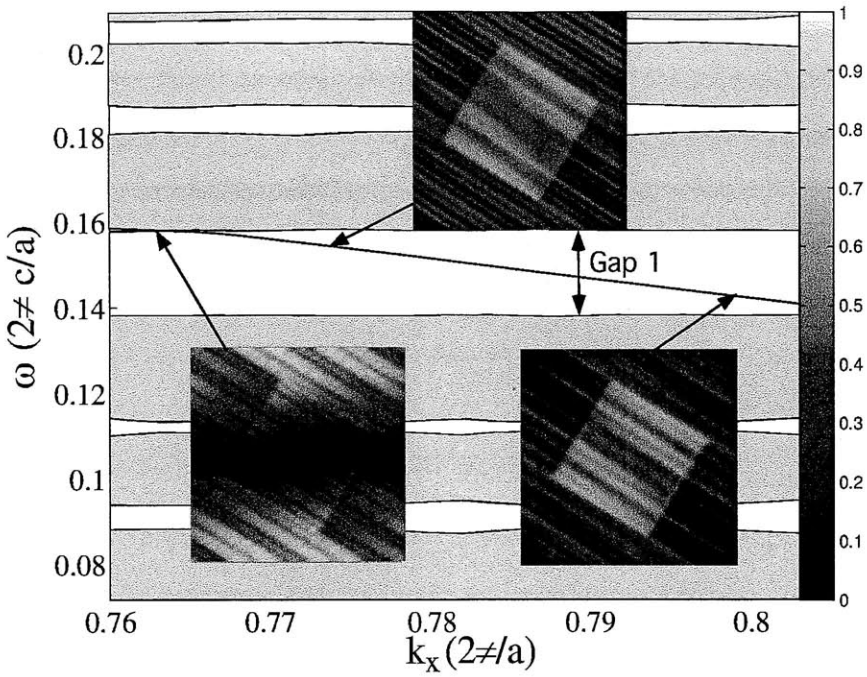

Figure 7-4: Enlarged view of the Fibonacci spectrum showing a gap with a spurious band crossing it. Insets show the magnetic field $|H_z|$ for the spurious band at various k_x—the localization of this mode around the X-parallel edges of the dielectric indicate that this is a discretization artifact.

resolution is increased), and the addition of one or two spurious bands is negligible.

Spurious modes

As the wavevector $\mathbf{k}$ varies, most of the bands in the spectrum of Fig. 7-3 are flat, except for certain modes (highlighted in blue) which appear to cross the band gaps relatively quickly. In fact, a simple argument shows that, in the limit of infinite resolution, the physical spectrum cannot depend on $\mathbf{k}$, and hence any strongly $\mathbf{k}$-dependent band must be a numerical artifact. First, ω cannot depend on the components of $\mathbf{k}$ in the unphysical directions Y, because the Maxwell operator of eq. (7.2) has no $\mathbf{y}$-derivatives (equivalently, any phase oscillations in $\mathbf{y}$ commute with the operator). Second, ω cannot depend on the components of $\mathbf{k}$ in the physical directions X, either. The reason is that, from Bloch's theorem, $\mathbf{k}$ and $\mathbf{k}+\mathbf{G}$ give the same eigensolutions for any reciprocal lattice vector $\mathbf{G}$, and the projections of the reciprocal lattice vectors

are dense in X for a quasicrystal.

These "spurious" bands that appear arise from the discretization of the dielectric interfaces parallel to the slice direction. Because the slice is at an irrational angle, it will never align precisely with a uniform grid, resulting in inevitable staircasing effects at the boundary. With ordinary electromagnetic simulations, these staircasing effects can degrade the accuracy [51], but here the lack of derivatives perpendicular to the slice allows spurious modes to appear along these staircased edges (there is no frequency penalty to being localized perpendicular to the slice). Indeed, if one looks at the field patterns for the spurious modes, one of which is shown in the inset of Fig. 7-3(right), one sees that the field intensity is peaked along the slice-parallel dielectric interfaces. Because they are localized to these interfaces and are therefore dominated by the unphysical staircasing, the spurious modes behave quite differently from the "real" solutions and are easily distinguished qualitatively and quantitatively (e.g via their $\mathbf{k}$-dependence). In one dimension, as the resolution is increased, the number of spurious modes in a given gap does not increase like all of the other bands, because the thickness of the staircased interface region decreases proportional to the resolution. This makes the gaps in the band structure obvious: here, they are the only frequency ranges for which the number of eigenvalues does not increase with resolution. Equivalently, as noted above, the contribution of the spurious bands to the density of states is asymptotically negligible as resolution is increased. However, in higher dimensions we have found that the presence of spurious modes is more pronounced and tends to obscure even the large bandgaps. Therefore, we desire a rigorous method to identify and eliminate spurious modes, which we now describe.

Examining the right panel of Fig. 7-5, which contains the frequency spectrum of the same Fibonacci lattice explored previously, we see that the dispersion curves of certain spurious in different bandgaps appear to fall along a straight line (the black dashed line in Fig. 7-5[right]). This dispersion curve is characteristic of modes in a uniform medium. This observation lead us to speculate that spurious modes appear at the boundaries of the reciprocal space, that is, at the extremal values of $\mathbf{k} + \mathbf{G}$ allowed in the computational cell. As they are at the cell boundaries, these modes are

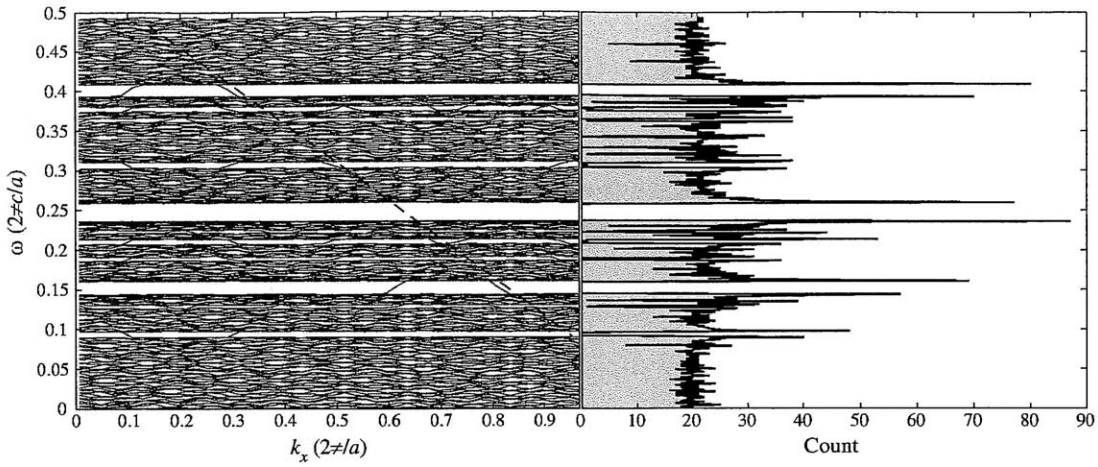

Figure 7-5: Identification and removal of spurious modes in one dimension. Left: spectrum of the Fibonacci quasicrystal, as in Fig. 7-3. We have superposed a black dashed line to indicate that the spurious modes appear to largely follow a linear dispersion relation. Right: density-of-states computed by removing all modes that satisfy $\lambda(\mathbf{H}) \geq 0.9$, where λ is defined in eq. (7.4). All spurious modes in the large bandgaps have vanished.

not represented accurately because their coupling to nearby values of $\mathbf{k}+\mathbf{G}$ are not accounted for. In normal planewave-expansion methods, this does not matter as one is usually interested in the low-frequency modes, which are not strongly affected by the truncation at high values of $\mathbf{k}+\mathbf{G}$. However, in our case high values of $|\mathbf{k}+\mathbf{G}|$ can correspond to low values of $|(\mathbf{k}+\mathbf{G})_{\mathbf{x}}|$ - therefore, this truncation may manifest itself even in the low-lying spectrum. Testing this hypothesis, we filtered the frequency spectrum of Fig. 7-5(Left) using the following measure

$$\lambda(\mathbf{H}) \equiv \frac{\sum_{\mathbf{G}\in\text{Extreme}} |\mathbf{H}_{\mathbf{G}}|^2}{\sum_{\mathbf{G}} |\mathbf{H}_{\mathbf{G}}|^2} \tag{7.4}$$

Here a reciprocal vector is "extreme" if it is at the boundary of the computational cell.

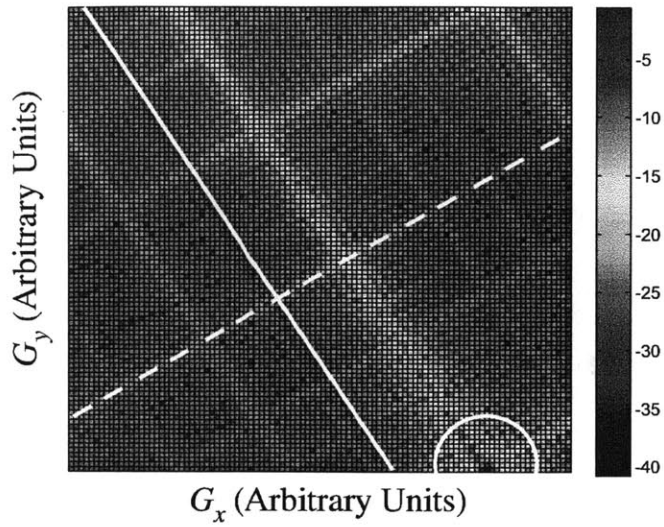

Figure 7-6: Fourier-space spectrum $|\mathbf{H_G}|^2$ of a spurious mode, on a log scale: dashed white line denotes the "physical" X direction in which fluctuations carry an energy penalty, and the solid white line denotes the "un-physical" Y direction. Circle denotes the peak in the mode's Fourier-space support, which occurs at the boundary of the computational cell.

If $\lambda(\mathbf{H}) > 0.9$, we exclude the mode. The filtered results are shown in Fig. 7-5(Right). We depict the results as a density of states because the bands now discontinuously jump across the bandgaps as k_x is varied. Shown in this way, we see that all spurious modes in the large bandgaps have been removed, validating our assumptions.

We can directly examine the behavior of spurious modes by examining the $\mathbf{H_G}$ directly in reciprocal space. These are shown in Fig. 7-6 and Fig. 7-7. The former depicts a spurious mode in the main bandgap, while the latter depicts a "physical" mode. There is a clear difference between the two modes, with the spurious mode strongly weighted at the cell boundary (in this case, the weight is over 99% on the boundary).

Visualizing the eigenmodes in superspace

Computing the eigenmodes in the higher-dimensional superspace immediately suggests a visualization technique: instead of plotting the quasiperiodic fields as a function of the physical coordinates x by taking a slice, plot them in the two-dimensional

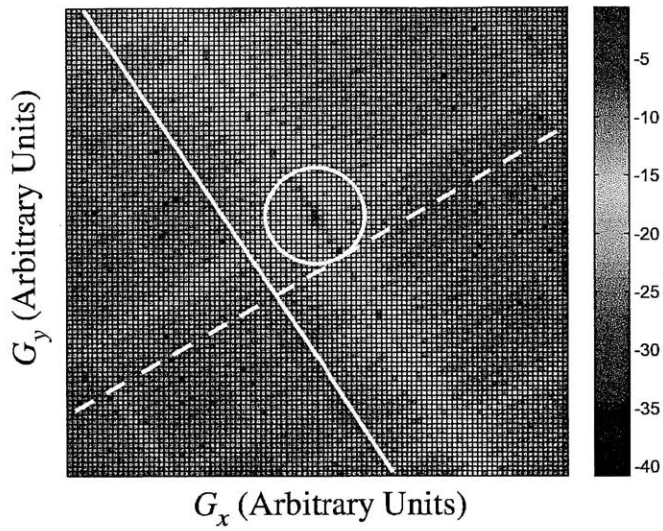

Figure 7-7: Fourier-space spectrum $|\mathbf{H_G}|^2$ of a physical mode, on a log scale. In contrast to Fig. 7-6, the primary support of this mode occurs in the center of the computational cell.

superspace. This has the advantage of revealing the entire infinite aperiodic field pattern in a single finite plot [36]. Such plots were already used above, to aid in understanding the spurious modes localized at staircased interfaces. A typical extended mode profile is shown in Fig. 7-8, plotted both as a function of the physical coordinate x for large supercell and also in the unit cell of the superspace (inset). In the inset superspace plot, one can clearly see the predicted field oscillations perpendicular to the slice plane, as well as a slower oscillation rate (inversely proportional to the frequency) parallel to the slice. In the plot versus x, one can see the longer-range quasi-periodic structure that arises from how the slice wraps around the unit cell in the superspace. The factor of three to four long-range variations in the field amplitude are suggestive of the critically localized states (power-law decay) that one expects to see in such quasicrystals [34, 86, 139].

By visualizing the bands in this way, we can demonstrate the origin of the quasicrystal band gap in an interesting way. In an ordinary photonic crystal, the gap arises because the lowest band concentrates its electric-field energy in the high-dielectric regions (due to the variational principle), while the next band (above the gap) is forced to have a nodal plane in these regions (due to orthogonality) [73].

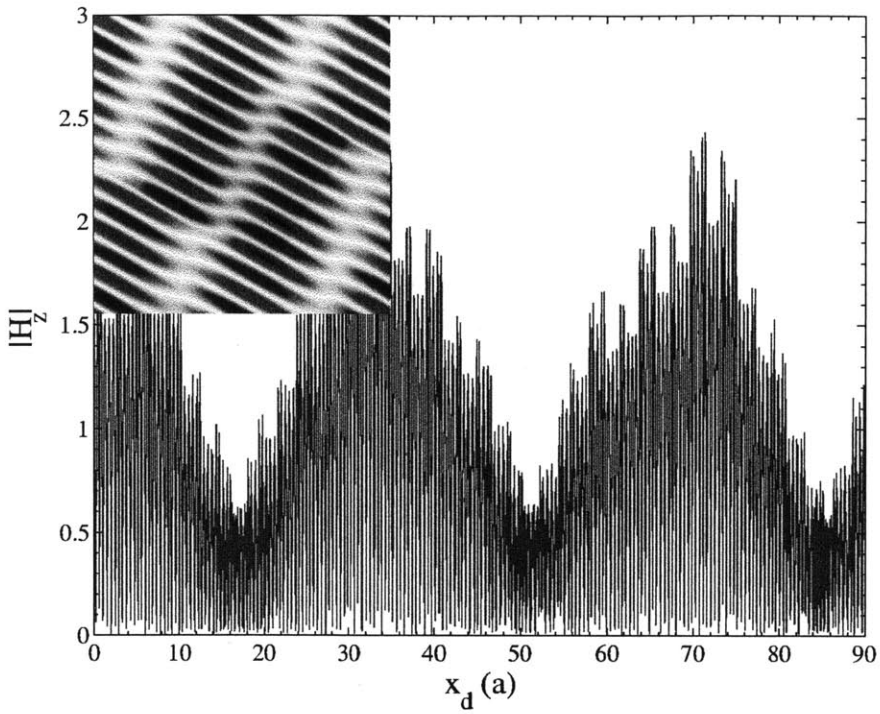

Figure 7-8: Plot of the magnetic field amplitude $|H_z|$ for a band-edge state taken along a slice of the two-dimensional superspace (in the ϕ direction). *Inset:* Two-dimensional superspace field profile (red/white/blue indicates positive/zero/negative amplitude).

A very similar phenomenon can be observed in the quasicrystal eigenmodes, when plotted in the superspace. In particular, Fig. 7-9 displays the electric-field energy distribution of the band-edge states just above and below gaps 1 and 2 of Fig. 7-3. Very similar to an ordinary two-dimensional photonic crystal, the bands just below the gaps are peaked in the dielectric squares, whereas the upper-edge bands have a nodal plane in these squares. If the same fields were plotted only in the physical coordinate space, the position of the peaks and nodes would vary between adjacent layers and this global pattern (including the relationship between the two gaps) might not be apparent. In contrast to a two-dimensional photonic crystal, on the other hand, the quasicrystalline field pattern has fractal oscillations in the superspace.

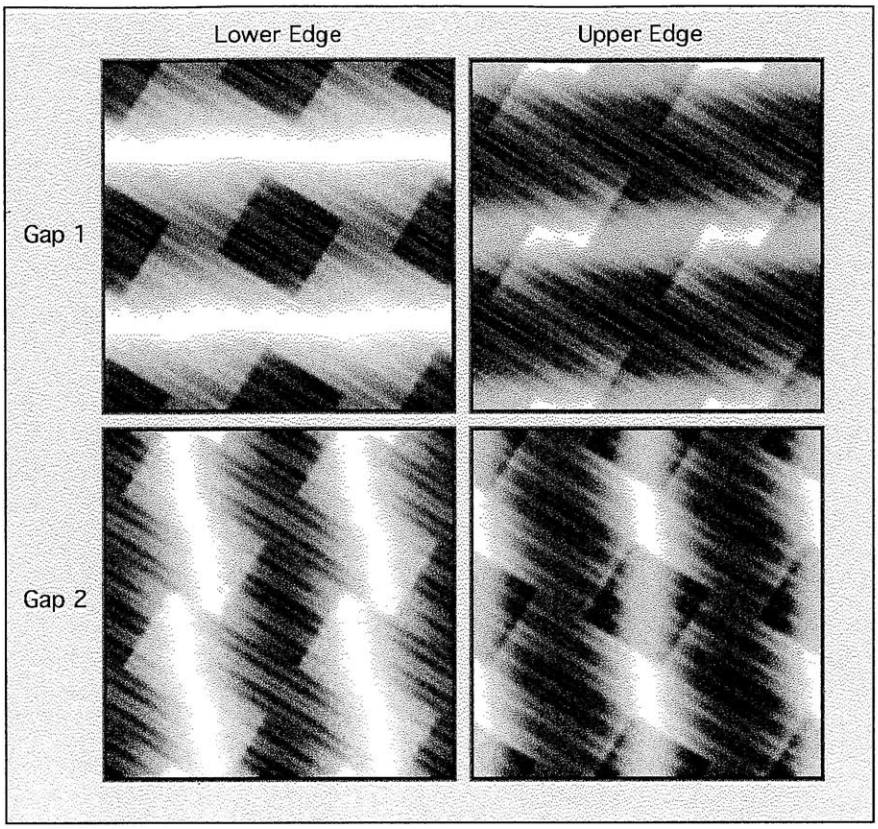

Figure 7-9: Electric field energy distribution of the band edge states of gaps 1 and 2 in Fig. 7-3. Although they have a complex small-scale structure, the large-scale variation is easily understood in terms of the structure of the superspace.

7.3.2 Defect modes

Much of the interest in quasicrystal band gaps, similar to the analogous case of band gaps in periodic structures, centers around the possibility of localized states: by introducing a defect in the structure, e.g. by changing the thickness of a single layer, one can create exponentially localized states in the gap [11, 28]. In periodic systems, because such defects break the periodicity, they necessitate a larger computational cell, or supercell, that contains many unit cells. In quasicrystal systems once the gaps are known, on the other hand, defect states are arguably *easier* to compute than the gaps of the infinite structure, because an exponentially localized defect mode can be computed accurately with a traditional supercell and the infinite quasicrystal per se need not be included. Nevertheless, the superspace approach allows one to compute

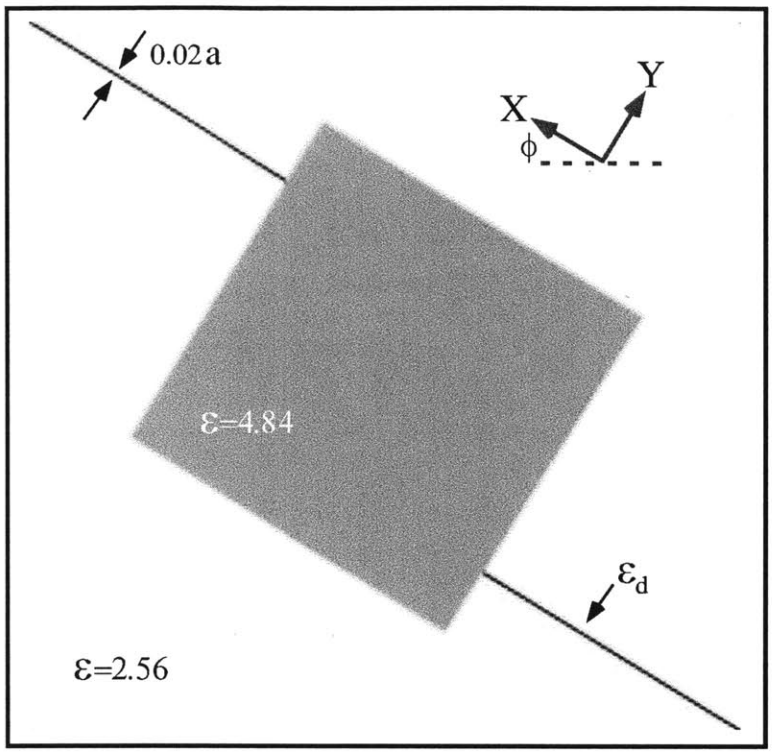

Figure 7-10: Dielectric for the Fibonacci chain with $\varepsilon = 2.56$ (light blue), and a defect—an additional $\varepsilon_d = 8.0$ layer, shown in gray.

defect modes using the same higher-dimensional unit cell, which demonstrates the flexibility of this approach and provides an interesting (but not obviously superior) alternative to traditional supercells for defect states.

Ideally, if one had infinite spatial resolution, a defect in the crystal would be introduced as a very thin perturbation parallel to the slice direction. As the thickness of this perturbation goes to zero, it intersects the physical slice at greater and greater intervals in the physical space, corresponding to localized defects that are separated by arbitrarily large distances. In practice, of course, the thickness of the perturbation is limited by the spatial resolution, but one can still obtain defects that are very widely separated—since the associated defect modes are exponentially localized, the coupling between the defects is negligible. In other words, one effectively has a very large supercell calculation, but expressed in only the unit cell of the higher-dimensional lattice.

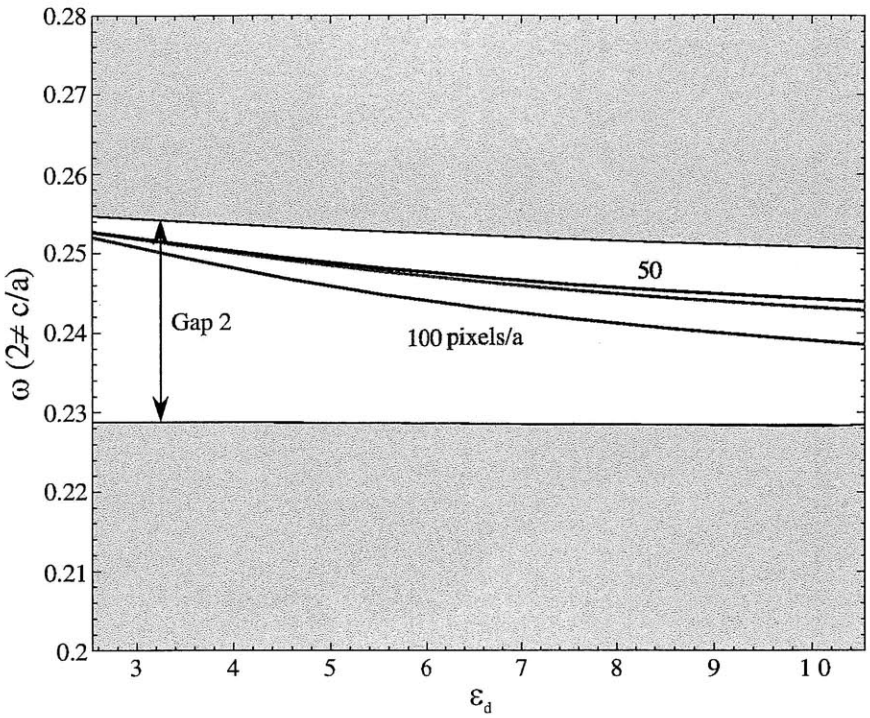

Figure 7-11: Varying the defect epsilon for resolutions 50 (blue) and 100 (red). The thickness of the defect is fixed to 0.02 lattice constants. The number of spurious modes increases with the resolution, the true defect state being the lowest of these modes.

As an example, we changed an $\varepsilon = 2.56$ layer to $\varepsilon = \varepsilon_d$ at one place in the Fibonacci quasicrystal. The corresponding superspace dielectric function is shown in Fig. 7-10, where the defect is introduced as a thin ($0.02a$) strip of ε_d parallel to the slice direction. We compute the band structure as a function of the defect dielectric constant ε_d, varying it from the normal dielectric $\varepsilon_d = 2.56$ up to $\varepsilon_d = 11$. The thickness of the defect in the unphysical direction was fixed to be ≈ 0.02. The resulting eigenvalues as a function of ε_d are shown in Fig. 7-11 for two different spatial resolutions of 50 (blue) and 100 (red) pixels/a. When the resolution is 50 the defect is only one pixel thick, the discretization effects might be expected to be large, although the frequency is within about 2% of the higher-resolution calculation. At the higher resolution, the frequency of the mode is converging (it is within 0.3% of a resolution-200 calculation, not shown). However, at the higher resolution there is a second, spurious mode due to the finite thickness (2 pixels) of the defect layer—this spurious

mode is easily identified when the field is plotted Fig. 7-12(bottom), because it has a sign oscillation perpendicular to the slice (which would be disallowed if we could make the slice infinitesimally thin).

The defect modes for the resolution 100 are plotted in Fig. 7-12 for both the real and the spurious modes, versus the physical coordinate (x) and also in the superspace unit cell (insets). When plotted versus the physical coordinate x on a semilog scale, we see that the modes are exponentially localized as expected. The defect mode appears at multiple x values (every $\sim 20a$ on average) because the defect has a finite thickness—the physical slice intersects it infinitely many times (quasiperiodically), as discussed above. The spurious mode (bottom panel) is also exponentially localized; it has a sign oscillation perpendicular to the slice direction (inset) which causes it to have additional phase differences between the different defects.

Nevertheless, as emphasized above, we feel that the main advantages of the superspace approach are for studying the gaps and modes of the infinite, defect-free quasicrystal rather than for localized defect modes.

7.3.3 Continuously varying the cut angle

The cut-and-project construction of quasicrystals provides a natural way to parameterize a family of periodic and quasiperiodic structures, via the cut angle ϕ. It is interesting to observe how the spectrum and gaps then vary with ϕ.

As ϕ is varied continuously from 0° to 45°, the structures vary from period a to quasi-periodic lattices (for $\tan\phi$ irrational) to long-period structures ($\tan\phi$ rational with a large denominator) to a period $a\sqrt{2}$ crystal. As we change ϕ, we rotate the objects in the unit cell, so that they are always extruded along the y direction with a length equal to the projection of the unit cell onto y $[a(\sin\phi + \cos\phi)]$, corresponding the usual cut-and-project construction [72]. In this case, the spectrum varies continuously with ϕ, where the rational $\tan\phi$ correspond to "rational approximates" of the nearby irrational $\tan\phi$ [189, 202]. For a general unit cell with a rational $\tan\phi$, the physical spectrum might depend on the slice offset $\mathbf{y}$ and hence different from the total superspace spectrum, but this is not the case for dielectric structures like the one

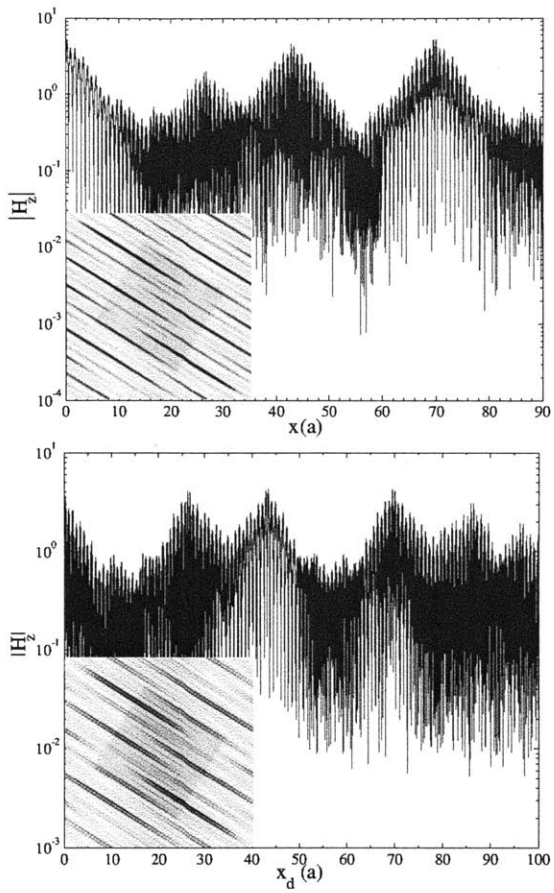

Figure 7-12: Semi-log plots of the magnetic field magnitude H_z for the lowest (top) and highest (bottom) defect state for the configuration shown in Fig. 7-10. *Insets:* Two-dimensional superspace visualizations of the defect states. Note the additional node in the lower figure (corresponding to an unphysical oscillation).

here, which satisfy a "closeness" condition [189] (the edges of the dielectric rods overlap when projected onto the Y direction). This makes the structure **y**-independent even for rational slices [189] The resulting structures are shown in the bottom panel of Fig. 7-13 for three values of ϕ.

The corresponding photonic band gaps are shown in the top panel of Fig. 7-13, as a continuous function of ϕ. Only the largest gaps are shown, of course, since we are unable to resolve the fractal structure to arbitrary resolution. As might be expected, there are isolated large gaps at $\phi = 0°$ and $\phi = 45°$ corresponding to the simple $ABAB\cdots$ periodic structures at those angles (with period a and $a/\sqrt{2}$,

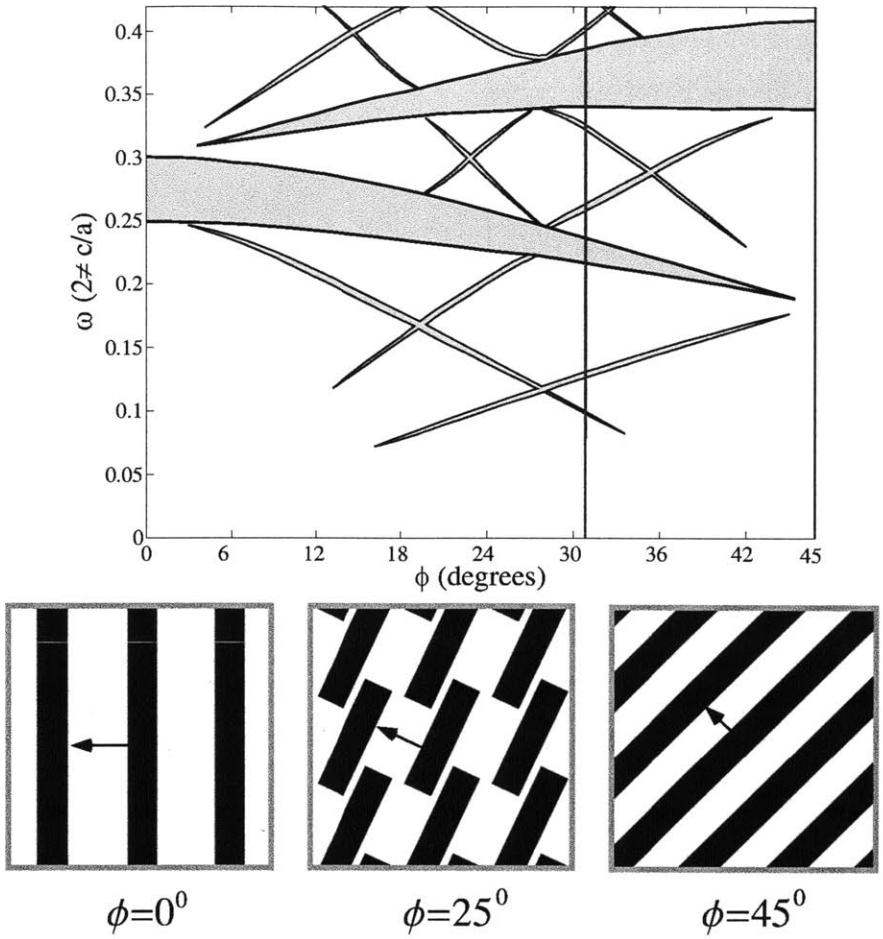

Figure 7-13: Projected band structure vs. cut angle ϕ, showing different one-dimensional quasicrystal realizations. The vertical red line indicates the spectrum when the slope is the golden ratio τ (the spectra of ϕ and $\pi - \phi$ are equivalent)

respectively, the latter resulting from two layers per unit cell). The $\phi = 45°$ gap is at a higher frequency because of its shorter period, but interestingly it is not continuously connected to the $\phi = 0°$ gap.

The reason for this is that the two gaps are dominated by different superspace reciprocal lattice vectors: $(1,0)\cdot 2\pi/a$ for $\phi = 0°$, and $(1,1)\cdot 2\pi/a$ for $\phi = 45°$. (In fact, it is possible to calculate, to first order, the locations of the gaps using the dynamic structure factor $S(\mathbf{k},\omega)$ obtained from the projection of the superspace lattice [153].) For intermediate angles, a number of smaller gaps open and then close. If we were able to show the spectrum with higher resolution, we would expect to see increasing

numbers of these smaller gaps opening, leading to the well-known fractal structure that arises e.g. for the Fibonacci crystal.

7.3.4 Smooth superspace structures

Until this point we have examined structures in which the dielectric attains only two values; such structures are the most realistic for fabrication. However, for theoretical purposes it can be enlightening to consider cases in which the sharp boundaries are smoothed out, in order to restrict the number of Fourier components appearing in the structure factor (for example, this is useful for examining the origin of bandgaps in one-dimensional photonic crystals [73]). Our superspace construction allows us to consider a new class of structures, in which the *superspace* dielectric is a smooth function. In particular, we examine the case in which the superspace dielectric function is given by:

$$\varepsilon(x, y) = 1 + 4e^{-(\sin^2(x)+\sin^2(y))} \tag{7.5}$$

The Fourier components of our previous square dielectric scales as $\varepsilon_{\mathbf{G}} \sim |\mathbf{G}|^{-1}$; however, the Fourier transform of eq. (7.5) converges *exponentially* for large $|\mathbf{G}|$. This implies [20] that the frequencies at the bandgaps will also converge exponentially with the resolution (i.e., the number of reciprocal vectors $\mathbf{G}$ retained in the computation). The bandstructure for the smooth dielectric is shown in Fig. 7-14; two resolution are shown, resolution 6 and 32. In order to confirm the exponential convergence of this bandstructure, we examine the value $\omega_{\text{lower}}(k_0)$ shown in Fig. 7-14, which is the extremal value of the band depicted in red. We fix the value of $k_x = k_0 = 0.075415(2\pi/a)$ and increase the resolution, examining the value of ω at the bottom of this bandgap. The results, shown in Fig. 7-15, confirm the exponential convergence with resolution. This is an interesting property, which may be useful for structural optimization, where the exponential convergence allows for efficient optimization with only a few number of grid parameters.

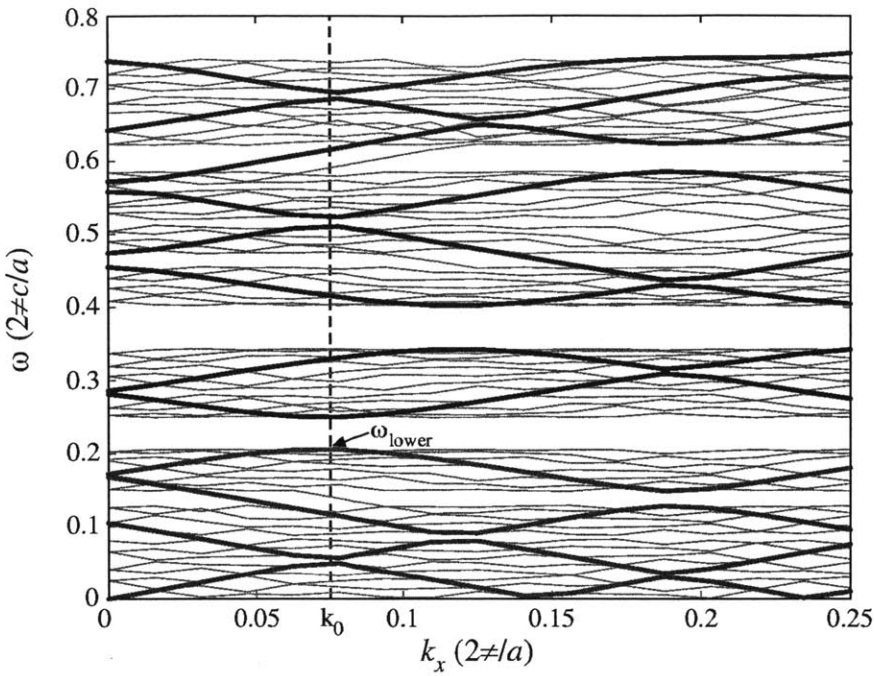

Figure 7-14: Bandstructure for the smooth superspace structure $\varepsilon(x,y) = 1 + 4e^{-(\sin^2(x)+\sin^2(y))}$ at two resolutions: thick lines denote 6 pixels / a, and thin lines denote 32 pixels / a. We will demonstrate that the bandstructure for this dielectric converges *exponentially* in resolution by examining the frequency ω_{lower}, indicated on the figure, which is at a relative maximum of the lower band edge (colored red) at a fixed $k_0 \approx 0.75(2\pi/a)$.

7.3.5 Optimization of one-dimensional smoothed structures

Previously, we examined the effect of varying the cut angle on the bandstructure. In this section, we examine the superspace structures that give the largest fractional photonic bandgaps, for a fixed cut angle. The superspace construction is very convenient for this purpose because the entire structure resides within one compact unit cell. We employ a technique called topology optimization [12, 18, 54, 81], specifically by using the method of moving asymptotes (MMA) algorithm [74, 193]. Here, each pixel ε_i of the dielectric is treated as a free parameter, and allowed to vary freely between the values $\varepsilon_{\text{min}} = 1$ and $\varepsilon_{\text{max}} = 10$. We start with the same geometry as Fig. 7-1 (although now with a higher index contrast). Above, we saw that smoothed superspace structures require much lower discretization to reach convergence. However, smoothed structures also have another useful property: a lack of local minima for

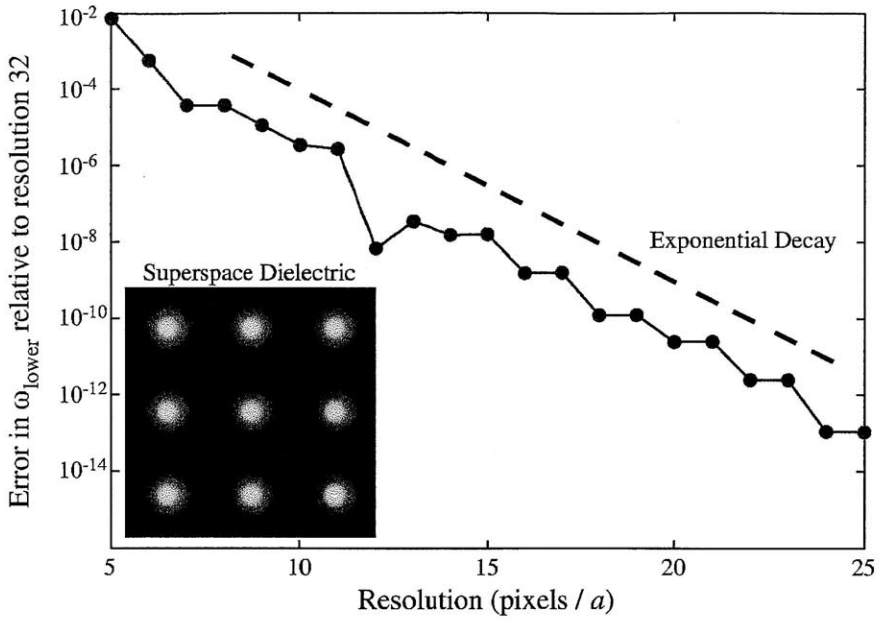

Figure 7-15: Demonstration of exponential convergence with resolution of a smooth superspace structure. A plot of the error in ω_{lower} from Fig. 7-14 (relative to resolution 32) shows exponential convergence. The superspace dielectric structure, given by eq. (7.5), is shown in the inset.

optimization. To obtain a smooth structure, we convolve the initial square of Fig. 7-1 with a gaussian kernel with standard deviation $\sigma = 0.25$. The resulting smoothed superspace structure is shown on the top left of Fig. 7-16, and its bandstructure is shown in the center. A continuous structural change will change the bandstructure continuously as well, therefore we can uniquely track the evolution of an individual bandgap through the optimization.[2] We will separately optimize the bandgaps labeled 1, 2, and 3 in this figure, using a resolution of 32 pixels per a (at this resolution, these bandgaps have lower edge 13, 20, and 32, respectively), although lower resolutions provide similar results.

The results of the topology optimization are shown in the different panels of Fig. 7-16. What is interesting is that, despite the aperiodic nature of the initial structure, the optimized structures are *periodic*, regardless of the cut angle. The optimization of different bandgaps results in different periodic structures, and is closely reminiscent

[2]This is not strictly true when spurious modes are encountered, however for this particular situation they are absent.

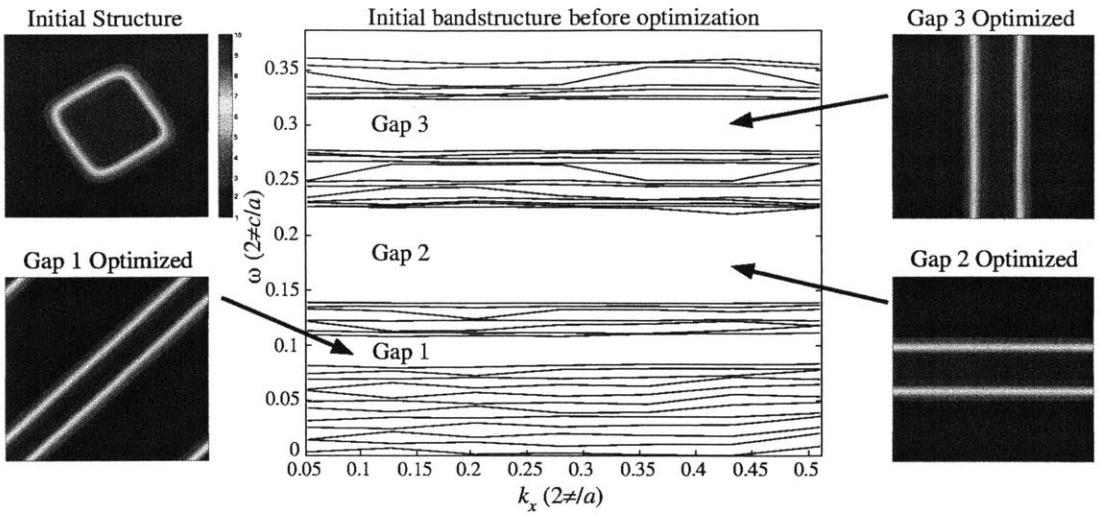

Figure 7-16: Optimization of the fractional bandgap for a 1d quasicrystal: starting with a smoothed version of the Fibonacci structure (top left), which has the indicated band structure, we allow every pixel to be a free parameter, ranging from $1 \leq \varepsilon \leq 10$. Even though the cut angle is $\tan\phi = \tau$, the three structures shown are actually *periodic*. After optimization, all structures exhibit an approximately 67% fractional bandgap, which is the same as an optimized 1d photonic crystal with the same smoothing parameters.

of Fig. 7-9. In fact, this is another manifestation of the 1d structure inheriting its behavior from the 2d superspace: the band edge states of Fig. 7-9 have a dominant wavevector that corresponds to a low-order superspace reciprocal vector; we expect the optimized structure to strongly couple to this reciprocal vector. For all structures, the optimized gap-midgap ratio is approximately 67%. Intuitively, we expect that this result should correspond to the optimized gap-midgap ratio for a purely 1d periodic structure. Using the same smoothing parameters and applying our topology optimization to the first bandgap of a 1d photonic crystal, we again get a 67% gap-midgap ratio, confirming this expectation; furthermore, the optimized 1d structure corresponds exactly to a quarter-wave stack (convolved with a $\sigma = 0.25$ gaussian).

7.4 Two-dimensional results

We now generalize our method to handle higher-dimensional quasicrystal structures. We focus on two-dimensional quasicrystals that can be represented by a four-dimensional superspace. The implementation in a planewave-expansion method is fairly simple: unlike finite-difference methods, it is straightforward to extend a planewave-expansion method to higher dimensions. This is because the process of differentiation, which for finite-difference methods requires knowledge of the lattice structure, is simply achieved by multiplying by $\mathbf{k} + \mathbf{G}$ in a planewave basis. The actual quasicrystal structure is represented by three matrices. $\overleftrightarrow{R}_{\text{Super}}$ defines the lattice structure in the superspace; the rows of this matrix represent the basis vectors; $\overleftrightarrow{R}_X$ defines the physical space - the rows of this matrix represent the superspace basis vectors; finally, $\overleftrightarrow{R}_Y$ defines the subspace perpendicular to the physical space. As with the one-dimensional quasicrystals of the previous section, the superspace dielectric is the Cartesian product of a "physical" profile and a "perpendicular" profile. In our case, we will take the physical profile to be a circle of radius r. The perpendicular profile, defined by cut-and-project, is the projection of the convex hull (i.e., the voronoi cell [72, 192]) of the superspace basis vectors onto the perpendicular space; that is, the convex hull of the set $\overleftrightarrow{R}_Y^T \overleftrightarrow{R}_{\text{Super}}$. We compute the convex hull using Qhull [1], a freely-available software program.

7.4.1 Octagonal Quasicrystals

The two-dimensional octagonal quasicrystal is constructed from slicing four-dimensional Cartesian space. The Fourier spectrum of the octagonal lattice has 8-fold rotational symmetry [26, 202]. Since the superspace lattice is Cartesian, the matrix $\overleftrightarrow{R}_{\text{Super}}$ is simply the 4×4 identity matrix. The other two matrices are [202]:

$$\overleftrightarrow{R}_X = \begin{pmatrix} \frac{1}{\sqrt{2}} & \frac{1}{2} & 0 & -\frac{1}{2} \\ 0 & \frac{1}{2} & \frac{1}{\sqrt{2}} & 0 \end{pmatrix} \tag{7.6}$$

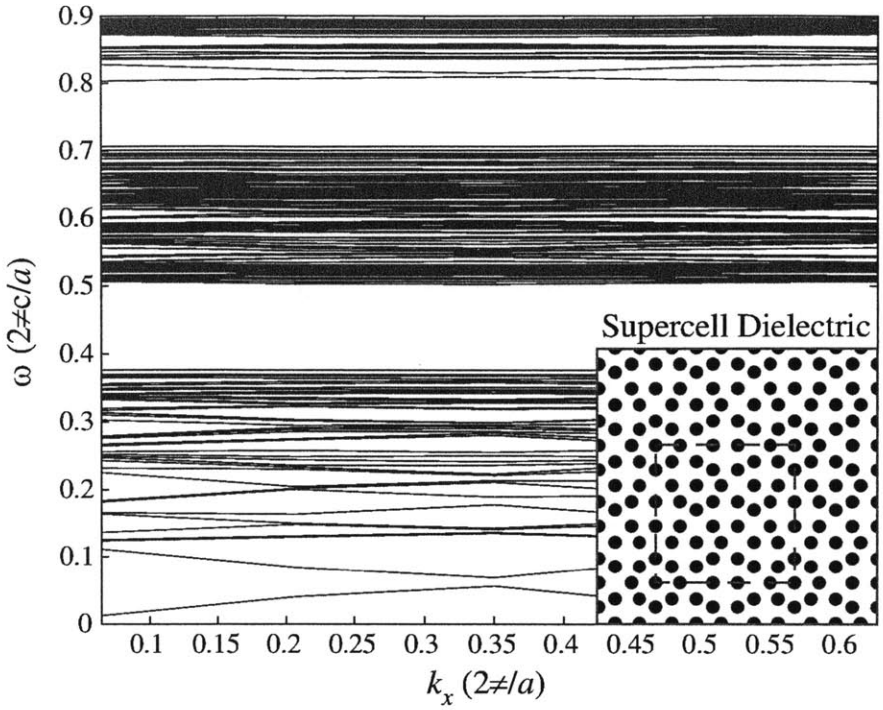

Figure 7-17: Bandstructure for a 3/2 supercell approximate to the octagonal PQC of high dielectric rods. The real-space structure is shown in the inset, with a unit cell marked by the dashed red box.

and

$$\overleftrightarrow{R}_Y = \begin{pmatrix} \frac{1}{\sqrt{2}} & \frac{1}{2} & 0 & \frac{1}{2} \\ 0 & -\frac{1}{2} & \frac{1}{\sqrt{2}} & -\frac{1}{2} \end{pmatrix}. \tag{7.7}$$

We first compute a bandstructure using a supercell with a rational approximate; the dielectric for the rational approximate can be constructed by following the same cut-and-project procedure as for the superspace, with the modification that $\sqrt{2}$ for $\overleftrightarrow{R}_X$ is replaced with p/q for integer p and q. The resulting $\overleftrightarrow{R}_Y$ will no longer be orthogonal to the physical subspace; rather, it is constructed from the rows of $\overleftrightarrow{R}_X$ using Gram-Schmidt orthogonalization. The supercell spectrum is shown in Fig. 7-17, where a $p = 3$, $q = 2$ rational approximate has been used (the 2d dielectric function has period ≈ 4.12, and is shown in Fig. 7-17[Inset]). We see the presence of two large bandgaps (the gap-midgap ratios are $\approx 30\%$ for the lower gap and $\approx 15\%$ for the upper gap).

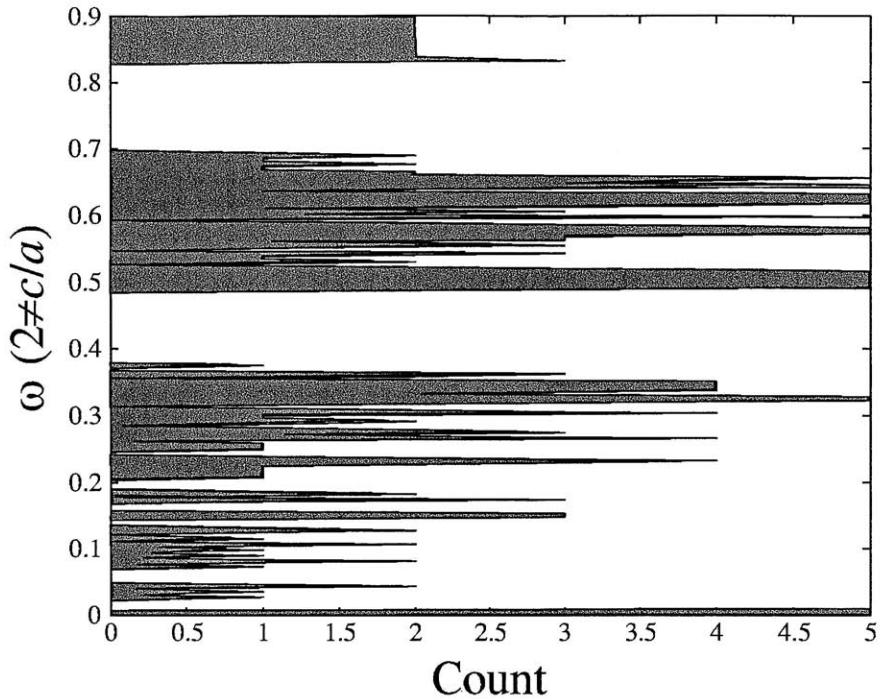

Figure 7-18: Mode density plot for the super*space* octagonal structure, with the same structural parameters as Fig. 7-17, for a resolution of 10 pixels per a. At this resolution, the bandgaps are not fully resolved to high accuracy.

Unfortunately, computational limitations restrict the resolution that can be applied to a four-dimensional planewave expansion; this is because for N pixels per a the computational resources (both space and time) scale as N^6. Therefore, we cannot go to a high enough resolution such that the method of spurious mode elimination discussed above becomes strictly valid, especially for the. A superspace bandstructure computation at resolution $a/10$ is shown in Fig. 7-18; this is shown as a mode-density plot. We identify both of the major bandgaps corresponding to the supercell bandstructure of Fig. 7-17. However, due to the low resolution we can only resolve the lower edge of the first bandgap to high accuracy. It remains to go to a sufficiently high resolution to fully reproduce this bandstructure using a superspace computation.

7.5 Concluding Remarks

We have presented a numerical approach to computing the spectra of photonic quasicrystals by directly solving Maxwell's equations extended to a periodic unit cell in higher dimensions, allowing us to exploit Bloch's theorem and other attractive properties of computations for periodic structures. In doing so, we extended the conceptual approach of cut-and-project techniques, which were developed as a way to *construct* quasicrystals, into a way to *simulate* quasicrystals. Compared to traditional supercell techniques, this allows us to capture the entire infinite aperiodic quasicrystal in a single finite computational cell, albeit at only a finite resolution. In this way, the single convergence parameter of spatial resolution replaces the combination of resolution and supercell size in traditional calculations, in some sense uniformly sampling the infinite quasicrystal. The resulting computations, applied to the test case of a Fibonacci quasicrystal, display the unique features of quasicrystals in an unusual fashion, in terms of higher-dimensional band structures and visualization techniques. This technique also allows defects and variation of cut angle (continuously varying between periodic and aperiodic structures) in a straightforward way. We have also seen how this method can be used to treat exponentially-convergent structures, and how these structures can be used for topology optimization of the photonic bandstructure. This includes a demonstration that the optimal fractional bandgap for 1d PQCs actually occurs for a periodic structure (the quarter-wave stack). Finally, we have generalized our method to compute spectra for higher-dimensional PQCs. We have reproduced part of the spectrum for a four-dimensional octagonal PQC, however computational limitations prevent us from applying the present method to more complex structures.

Appendix

In this appendix, we give an explicit derivation of the fact that an "irrational" slice densely fills the superspace unit cell, or rather a definition of the necessary conditions to be an "irrational" slice. These concepts are widely used in the quasicrystal

literature, but a precise definition seems hard to find (one commonly requires that all of the Miller indices have incommensurate ratios, but this condition is stronger than necessary). We then give a rigorous proof that the extended state spectrum obtained from a superspace calculation will be identical to the spectrum of the physical real-space slice (this supplements the intuitive discussion given in the main text).

7.5.1 Minimum sufficient conditions for a slice to densely fill the superspace unit cell

Without loss of generality, we can consider the unit cell in the superspace $Z = \mathbb{R}^n$ to be the unit cube (related to any lattice by an affine transformation) with lattice vectors along the coordinate directions. The physical slice X is d-dimensional, and it will be convenient to write the coordinates of a vector $\mathbf{z}$ as $\mathbf{z} = (s_1, \ldots, s_d, t_1, \ldots, t_{n-d}) = (\mathbf{s}, \mathbf{t})$. By taking every coordinate modulo 1, we can map X to a set $\bar{X}$ consisting of X's intersection with each unit cell. We wish to show necessary and sufficient conditions for $\bar{X}$ to densely fill the unit cell.

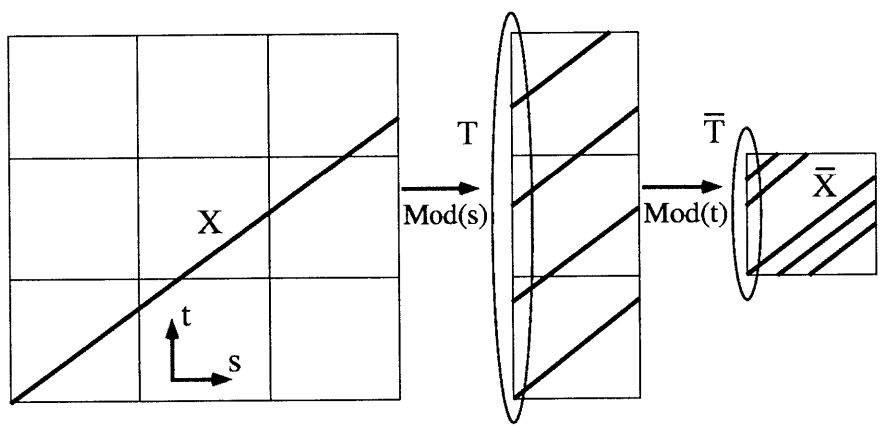

Figure 7-19: Schematic showing the superspace slice X (left) and the projected slice modulo 1 into the unit cell $\bar{X}$ (right), along with the intersection $\bar{T}$ of $\bar{X}$ with the $s = 0$ hyperplane.

Assuming that the slice is not orthogonal to any of the coordinate axes (as otherwise it would clearly not densely fill the unit cell), we can parameterize the points $\mathbf{z}$ of X so that the last $n - d$ coordinates $(t_1, \ldots, t_{n-d})$ are written as a linear function

$\mathbf{t}(s_1, \ldots s_d) \equiv \mathbf{t}(\mathbf{s})$ of the first d coordinates.

Consider the set T in $\mathbb{R}^{n-d}$ formed by the $\mathbf{t}(\mathbf{s})$ coordinates of X when the components of $\mathbf{s}$ take on integer values. This is a subset of X, and the corresponding set $\bar{T}$ formed by taking $\mathbf{t} \in T$ modulo 1 is a subset of $\bar{X}$. The key fact is that $\bar{X}$ is dense in the n-dimensional unit cell if and only if $\bar{T}$ is dense in the $(n-d)$-dimensional unit cell, and this is the case that we will analyze. This equivalence follows from the fact that $\bar{X}$ is simply $\bar{T}$ translated continuously along the slice directions (every point in $\bar{X}$ is related to a point in $\bar{T}$ by a simple projection). The set T is a lattice in $\mathbb{R}^{n-d}$ consisting of all integer linear combinations of the basis vectors $\mathbf{t}_k = \mathbf{t}(s_j = \delta_{jk})$, since $\mathbf{t}(\mathbf{s})$ is a linear function.

For each basis vector $\mathbf{t}_k$, it is a well-known fact [141] that if it consists of m incommensurate irrational components, the set of integer multiples $\ell \mathbf{t}_k$ modulo 1 will densely fill an m-dimensional slice of the unit cell. More precisely, write $\mathbf{t}_k = \sum_{j=1\ldots m_k} \alpha_k^j \mathbf{b}_k^j + \mathbf{q}_k$, where the $\mathbf{b}_k^j$ and $\mathbf{q}_k$ have purely rational components and the $\{\alpha_j\}$ are incommensurate irrational numbers, and m_k is therefore the number of incommensurate irrational components of $\mathbf{t}_k$. Then the set of integer multiples of $\mathbf{t}_k$ modulo 1 densely fills an m_k-dimensional slice of the unit cell of $\mathbb{R}^{n-d}$. The basis vectors of this slice are precisely the vectors $\mathbf{b}_k^j$, which are rational and therefore commensurate with the basis vectors of $\mathbb{R}^{n-d}$, while the vector $\mathbf{q}_k$ is simply a rational shift. This slice therefore cuts the unit cell of $\mathbb{R}^{n-d}$ a finite number of times.

The set $\bar{T}$ is then obtained as the direct sum of these dense slices for all $n-d$ vectors $\mathbf{t}_k$. This is then dense if and only if the set of vectors $\{\mathbf{b}_k^j\}_{k=1\ldots d}^{j=1\ldots m_k}$ spans $\mathbb{R}^{n-d}$. In other words, an "irrational slice," which densely fills the unit cell, is one in which there are $n-d$ independent incommensurate slice components as defined above.

7.5.2 Spectral Correspondence

We will show that the extended state spectrum obtained from a superspace calculation, for a suitable dielectric (defined below), will have the same result as the extended state spectrum of the physical slice.

The physical slice is an element of the superspace unit cell, so the frequencies

obtained from a superspace calculation will include all frequencies of the physical slice.

For the other direction, we will give a sufficient condition for spectral equivalence.

Given a superspace slice S_0 and a sequence $\{S_i\}$ of parallel slices obtained by translating S_0 by some set of directions v_j, where v_j are in the unphysical Y direction, are parallel and $|v_j| \to 0$ as $j \to \infty$.

Define the following function:

$$f(j) = \lim_{L\to\infty} \frac{\int_{x\in S_0, |x|<L} |\epsilon(x) - \epsilon(x+v_j)|}{L^d} \tag{7.8}$$

Then if $f(j) \to 0$ this says that the average dielectric difference between the two supercells goes to zero. Assume further that no defect states are created - there are no layers of zero thickness in the Y direction. This way all states are extended in the physical direction, and first order perturbation theory can be applied between the energy levels of S_0 and S_j. If the energy spectrum is the same for the slices $\{S_j\}$, then S_0 will also have that spectrum.

Now assume that from any dense set of slices a sequence converging to any slice can be formed that satisfies $f(j) \to 0$. If no defects exist, the superspace spectrum will be the same as the physical spectrum.

Most configurations of interest involve a set of n-dimensional blocks. The boundaries of these blocks are $n-1$-dimensional hypersurfaces, parallel to the Y or X direction. Boundaries parallel to the Y direction will result in (locally) identical physical dielectrics, while the finite number of boundaries in the X direction will give discrete jumps that may not go to zero as $j \to \infty$. However, these boundaries are infinitely thin in the Y direction, and because the slice is dense it cannot pass through the same boundary hyperplane more than once. This ensures that as $L \to \infty$, the discontinuity of the boundaries will give at most a finite contribution, and we will have $f(j) \to 0$.

Chapter 8

Conclusions and Outlook

In this thesis I have presented several examples demonstrating the extension of techniques from classical computational electromagnetism to new and interesting topics. These techniques can be used to explore systems not amenable to analytic treatment, and novel physical effects can be discovered.

For quantum fluctuations, we have seen the extent to which geometry can be used to modulate the Casimir force. Despite the seemingly ubiquitous claims of "strong" geometry dependence in the Casimir literature, it is my opinion that this dependence is actually quite weak: it is very difficult to identify qualitatively different from the near-field and far-field. When we have done so, the novel effects are extremely weak: the sign change for our anisotropic metamaterial my be barely detectable in the highest-precision experiments, and despite our best efforts the repulsive effect is still too small to even be detectable, must less useful in device applications. We have applied our techniques to thermal fluctuations and have seen several interesting geometric effects in this case.

Finally, I have presented an interesting approach to computing the bandstructures of photonic quasicrystals. This method is not very practical for computing bandstructures, especially in higher dimensions, due to the high computational overhead and the presence of spurious modes. However, in 1d I feel this method offers considerable physical insight into these systems, especially concerning the properties that these 1d structures inherit from their higher-dimensional superspace.

It is difficult to see what more can be added to the field of equilibrium fluctuations. For future research in Casimir physics, non-equilibrium systems seem to be the more promising. The non-equilibrium component of the physics is governed by fluctuations on length scales on the order of the thermal wavelength, so large geometries with separations on the order of several microns are required to observe this effect. There may be even more interesting applications in heat transfer; due to the slower power-law decay of heat transfer relative to Casimir forces we have seen that geometry can have a stronger effect for thermal fluctuations. Future tasks would include looking at thermal transfer in more elaborate geometries. Additionally, the computational method that we have developed is capable of handling the sphere-plate geometry at very small separations - this method can be used to verify the crossover to the PFA regime.

Regarding quasicrystals, much remains unknown about the mathematical properties of bandstructures for higher-dimensional PQCs, and this method may provide insight into what properties these PQCs inherit from their higher-dimensional superspace. Two possible examples come to mind. One is the existence of localized states in certain 2d PQC structures and their absence in others [39, 85] - it may be that the dielectric structure in superspace makes this localization clear. Another is the application of a more sophisticated multifractal analysis [64] applied to the superspace eigenmodes. Such analyses have been applied to the supercell eigenmodes [79, 184], but it is likely that simpler behavior may emerge from a direct mathematical analysis of superspace. Finally, figuring out a way to compute higher-dimensional bandstructures at higher spatial resolution is crucial in order to apply this method to, e.g., three-dimensional PQCs.

Bibliography

[1] `http://www.qhull.org`.

[2] Della Villa A., S. Enoch, G. Tayeb, V. Pierro, V. Galdi, and F. Capolino. Bang gap formation and multiple scattering in photonic quasicrystals with Penrose-type lattice. *Phys. Rev. Lett.*, 94:183903, 2005.

[3] Milton Abramowitz and Irene A. Stegun, editors. *Handbook of Mathematical Functions.* Dover, New York, 1972.

[4] George B. Arfken and Hans J. Weber. *Mathematical Methods for Physicists.* Harcourt, San Diego, fifth edition, 2001.

[5] N. W. Ashcroft and N. D. Mermin. *Solid State Physics.* Holt Saunders, Philadelphia, 1976.

[6] Gan Bao, Lawrence Cowsar, and Wen Masters, editors. *Mathematical Modeling in Optical Science*, volume 22 of *Frontiers in Applied Mathematics*, chapter 7. SIAM, 2001.

[7] Y. Barash. On the moment of van derWaals forces between anisotropic bodies. *Izv. Vyssh. Uchebn. Zaved. Radiofiz.*, 21:1637, 1978.

[8] Y. Barash and V. Ginzburg. *Usp. Fiz. Nauk*, 116:5, 1975.

[9] R. Barrett, M. Berry, T. F. Chan, J. Demmel, J. Donato, j. Dongarra, V. Eijkhout, R. Pozo, C. Romine, and H. Van der Vorst. *Templates for the Solution of Linear Systems: Building Blocks for Iterative Methods.* SIAM, Philadelphia, 2nd edition, 1994.

[10] S. Basu, Z. M. Zhang, and C. J. Fu. Review of near-field thermal radiation and its application to energy conversion. *Int. J. Energy Res.*, 33:1203–1232, 2009.

[11] M. Bayinding, E. Cubukcu, I. Bulu, and E. Ozbay. Photonic band gaps and localization in two-dimensional metallic quasicrystals. *Europhys. Lett.*, 56(1):41–46, 2001.

[12] Martin Philip Bendsoe and Sigmund Ole. *Topology Optimization: Theory, Methods, and Applications.* Springer, Berlin, 2nd edition, 2003.

[13] Jean-Paul Bérenger. A perfectly matched layer for the absorption of electromagnetic waves. *J. Comput. Phys.*, 114(1):185–200, 1994.

[14] Lennart Bergstrom. Hamaker constants of inorganic materials. *Adv. Colloid and Interface Science*, 70:125–169, 1997.

[15] Peter Bienstman and R. Baets. Optical modelling of photonic crystals and VCSELs using eigenmode expansion and perfectly matched layers. *Optical and Quantum Electron.*, 33(4–5):327–341, 2001.

[16] Michael J. Biercuk, Hermann Uys, Joe W. Britton, Aaron P. VanDevender, and John J. Bollinger. Ultrasensitive detection of force and displacement using trapped ions. *Nature Nanotechnology*, 5:646, 2010.

[17] Giuseppe Bimonte. Scattering approach to Casimir forces and radiative heat transfer for nanostructured surfaces out of thermal equilibrium. *Phys. Rev. A*, 80(4):042102, 2009.

[18] P. I. Borel, A. Harpoth, L. H. Frandsen, M. Kristensen, P. Shi, J. S. Jensen, and O. Sigmund. Topology optimization and fabrication of photonic crystal structures. *Opt. Express*, 12:1996, 2004.

[19] Max Born and Emil Wolf. *Principles of Optics.* Cambridge University Press, Cambridge, UK, sixth edition, 1997.

[20] J. P. Boyd. *Chebychev and Fourier Spectral Methods.* Dover, New York, 2nd edition, 2001.

[21] Timothy H. Boyer. Van der Waals forces and zero-point energy for dielectric and permeable materials. *Phys. Rev. A*, 9:2078–2084, 1974.

[22] M. Brown-Hayes, D. A. R. Dalvit, F. D. Mazzitelli, W. J. Kim, and R. Onofrio. Towards a precision measurement of the Casimir force in a cylinder-plane geometry. *Phys. Rev. A*, 72:052102, 2005.

[23] R. Büscher and T. Emig. Nonperturbative approach to Casimir interactions in periodic geometries. *Phys. Rev. A*, 69:062101, 2004.

[24] H. B. G. Casimir and D. Polder. The influence of retardation on the London-van der Waals forces. *Phys. Rev.*, 13(4):360–372, 1948.

[25] David L. C. Chan, Marin Soljačić, and J. D. Joannopoulos. Direct calculation of thermal emission for three-dimensionally periodic photonic crystal slabs. *Phys. Rev. E*, 74(3):036615, 2006.

[26] Y. S. Chan and Z. Y. Liu. Photonic band gaps in two dimensional photonic quasicrystals. *Phys. Rev. Lett.*, 80(5):956–959, 1998.

[27] F. Chen, U. Mohideen, G. L. Klimchitskaya, and V. M. Mostepanenko. Demonstration of the lateral Casimir force. *Phys. Rev. Lett.*, 88:101801, 2002.

[28] Samuel S. M. Cheng, Lie-Ming Li, C. T. Chan, and Z. Q. Zhang. Defect and tranasmission properties of two-dimensional quasiperiodic photonic band-gap systems. *Phys. Rev. B*, 59(6):4091–4099, 1999.

[29] H.-C. Chiu, G. L. Klimchitskaya, V. N. Marachevsky, V. M. Mostepanenko, and U. Mohideen. Lateral Casimir force between sinusoidally corrugated surfaces: asymmetric profiles, deviations from the proximity force approximation, and comparison with exact theory. *Phys. Rev. B*, 81(11):115417, 2010.

[30] Robert E. Collin. *Field Theory of Guided Waves.* IEEE Press, New York, NY, second edition, 1991.

[31] W. A. Coppel. *Number theory: an introduction to mathematics.* Springer, New York, 2nd edition, 2009.

[32] J. A. Crosse, Simen A. Ellingsen, Kate Clements, Stefan Y. Buhmann, and Stefan Scheel. Thermal casimir-polder shifts in rydberg atoms near metallic surfaces. *Phys. Rev. A*, 82:010901(R), 2010.

[33] L. Dal Negro, M. Stolfi, Y. Yi, J. Michel, X. Duan, L. C. Kimerling, J. LeBlanc, and J. Haavisto. Photon band gap properties and omnidirectional reflectance in si/siO_2 thue-morse quasicrystals. *Appl. Phys. Lett.*, 84(25):5186–5188, 2004.

[34] Luca Dal Negro, Claudio J. Oton, Zeno Gaburro, Lorenzo Pavesi, Patrick Johnson, Ad Lagendijk, Roberto Righini, Marcello Colocci, and Diedrik Wiersma. Light transport through the band-edge states of Fibonacci quasicrystals. *Phys. Rev. Lett.*, 90(5):055501, 2003.

[35] P. S. Davids, F. Intravaia, F. S. S. Rosa, and D. A. R. Dalvit. Modal approach to Casimir forces in periodic structures. *Phys. Rev. A*, 82(6):062111, 2010.

[36] C. de Lange and T. Janssen. Electrons in incommensurate crystals: Spectrum and localization. *Phys. Rev. B*, 28(1):195–209, 1983.

[37] S. de Man, K. Heeck, and D. Iannuzzi. Halving the Casimir force with conductive oxides: experimental details. *Phys. Rev. A*, 82:062512, 2010.

[38] S. de Man, K. Heeck, R. J. Wijngaarden, and D. Iannuzzi. Contact potentials in Casimir force setups: An experimental analysis. *J. Vac. Sci. Technol. B*, 28, 2010.

[39] A. Della Villa, S. Enoch, G. Tayeb, V. Pierro, and V. Galdi. Localized modes in photonic quasicrystals with Penrose-type lattice. *Opt. Express*, 14(21):10021–10027, 2006.

[40] Alessandro Della Villa, Vincenzo Galdi, Filippo Capolino, Vincenzo Pierro, Stefan Enoch, and Gerard Tayeb. A comparative study of representative categories of EGB dielectric quasi-crystals. *IEEE Ant. Wireless Prop. Lett.*, 5:331–333, 2006.

[41] B. V. Derjaguin. Untersuchungen über die reibung und adhäsion. *Kolloid Z.*, 69:155, 1934.

[42] B. V. Derjaguin, I. I. Abrikosova, and E. M. Lifshitz. Direct measurement of molecular attraction between solids separated by a narrow gap. *Q. Rev. Chem. Soc.*, 10:295–329, 1956.

[43] Laurent Duraffourg and Philippe Andreucci. Casimir force between doped silicon slabs. *Phys. Lett. A*, 359:406–411, 2006.

[44] I. E. Dzyaloshinskiĭ, E. M Lifshitz, and L. P. Pitaevskiĭ. The general theory of van der Waals forces. *Adv. Phys.*, 10(38):165–209, 1961.

[45] W. Eckhardt. Macroscopic theory of electromagnetic fluctuations and stationary radiative heat transfer. *Phys. Rev. A*, 29(4):1991, 1984.

[46] Simen A. Ellingsen. Private communication. 2010.

[47] Simen A. Ellingsen, Stefan Yoshi Buhmann, and Stefan Scheel. Temperature-independent casimir-polder forces despite large thermal photoni numbers. *Phys. Rev. Lett.*, 104:223003, 2010.

[48] T. Emig, A. Hanke, R. Golestanian, and M. Kardar. Normal and lateral Casimir forces between deformed plates. *Phys. Rev. A*, 67:022114, 2003.

[49] Thornsten Emig. Casimir-force-driven ratchets. *Phys. Rev. Lett.*, 98:160801, 2007.

[50] Thornsten Emig, N. Graham, R. L. Jaffe, and Mehran Kardar. Casimir forces between arbitrary compact objects. *Phys. Rev. Lett.*, 99:170403, 2007.

[51] Ardavan Farjadpour, David Roundy, Alejandro Rodriguez, M. Ibanescu, Peter Bermel, Jeff Burr, J. D. Joannopoulos, and Steven G. Johnson. Improving accuracy by subpixel smoothing in the finite-difference time domain. *Opt. Lett.*, 31:2972–2974, 2006.

[52] Zhifang Feng, Xiangdong Zhang, Yiquan Wang, Zhi-Yuan Li, Bingying Cheng, and Dao-Zhong Zhang. Negative refraction and imaging using 12-fold-symmetry quasicrystals. *Phys. Rev. Lett.*, 94(24):247402, 2005.

[53] Barak Freedman, Guy Bartal, Mordechai Segev, Ron Lifshitz, Demetrios N. Christodoulides, and Jason W. Fleischer. Wave and defect dynamics in nonlinear photonic quasicrystals. *Nature*, 440:1166–1169, April 2006.

[54] W. R. Frei, D. A. Tortorelli, and H. T. Johnson. Geometry projection method for optimizing photonic nanostructures. *Opt. Lett.*, 32:77, 2007.

[55] Robert C. Gauthier and Khaled Mnaymneh. FDTD analysis of 12-fold photonic quasicrystal central pattern localized states. *Opt. Comm.*, 264:78–88, 2006.

[56] Robert C. Gauthier and Khaled Mnaymueh. Photonic band gaps properties of 12-fold quasicrystal determined through fdtd analysis. *Opt. Express*, 13(6):1985–1998, 2005.

[57] W. Gellermann, M. Kohmoto, B. Sutherland, and P.C. Taylor. Localization of light waves in fibonacci dielectric multilayers. *Phys. Rev. Lett.*, 72(5):633–636, 1994.

[58] W. A. Goddard, D. Brenner, S. E. Lyshevski, and G. J. Iafrate, editors. CRC Press, Boca Raton, FL, 2nd edition, 2007.

[59] C. Godreche. Indexing the diffraction spectrum of a non-pisot self-similar structure. *Phys. Rev. B*, 45(1):176–185, 1992.

[60] Israel Gohberg, Sehmour Goldberg, and Marinus A. Kaashoek. *Basic Classes of Linear Operators.* Birkhäuser, Basel, 2000.

[61] Nigel Goldengeld. *Lectures on phase transitions and the renormalization group.* Perseus Books, 1992.

[62] Herbert Goldstein. *Classical Mechanics.* Addison-Wesley, Reading, Mass., second edition, 1980.

[63] Gene H. Golub and Charles F. Van Loan. *Matrix Computations.* The Johns Hopkins University Press, Baltimore, Maryland, 3rd edition, 1996.

[64] Thomas C. Halsey, Mogens H. Jensen, Leo P. Kadanoff, Itamar Procaccia, and Boris I. Shraiman. Fractal measures and their singularities: The characterization of strange sets. *Phys. Rev. A*, 33:1141, 1986.

[65] G. H. Hardy and E. M. Wright. *An Introduction to the Theory of Numbers.* Oxford University Press, Oxford, 5th edition, 1979.

[66] Masashi Hase, Hiroshi Miyazaki, Mitsuru Egashira, Norio Shinya, Kenji Kojima, and Shin-ichi Uchida. Photonic band gap and anisotropic structures in transmission spectra of two-dimensional fivefold and eightfold symmetric quasiperiodic photonic crystals. *Phys. Rev. B*, 66:214205–214212, 2002.

[67] C. Henkel and K. Joulain. Casimir force between designed materials: What is possible and what not. *Europhys. Lett.*, 72:929–935, 2005.

[68] C. Hertlein, L. Helden, A. Gambassi, S. Dietrich, and C. Bechinger. Direct measurement of critical Casimir forces. *Nature*, 451:172, 2008.

[69] X. Q. Huang, S. S. Juang, R. W. Peng, and A. Hu. Perfect transmission and self-similar optical transmission spectra in symmetric Fibonacci-class multilayers. *Phys. Rev. B*, 63:245104–245112, 2001.

[70] J. N. Israelachvili. *Intermolecular and Surface Forces.* Academic Press, London, 1991.

[71] J. D. Jackson. *Classical Electrodynamics.* Wiley, New York, third edition, 1998.

[72] C. Janot. *Quasicrystals.* Clarendon Press, 1992.

[73] J. D. Joannopoulos, R. D. Meade, and J. N. Winn. *Photonic Crystals: Molding the Flow of Light.* Princeton Univ. Press, 1995.

[74] Steven G. Johnson. The nlopt nonlinear-optimization package. `http://ab-initio.mit.edu/nlopt`.

[75] Steven G. Johnson. Numerical methods for computing Casimir interactions. *arXiv:quant-ph/1007.0966*, 2010. to appear in "Lecture Notes in Physics: Casimir physics (Springer, eds. D. A. R. Dalvit, P. W. Milonni, D. C. Roberts, and F. S. S. Rosa.

[76] Steven G. Johnson and J. D. Joannopoulos. Block-iterative frequency-domain methods for Maxwell's equations in a planewave basis. *Opt. Express*, 8(3):173–190, 2001.

[77] Steven G. Johnson and Alexander P. McCauley. Quasi-periodic optics: theory and methods. to appear in "Optics of Aperiodic Structures: Fundamentals and Device Applications" (Pan Stanford Publishing, ed. Luca Dal Negro).

[78] Karl Joulain, Jean-Phillipe Mulet, Francois Marquier, Remi Carminati, and Jean-Jacques Greffet. Surface electromagnetic waves thermally excited: Radiative heat transfer, coherence properties and casimir forces revisited in the near field. *Surf. Sci. Reports*, 57(3–4):59–112, 2005.

[79] M. A. Kaliteevski, S. Brand, R. A. Abram, T. F. Krauss, R. M. De La Rue, and P. Millar. Two-dimensional penrose-tiled photonic quasicrystals: Diffraction of light and fractal density of modes. *J. Mod. Opt.*, 47:1771–1778, 2000.

[80] M. A. Kaliteevski, S. Brand, R. A. Abram, T. F. Krauss, P. Millar, and R. De La Rue. Diffraction and transmission of light in low-refractive index Penrose-tiled photonic quasicrystals. *J. Phys: Cond. Mat.*, 13:10459–10470, 2001.

[81] C. Y. Kao, S. Osher, and E. Yablonovitch. Maximizing band gaps in two-dimensional photonic crystals by using level set methods. *Appl. Phys. B*, 81:235, 2005.

[82] O. Kenneth and S. Nussinov. New "polarized version" of the Casimir effect is measurable. *Phys. Rev. D*, 63:121701(R), 2001.

[83] Oded Kenneth and Israel Klich. Opposites attract: A theorem about the Casimir force. *Phys. Rev. Lett.*, 97:160401, 2006.

[84] Oded Kenneth and Israel Klich. Casimir forces in a T-operator approach. *Phys. Rev. B*, 78:014103, 2008.

[85] Sun-Kyung Kim, Jee-Hye Lee, Se-Heon Kim, In-Kang Hwang, and Yong-Hee Lee. Photonic quasicrystal single-cell cavity mode. *Appl. Phys. Lett.*, 86:031101, 2005.

[86] Mahito Kohmoto, Leo P. Kadanoff, and Chao Tang. Localization problem in one dimension: Mapping and escape. *Phys. Rev. Lett.*, 50(23):1870–1872, 1983.

[87] Mahito Kohmoto, Bill Sutherland, and K. Iguchi. Localization in optics: Quasiperiodic media. *Phys. Rev. Lett.*, 58(23):2436–2438, 1987.

[88] Matthias Krüger. Private communication. 2011.

[89] Matthias Krüger, Thornsten Emig, and Mehran Kardar. Non-equilibrium electromagnetic fluctuations: heat transfer and interactions. *Phys. Rev. Lett.*, 106:210404, 2011.

[90] Matthias Krüger, Thorsten Emig, Giuseppe Bimonte, and Mehran Kardar. Non-eqiulibrium thermal transfer. *In Preparation*, 2011.

[91] T. Kushta and K. Yasumoto. Electromagnetic scattering from periodic arrays of two circular cylinders per unit cell. *PIER*, 29:69, 2000.

[92] M. Kuzuoglu and R. Mittra. Frequency dependence of the constitutive parameters of causal perfectly matched anisotropic absorbers. *IEEE Microwave and Guided Wave Lett.*, 6:447, 1996.

[93] Astrid Lambrecht and V. N. Marachevsky. Casimir interactions of dielectric gratings. *Phys. Rev. Lett.*, 101:160403, 2008.

[94] S. Lamoreaux. Progress in experimental measurements of the surface-surface Casimir force: Electrostatic calibrations and limitations to accuracy. Preprint at http://arxiv.org/abs/1008.3640 (2010).

[95] S. K. Lamoreaux. Demonstration of the Casimir force in the 0.6 to 6μm range. *Phys. Rev. Lett.*, 78:5, 1997.

[96] L. D. Landau, E. M. Lifshitz, and L. P. Pitaevskiĭ. *Electrodynamics of Continuous Media*, volume 8. Pergamon Press, Oxford, 1960.

[97] L. D. Landau, E. M. Lifshitz, and L. P. Pitaevskiĭ. *Statistical Physics Part 2*, volume 9. Pergamon, Oxford, 1960.

[98] Alexandra Ledermann, Ludovico Cademartiri, Martin Hermatschweiler, Costanza Tonninelli, Geoffrey A. Ozin, Diederik S. Weirsma, Martin Wegener, and Georg Von Freymann. Three-dimensional silicon inverse photonic quasicrystals for infrared wavelengths. *Nature Mat.*, 5:942–945, December 2006.

[99] Ulf Leonhardt and Thomas G. Philbin. Quantum levitation by left-handed metamaterials. *New J. Phys.*, 9:254, 2007.

[100] Michael Levin and Steven G. Johnson. Is the electrostatic force between a point charge and a neutral metallic object always attractive? *arXiv:1007.2175*, 2010.

[101] Michael Levin, Alexander P. McCauley, Alejandro W. Rodriguez, M. T. Homer Reid, and Steven G. Johnson. Casimir repulsion between metallic objects in vacuum. *Phys. Rev. Lett.*, 105:090403, 2010.

[102] Jing Li, Degang Zhao, and Zhengyou Liu. Zero-$\bar{n}$ photonic band gap in a quasiperiodic stacking of positive and negative refractive index materials. *Phys. Lett. A*, 332:461–468, 2004.

[103] Mo Li, PerniceW H. P., and TangH X. Tunable bipolar optical interactions between guided lightwaves. *Nat Photon*, 3(8):464–468, 2009.

[104] E. M. Lifshitz. *Dokl. Akad. Nauk. SSSR*, 100:879, 1955.

[105] E. M. Lifshitz and Lev P. Pitaevskii. *Statistical Physics: Part 2.* Pergamon, Oxford, 1980.

[106] R. Lifshitz. The square fibonacci tiling. *J. of Alloys and Compounds*, 342:186–190, 2000.

[107] Ron Lifshitz, Andy Arie, and Alon Bahabad. Photonic quasicrystals for nonlinear optical frequency conversion. *Phys. Rev. Lett.*, 95:133901, 2005.

[108] J. J. Loomis and H. J. Maris. Theory of heat transfer by evanescent electromagnetic waves. *Phys. Rev. B*, 50:18517–18524, 1994.

[109] Jian Ping Lu and Joseph L. Birman. Electronic structure of a quasiperiodic system. *Phys. Rev. B*, 36(8):4471–4474, 1987.

[110] M. F. Maghrebi. A diagrammatic expansion of the Casimir energy in multiple reflections: theory and applications. *Phys. Rev. D*, 83:045004, 2011.

[111] Mohammad F. Maghrebi, Sahand J. Rahi, Thornsten Emig, Noah Graham, Robert L. Jaffe, and Mehran Kardar. Casimir force between sharp-shaped conductors. *Proc. Natl. Acad. Sci.*, 108:6867, 2011.

[112] J. Mahanty and B. W. Ninham. *Dispersion Forces.* Academic Press, London, 1976.

[113] P. A. Maia Neto, A. Lambrecht, and S. Reynaud. Casimir energy between a plane and a sphere in electromagnetic vacuum. *Phys. Rev. A*, 78:012115, 2008.

[114] Martin Maldovan and Edwin L. Thomas. Diamond-structured photonic crystals. *Nature Materials*, 3:593–600, 2004.

[115] H. J. Mamin. Thermal writing using a heated atomic force microscope tip. *Appl. Phys. Lett.*, 69:433, 1996.

[116] Weining Man, Mischa Megens, Paul J. Steinhardt, and P. M. Chaikin. Experimental measurement of the photonic crystal properties of icosahedral quasicrystals. *Nature*, 436:993–996, August 2005.

[117] Valery N. Marachevsky. Casimir interaction of two plates inside a cylinder. *Phys. Rev. D*, 75:085019, 2007.

[118] Alexander P. McCauley, M. T. Homer Reid, Matthias Krüger, and S. G. Johnson. Modeling near-field radiative heat transfer from sharp objects using a general 3d numerical scattering technique. *arXiv:1107:2111*, 2011.

[119] Alexander P. McCauley, Alejandro W. Rodriguez, J. D. Joannopoulos, and Steven G. Johnson. Casimir forces in the time domain: applications. *Phys. Rev. A*, 81:012119, 2010.

[120] Alexander P. McCauley, Alejandro W. Rodriguez, M. T. Homer Reid, and Steven G. Johnson. Casimir repulsion beyond the dipole regime. *arXiv:1105.0404*, 2011.

[121] Alexander P. McCauley, F. S. S. Rosa, Alejandro W. Rodriguez, John D. Joannopoulos, D. A. R. Dalvit, and Steven G. Johnson. Structural anisotropy and orientation-induced casimir repulsion in fluids. *Phys. Rev. A*, 83:052503, 2011.

[122] Alexander P. McCauley, Rongkuo Zhao, M. T. Homer Reid, Alejandro W. Rodriguez, Juangfeng Zhuo, F. S. S. Rosa, J. D. Joannopoulos, D. A. R. Dalvit, Costas M. Soukoulis, and Steven G. Johnson. Microstructure effects for Casimir forces in chiral metamaterials. *Phys. Rev. B*, 82:165108, 2010.

[123] E. Merzbacher. *Quantum Mechanics.* John Wiley and Sons, New York, 1998.

[124] Ricardo Messina and Mauro Antezza. Casimir-lifshitz force out of thermal equilibrium and heat transfer between arbitrary bodies. *arXiv*, 1012.5183, 2011.

[125] A. Milling, Paul Mulvaney, and Ian Larson. Direct measurement of repulsive van der Waals interactions using an atomic force miscroscope. *J. Colloid Interface Sci.*, 180(2):460–465, 1996.

[126] P. W. Milonni. *The Quantum Vacuum: An Introduction to Quantum Electrodynamics.* Academic Press, San Diego, 1993.

[127] K. A. Milton. *The Casimir Effect: Physical Manifestations of Zero-Point Energy.* Singapore: World Scientific, 2001.

[128] Khaled Mnaymneh and Robert C. Gauthier. Mode localization and band-gap formation in defect-free photonic quasicrystals. *Opt. Express*, 15(8):5089–5099, 2007.

[129] M. G. Moharam, E. B. Grann, D. A. Pommet, and T. K. Gaylord. Formulation for stable and efficient implementation of the rigorous coupled-wave analysis of binary gratings. *J. Opt. Soc. Am. A*, 12:1077, 1995.

[130] U. Mohideen and A. Roy. Precision measurement of the Casimir force from 0.1 to 0.9 μm. *Phys. Rev. Lett.*, 81:4549–4552, 1998.

[131] D. Morecroft, J. K. W. Yang, S. Schuster, K. K. Berggren, Q. Xia, W. Wu, and R. S. Williams. Sub-15 nm nanoimprint molds and pattern transfer. *J. Vac. Sci. Technol. B*, 27:2837, 2009.

[132] J. P. Mulet, K. Joulain, R. Carminati, and J. J. Greffet. Nanoscale radiative heat transfer between a small particle and a plane surface. *Appl. Phys. Lett.*, 78:2931–2933, 2001.

[133] J. N. Munday, D. Iannuzzi, Y. Barash, and F. Capasso. Torque induced on birefringent plates by quantum fluctuations. *Phys. Rev. A*, 71:042102, 2005.

[134] Jeremy Munday, Federico Capasso, and V. Adrian Parsegian. Measured long-range repulsive Casimir-lifshitz forces. *Nature*, 457:170–173, 2009.

[135] A. Narayanaswamy and G. Chen. Thermal near-field radiative transfer between two spheres. *Phys. Rev. B*, 77:075125, 2008.

[136] Arvind Narayanaswamy and Gang Chen. Thermal near-field radiative transfer between two spheres. *Phys. Rev. B*, 77(7):075125, 2008.

[137] M. Notomi, H. Suzuki, T. Tamamura, and K. Edagawa. Lasing action due to the two-dimensional quasiperiodicity of photonic qyasicrystals with Penrose lattice. *Phys. Rev. Lett.*, 92(12):123906, 2004.

[138] J. M. Obrecht, R. J. Wild, M. Antezza, L. P. Pitaevskii, S. Stringari, and E. A. Cornell. Measurement of the temperature dependence of the Casimir-Polder force. *Phys. Rev. Lett.*, 98(6):063201, 2007.

[139] Stellan Ostlund, Rahul Pandit, David Rand, Hans Scheller, and Eric Siggia. One-dimensional Schrödinger equation with an almost periodic potential. *Phys. Rev. Lett.*, 50(23):1873–1876, 1983.

[140] Clayton Otey and Shanhui Fan. Exact microscopic theory of electromagnetic heat transfer between a dielectric sphere and plate. *arXiv*, 1103.2668, 2011.

[141] Edward Ott. *Chaos in Dynamical Systems.* Cambridge University Press, 2nd edition, 2002.

[142] J.L. Pan, H.K.H. Choy, and Jr. Fonstad, C.G. Very large radiative transfer over small distances from a black body for thermophotovoltaic applications. *Electron Devices, IEEE Transactions on*, 47(1):241 –249, jan. 2000.

[143] Kai Pan, Alexander P. McCauley, Alejandro W. Rodriguez, M. T. Homer Reid, Jacob K. White, and Steven G. Johnson. Calculation of nonzero-temperature Casimir forces in the time domain. *Phys. Rev. A*, 83:040503(R), 2011.

[144] G. J. Parker, M. D. B. Charlton, M. E. Zoorob, J. J. Baumberg, M. C. Netti, and T. Lee. Highly engineered mesoporous structures for optical processing. *Phil. Trans. Soc. A*, 364:189–199, 2006.

[145] V. A. Parsegian and George H. Weiss. Dielectric anisotropy and the van der waals interaction between bulk media. *J. Adh.*, 3(4):259–267, 1972.

[146] S. Pasquali and A. C. Maggs. Numerical studies of Lifshitz interactions between dielectrics. *Phys. Rev. A.*, 79:020102(R), 2009.

[147] J. B. Pendry. Radiative exchange of heat between nanostructures. *J. Phys.: Condens. Matter*, 11:6621–6633, 1999.

[148] J. B. Pendry, A. J. Holden, W. J. Stewart, and I. Youngs. Extremely low frequency plasmons in metallic mesostructures. *Phys. Rev. Lett.*, 76:4773, 1996.

[149] T. G. Philbin and U. Leonhardt. *Phys. Rev. A*, 78:042107, 2008.

[150] Mulet Phillipe-Jean, Karl Joulain, Remi Carminati, and Jean-Jacques Greffet. Enhanced radiative heat transfer at nanometric distances. *Micro. Therm. Eng.*, 6:209–222, 2002.

[151] D. Polder and M. Van Hove. Theory of radiative heat transfer between closely spaced bodies. *Phys. Rev. B*, 4(10):3303–3314, 1971.

[152] M. L. Povinelli, M. Loncar, M. Ibanescu, E. J. Smythe, S. G. Johnson, F. Capasso, and J. D. Joannopoulos. Evanescent-wave bonding between optical waveguides. *Opt. Lett.*, 30:3042, 2005.

[153] M. Quilichini. Phonon excitations in quasicrystals. *Reviews of Modern Physics*, 69(1):277–314, 1997.

[154] S. J. Rahi, Thornsten Emig, N. Graham, Robert L. Jaffe, and Mehran Kardar. Scattering theory approach to electrodynamic Casimir forces. *Phys. Rev. D*, 80:085021, 2009.

[155] S. J. Rahi, Mehran Kardar, and Thornsten Emig. Constraints on stable equilibria with fluctuation-induced forces. *Phys. Rev. Lett.*, 105:070404, 2010.

[156] S. J. Rahi, Alejandro W. Rodriguez, Thorsten Emig, Robert L. Jaffe, Steven G. Johnson, and Mehran Kardar. Nonmonotonic effects of parallel sidewalls on Casimir forces between cylinders. *Phys. Rev. A*, 77(3):030101(R), 2008.

[157] S. Anantha Ramakrishna. Physics of negative refractive index materials. *Rep. Prog. Phys.*, 68(2):449, 2005.

[158] R. K. Rao and P. Yip. *Discrete Cosine Transform: Algorithms, Advantages, Applications.* Academic Press, Boston, 1990.

[159] S. Rao, D. Wilton, and A. Glisson. Electromagnetic scattering by surfaces of artibrary shape. *IEEE Trans. Anten. Prop.*, 30:409, 1982.

[160] Homer Reid, Jacob White, and Steven G. Johnson. Efficient computation of Casimir interactions between arbitrary 3d objects with arbitrary material properties. Preprint at http://arxiv.org/abs/1010.5539 (2010).

[161] M. T. Homer Reid. *Fluctuating Surface Currents: A New Algorithm for Efficient Prediction of Casimir Interactions among Arbitrary Materials in Arbitrary Geometries.* PhD thesis, MIT, 2010.

[162] M. T. Homer Reid, Alejandro W. Rodriguez, Jacob White, and Steven G. Johnson. Efficient computation of three-dimensional Casimir forces. *Phys. Rev. Lett.*, 103(4):040401, 2009.

[163] M. T. Homer Reid et. al. 2d bem method. *In Preparation*, 2011.

[164] Frederick Reif. *Fundamentals of statistical and thermal physics.* McGraw-Hill Series in Fundamentals of Physics, 1965.

[165] R. B. Rodrigues, P. A. Maia Neto, A. Lambrecht, and S. Reynaud. Vacuum-induced torque between corrugated metallic plates. *Europhys. Lett.*, 75(5):822–828, 2006.

[166] Alejandro Rodriguez, M. Ibanescu, David Iannuzzi, Federico Capasso, J. D. Joannopoulos, and Steven G. Johnson. Computation and visualization of Casimir forces in arbitrary geometries: Non-monotonic lateral-wall forces and failure of proximity force approximations. *Phys. Rev. Lett.*, 99(8):080401, 2007.

[167] Alejandro Rodriguez, M. Ibanescu, David Iannuzzi, J. D. Joannopoulos, and Steven G. Johnson. Virtual photons in imaginary time: computing Casimir forces in arbitrary geometries via standard numerical electromagnetism. *Phys. Rev. A*, 76(3):032106, 2007.

[168] Alejandro W. Rodriguez, Federico Capasso, and Steven G. Johnson. The Casimir effect in microstructured geometries. *Nature Phot.*, 5:211–221, 2011.

[169] Alejandro W. Rodriguez, Ognjen Ilic, Peter Bermel, Ivan Celanovic, John D. Joannopoulos, Marin Soljačić, and Steven G. Johnson. Frequency-selective near-field enhancement of radiative heat transfer via photonic-crystal slabs: A general computational approach. *arXiv*, 1105.0708, 2011.

[170] Alejandro W. Rodriguez, J. D. Joannopoulos, and Steven G. Johnson. Repulsive and attractive Casimir forces in a glide-symmetric geometry. *Phys. Rev. A*, 77(6):062107, 2008.

[171] Alejandro W. Rodriguez, Alexander P. McCauley, Yehuda Avniel, and Steven G. Johnson. Computation and visualization of photonic quasicrystal spectra via blochs theorem. *Phys. Rev. B*, 77(10):104201, 2008.

[172] Alejandro W. Rodriguez, Alexander P. McCauley, J. D. Joannopoulos, and Steven G. Johnson. Casimir forces in the time domain: theory. *Phys. Rev. A*, 80(1):012115, 2009.

[173] Alejandro W. Rodriguez, Alexander P. McCauley, J. D. Joannopoulos, and Steven G. Johnson. Theoretical ingredients of a Casimir analog computer. *Proc. Natl. Acad. Sci.*, 107:9531–9536, 2010.

[174] Alejandro W. Rodriguez, Jeremy Munday, Diego Davlit, Federico Capasso, J. D. Joannopoulos, and Steven G. Johnson. Stable suspension and dispersion-induced transition from repulsive Casimir forces between fluid-separated eccentric cylinders. *Phys. Rev. Lett.*, 101(19):190404, 2008.

[175] Alejandro W. Rodriguez, David Woolf, Pui-Chuen Hui, Eiji Iwase, Alexander P. McCauley, Federico Capasso, Marko Loncar, and Steven G. Johnson. Torward all-optical control and measurement of Casimir forces via evanescent optical forces. *arXiv*, 1101.4237, 2011.

[176] M. B. Romanowsky and F. Capasso. Orientation-dependent Casimir force arising from highly anisotropic crystals: application to $bi_2sr_2cacu_2o_{8+}$. *Phys. Rev. A*, 78:042110, 2008.

[177] J. Romero-Vivas, D. N. Chigrin, A. V. Lavrinenko, and C. M. Sotomayor Torres. Photonic quasicrystals for application in WDM systems. *Phys. Stat. Sol.*, 202(6):997–1001, 2005.

[178] F. S. S. Rosa. On the possibility of Casimir repulsion using metamaterials. *J. Phys. Conf. Ser.*, 161:012039, 2009.

[179] F. S. S. Rosa, D. A. R. Dalvit, and P. W. Milonni. Casimir interactions for anisotropic magnetodielectric metamaterials. *Phys. Rev. A*, 78:032117, 2008.

[180] F. S. S. Rosa, D. A. R. Dalvit, and P. W. Milonni. Casimir-Lifshitz theory and metamaterials. *Phys. Rev. Lett.*, 100:183602, 2008.

[181] Emmanuel Rousseau, Alessandro Siria, Guillaume Jourdan, Sebastian Volz, Fabio Comin, Joel Chevrier, and Jean-Jacques Greffet. Radiative heat transfer at the nanoscale. *Nature Photonics*, 3:514–517, 2009.

[182] W. Rudin. *Real and Complex Analysis.* McGraw-Hill, New York, 1966.

[183] S. M. Rytov, Yu. A. Kravtsov, and V. I. Tatarskii. *Principles of Statistical Radiophsics III.* Springer-Verlag, 1989.

[184] Mattias Severin and Rolf Riklund. Coexistence of localized, critical, and extended states in a one-dimensional substitutional non-fibonaccian quasicrystal: A multifractal analysis. *Phys. Rev. B*, 39:10362, 1989.

[185] Cheng-Gang Shao, Ai-Hong Tong, and Jun Luo. Casimir torque between birefringent plates. *Phys. Rev. A*, 72:022102, 2005.

[186] D. Shechtman, I. Blech, D. Gratias, and J. W. Cahn. Metallic phase with long-range orientational order and no translational symmetry. *Phys. Rev. Lett.*, 53:1951, 1984.

[187] Sheng Shen, Arvind Narayanaswamy, and Gang Chen. Surface phonon polaritons mediated energy transfer between nanoscale gaps. *Nano Letters*, 9(8):2909–2913, 2009.

[188] M. G. Silveirinha and S. I. Maslovski. Comment on "repulsive Casimir forces in chiral metamaterials". *arXiv:1007.1582v1*, 2010.

[189] Walter Steurer and Torsten Haibach, editors. *Physical Properties of Quasicrystals*, chapter 2. Springer, 1999.

[190] Walter Steurer and Daniel Sutter-Widmer. Photonic and phononic quasicrystals. *J. Phys. D*, 40:R229–R247, 2007.

[191] Julius Adams Stratton. *Electromagnetic Theory.* McGraw-Hill, New York, 1941.

[192] J. B. Suck, M. Schreiber, and P. Haussler, editors. *Quasicrystals*, chapter 2. Springer, 2004.

[193] K. Svanberg. A class of globally convergent optimization methods based on conservative convex separable approximations. *SIAM J. Optim.*, 12:555, 2002.

[194] Allen Taflove and Susan C. Hagness. *Computational Electrodynamics: The Finite-Difference Time-Domain Method.* Artech, Norwood, MA, 2000.

[195] C. Thelander, P. Agarwal, S. Brongersma, J. Eymery, L. F. Feiner, A. Forchel, M. Scheffler, W. Reiss, B. J. Ohlsson, U. Goesele, and L. Samuelson. Nanowire-based one-dimensional electronics. *Mat. Today*, 9:28, 2006.

[196] Lloyd N. Trefethen and David Bau. *Numerical linear algebra.* SIAM, Philadelphia, 1st edition, 1997.

[197] S. Tretyakov, A. Shivola, and L. Jylha. Backward-wave regime and negative refraction in chiral composites. *Photon. and Nano.*, 2:107, 2005.

[198] L. Tsang, J. A. Kong, and K.-H. Ding. *Scattering of Electromagnetic Waves.* Wiley, New York, 2000.

[199] S. J. van Enk. Casimir torque between dielectrics. *Phys. Rev. A*, 52(4):2569–2575, 1995.

[200] A. I. Volokitin and B. N. J Persson. Radiative heat transfer between nanostructures. *Phys. Rev. B*, 63(20):205404, 2001.

[201] A. I. Volokitin and B. N. J. Persson. Near-field radiative heat transfer and noncontact friction. *Rev. Mod. Phys.*, 79(4):1291–1329, 2007.

[202] K. Wang, S. David, A. Chelnokov, and J. M. Lourtioz. Photonic band gaps in quasicrystal-related approximant structures. *J. Mod. Opt.*, 50(13):2095–2105, 2003.

[203] Yiquan Wang, Cheng Bingying, and Daozhong Zhang. The density of states in quasiperiodic photonic crystals. *J. Phys.: Cond. Mat.*, 15:7675–7680, 2003.

[204] Q. Wei, D. A. R. Dalvit, F. C. Lombardo, F. D. Mazzitelli, and R. Onofrio. Results from electrostatic calibrations for measuring the Casimir force in the cylinder-plate geometry. *Phys. Rev. A*, 81:052115, 2010.

[205] D. S. Wiersma, R. Sapienza, S. Mujumdar, M. Colocci, M. Ghulinyan, and L. Pavesi. Optics of nanostructured dielectrics. *J. Opt. A: Pure and Appl. Opt.*, 7:S190–S197, 2005.

[206] K. Wilder, C. F. Quate, D. Adderton, R. Bernstein, and V. Elings. Noncontact nanolithography using the atomic force microscope. *Appl. Phys. Lett.*, 73:2527, 1998.

[207] Ping Xie, Zhao-Qing Zhang, and Xiangdong Zhang. Gap solitons and soliton trains in finite-sized two-dimensional periodic and quasiperiodic photonic crystals. *Phys. Rev. E*, 67:026607, 2003.

[208] K. Yasumoto and H. Jia. Analysis of electromagnetic scattering from layered crossed-gratings of circular cylinders using lattice sum techniques. In Y. Jin, editor, *Wave Prop., Scatt. and Emission in Complex Media*, pages 225–249, Singapore, 2004. World Scientific.

[209] J. Y. Zhang, H. L. Tam, W. H. Wong, Y. B. Pun, J. B. Xia, and K. W. Cheah. Isotropic photonic bandgap in Penrose textured metallic microcavity. *Sol. State Comm.*, 138:247–249, 2006.

[210] Xiangdong Zhang, Zhao-Qing Zhang, and C. T. Chan. Absolute photonic band gaps in 12-fold symmetric photonic qusicrystals. *Phys. Rev. B*, 63:081105–081108, 2001.

[211] Z. S. Zhang, B. Zhang, J. Xu, Z. J. Yang, Z. X. Qin, T. J. Yu, and D. P. Yu. Effects of symmetry of GaN-based two-dimensional photonic crystal with quasicrystal lattices on enhancement of surface light extraction. *Appl. Phys. Lett.*, 88:171103, 2006.

[212] Zhuomin M. Zhang. *Nano/Microscale heat transfer.* McGraw-Hill, 2007.

[213] R. Zhao, T. Koschny, E. N. Economou, and C. M. Soukoulis. Comparision of chiral metamaterial designs for repulsive Casimir force. *arXiv:0911.2019*, 2009.

[214] R. Zhao, J. Zhou, Th. Koschny, E. N. Economou, and C. M. Soukoulis. Repulsive Casimir forces in chiral metamaterials. *Phys. Rev. Lett.*, 103:103602, 2009.

[215] E. S. Zijlstra and T. Janssen. Non-spiky density of states of an icosahedral quasicrystal. *Europhys. Lett.*, 52(5):578–583, 2000.

[216] Richard W. Ziolkowski. *Metamaterials: Physics and Engineering Explorations.* John and Wiley and Sons, Inc., Hoboken, NJ, 2006.

[217] M. E. Zoorob, M. D. B. Charlton, G. J. Parker, J. J. Baumberg, and M. C. Netti. Complete and absolute photonic bandgaps in highly symmetric photonic quasicrystals embedded in low regractive index materials. *Mat. Science and Eng.*, 74:168–174, 2000.

[218] M. E. Zoorob, M. D.B. Charlton, G. J. Parker, J. J. Baumberg, and M. C. Netti. Complete photonic bandgaps in 12-fold symmetric quasicrystals. *Nature*, 404:740–743, 2000.

[219] J. Zou, Z. Marcet, Alejandro W. Rodriguez, M. T. Homer Reid, Alexander P. McCauley, I. Kravchenko, Y. Bao, Steven G. Johnson, and H. B. Chan. Casimir force between monolithic silicon microstructures. *Submitted*, 2011.